SOIL LIQUEFACTION DURING EARTHQUAKES

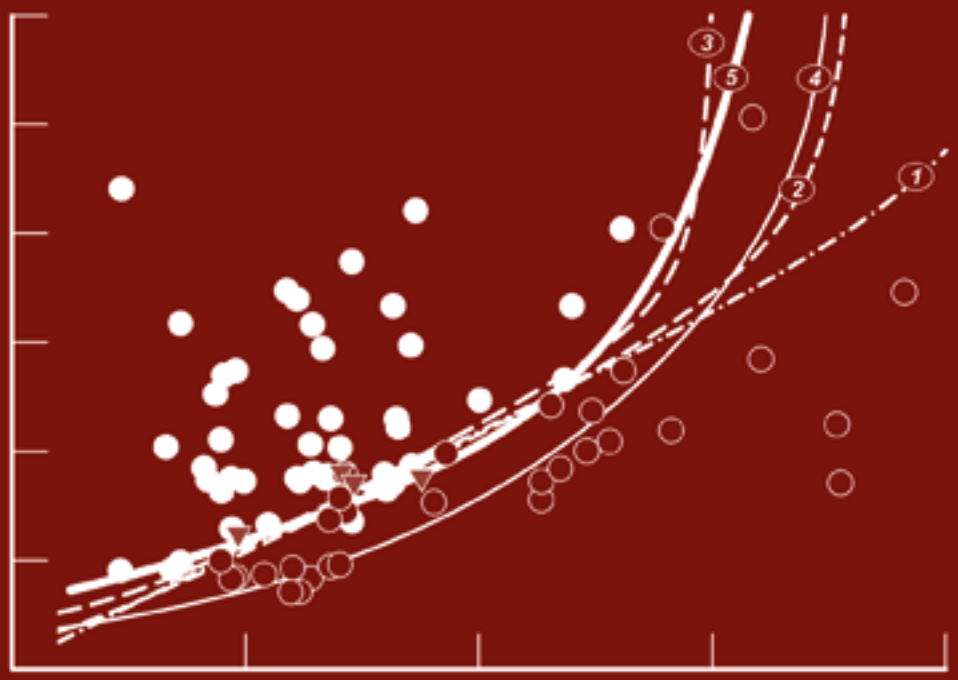

I. M. IDRISS
R. W. BOULANGER

EARTHQUAKE ENGINEERING RESEARCH INSTITUTE

Become a member of The **Earthquake Engineering Research Institute!**

Benefits of Membership

16 great reasons to join the Earthquake Engineering Research Institute
(18 if you're a student!)

- EERI is the principal national society in the U.S. for earthquake professionals. EERI's members are dedicated to reducing earthquake risk by staying on top of the latest scientific and engineering advances, better understanding the social and economic impacts of earthquakes, and serving as advocates for seismic safety.

- Our 2,300 members come from nearly every state in the nation and 60 foreign countries and include the world's leading engineers and earth scientists, architects and urban planners, and experts in the policy and social sciences. EERI members come from all areas of professional practice, government, and academia.

- EERI works to keep earthquake policy issues on the front burner and to press for more support for research and implementation. EERI's advocacy activities and high-profile

national conferences have opened the doors of influential members of congress and federal agencies to concerns about seismic research and practice.

EERI provides members with many ways to stay on top of the latest research and professional developments. EERI members receive:

Earthquake Spectra, EERI's prestigious quarterly peer-reviewed journal, containing professional papers that bear directly on the practice of earthquake engineering and related disciplines

The monthly EERI Newsletter, filled with timely information on recent earthquakes, new publications, conferences, and news of the profession

The Membership Roster, an invaluable sourcebook of professionals in the field

- Latest information about recent earthquakes and post-earthquake **reconnaissance reports** on the Learning from Earthquakes Program website
- Access to the resources of the **World Housing Encyclopedia**: http://www.world-housing.net/
- **Technical publications**: monographs, oral histories, and specialty reports

EERI offers special deals to graduating Student Members:

- Each EERI Student Member who joins EERI as a Young Professional within 12 months of graduation is eligible to receive a **coupon from Computers and Structures, Inc.**, that is good for an 80% discount on any CSI software products — up to a limit of $10,000! The coupon may be redeemed anytime within two years of enrollment as an EERI Young

Professional Member or Regular Member. The coupon is not transferable and may be redeemed only by the Young Professional Member and his/her employer.

- As if that weren't enough incentive to sign up as a Young Professional Member, graduating Student Members who do so also get their first year of membership absolutely **free**! Click here to download application (or visit the eeri.org website). Dues the following year will be only half the Young Professional rate and for the next three years the full Young Professional rate, which is still a bargain at just half of regular member dues.

EERI offers reduced member-only fees to meetings, national and specialty conferences, and technical seminars.

- EERI's **technical seminars** bring the latest in cutting-edge research to those in practice. Recent seminars have focused on seismic performance of existing concrete construction and issues in geotechnical engineering of importance to practicing geotechnical and structural engineers.

- EERI members are now able to **download videos** of the live presentations from these seminars through our online store at http://www.eeri.org

- EERI members receive substantial **price reductions** on these technical videos.

- EERI members receive significant **member-only discounts** on materials in the Online EERI store, and on registration fees for technical seminars, meetings, and conferences.

- EERI's committees and student and regional chapters provide immediate **opportunities** to apply your knowledge and skills to make the world a safer place.

- **Advance information and reduced fees** for Seminars, Annual Meetings and Continuing Education programs

- The opportunity to **participate** in technical committees and projects

Join us today to stay on top of the latest developments in research and practice, and share your knowledge and expertise to help reduce earthquake risk throughout the world!

Join EERI Today!

Visit us at: http://www.eeri.org

SOIL LIQUEFACTION DURING EARTHQUAKES

For more monographs, publications, or videos, visit http://www.eeri.org

ORIGINAL MONOGRAPH SERIES

Engineering Monographs on Earthquake Criteria,
Structural Design, and Strong Motion Records

Coordinating Editor: Mihran S. Agbabian

MNO-1 *Reading and Interpreting Strong Motion Accelerograms,* by Donald E. Hudson, 1979

MNO-2 *Dynamics of Structures, A Primer,* by Anil K. Chopra, 1982 (out of print)

MNO-3 *Earthquake Spectra and Design,* by Nathan M. Newmark and William J. Hall, 1982

MNO-4 *Earthquake Design Criteria,* by George W. Housner and Paul C. Jennings, 1982

MNO-5 *Ground Motions and Soil Liquefaction During Earthquakes,* by H. Bolton Seed and I. M. Idriss, 1983

MNO-6 *Seismic Design Codes and Procedures,* by Glen V. Berg, 1983 (out of print)

MNO-7 *An Introduction to the Seismicity of the United States,* by S. T. Algermissen, 1983

SECOND MONOGRAPH SERIES

Engineering Monographs on Miscellaneous Earthquake
Engineering Topics

MNO-8 *Seismic Design with Supplemental Energy Dissipation Devices,* by Robert D. Hanson and Tsu T. Soong, 2001

MNO-9 *Fundamentals of Seismic Protection for Bridges,* by Mark Yashinsky and M. J. Karshenas, 2003

MNO-10 *Seismic Hazard and Risk Analysis,* by Robin K. McGuire, 2004

MNO-12 *Soil Liquefaction during Earthquakes,* by I. M. Idriss and R. W. Boulanger, 2008

SECOND EDITION

MNO-11 *Earthquake Dynamics of Structures, A Primer,* by Anil K. Chopra, 2005 (first edition: MNO-2)

For more monographs, publications, or videos, visit http://www.eeri.org

SOIL LIQUEFACTION DURING EARTHQUAKES

by

I. M. IDRISS

Department of Civil and Environmental Engineering, University of California at Davis

and

R. W. BOULANGER

Department of Civil and Environmental Engineering, University of California at Davis

This monograph was sponsored by the
Earthquake Engineering Research Institute
with support from the Federal Emergency Management Agency

EARTHQUAKE ENGINEERING RESEARCH INSTITUTE
MNO-12

For more monographs, publications, or videos, visit http://www.eeri.org

©2008 Earthquake Engineering Research Institute (EERI), Oakland, California, USA. All rights reserved. No part of this book may be reproduced in any form or by any means without the prior written permission of the publisher.

The publication of this book was supported by FEMA/U.S. Department of Homeland Security under grant #EMW-2004-CA-0297.

EERI is a nonprofit corporation. The objective of EERI is to reduce earthquake risk by advancing the science and practice of earthquake engineering; by improving the understanding of the impact of earthquakes on the physical, social, economic, political, and cultural environment; and by advocating comprehensive and realistic measures for reducing the harmful effects of earthquakes. Any opinions, findings, conclusions, or recommendations expressed herein are the authors' and do not necessarily reflect the views of FEMA or EERI.

Copies of this publication may be ordered from: EERI, 499 14th Street, Suite 320, Oakland, CA 94612-1934; tel: (510) 451-0905; fax: (510) 451-5411; e-mail: eeri@eeri.org; web site: http://www.eeri.org.

Printed in the United States of America.
ISBN #978-1-932884-36-4
EERI Publication No. MNO-12
Technical Editor: Douglas Becker
Production Coordinator: Eloise Gilland
Layout and Production: ICC Macmillan Inc.
Printing: Lynx Communication Group, Inc.

For more monographs, publications, or videos, visit http://www.eeri.org

Dedicated to the memory of Professor H. Bolton Seed—
truly the father of geotechnical earthquake engineering:
a teacher, an advisor, a mentor, an esteemed colleague,
and a true friend.

For more monographs, publications, or videos, visit http://www.eeri.org

For more monographs, publications, or videos, visit http://www.eeri.org

TABLE OF CONTENTS

Foreword xi
Preface xiii
Symbols and Acronyms xv
1 Soil Liquefaction During Earthquakes 1
1.1 Effects of Soil Liquefaction 1
1.2 Development of Engineering Procedures for Assessing and Mitigating Liquefaction 6
1.3 Purpose and Scope of This Monograph 7
2 Fundamentals of Liquefaction Behavior 11
2.1 Monotonic Loading of Saturated Sands 11
2.2 Cyclic Loading Behavior of Saturated Sands 20
2.3 Laboratory Testing of Field Samples and the Effects of Sampling Disturbance 46
2.4 Field Processes Not Replicated in Laboratory Tests . . 52
3 Triggering of Liquefaction 59
3.1 Liquefaction Susceptibility of Soil Deposits 59
3.2 Analysis Framework for Developing Liquefaction Triggering Correlations 63
3.3 Simplified Procedure for Estimating Earthquake-Induced Stresses 66
3.4 In-Situ Tests as Indices for Liquefaction Characteristics 70
3.5 Overburden Correction of in-Situ Test Results 84
3.6 Magnitude Scaling Factor 89
3.7 Overburden Correction Factor, K_σ 94
3.8 Static Shear Stress Correction Factor, K_α 96
3.9 Development of Liquefaction Triggering Correlations from Case Histories 98

For more monographs, publications, or videos, visit http://www.eeri.org

3.10 SPT and CPT Correlations for Triggering of Liquefaction in Clean Sands 100
3.11 SPT and CPT Correlations for Triggering of Liquefaction in Silty Sands 105
3.12 Probabilistic SPT and CPT Correlations for Triggering of Liquefaction 113
3.13 V_s-Based Correlations for Triggering of Liquefaction 115
3.14 Liquefaction Triggering Analyses—Examples and Discussion 117
4 Consequences of Liquefaction 121
4.1 General Considerations 121
4.2 Instability and the Residual Shear Strength of Liquefied Soil 122
4.3 Lateral Spreading Deformations 133
4.4 Post-liquefaction Reconsolidation Settlement 152
4.5 Examples of Lateral Displacement and Settlement Calculations 159
4.6 Margin of Safety 164
5 Mitigation of Liquefaction Hazards 167
5.1 Evaluating and Selecting Possible Mitigation Strategies 167
5.2 Methods of Ground Improvement 168
5.3 General Design and Construction Considerations 181
6 Cyclic Softening in Clays and Plastic Silts 185
6.1 Behavior of Saturated Clays and Plastic Silts during Earthquakes 185
6.2 Relating Monotonic and Cyclic Undrained Shear Strengths 187
6.3 Number of Equivalent Uniform Loading Cycles and MSF 191
6.4 Static Shear Stress Correction Factor 193
6.5 Estimating CRRs 196
6.6 Factors of Safety and Choice of Reference Stress 200
6.7 Transition from Sand-Like to Clay-Like Behavior in Fine-Grained Soils 201
6.8 Consequences of Cyclic Softening in Clays and Plastic Silts 205

For more monographs, publications, or videos, visit http://www.eeri.org

7 Concluding Remarks 209
References 211
Appendix A: Example of SPT-Based Liquefaction Triggering Analysis for a Single Boring 238
Appendix B: Example of CPT-Based Liquefaction Triggering Analysis for a Single Sounding 240
Appendix C: Example of SPT-Based Calculation of Lateral Displacement Index (LDI) and 1-D Reconsolidation Settlement 242

For more monographs, publications, or videos, visit http://www.eeri.org

For more monographs, publications, or videos, visit http://www.eeri.org

FOREWORD

The original seven EERI monographs were published between 1979 and 1983 and grew out of a seminar series on earthquake engineering organized by EERI and presented in several cities. The monographs covered the basic aspects of earthquake engineering in some detail, including seismicity, strong motion records, earthquake spectra, liquefaction, dynamics, design criteria, and codes. The themes were fundamental and focused, and the content was thorough and generally non-controversial. These monographs filled a gap in available documents and were highly acclaimed.

This monograph is intended to update a subject area covered in the original series. The 1982 monograph entitled *Ground Motions and Soil Liquefaction During Earthquakes,* authored by H. Bolton Seed and I.M. Idriss, became a classic text used around the world, primarily for the prediction of liquefaction considering local soils conditions and seismicity. It was so popular and well-used that requests for updates have been persistent for fifteen years.

The material on ground motion covered in the 1982 monograph has become a major field of research and is now well covered in the literature. For example, the influence of soil conditions on local ground motion is now completely accepted and is incorporated into building codes. The use of response spectra to characterize seismic demand at a site is universal. Attenuation relationships not only for peak ground acceleration but also for spectral ordinates are in their third generation, including the recently completed next generation attenuations (NGA) developed under the coordination of the Pacific Earthquake Engineering Research Center.

This monograph therefore focuses on liquefaction and covers liquefaction triggering analysis, consequences and mitigation of liquefaction, and includes an important chapter on cyclic softening of saturated clays not covered in the 1982 monograph. The material has

For more monographs, publications, or videos, visit http://www.eeri.org

been painstakingly collated and edited and has been thoroughly reviewed by a large group of experts, including Jonathan Bray, Steven Kramer, James Mitchell, Jonathan Stewart, Bruce Kutter, Lelio Mejia, Yoshi Moriwaki, and Dan Wilson.

William T. Holmes
Chair, EERI Monograph Committee
April 2008

For more monographs, publications, or videos, visit http://www.eeri.org

PREFACE

The 1982 monograph, *Ground Motions and Soil Liquefaction during Earthquakes,* by H. Bolton Seed and I. M. Idriss, met the need at that time for a simple representation of the essential elements of both earthquake ground motions and soil liquefaction that could be readily understood by engineers who have no particular familiarity with the field.

When we set out to update that monograph, it quickly became clear that a single monograph could no longer provide sufficient coverage of both earthquake ground motions and soil liquefaction. The body of knowledge about these topics has grown so considerably that the current need, which is markedly different from 26 years ago, is for a thorough synthesis of the last 26 years of progress into one accessible resource for students, practicing engineers, and other professionals. Fulfilling such a need for both ground motions and soil liquefaction was impractical within the format of a single monograph, and therefore we chose to focus this monograph on soil liquefaction.

A draft of this monograph was sent to Drs. Jonathan D. Bray, Steven L. Kramer, Bruce L. Kutter, Lelio H. Mejia, James K. Mitchell, Yoshi Moriwaki, Jonathan P. Stewart, and Daniel W. Wilson for their review and comments. Dr. Wilson also checked the equations and the figures for correctness and consistency.

The comments and suggestions we received were extensive, detailed, comprehensive, and on target. We believe that, in addressing these comments and incorporating many of the suggestions, the quality of the monograph has been significantly enhanced.

We are very grateful to these colleagues for generously giving of their time and for providing such valuable and thorough input.

For more monographs, publications, or videos, visit http://www.eeri.org

It is hoped that this monograph on soil liquefaction will serve its intended purpose and, hence, prove useful to readers as a resource in understanding and addressing soil liquefaction problems in teaching, research, and engineering practice.

I. M. Idriss,
Santa, Fe, New Mexico

and

R. W. Boulanger,
Davis, California
July 2008

For more monographs, publications, or videos, visit http://www.eeri.org

SYMBOLS AND ACRONYMS

a_{max}	maximum acceleration, or maximum horizontal ground surface acceleration
a_y	yield acceleration
ACU	anisotropically consolidated undrained
BPT	Becker penetration test
C_E	SPT correction factor for energy ratio
C_B	SPT correction factor for borehole diameter
C_N	SPT or CPT overburden correction factor
C_R	SPT correction factor for rod length
C_S	SPT correction factor for omitting sampler liners
C_{2D}	adjustment factor for the effects of two-directional cyclic loading
CPT	cone penetration test
CRR	cyclic resistance ratio
$\mathrm{CRR_M}$	cyclic resistance ratio at a given earthquake magnitude
CSL	critical-state line
CSR	cyclic stress ratio
D_R	relative density
$D_{R,cs}$	relative density at critical state
DSS	direct simple shear
ER_m	measured value of SPT energy ratio
F	CPT friction ratio
FC	fines content
FS	factor of safety
FS_{liq}	factor of safety against triggering of liquefaction
H	depth to bottom of liquefied layer

For more monographs, publications, or videos, visit http://www.eeri.org

H_{ff}	height of free face for a lateral spread
i	hydraulic gradient
I_c	soil behavior type index from CPT data
I_{RD}	relative dilatancy index
ICD	isotropically consolidated drained
ICU	isotropically consolidated undrained
K_α	correction factor for the effects of an initial static shear stress ratio
K_o	coefficient of lateral earth pressure at rest
K_σ	overburden correction factor
L	distance from the free face in a lateral spread
LD	lateral displacement
LDI	lateral displacement index
LI	liquidity index
LPT	large penetrometer test
M	earthquake magnitude
M_c	critical-state stress ratio in triaxial compression
MSF	magnitude scaling factor
N	number, number of blows, or number of loading cycles
N_e	number of equivalent uniform loading cycles
N_{liq}	number of equivalent uniform loading cycles required to trigger liquefaction
$(N_1)_{60}$	SPT blow count corrected to $ER = 60\%$ and an effective overburden stress of 1 atm
$(N_1)_{60cs}$	equivalent clean sand $(N_1)_{60}$ for computing the CRR
$(N_1)_{60cs-Sr}$	equivalent clean sand $(N_1)_{60}$ for computing residual shear strength
NCEER	National Center for Earthquake Engineering Research
NRC	National Research Council
NSF	National Science Foundation
OCR	overconsolidation ratio
p	mean total stress
p'	mean effective stress
p'_c	mean effective stress at consolidation
P_a	atmospheric pressure

For more monographs, publications, or videos, visit http://www.eeri.org

P_L	probability of liquefaction
PI	plasticity index
q	deviator stress
q_{cyc}	cyclic deviator stress
q_c	cone tip resistance
q_{c1}	cone tip resistance corrected to an effective overburden stress of 1 atm
q_{c1N}	normalized overburden corrected cone tip resistance
Q	normalized cone tip resistance for soil classification, or parameter in I_{RD} and ξ_R relationships
QSSL	quasi-steady-state line
r_d	shear stress reduction coefficient
r_u	excess pore water pressure ratio
$r_{u,lim}$	limiting residual value of excess pore water pressure ratio
r_e	reference stress level
S	value of s_u/σ'_{vc} for OCR = 1
S_{CS}	undrained shear strength at critical state
S_{QSS}	undrained shear resistance at quasi-steady state
s_u	undrained shear strength
s_{ur}	remolded undrained shear strength
S_r	residual shear strength of liquefied soil in the field
S_t	sensitivity
SASW	spectral analysis of surface waves
SPT	standard penetration test
S_{v-1D}	settlement due to postliquefaction one-dimensional reconsolidation
u_o	initial pore water pressure
V_s	shear wave velocity
V_{s1}	shear wave velocity corrected to an effective overburden stress of 1 atm
w_n	natural water content
z_{max}	maximum depth
α	initial static shear stress ratio
Δu	excess pore water pressure

For more monographs, publications, or videos, visit http://www.eeri.org

ε_a	axial strain
ε_v	volumetric strain
ϕ'	effective friction angle
ϕ'_{cv}	critical-state effective friction angle
γ	total unit weight, or shear strain
γ_{lim}	limiting value of shear strain
γ_{max}	maximum shear strain
ξ_R	relative state parameter, or relative state parameter index
σ_1	major principal total stress
σ_3	minor principal total stress
σ_v	vertical total stress
σ'	effective stress (e.g., σ'_v = vertical effective stress)
σ'_c	effective stress at consolidation (e.g., σ'_{vc} = vertical effective stress at consolidation)
σ'_p	effective preconsolidation stress (e.g., σ'_{vp} = vertical effective preconsolidation stress)
τ_{cyc}	cyclic shear stress
τ_{max}	maximum shear stress
τ_s	static shear stress

For more monographs, publications, or videos, visit http://www.eeri.org

1 SOIL LIQUEFACTION DURING EARTHQUAKES

1.1 Effects of Soil Liquefaction

One of the most dramatic causes of damage to structures during earthquakes is the occurrence of liquefaction in saturated sand deposits. Loose sand tends to contract under the cyclic loading imposed by earthquake shaking, which can transfer normal stress from the sand matrix onto the pore water if the soil is saturated and largely unable to drain during shaking. The result is a reduction in the effective confining stress within the soil and an associated loss of strength and stiffness that contributes to deformations of the soil deposit.

A common manifestation of liquefaction is the formation of sand boils or mud spouts at the ground surface by seepage of water through ground cracks or, in some cases, by the development of quicksand-like conditions over substantial areas. Figure 1 shows sand boiling along a fissure in the ground caused by an earthquake, and Figure 2 shows a sand boil after the liquefaction-induced boiling has ceased. The damage from liquefaction is seldom, however, due to the sand boils themselves, but rather due to the loss of strength and stiffness in the soils that have liquefied and the associated ground deformations that ensue.

Some of the most dramatic illustrations of liquefaction-related damage to civil infrastructure were observed after the 1964 Niigata, Japan earthquake and 1964 Prince William Sound, Alaska earthquake, which helped to identify liquefaction as a major problem in earthquake engineering. For example, the loss of shear strength and stiffness in liquefied sands during the 1964 Niigata earthquake resulted in dramatic bearing failures beneath buildings (Figure 3), the floating of buried tanks and other buoyant structures (Figure 4), and the collapse of bridges, including the Showa Bridge (Figure 5).

For more monographs, publications, or videos, visit http://www.eeri.org

Figure 1. Sand boiling caused by liquefaction of underlying sediments during the 1978 Miyagi-ken-Oki, Japan earthquake (original source unknown).

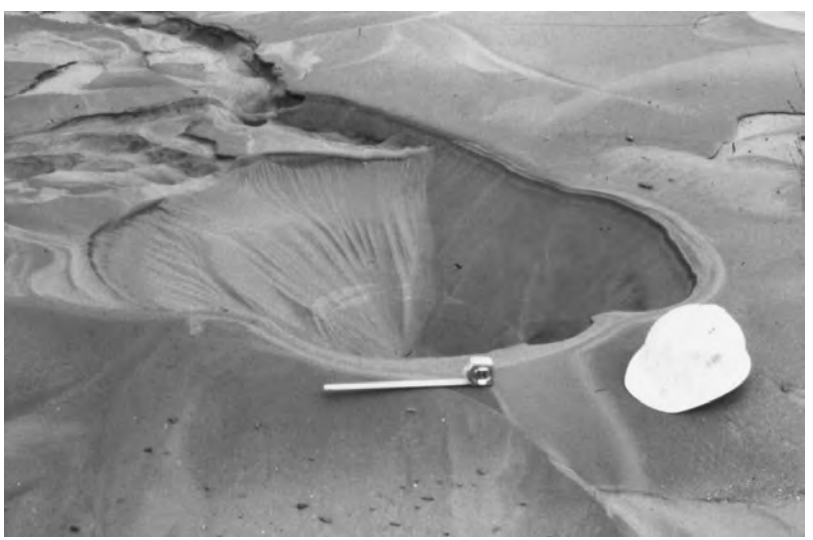

Figure 2. Sand boil after liquefaction-induced boiling from the 1989 Loma Prieta, California earthquake has ceased.

For more monographs, publications, or videos, visit http://www.eeri.org

Figure 3. Tilting of apartment buildings caused by the 1964 Niigata earthquake (photo: National Information Service for Earthquake Engineering, EERC, University of California, Berkeley).

Figure 4. Floating of buried tank in liquefied ground, caused by the 1964 Niigata earthquake (photo: Kawasumi 1968).

For more monographs, publications, or videos, visit http://www.eeri.org

Figure 6. Slide in the upstream shell of the Lower San Fernando Dam after the 1971 San Fernando earthquake (photo: California Department of Water Resources).

with no more than about 1 m of freeboard against release of the reservoir and necessitated the evacuation of about 80,000 people who were living downstream of the dam. The dramatic extent of the slope failure is shown by a photo (Figure 6) taken after the reservoir had been drawn down, with the distorted pavement of the former road across the dam crest marking the extent of the slide movements. This near-catastrophe marked a major change in embankment dam engineering throughout the world and has been the subject of numerous research efforts.

The 1995 Kobe earthquake caused pervasive liquefaction throughout the reclaimed lands and manmade islands in the Kobe region, which is home to one of the largest container port facilities in the world. Liquefaction in these fills caused extensive damage to quay walls around the port facilities and associated damage to the cranes and other supporting facilities. For example, Figure 7 shows quay wall displacements of a few meters, graben formation behind the quay wall, and damaged and collapsed cranes in the background. The pervasiveness of liquefaction-induced damage caused an almost complete loss of functionality for the ports around Kobe, and the resulting economic loss was far higher than the direct costs of repairing the physical damage.

For more monographs, publications, or videos, visit http://www.eeri.org

Figure 7. Quay wall deformation, graben formation, and crane collapses at Port Island after the 1995 Kobe earthquake.

1.2 Development of Engineering Procedures for Assessing and Mitigating Liquefaction

To assess and mitigate potential liquefaction hazards at a specific site, several questions must be addressed:

- Will liquefaction be "triggered" by the design ground motions?
- What will be the consequences for the structure or facility?
- What are the options for mitigating the potential consequences?

The development of engineering procedures that address these questions has involved the synthesis of theoretical as well as empirical considerations that have emerged over the last several decades.

For example, in evaluating the potential for triggering liquefaction, an essential component is to identify an appropriate means of measuring, or estimating, the soil's resistance to liquefaction during seismic (cyclic) loading. In principle, the cyclic behavior of a soil could be determined by obtaining high-quality field samples and then testing them in an appropriate laboratory device. Experience has shown that sand samples obtained by conventional sampling techniques are sufficiently disturbed to render the resulting measurements of cyclic strength unreliable in most situations. More reliable sampling techniques are available that lessen this disturbance to acceptable levels, but only at great expense. Consequently, recourse is

For more monographs, publications, or videos, visit http://www.eeri.org

generally sought by using in-situ tests—standard penetration tests (SPTs), cone penetration tests (CPTs), Becker penetration tests (BPTs), and shear wave velocity (V_s) measurements—as indices for estimating the liquefaction resistance of sands and other cohesionless soils.

Cohesive sediments (e.g., clays and plastic silts) can also develop significant strains that result in ground deformations during earthquake loading, particularly where (a) the sediments are soft and sensitive, (b) there is a significant driving shear stress (e.g., a slope or foundation load), and (c) the shaking is sufficiently strong. The difference in shear strength characteristics between cohesionless and cohesive soils, however, affects the choice and outcome of engineering procedures for evaluating a soil's response to seismic loading (e.g., clays can be sampled and tested with reasonable confidence and expense). For this reason, it is preferable to use the term "liquefaction" to describe the behavior of cohesionless soils (gravels, sands, and very-low-plasticity silts) and the term "cyclic softening" to describe the behavior of clays and plastic silts. Criteria and procedures for evaluating the potential for cyclic softening in cohesive soils are described in Section 6 of this monograph.

The development of analytical procedures for assessing liquefaction triggering has relied on empirical data to provide the link between liquefaction resistance and various in-situ test indices. This development can be described by the following steps:

- Establishing a framework of analysis that is well founded in the fundamentals of soil mechanics and physics
- Collecting case histories that represent a range of observed liquefaction characteristics, including cases in which liquefaction did not occur
- Interpreting the case histories by using the established analysis framework, from which semi-empirical relationships that distinguish between the occurrence and nonoccurrence of liquefaction can be derived

As with assessment, the development of engineering procedures for evaluating the potential consequences of liquefaction and designing mitigation strategies has involved a synthesis of theoretical and empirical considerations.

1.3 Purpose and Scope of This Monograph

The purpose of this monograph is markedly different from the purpose of the 1982 monograph, *Ground Motions and Soil*

For more monographs, publications, or videos, visit http://www.eeri.org

Liquefaction during Earthquakes. At the time of the earlier work, there was a need for a simple representation of the essential elements of liquefaction that could be readily understood by engineers who have no particular familiarity with it. Since then, the body of literature and knowledge about liquefaction has grown considerably, and the evaluation of liquefaction effects has become common in consulting practice. The current need is for a thorough synthesis of the progress from the last 25 years into one accessible resource for students, practicing engineers, and other professionals. Accordingly, the remaining sections of this monograph present the following topics:

- Fundamentals of liquefaction behavior. Fundamental aspects of liquefaction behavior are summarized, to provide a framework for a common understanding of the development and limitations of various engineering analytical procedures. Monotonic and cyclic loading behaviors of saturated sands are described with reference to critical-state soil mechanics concepts, which are particularly valuable for organizing observations pertaining to the combined effects of relative density and confining stress. The laboratory testing of field samples is discussed, to illustrate some additional fundamental features of soil behavior and the challenges posed by the effects of sampling disturbance. Field processes that are not replicated in laboratory tests but can be extremely important in how geotechnical structures perform are also described.
- Triggering of liquefaction. Methods for evaluating the potential for liquefaction triggering are described and illustrated. This section discusses the liquefaction susceptibility of different sedimentary deposits, the analytical framework for site-specific liquefaction triggering evaluations, important features of the in-situ tests used as indices for liquefaction characteristics, liquefaction triggering correlations for sands and silty sands, and examples of liquefaction triggering analyses.
- Consequences of liquefaction. The potential consequences of liquefaction are discussed, with an emphasis on three of the more common consequences that are of concern in engineering practice: (a) the residual strength of liquefied soil and the potential for slope instability, (b) lateral spreading of gently sloping or nearly level ground profiles, and (c) post-liquefaction settlement that is due to liquefaction beneath gently sloping or nearly level ground profiles. Examples of lateral spreading and

For more monographs, publications, or videos, visit http://www.eeri.org

post-liquefaction settlement analyses are presented, followed by a discussion of the margin of safety in engineering practice.

- Mitigation of liquefaction hazards. The evaluation and selection of possible mitigation strategies are discussed, followed by an overview of many of the more common methods for ground improvement. General design and construction considerations are also discussed.
- Cyclic softening of clays and plastic silts. The potential for cyclic softening of cohesive fine-grained soils during earthquake shaking is discussed, and engineering procedures for evaluating their potential performance are presented. Low-plasticity fine-grained soils can transition from behavior that is more like sands to behavior that is more like clays, and simple index criteria for deciding how best to evaluate these types of soils are discussed. The potential consequences of cyclic softening, and the factors affecting those consequences, are also discussed.

For more monographs, publications, or videos, visit http://www.eeri.org

For more monographs, publications, or videos, visit http://www.eeri.org

2 FUNDAMENTALS OF LIQUEFACTION BEHAVIOR

This section reviews the fundamental aspects of soil liquefaction behavior that are particularly important in understanding the development and limitations of the various engineering procedures that are presented in subsequent sections and provides a framework for guiding practical judgments and design decisions in many situations. The principal features of the response of saturated sand to drained and undrained monotonic and cyclic loading are described first. Then the issues involved in laboratory testing of field samples, and particularly the effects of sampling disturbance, are presented. Last, field processes that are not replicated in laboratory tests but can be extremely important in the way geotechnical structures perform are described.

2.1 Monotonic Loading of Saturated Sands

The stress-strain response of sand to monotonic or cyclic loading is strongly dependent on the sand's relative density (D_R), effective confining stress, stress history, mode of deposition, and several other factors. The concepts of critical-state soil mechanics are particularly valuable for organizing observations pertaining to the combined effects of D_R and confining stress on the material response in laboratory element tests (e.g., Schofield and Wroth 1968). The term "critical state" refers to the conditions that exist in sand when it is being sheared continuously and no further changes in volume or stress are occurring, and it is described by the critical-state line (CSL), which represents all possible combinations of void ratio and confining stress at the critical state. The term "steady state" refers to the critical-state condition with the additional requirement of a steady rate of deformation. Inasmuch as the steady state and critical state are essentially synonymous, the term "critical state" is used in this monograph.

For more monographs, publications, or videos, visit http://www.eeri.org

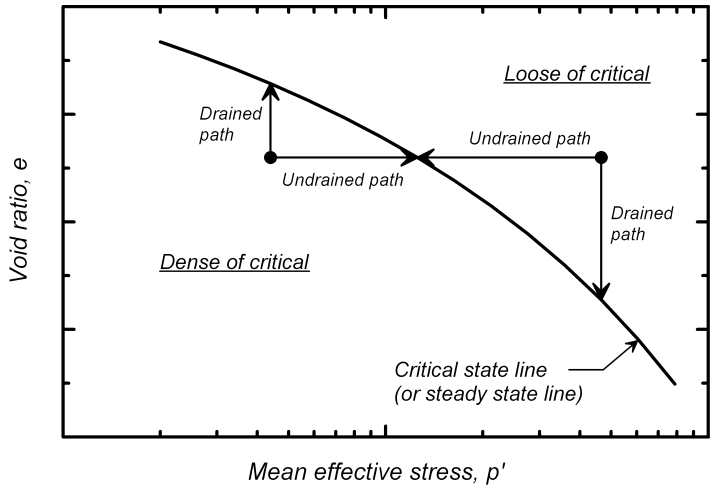

Figure 8. The stress paths for monotonic drained loading with constant p' and undrained loading (constant volume shearing) of saturated loose-of-critical and dense-of-critical sands.

Figure 8 illustrates the paths of saturated sands to drained and undrained monotonic loading for initial states that are "loose of critical" and for those that are "dense of critical." The drained paths are shown for a constant mean effective stress (p') loading condition, and the undrained paths occur at constant volume (or void ratio).

Examples of drained and undrained responses for sands prepared loose and dense of critical are presented subsequently to illustrate these and other aspects of their behavior.

Drained Loading

The response of sand to drained monotonic loading is illustrated by the results from isotropically consolidated drained (ICD) triaxial compression tests on Sacramento River sand, as shown in Figure 9 (Lee and Seed 1967). The symbol P_a shown in these plots represents atmospheric pressure, which is equal to 1.03 kg/cm^2, 1.06 tsf, or 101 kPa, and σ'_{3c} is the effective confining stress used to consolidate the specimen before shearing. The principal stress ratio at failure is related to the effective friction angle (ϕ') as follows:

$$\left(\frac{\sigma'_1}{\sigma'_3}\right)_f = \tan^2\left(45 + \frac{\phi'}{2}\right) \tag{1}$$

For more monographs, publications, or videos, visit http://www.eeri.org

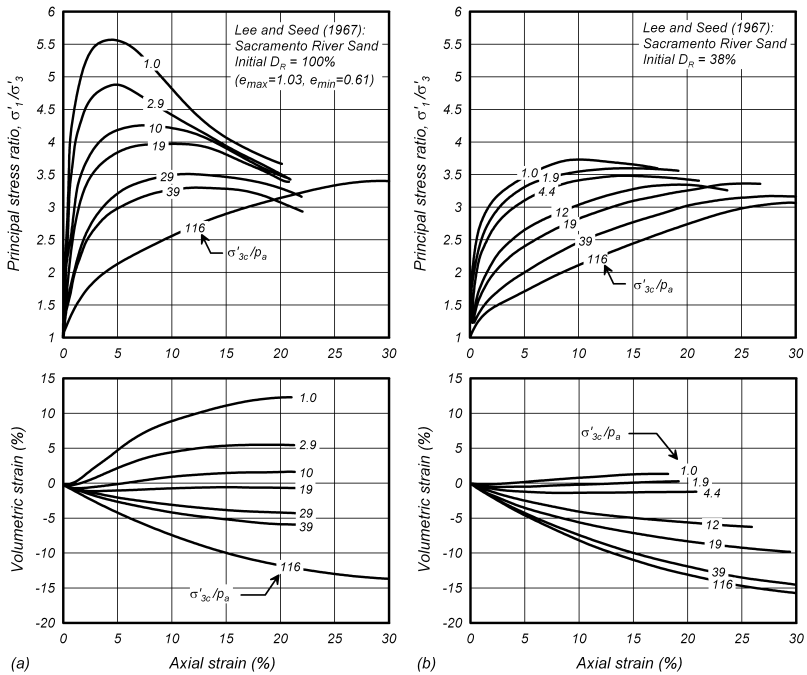

Figure 9. Monotonic loading response of dense ($D_R = 100\%$) and loose ($D_R = 38\%$) specimens of Sacramento River sand in drained triaxial compression tests, as shown in graphs (a) and (b) respectively (after Lee and Seed 1967, with permission from ASCE).

with the peak principal stress ratio corresponding to the peak effective friction angle (ϕ'_{pk}) and the residual principal stress ratio at large strains corresponding to the critical-state or constant-volume effective friction angle (ϕ'_{cv}).

The $D_R = 100\%$ specimens in Figure 9a were dilatant (loosened) during drained shear with effective confining stresses, $\sigma'_{3c} \leq 10$ atm (approximately 1,000 kPa). The dilation can be conceptually viewed as arising from the need for the sand particles, which are densely packed, to ride up over each other (creating more void space between them) in order to shear past each other.

At $\sigma'_{3c} \geq 19$ atm, the $D_R = 100\%$ specimens became contractive (densified) during drained shear. At these very high confining stresses, shear deformations can be accommodated through particle breakage and particle rearrangement without the particles necessarily having to roll or rotate up over each other.

For more monographs, publications, or videos, visit http://www.eeri.org

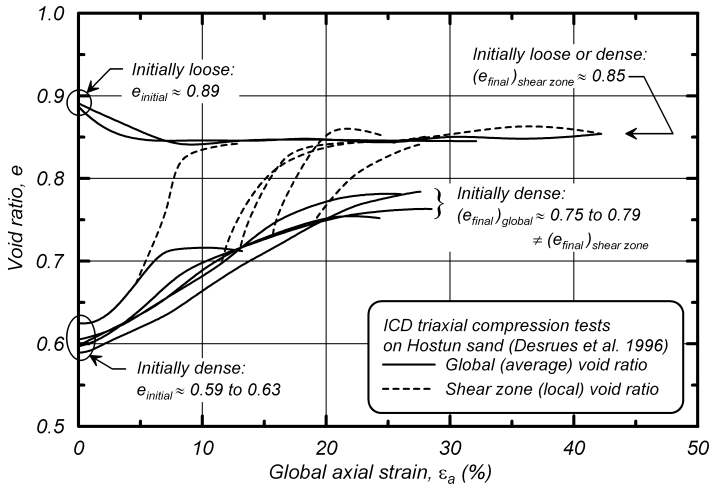

Figure 10. Global and local void ratios within triaxial sand specimens of loose and dense Hostun sand from x-ray computed tomography (adapted from Desrues et al. 1996 and Frost and Jang 2000, with permission from ASCE).

The $D_R = 38\%$ specimens in Figure 9b were dilatant (loosened) during drained shear with σ'_{3c} of 1 atm, showed only minor volume changes with σ'_{3c} of 1.9 atm, and were contractive (densified) with $\sigma'_{3c} > 4.4$ atm.

The ultimate or critical-state values for the principal effective stress ratio were all trending toward a consistent value of roughly 3.3 for the $D_R = 38\%$ and for the $D_R = 100\%$ specimens, regardless of the initial consolidation stress. This principal effective stress ratio corresponds to a critical-state friction angle (ϕ'_{cv}) of about 32° for this sand.

Nonuniformities of strain within laboratory test specimens complicate the experimental determination of the CSL (e-p'), as illustrated in Figure 10, which shows global and local void ratios in loose and dense sand specimens sheared in drained triaxial compression (Desrues et al. 1996). Shear bands occur within dense sand specimens during drained loading and result in post-peak strain softening; once a shear band forms, it becomes weaker than the surrounding soil, and thus any further deformation is concentrated on the already-formed shear band. The void ratios within the shear band are substantially different from void ratios outside the shear band. Shear bands do

For more monographs, publications, or videos, visit http://www.eeri.org

not tend to form in loose (contracting) sand during drained loading, because the soil strain-hardens as it continually gets denser during drained shear, in such a way that the onset of shearing on one plane means that it gets stronger than other potential shear planes, and thus any further deformation shifts away from the current shear plane. One consequence of shear band localizations in dense sands during drained shear is that the global void ratio (the average over the entire specimen) does not correspond to the critical-state void ratio. Instead, only the void ratio within the shear band corresponds to the critical state, and measuring the void ratio within a shear band requires very sophisticated measurements like x-ray tomography (e.g., Desrues et al. 1996) or digital image correlation techniques (e.g., Finno and Rechenmacher 2003).

Undrained Loading

The response of sand to undrained monotonic loading is illustrated by the results from isotropically consolidated undrained (ICU) triaxial compression tests on saturated Toyoura sand, as shown in Figure 11 (Ishihara 1993). Volumetric strains are approximately zero during undrained shearing of saturated sand, and thus the void ratio of the specimens stays constant during undrained loading (local changes in the void ratio can occur, but the average for the entire specimen is constant). The deviator stress q and mean principal total and effective stresses p and p' are defined as

$$q = \sigma_1 - \sigma_3 = \sigma_1' - \sigma_3' \tag{2}$$

$$p = \frac{\sigma_1 + \sigma_2 + \sigma_3}{3} \tag{3}$$

$$p' = \frac{\sigma_1' + \sigma_2' + \sigma_3'}{3} = p - u \tag{4}$$

The intermediate and minor principal effective stresses are equal in a triaxial compression test. As for notation, the effective stresses at the time of consolidation (before undrained loading) are identified by a subscript c, so the minor principal effective consolidation stress is σ_{3c}', the major principal effective consolidation stress is σ_{1c}', and the mean effective consolidation stress is p_c'.

The ratio of q/p' at critical state in triaxial compression is defined by the parameter M_c, which is related to the effective friction angle

For more monographs, publications, or videos, visit http://www.eeri.org

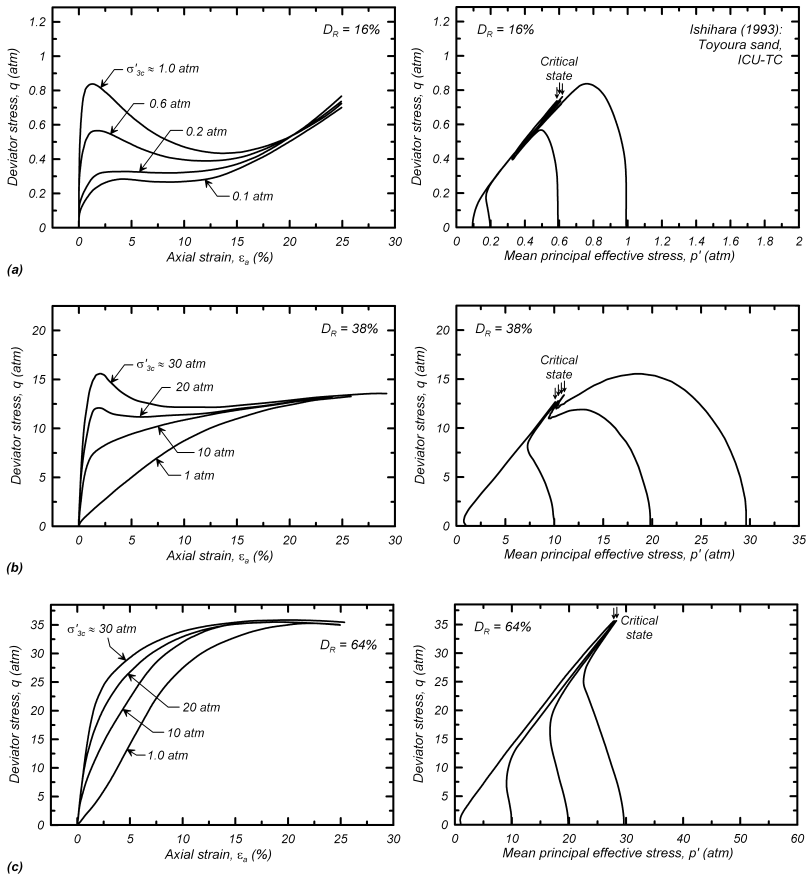

Figure 11. Monotonic loading response of saturated Toyoura sand in ICU triaxial compression tests (after Ishihara 1993): (a) $D_R = 16\%$, (b) $D_R = 38\%$, (c) $D_R = 64\%$.

ϕ'_{cv} as follows:

$$M_c = \left(\frac{q}{p'}\right)_{cv} = \frac{6 \cdot \sin\left(\phi'_{cv}\right)}{3 - \sin\left(\phi'_{cv}\right)} \tag{5}$$

$$\sin\left(\phi'_{cv}\right) = \frac{3 \cdot M_c}{6 + M_c} \tag{6}$$

The $D_R = 16\%$ specimens in Figure 11a were tested with $\sigma'_{3c} = 0.1 - 1.0$ atm (10–100 kPa). For $\sigma'_{3c} = 0.6$ atm and $\sigma'_{3c} = 1.0$ atm, the specimens showed some post-peak strain softening, followed by some strain hardening toward the constant volume shearing condition

For more monographs, publications, or videos, visit http://www.eeri.org

(or critical state). These specimens were initially contractive in their tendencies (i.e., they would have contracted if drained) and thus developed positive excess pore water pressures (Δu), with corresponding decreases in p' during the initial loading and post-peak softening portions of loading response. Then, at strains of 10–15%, the specimens became incrementally dilative in their tendencies, and thus the pore pressures began to incrementally decrease, and p' began to incrementally increase with increasing strains. The two specimens at σ'_{3c} of only 0.1 and 0.2 atm showed strain-hardening behavior through almost the full range of imposed strains. This strain-hardening behavior is due to their dilatant tendencies, which result in increasing p' (decreasing u) during undrained shear loading. Most importantly, the four specimens tended toward the same critical-state strength at large strains, despite having been initially consolidated at very different confining stresses.

The $D_R = 38\%$ specimens in Figure 11b were tested with $\sigma'_{3c} =$ 1.0–30 atm (100–3,000 kPa). The specimens that had the lower consolidation stresses exhibited a strain-hardening response (i.e., increasing p' due to dilatant tendency) during undrained loading, while the specimens at the higher consolidation stresses exhibited some post-peak strain softening (i.e., decreasing p' due to contractive tendency). The four specimens had the same critical-state strength at large strains, which was about 18 times larger than the critical-state strength for the $D_R = 16\%$ specimens.

The $D_R = 64\%$ specimens in Figure 11c were also tested with $\sigma'_{3c} = 1.0$–30 atm. The four specimens showed strain-hardening responses and again reached the same critical-state strength at large strains. For these specimens, the critical-state strength was almost 3 times greater than for the $D_R = 38\%$ specimens.

The transition from incrementally contractive tendencies (p' decreasing) to incrementally dilative tendencies (p' increasing) during undrained shearing is called "phase transformation" (Ishihara et al. 1975). Phase transformation for the tests shown in Figure 12 occurs at points P and Q, which are also points of minimum shear resistance. The various states of stress and void ratio at this phase transformation point during monotonic undrained loading define what is called the "quasi-steady-state" line (QSSL), and the corresponding shear resistance is called the quasi-steady-state strength. The quasi-steady-state strength can be substantially smaller than the critical-state strength and is usually reached at strains equal to a few percent.

The direction of shear loading can also have a large effect on the sand's undrained stress-strain behavior. For example, Figure 13

For more monographs, publications, or videos, visit http://www.eeri.org

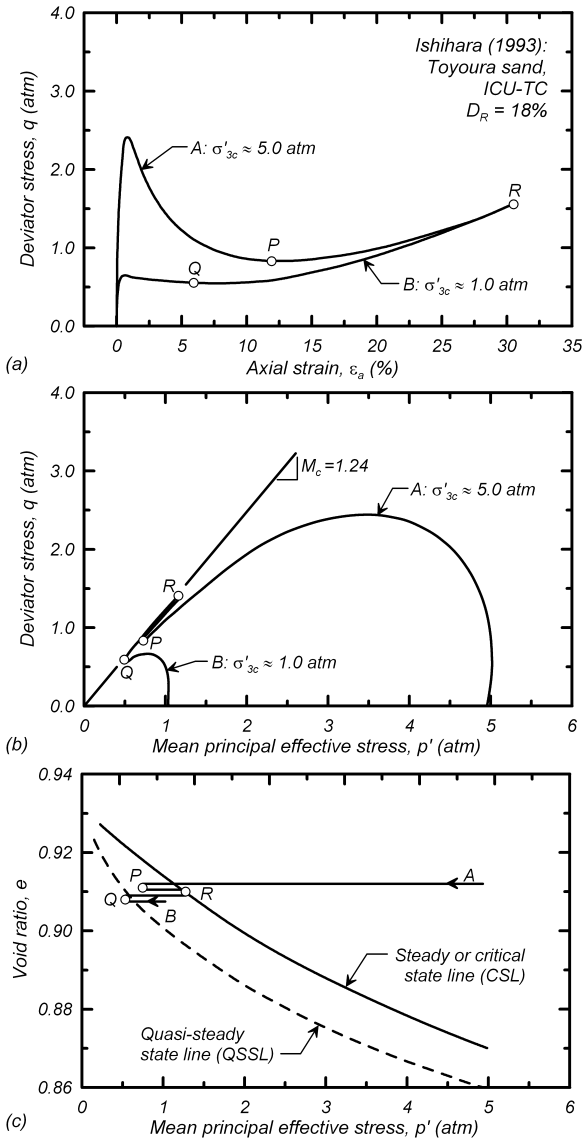

Figure 12. Quasi-steady-state (QSS) and steady-state behavior of very loose Toyoura sand in ICU triaxial compression tests (after Ishihara 1993).

For more monographs, publications, or videos, visit http://www.eeri.org

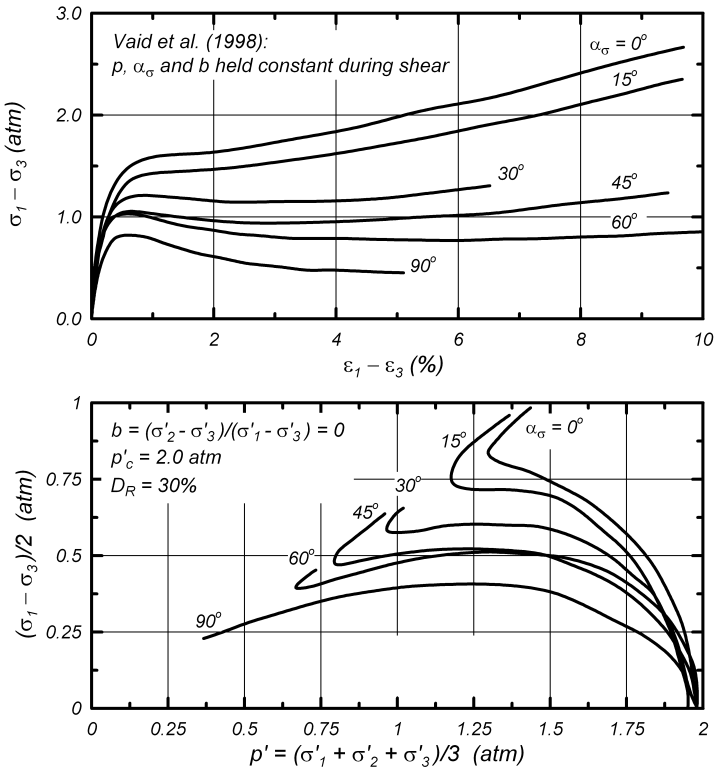

Figure 13. Undrained stress-strain and stress-path responses of Fraser River sand tested along different stress paths in a torsional hollow cylinder (after Vaid et al. 1998).

shows the results of undrained loading tests on Fraser River sand in a special laboratory device that allows the deviator stress to be applied at different inclinations from the vertical (Vaid and Eliadorani 1998). The shear resistance of the sand when loaded horizontally ($\alpha_\sigma = 90^\circ$, similar to triaxial extension loading) was less than half of the shear resistance when the sand was loaded vertically ($\alpha_\sigma = 0^\circ$, similar to triaxial compression loading), even though the specimens had the same initial relative density (void ratio) and consolidation stress. These results illustrate how the direction of loading and fabric anisotropy can have a strong effect on the undrained stress-strain response of sands and the corresponding values of QSS strengths. These data also raise questions about the uniqueness of a CSL, since these specimens did not reach the same shear resistance at large strains. These

For more monographs, publications, or videos, visit http://www.eeri.org

and other experimental results (e.g., Finno and Rechenmacher 1997, Riemer and Seed 1997) suggest that the CSL may depend on factors that include the initial state, fabric, consolidation stress history, and loading path.

2.2 Cyclic Loading Behavior of Saturated Sands

Drained Cyclic Loading

Drained cyclic loading with shear stress reversals can cause a net contraction (densification) of sand over a wide range of relative densities. This is why vibration is effective in compacting dry sand to a high relative density.

The progressive densification of a sand specimen subjected to strain-controlled, drained, cyclic loading is shown in Figure 14 (Youd

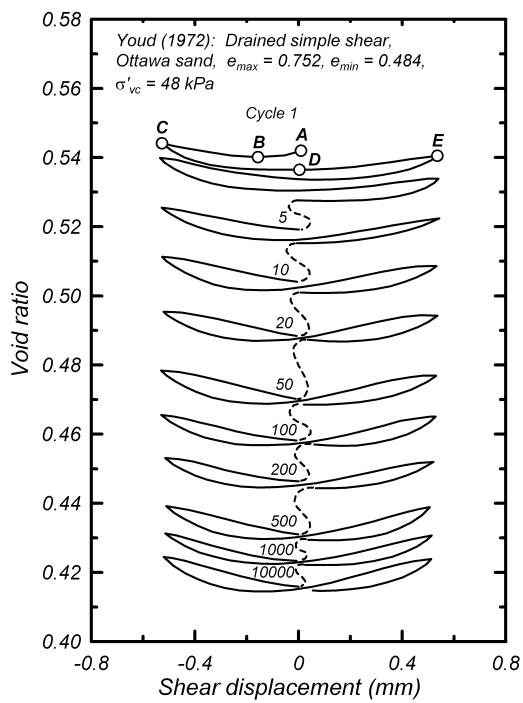

Figure 14. Void ratio versus cyclic shear displacement, showing densification of a sand specimen with successive cycles of drained simple shear loading (after Youd 1972, with permission from ASCE).

For more monographs, publications, or videos, visit http://www.eeri.org

1972). The specimen went through alternating cycles of incremental contraction (a decrease in void ratio) and incremental dilation (an increase in void ratio), with the net effect being an accumulation of contractive strains. As shown in the figure, the initial shear loading caused the specimen to contract from point A to point B, after which further shear loading caused incremental dilation from point B to point C. At point C, the specimen was looser than it was at the start of the test (that is, at point A). Upon reversal of the shear loading, the specimen then incrementally contracted from point C to point D (where it was now denser than at the start of the test) before it transitioned to incremental dilation from point D to E. This process repeated within each cycle of shear loading, resulting in a steady accumulation of net contractive strains. The specimen became progressively denser as cyclic loading continued, with the change in void ratio per loading cycle becoming progressively smaller.

The magnitude of the volumetric strains that a sand develops during drained cyclic loading depends on the magnitude of the imposed shear strains (or stress), the number of loading cycles, the initial relative density, the difference between the maximum and minimum void ratios, the effective confining stress, and the overconsolidation ratio (e.g., Silver and Seed 1971, Youd 1972, Shamoto and Zhang 1998, Duku et al. 2008).

The drained cyclic behavior shown in Figure 14 can be directly related to certain features of behavior in undrained cyclic loading, as described below. In particular, the fact that the sand transitioned from incrementally dilative during application of shear loads to incrementally contractive during unloading has a strong counterpart in the undrained loading response.

Undrained Cyclic Loading

In an undrained cyclic loading test, the sand matrix or skeleton can tend to contract under the cyclic loads, but the resulting rearrangement of sand particles instead transfers normal stresses from the sand matrix to the pore water (i.e., σ stays constant, while σ' decreases and u increases). This process is schematically illustrated in Figure 15 and can be described as follows. The cyclic loading causes a plastic volumetric contraction of the sand skeleton that would result in moving from point A to point B if the sand were drained. For undrained, saturated conditions, the plastic volumetric strain is counterbalanced by an elastic rebound (expansion) of the skeleton under a reduced effective stress (i.e., moving from point

For more monographs, publications, or videos, visit http://www.eeri.org

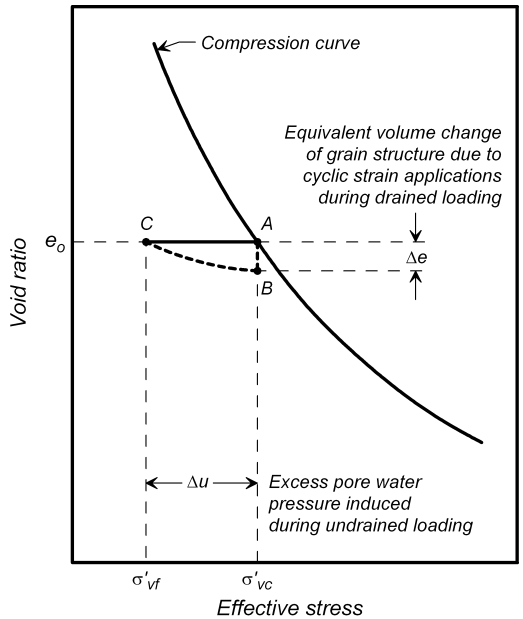

Figure 15. Mechanism of pore pressure generation during cyclic loading.

B to point C). In the limit, the cyclic loading would completely break apart the load-bearing contacts among sand particles in such a way that the sand skeleton would be carrying zero normal stress ($\sigma' = 0$), and the pore water would be carrying the entire normal stress ($u = \sigma$).

The cyclic undrained loading behavior is illustrated in Figure 16 by the results from an anisotropically consolidated undrained (ACU) cyclic triaxial test on medium-dense clean sand with uniform sinusoidal stress loading. The excess pore water pressure (Δu) generated during undrained cyclic triaxial loading is normalized by the minor effective consolidation stress (σ'_{3c}); this ratio is called the excess pore water pressure ratio (r_u):

$$r_u = \frac{\Delta u}{\sigma'_{3c}} \tag{7}$$

The standard cyclic triaxial test keeps the minor principal total stress constant, so the maximum possible value for r_u is 1.0 (or 100%), which occurs when $\Delta u = \sigma'_{3c}$ and $\sigma'_3 = 0$.

For more monographs, publications, or videos, visit http://www.eeri.org

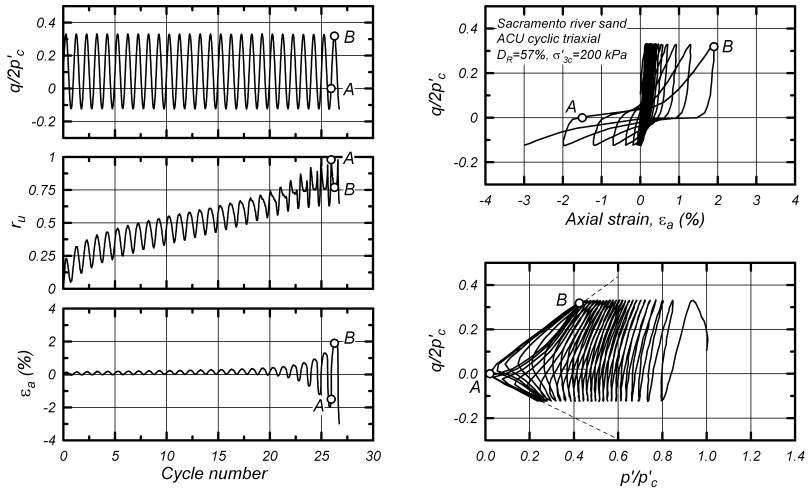

Figure 16. Response of Sacramento River sand to undrained cyclic triaxial loading (test from Boulanger and Truman 1996).

For standard cyclic simple shear tests, r_u is instead computed on the basis of the vertical effective consolidation stress (σ'_{vc}):

$$r_u = \frac{\Delta u}{\sigma'_{vc}} \tag{8}$$

The maximum possible value for r_u is again 1.0 when the total vertical stress is held constant, as in a standard cyclic simple shear test.

The $r_u = 1.0$ condition is often called "initial liquefaction." There are, however, advantages to using the more explicit phrase "excess pore pressure ratio of 100%," because the term "liquefaction" has also been used in the literature to describe other specific field and laboratory conditions, as discussed subsequently in this monograph. It is also worth noting that r_u values above 100% can develop if the mean total stress increases, such as can occur under the more general loading conditions produced in the field, in centrifuge models, or in numerical models. In such cases, it is more useful to focus directly on the values of effective stress rather than on excess pore pressure ratios.

Several features of the behavior in Figure 16 are worth noting. The r_u increased progressively throughout cyclic loading until $r_u = 1.0$ was reached after about 27 cycles of loading. The axial strains (ε_a) remained relatively small (a fraction of 1%) until p' approached zero and r_u approached 100%, after which the axial strains increased to about 2% in less than 2 additional cycles of loading.

For more monographs, publications, or videos, visit http://www.eeri.org

Axial strains would have increased very rapidly with continued cyclic loading, although this particular test was stopped after reaching 3% strain. The corresponding stress-strain response shows rapid softening as p' approached zero, with the hysteretic loops taking on an inverted s-shape. The stress path—that is, $q/(2p'_c)$ versus p'/p'_c—moved progressively toward the origin during cyclic loading until it stabilized with repeating loops emanating from the origin.

The interconnections among the various plots in Figure 16 can be illustrated by considering the positions of the points A and B. Point A corresponds to the time when $r_u = 100\%$ (i.e., $p' = 0$), which occurs only when $q = 0$ (i.e., the specimen is under an isotropic state of stress). Point A occurs as the specimen is unloaded to $q = 0$, at which time the strains are only slightly smaller than the peak during that particular loading cycle. The specimen stiffness is very small at point A, and the subsequent application of shear stress in the positive direction results in the rapid growth of strains in that direction. As the shear stress increases toward Point B, the specimen progressively stiffens, with r_u decreasing and p' increasing. Point B, therefore, corresponds to a local minimum in r_u (0.77) and to the largest axial strain in that direction of loading. The specimen is stable under this applied peak shear stress, which reflects the fact that it is dense of critical. This accumulation of limited strains, after $r_u = 100\%$ has temporarily occurred, has been called "cyclic mobility" behavior (Casagrande 1976, Castro 1975) or "cyclic ratcheting" behavior (Castro 2008, personal communication).

The inverted s-shaped stress-strain behavior that develops as r_u nears 100% (i.e., p' nears zero) arises because the specimen alternates between having incrementally dilative tendencies during shear loading and incrementally contractive tendencies during unloading. This is directly comparable to the drained cyclic loading response shown in Figure 14, in which the specimen alternated between incremental dilation and incremental contraction during loading and unloading, respectively. For undrained conditions, however, the tendency of sand to dilate increases p' and hence increases tangent stiffness, while the tendency to contract decreases p' and hence decreases tangent stiffness.

Figure 16 also illustrates that $r_u = 100\%$ is a temporary condition that occurs only under isotropic states of stress (i.e., zero shear stress) and that $r_u = 100\%$ can be generated in sands that are dense of critical (i.e., they would have a dilative tendency under monotonic drained loading). Liquefaction of a dense-of-critical sand during cyclic loading results in limited strains (or cyclic ratcheting),

For more monographs, publications, or videos, visit http://www.eeri.org

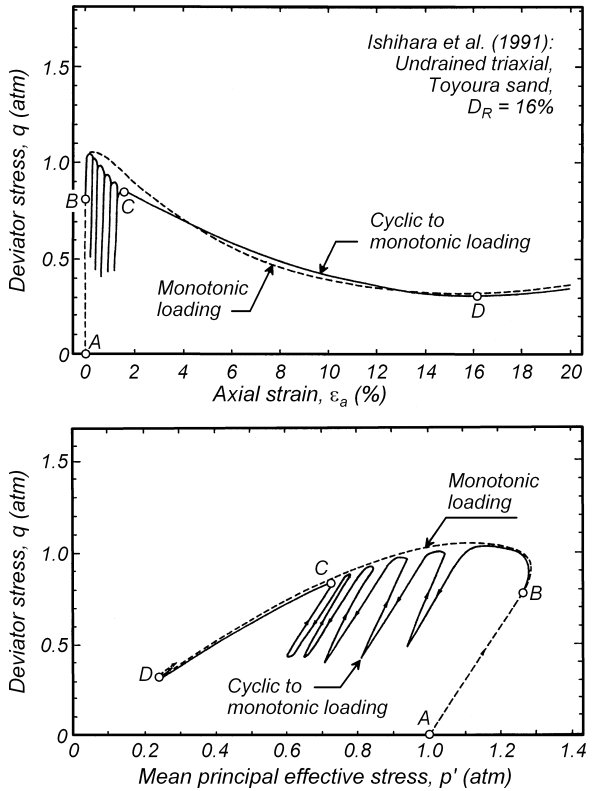

Figure 17. Undrained behavior of Toyoura sand in monotonic loading versus cyclic-to-monotonic loading in triaxial tests of loose-of-critical sand (after Ishihara et al. 1991).

because the sand exhibits dilative behavior under subsequent monotonic loading.

Undrained Cyclic Loading of Loose-of-Critical and Dense-of-Critical Sands

The undrained cyclic loading response of dense-of-critical sand versus loose-of-critical sand is illustrated by the test results in Figures 17 and 18. These two figures show the response of sand to undrained monotonic loading and to undrained cyclic loading followed by undrained monotonic loading. The initial states of these specimens (e and p') can be plotted against the critical-state (steady-state) line for this sand (Figure 12), showing that one state is initially above the critical-state line while the other state is initially below that

For more monographs, publications, or videos, visit http://www.eeri.org

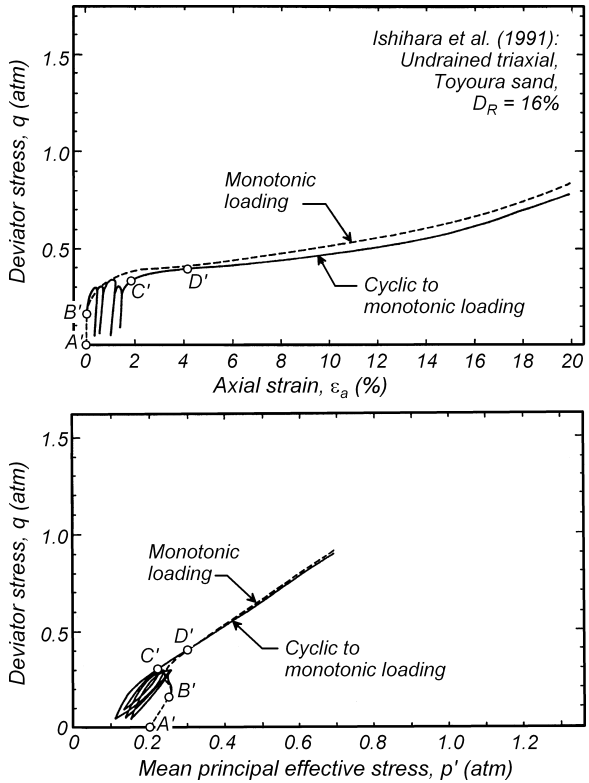

Figure 18. Undrained behavior of Toyoura sand in monotonic loading versus cyclic-to-monotonic loading in triaxial tests of dense-of-critical sand (after Ishihara et al. 1991).

line. The specimens in both tests were anisotropically consolidated in such a way that the specimens were carrying an initial static shear stress before undrained loading (point B in Figure 17 and point B′ in Figure 18). The specimens were then subjected to undrained cyclic loading that produced high excess pore pressures and axial strains slightly smaller than 2% (points C and C′). Note that the cyclic stress amplitude was smaller than the initial static shear stress, so the deviator stress (q) was never equal to zero; thus neither specimen reached a state of $r_u = 100\%$ (or $p' = 0$).

The loose-of-critical specimen in Figure 17 collapsed toward the critical state after cyclic loading, with its shear resistance becoming smaller than the initial static deviator stress. The postcyclic shear

For more monographs, publications, or videos, visit http://www.eeri.org

resistance from point C to point D is essentially the same as that for a monotonic undrained test for sand of the same density, indicating that the cyclic loading did not affect the specimen's critical-state strength. The cyclic loading was, however, sufficient to "trigger" the collapse of the specimen and the development of large uncontrolled deformations (i.e., "flow liquefaction"). The collapse occurred while the effective stresses remained greater than zero (i.e., $r_u < 100\%$) and the soil maintained a nonzero shear resistance.

The dense-of-critical specimen in Figure 18 developed limited strains from the cyclic loading but always maintained enough shear resistance to remain stable. The excess pore pressures generated by the cyclic loading in fact moved the specimen's state further away from the CSL in e-log(p') space (i.e., reducing p' while e remained constant). The specimen subsequently strain-hardened during the postcyclic undrained monotonic loading, during which its dilative tendencies increased p' as it moved back toward the critical state. The postcyclic monotonic loading resistance is again similar to that for an undrained monotonic test on sand of the same density.

Dependence of Cyclic Strength on the Number of Loading Cycles, Relative Density, and Confining Stress

The resistance of sand to the triggering of liquefaction (i.e., its cyclic strength) depends on several factors, including the number of loading cycles, relative density, confining stress, depositional method, fabric, prior stress-strain history, age, cementation, and other environmental factors. This section discusses in some detail the effects of the number of loading cycles, relative density, and confining stress. The other factors are discussed separately in subsequent sections.

Liquefaction of saturated sands can be triggered by different combinations of uniform cyclic shear stress ratio (CSR), which is the uniform cyclic shear stress divided by the initial effective confining stress, and the number of loading cycles (N). A greater CSR will trigger liquefaction (e.g., $r_u = 100\%$ or a cyclic shear strain, $\gamma = 3\%$) in fewer loading cycles, whereas a smaller CSR will require more loading cycles. This aspect of behavior is illustrated by the results of the shaking table tests by De Alba et al. (1976), as shown in Figure 19. Note that the CSR for shaking table tests or simple shear tests is defined as the cyclic shear stress (τ_{cyc}) acting on horizontal planes divided by the vertical effective consolidation stress (σ'_{vc}),

$$\mathrm{CSR} = \frac{\tau_{cyc}}{\sigma'_{vc}} \tag{9}$$

For more monographs, publications, or videos, visit http://www.eeri.org

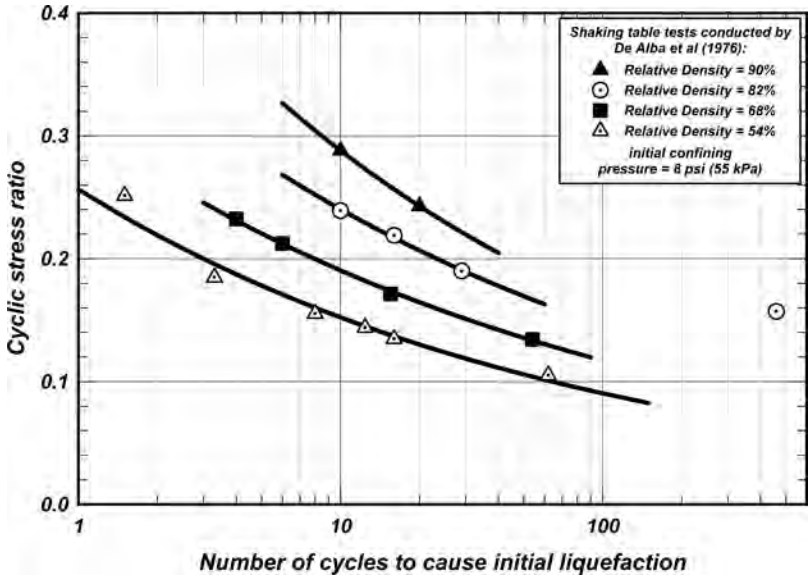

Figure 19. The CSR required to reach initial liquefaction ($r_u = 100\%$), from shaking table tests by De Alba et al. (1976).

whereas the CSR for isotropically consolidated cyclic triaxial tests is defined as the maximum cyclic shear stress ($q_{cyc}/2$) divided by the isotropic consolidation stress (σ'_{3c}),

$$\mathrm{CSR} = \frac{q_{cyc}}{2\sigma'_{3c}} \tag{10}$$

The CSR that is required to reach liquefaction in a specified number of loading cycles may also be called the sand's cyclic resistance ratio (CRR), for notational convenience. The relationship between the CRR and N, within the range of cycles of interest for earthquake engineering, can generally be approximated with a power function as

$$\mathrm{CRR} = a \cdot N^{-b} \tag{11}$$

where the parameters a and b are determined by regression against the experimental data. Note that the CRR versus N relationship plots as a straight line on a log-log plot, whereas it plots as a curve on the semilog plot format of Figure 19. The parameter b for clean sands is typically about 0.34, whereas the parameter a depends on a wide range of factors. The dependence of the CRR on N means that any reference to a sand's CRR must specify N.

For more monographs, publications, or videos, visit http://www.eeri.org

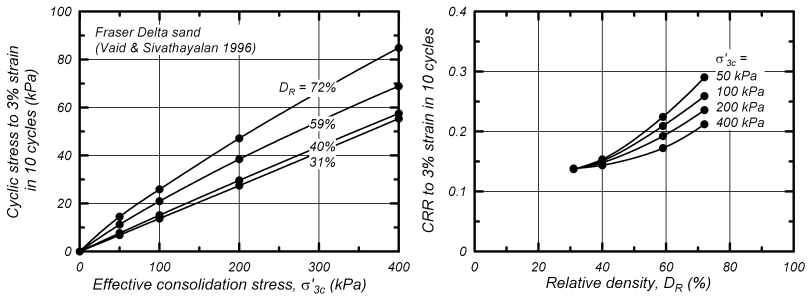

Figure 20. Cyclic triaxial test results for clean Fraser Delta sand, showing that cyclic stress and the CRR cause 3% shear strain in 10 uniform cycles at D_R values of 31–72% and effective consolidation stresses of 50–400 kPa (original data from Vaid and Sivathayalan 1996).

The CRR of sand increases with increasing relative density, as illustrated by the shaking table test results in Figure 19.

The CRR of sand also depends on the effective confining stress, which reflects the fact that the tendency of sand to dilate or contract depends on confining stress. This aspect of behavior is illustrated by the ICU cyclic triaxial test results on Fraser Delta sand by Vaid and Sivathayalan (1996), shown in Figure 20. The plot at left shows the cyclic stress ($q_{cyc}/2$) required to reach 3% shear strain in 10 cycles versus the effective consolidation stress for specimens at D_R values of 31, 40, 59, and 72%. This plot shows that cyclic strength increased with increasing consolidation stress for all values of D_R, but the shape of these relationships ranged from being nearly linear at the lowest D_R to being most strongly concave at the highest D_R. The plot at right shows the ratio of $q_{cyc}/2$ divided by σ'_{3c} that is required to cause 3% axial strain in 10 cycles (i.e., the CRR at 10 cycles) versus D_R for different consolidation stresses. This plot shows that the CRR increased with increasing D_R but that it also decreased as the effective consolidation stress was increased from 50 kPa to 400 kPa for D_R values greater than 30%.

Seed (1983) introduced the overburden correction factor (K_σ) as a way to represent the dependence of the CRR on consolidation stress, with K_σ defined as

$$K_\sigma = \frac{\mathrm{CRR}_{\sigma'_c}}{\mathrm{CRR}_{\sigma'_c=1}} \tag{12}$$

where $\mathrm{CRR}_{\sigma'_c}$ is the CRR of a soil under a specific value of effective consolidation stress σ'_c, and $\mathrm{CRR}_{\sigma'_c=1}$ is the CRR of the same soil

For more monographs, publications, or videos, visit http://www.eeri.org

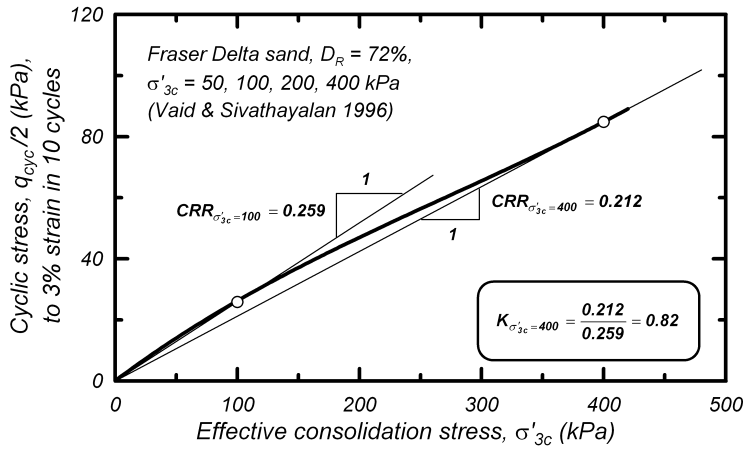

Figure 21. The amount of cyclic stress required to cause 3% strain in 10 uniform cycles versus effective consolidation stress in ICU cyclic triaxial tests on Fraser Delta sand.

when $\sigma'_c = 1$ atm ($\sim$100 kPa). The definition of the K_σ factor is illustrated in Figure 21, which shows the cyclic stress required to reach 3% strain in 10 cycles versus the effective consolidation stress for Fraser Delta sand at $D_R = 72\%$. The relationship between cyclic stress and consolidation stress is curved, thus its secant slope (which is the CRR) decreases with increasing consolidation stress. For example, the data in Figure 21 show that the CRR at an effective consolidation stress of 400 kPa is 18% smaller than at 100 kPa. This slight curvature is analogous to the slight curvature in the failure envelopes for drained shearing tests and the associated observation that peak (secant) effective friction angles decrease with increasing confining stress.

The K_σ factor varies with D_R and with the test device (i.e., simple shear versus triaxial) and appears to be different for freshly reconstituted laboratory specimens as compared with tube samples of natural soils, as shown in Figure 22.

The dependence of the CRR on both D_R and confining stress can be related to the sand's "state" (position) with respect to its CSL. Been and Jefferies (1985) introduced the state parameter (ξ) as a measure of state, where ξ is the difference between the current void ratio (e) and the critical-state void ratio (e_{cs}) for the current value of p'. Konrad (1988) later showed that the value of ξ can be normalized by the difference in the maximum and minimum void ratios ($e_{max} - e_{min}$) to

For more monographs, publications, or videos, visit http://www.eeri.org

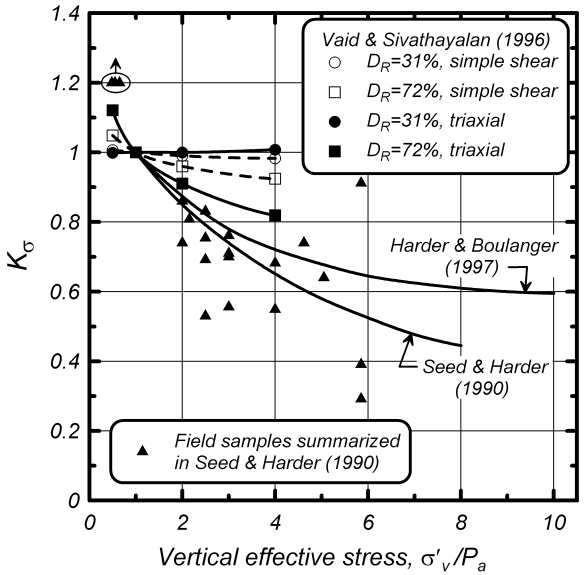

Figure 22. Comparison of K_σ relationships with data from reconstituted Fraser Delta sand specimens and various field samples.

arrive at a relative state parameter that provides improved correlations with the shear behavior of sand. Determining the state or relative state parameters requires detailed experimental testing to define a sand's CSL, its minimum and maximum void ratios, and its in-situ void ratio. The natural heterogeneity of sand deposits, however, makes it impractical to perform sufficient experimental tests to define CSLs for all the different zones within a natural deposit.

Boulanger (2003a) introduced an index for representing the relative state parameter. This index, ξ_R, is defined in Figure 23 and represents the difference between the current D_R and an empirical critical state D_R (denoted $D_{R,cs}$) for the same mean effective normal stress (p'). The empirical CSL and the expression for $D_{R,cs}$ in Figure 23 were derived by using Bolton's (1986) relative dilatancy index (I_{RD}). The parameter Q in Figure 23 determines the stress at which the CSL curves sharply downward—which indicates the onset of significant particle crushing—and the parameter's value depends on grain type, with $Q \approx 10$ for quartz and feldspar, 8 for limestone, 7 for anthracite, and 5.5 for chalk (Bolton 1986). The resulting ξ_R parameter provides a rational means for including the interaction between relative

For more monographs, publications, or videos, visit http://www.eeri.org

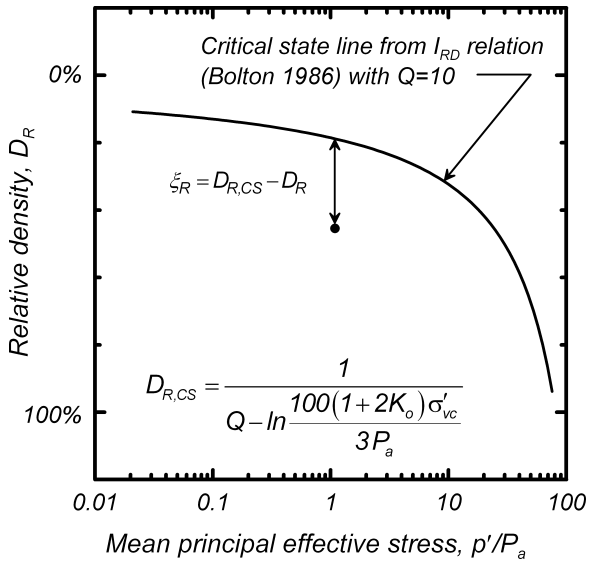

Figure 23. Definition of the relative state parameter index, ξ_R (after Boulanger 2003a, with permission from ASCE).

density and confining stress in the analytical framework that is used to evaluate liquefaction potential.

The CRR of sand for a given test type can be expressed as an approximately unique function of ξ_R, as illustrated in Figure 24 with data from Vaid and Sivathayalan (1996) for Fraser Delta sand. These results are for specimens prepared at D_R values of 31–72% under effective consolidation stresses of 50–400 kPa, with the CRR corresponding to the development of 3% shear strain in 10 uniform loading cycles. These data suggest that ξ_R can reasonably represent the combined effects of D_R and σ'_{vc} on the CRR.

In Figure 25, the ICU cyclic triaxial test results for Fraser Delta sand illustrate the interrelations among K_σ, ξ_R, CRR, D_R, and consolidation stress. The CRR versus D_R relationship (for a given consolidation stress) curves upward with increasing D_R, which directly relates to the CRR versus ξ_R relationship curving upward with decreasing ξ_R. Increasing the consolidation stress from 100 kPa to some higher value results in the same decrease in ξ_R for all values of D_R. This $\Delta\xi_R$ changes the CRR by amounts that depend on the initial D_R, because of the curvature of the CRR versus ξ_R relationship (which applies to all values of D_R and consolidation stresses). Thus, the

For more monographs, publications, or videos, visit http://www.eeri.org

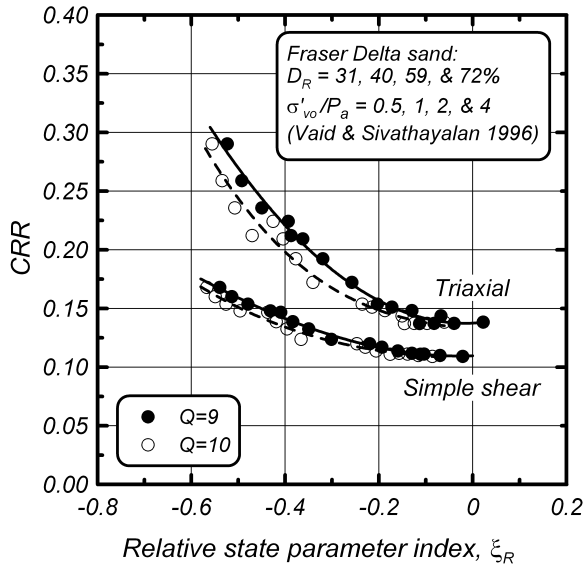

Figure 24. CRR versus ξ_R for reconstituted specimens of Fraser Delta sand (Boulanger 2003a, with permission from ASCE).

reduction in the CRR, as expressed through the K_σ factor, depends on the initial D_R. The K_σ relationships derived from the CRR versus ξ_R relationship (Figures 24 and 25) match the relationships derived directly from the experimental results (Figures 20 and 22), as expected.

Relating Cyclic Strength from Triaxial and Simple Shear Tests to Field Conditions

The differences in the CRR measured in cyclic simple shear and cyclic triaxial tests are largely related to their different states of consolidation stress. A normally consolidated sand specimen that is one-dimensionally consolidated in a simple shear device will have K_o values of 0.45–0.5, whereas K_o would equal 1 if tested in an ICU cyclic triaxial test. Ishihara et al. (1977, 1985) performed cyclic torsional shear tests with different K_o values and showed that the CRR for anisotropically consolidated specimens ($K_o \neq 1$) can be approximately related to the CRR for isotropically consolidated specimens ($K_o = 1$) as

$$\mathrm{CRR}_{K_o \neq 1} = \left(\frac{1 + 2K_o}{3}\right) \mathrm{CRR}_{K_o = 1} \tag{13}$$

For more monographs, publications, or videos, visit http://www.eeri.org

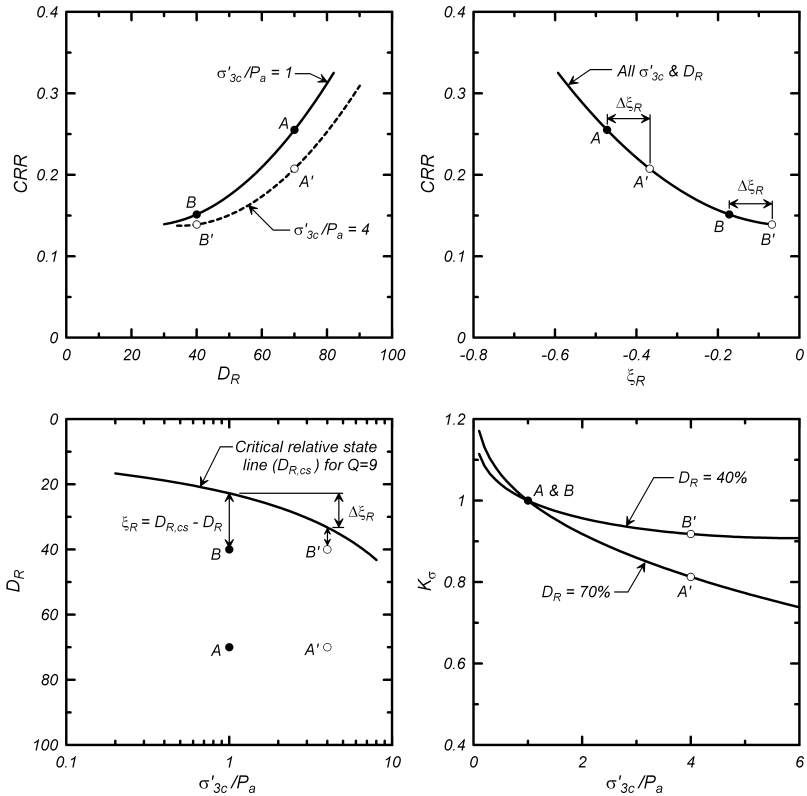

Figure 25. The relationships among CRR, relative density, effective confining stress, relative state parameter index, and K_σ, illustrated by using the CRR versus ξ_R relationship from cyclic triaxial tests on Fraser Delta sand.

Consequently, increasing K_o from 0.4 to 0.8 causes an increase of about 44% in the CRR.

Similarly, the CRR from the simple shear test can be related to the CRR from the ICU triaxial test as

$$\mathrm{CRR}_{SS} = \left(\frac{1 + 2\,(K_o)_{SS}}{3}\right) \mathrm{CRR}_{TX} \tag{14}$$

For normally consolidated sand, K_o would be about 0.45–0.50, which results in

$$\mathrm{CRR}_{SS} = (0.63 \text{ to } 0.67)\,\mathrm{CRR}_{TX} \tag{15}$$

For more monographs, publications, or videos, visit http://www.eeri.org

This relationship between the CRR for simple shear and triaxial tests is consistent with the range of results obtained or recommended by a number of researchers (Seed and Peacock 1971, Finn et al. 1971, Ishibashi and Sherif 1974, Castro 1975, Seed 1979).

One- and two-directional cyclic simple shear tests and shaking table tests have further shown that adding a second direction of cyclic loading reduces the CRR by about 10–15%, as summarized by Pyke et al. (1974), Seed (1979), and Ishihara (1996). This adjustment is needed whenever unidirectional cyclic laboratory tests are being used to estimate the CRR of in-situ sand. For level ground conditions, earthquake loading is best approximated as two-directional simple shear loading, so the CRR from a unidirectional simple shear test would be reduced by 10% to represent in-situ conditions. Note that vertical shaking of saturated soils beneath a level ground surface has a negligible effect on the soil's CRR. Consequently, the in-situ CRR for two-dimensional shaking would be estimated from ICU cyclic triaxial tests as

$$\mathrm{CRR}_{field} = 0.9 \left(\frac{1 + 2\,(K_o)_{field}}{3} \right) \mathrm{CRR}_{TX} \tag{16}$$

and from cyclic direct simple shear tests as

$$\mathrm{CRR}_{field} = 0.9 \left(\frac{1 + 2\,(K_o)_{field}}{1 + 2\,(K_o)_{SS}} \right) \mathrm{CRR}_{SS} \tag{17}$$

For example, if the sand is normally consolidated in situ with an estimated K_o of 0.5, and the CRR is determined by ICU cyclic triaxial tests, then the CRR would be multiplied by 0.60 (i.e., the product of 0.9 and 0.67) to represent in-situ conditions and bidirectional shaking.

Other Factors Affecting the Cyclic Strength of Sand

Laboratory element tests have also shown that the CRR of saturated sands depends on depositional method, fabric, prior stress-strain history, age, cementation, and other environmental factors.

Ladd (1974, 1977) and Mulilis et al. (1977) showed how specimens of the same sand prepared to the same D_R by different reconstitution techniques can result in a CRR that varies by almost a factor of 2 from highest to lowest (Figure 26). The effect of the sample preparation method is attributed primarily to differences in the fabric of the resulting sand particle matrix.

Overconsolidation has also been shown to increase the CRR beyond the amount that is due to associated increases in K_o, but the

For more monographs, publications, or videos, visit http://www.eeri.org

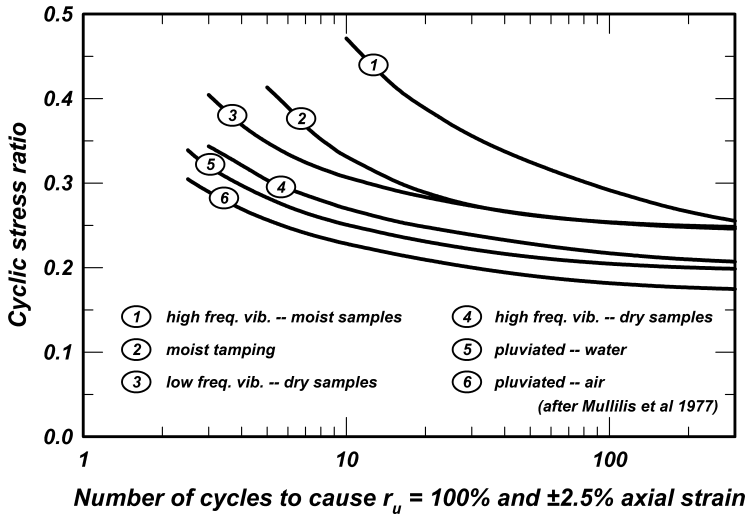

Figure 26. Results of cyclic triaxial tests, showing the influence of the sample preparation method on the CRR of Monterey No. 0 sand at $D_R = 50\%$ (after Mulilis et al. 1977, with permission from ASCE).

increase in the CRR has ranged from being relatively minor to as much as being proportional to the square root of the overconsolidation ratio (Lee and Focht 1975, Ishihara and Takatsu 1979, Finn 1981).

The effects of strain history have been shown to be very significant and to range from a beneficial effect at small prestrain levels to a detrimental effect at large prestrain levels (Suzuki and Toki 1984, Seed et al. 1977, Finn et al. 1970). For example, cyclic triaxial test results by Singh et al. (1982) and Goto and Nishio (1988), as presented later in Section 2.3, showed increases in the CRR of 30–100% from prior cyclic straining at strain levels that did not significantly change the density of the specimens. Cyclic straining at larger strain levels will produce associated volumetric strains, which may range from a net contraction to a net loosening. The effect of larger prestrain levels on sand behavior during subsequent undrained cyclic loading depends on the volumetric strains induced by the prestraining and their uniformity within the laboratory testing device.

Effect of Static Shear Stresses on Cyclic Behavior

The effect of an initial static shear stress on the undrained cyclic loading behavior of saturated sand is illustrated by the cyclic simple shear test results for Sacramento River sand shown in Figure 27. This

For more monographs, publications, or videos, visit http://www.eeri.org

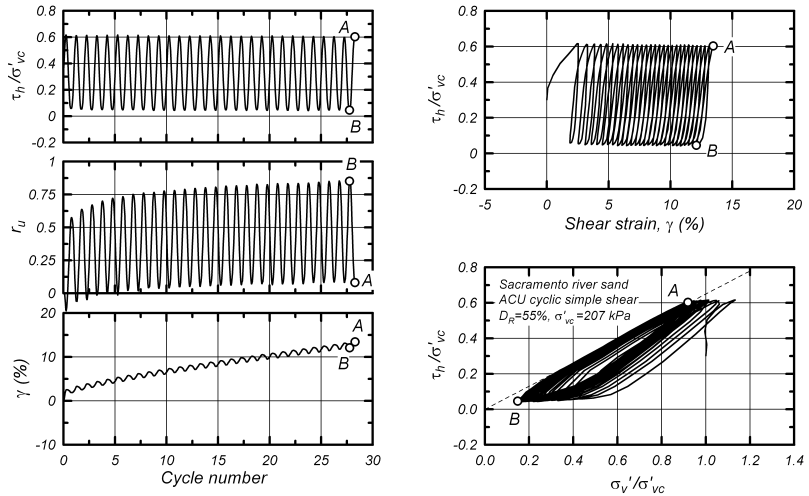

Figure 27. Response of Sacramento River sand to undrained cyclic simple shear loading with an initial static shear stress ratio of 0.32 (test from Boulanger et al. 1991).

simple shear test specimen was consolidated with a static horizontal shear stress (τ_s) equal to 0.32 times the vertical effective consolidation stress, which is called an initial static shear stress ratio ($\alpha = \tau_s/\sigma'_{vc}$) of 0.32. The applied CSR was about 0.28, which means that the horizontal shear stress was always positive (about 0.04–0.60). The induced r_u increased quickly in the first few loading cycles and then increased slowly with each subsequent cycle of loading but was always less than 100%. The shear strain quickly reached 2–3% in the direction of the static shear stress, after which the specimen slowly accumulated additional shear strains with each additional loading cycle. The stress path (τ_h versus σ'_v) moved over toward the failure line, after which it stabilized on an essentially repeating pattern. When the behavior for this specimen is compared with that in Figure 16 for a specimen with zero initial static shear stress ($\alpha = 0$), it is clear that the presence of the static shear stress had strong effects on the pore pressure and shear strain generation behavior.

The effect of a static shear stress ratio on the cyclic strength of clean sand at different D_R values is illustrated by the simple shear test results for Ottawa sand in Figure 28a. Data are shown for the τ_{cyc}/σ'_{vc} causing 3% shear strain in 10 cycles of loading for specimens at D_R values of 50% and 68% under σ'_{vc} of 200 kPa (Vaid and Finn 1979). The $D_R = 68\%$ specimens exhibit a progressive increase

For more monographs, publications, or videos, visit http://www.eeri.org

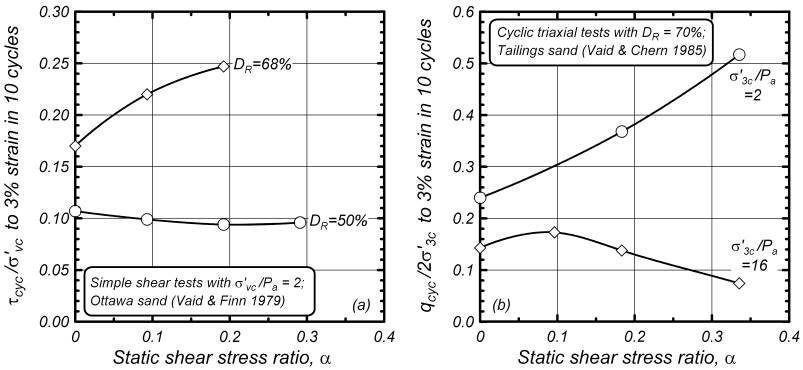

Figure 28. Variation of the CRR for 3% shear strain in 10 cycles with the initial static shear stress ratio, α. Graph (a) shows the effect of varying the relative density, and graph (b) shows the effect of varying the effective consolidation stress.

in the cyclic strength with increasing initial static shear stress ratio, whereas the $D_R = 50\%$ specimens exhibit a lower cyclic strength with increasing initial static shear stress ratio. This effect of D_R is attributed to the differences in the dilative tendencies of the sand, with the sand becoming more strongly dilatant in shear as D_R is increased (at the same effective confining stress).

The effect of a static shear stress ratio on the cyclic strength of sand at different effective confining stresses is illustrated by the cyclic triaxial tests on tailings sand in Figure 28b. Data are shown for specimens at a D_R of 70% consolidated at minor principal effective stresses (σ'_{3c}) of 200 and 1,600 kPa (Vaid and Chern 1985). For triaxial tests, the static shear stress ratio is computed from the shear and normal stresses on the potential failure planes (i.e., planes inclined at $45 + \phi'/2$ degrees from the horizontal, as used by Seed et al. 1975a). The specimens at $\sigma'_{3c} = 200$ kPa exhibit a progressive increase in the cyclic strength with an increasing initial static shear stress ratio, whereas the specimens at $\sigma'_{3c} = 1{,}600$ kPa exhibit a lower cyclic strength at high initial static shear stress ratios. This effect of σ'_{3c} is similarly attributed to its influence on the dilative tendencies of the sand, with the sand being more strongly dilatant in shear at the lower effective confining stress (at the same D_R).

The generation of excess pore pressure and shear strains during undrained cyclic loading of saturated sand is significantly affected by the rotation of principal stress directions, which reverses the shear stress direction on certain planes. In cyclic triaxial tests with an initial

For more monographs, publications, or videos, visit http://www.eeri.org

static deviator (shear) stress, there is no rotation of principal stresses until the cyclic deviator stress exceeds the static deviator stress, after which there is a 90° rotation of the principal stress directions (and hence shear stress reversal on all possible planes). In cyclic simple shear or torsional shear tests, there is a continuous rotation of the principal stress directions during cyclic loading, regardless of the initial static shear stress. The effect of this difference is evident in the shapes of the cyclic strength versus α relationships obtained in different testing devices. For example, this is why the cyclic triaxial test results for $\sigma'_{3c} = 1{,}600$ kPa in Figure 28b exhibit an initial increase in the cyclic strength up to about $\alpha \approx 0.1$, followed by a subsequent decrease in the cyclic strength at higher values of α.

Seed (1983) developed the K_α correction factor to represent the effects of an initial static shear stress ratio (α) on the cyclic strength. K_α is defined as the cyclic strength for some value of α, divided by the cyclic strength for $\alpha = 0$:

$$K_\alpha = \frac{\mathrm{CRR}_\alpha}{\mathrm{CRR}_{\alpha=0}} \tag{18}$$

Numerous researchers have studied this phenomenon by using cyclic triaxial, cyclic simple shear, torsional shear, and torsional ring shear devices. These studies have shown that K_α depends on relative density and confining stress, as illustrated in Figure 28, which simply reflect the state of the sand in relation to its critical state (e.g., Vaid and Chern 1985, Mohamad and Dobry 1986). In addition, K_α depends on the failure criteria that are used to define the CRR and depends somewhat on the laboratory test device, with simple shear preferred over triaxial loading because it more closely approximates the in-situ rotation of principal stress directions expected during earthquake shaking. A review of these studies is in Harder and Boulanger (1997).

The general trends in K_α data are illustrated in Figure 29, which shows simple shear test results for Sacramento River sand, along with the simple shear test results for Ottawa sand (Figure 28a). The data for Ottawa sand are at D_R values of 50% and 68% under σ'_{vc} of 200 kPa (Vaid and Finn 1979), and the data for Sacramento River sand are at D_R values of 35% and 55% under σ'_{vc} of 200 kPa (Boulanger et al. 1991). These results correspond to 10 cycles of loading and a failure criterion of 3% shear strain. The ξ_R value for each set of test data is shown beside the corresponding K_α curve in Figure 29. There is a consistent progression in K_α values from less than 1.0 for the loosest sand ($\xi_R = -0.16$) to greater than 1.0 for the densest sand

For more monographs, publications, or videos, visit http://www.eeri.org

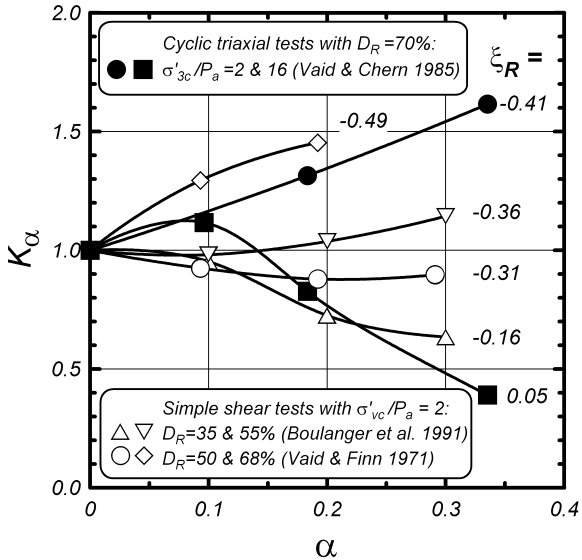

Figure 29. Effect of the relative state parameter index ξ_R on the static shear stress ratio correction factor K_α (Boulanger 2003a).

($\xi_R = -0.49$), with the ξ_R values simply tracking the progression from $D_R = 35\%$–68%, since all tests were at the same confining stress.

The dependence of K_α on the effective confining stress is also depicted in Figure 29 by the results of the cyclic triaxial tests on tailings sand by Vaid and Chern (1985) (Figure 28b). For determining K_α from these triaxial tests, the cyclic resistances were normalized by the mean effective consolidation stresses (Boulanger 2003a). The ξ_R values and K_α relationships for these specimens are consistent with the trends obtained on the clean sands at the lower confining stress only. In particular, the ξ_R value for the $D_R = 70\%$ tailings sand at $\sigma'_{3c} = 1{,}600$ kPa is greater than the ξ_R value for $D_R = 35\%$ Sacramento River sand at $\sigma'_{vc} = 200$ kPa, and this correctly indicates that the tailings sand would be more contractive and hence have a smaller K_α value at high values of α. In this manner, the ξ_R index appears to provide a reasonable means of accounting for the combined influence of relative density and confining stress on K_α relationships for sands.

For more monographs, publications, or videos, visit http://www.eeri.org

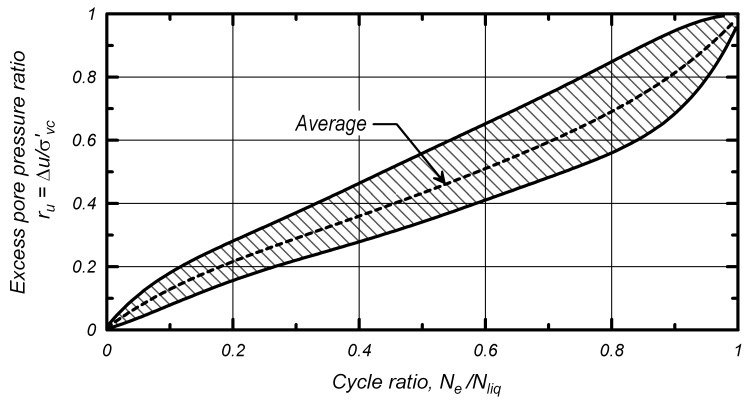

Figure 30. Excess pore water pressure generation versus the number of loading cycles divided by the number of loading cycles to liquefaction (after Seed et al.1976, with permission from ASCE).

Excess Pore Pressures at Different Factors of Safety against Liquefaction

The generation of excess pore pressure during uniform cyclic undrained loading of saturated sands depends on the presence or absence of any initial static shear stress. Laboratory tests with $\alpha = 0$ are considered most representative of the conditions that exist beneath level ground surfaces where the shear stresses on horizontal planes are zero. In this case, the generation of r_u can be related to the ratio N_e/N_{liq}, as shown in Figure 30, where N_e is the number of equivalent uniform loading cycles, and N_{liq} is the number of equivalent uniform loading cycles required to trigger liquefaction.

For level ground conditions, the residual r_u that remains after cyclic loading of sands and gravels can also be related to the factor of safety against liquefaction, FS_{liq}, as shown in Figure 31. The FS_{liq} is determined as

$$FS_{liq} = \frac{\text{CRR}}{\text{CSR}} \tag{19}$$

and is related to the ratio N_e/N_{liq} through the power relation presented previously. Figure 31 shows residual r_u values dropping to 0.1–0.65 with an FS_{liq} of 1.2.

The presence of sustained static shear stresses ($\alpha > 0$), such as exist beneath sloping ground, affects both the rate of pore pressure generation and the magnitude of the residual pore pressure (i.e., the

For more monographs, publications, or videos, visit http://www.eeri.org

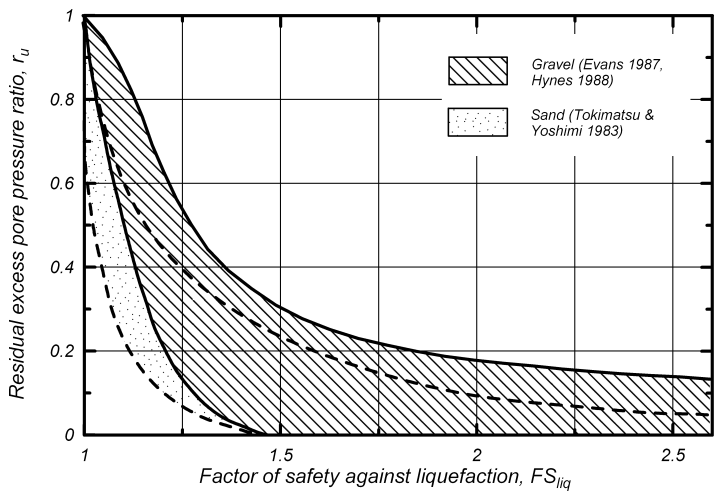

Figure 31. Excess pore water pressure ratio versus FS_{liq} under level ground conditions, from laboratory test data (after Marcuson et al. 1990).

residual is what remains after cyclic loading has ceased). The limiting value of the residual r_u will be less than 100%, as shown by Ishihara and Nagase (1980) and Boulanger (1990), and is illustrated by the experimental results in Figure 27. The value of $r_{u,lim}$ decreases with increasing α, as shown in Figure 32 for cyclic simple shear tests on Fuji River sand (Ishihara and Nagase 1980). The rate of pore pressure generation in the presence of a sustained static shear stress ratio is also significantly different from that for level ground conditions (Finn 1981, Boulanger et al. 1991), as illustrated in Figure 33, and thus the final relationship between FS_{liq} and residual r_u is significantly different from that derived for level ground conditions.

Strain-Based Evaluations of Undrained Cyclic Loading Behavior

The undrained cyclic loading behavior of saturated sands can also be evaluated via strain-based approaches. Experimental data show that the generation of excess pore pressures is more uniquely related to imposed shear strains than to imposed shear stresses. In practical applications, the use of a strain-based approach would then require estimating shear strains induced by ground shaking, which requires estimating both induced shear stresses and the soils' shear moduli. Consequently, a stress-based approach has remained preferable in practice, and thus only a brief discussion of strain-based findings is presented here.

For more monographs, publications, or videos, visit http://www.eeri.org

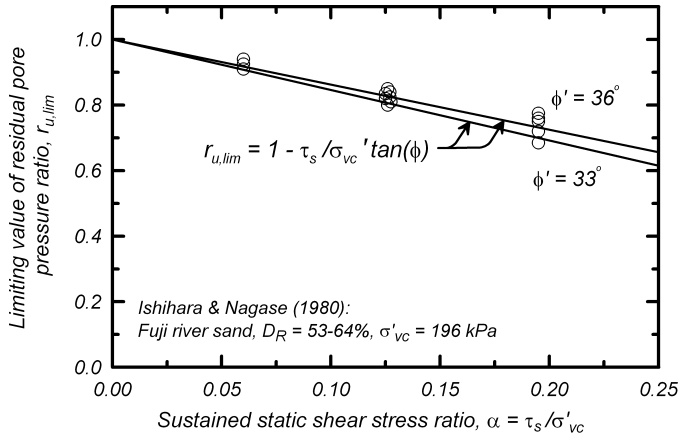

Figure 32. Limiting residual pore pressure ratio versus a sustained static shear stress ratio in undrained cyclic simple shear tests (after Ishihara and Nagase 1980).

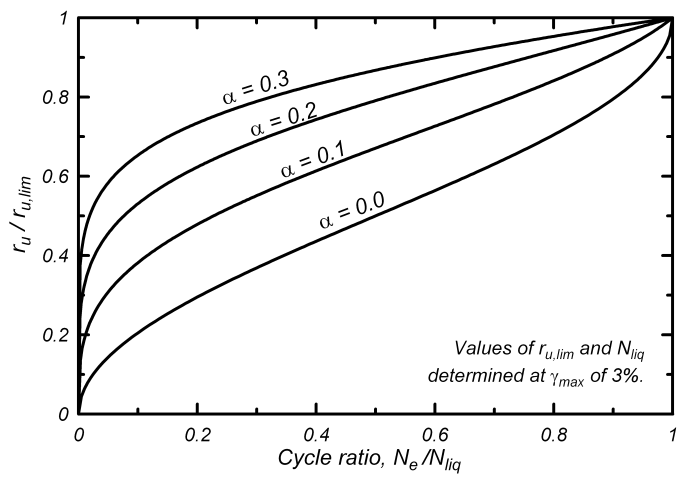

Figure 33. Pore pressure as a fraction of the limiting residual value ($r_u/r_{u,lim}$) versus the cycle ratio (N_e/N_{liq}) for different sustained static shear stress ratios (α) (data from Boulanger et al. 1991).

The stress-strain response of saturated sand to strain-controlled cyclic undrained loading in illustrated in Figure 34, which shows the results of an ICU triaxial test on loose Sacramento River sand (Seed and Lee 1966) and an ICU hollow-cylinder torsional shear test on

For more monographs, publications, or videos, visit http://www.eeri.org

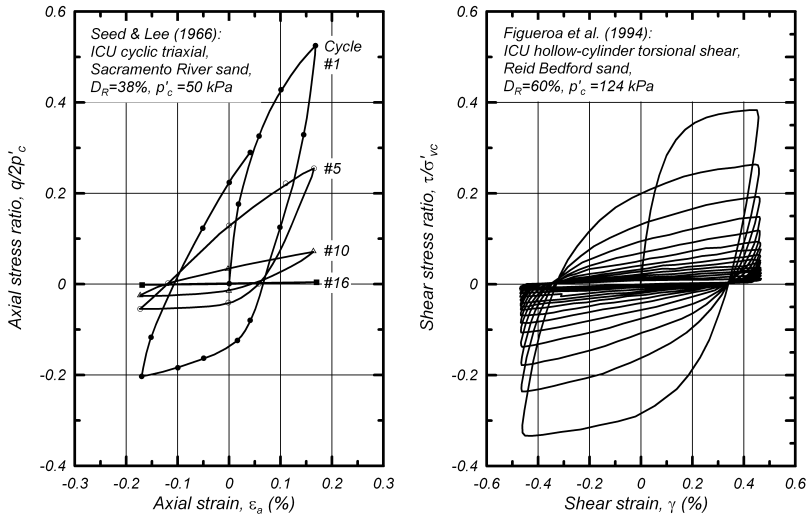

Figure 34. Stress-strain response of sand in strain-controlled cyclic undrained loading in a triaxial test (Seed and Lee 1966) and a torsional shear test (Figueroa et al. 1994) (both with permission from ASCE).

medium-dense Reid Bedford sand (Figueroa et al. 1994). The imposed cyclic loading with an axial strain amplitude of 0.17% in the triaxial test caused the specimen to progressively soften (i.e., the mobilized shear stress decreased with each cycle of loading) as r_u progressively increased to 100% in about 16 cycles. The torsional shear test showed very similar stress-strain behavior, with r_u reaching 100% after about 8–10 cycles of loading at a shear strain amplitude of 0.46%. After r_u had reached 100% in each test, the specimens had nearly zero tangent stiffness in subsequent loading cycles. The negligible stiffness of the specimen after r_u reaches 100% is comparable to the very low stiffness that temporarily develops during stress-controlled loading after r_u has temporarily reached 100%. The difference is that the stress-controlled tests cause the strains to increase with each cycle of loading (exceeding the maximum value from the prior loading cycle), and this additional strain is what enables the specimen to transition to an incrementally dilative tendency.

Dobry (NRC 1985) showed that the generation of r_u for a given number of cycles at different cyclic shear strain amplitudes falls within a relatively narrow band for a broad range of sand types, relative densities, and consolidation stresses, as shown in Figure 35. The data in this figure show that 10 cycles at a shear strain amplitude of

For more monographs, publications, or videos, visit http://www.eeri.org

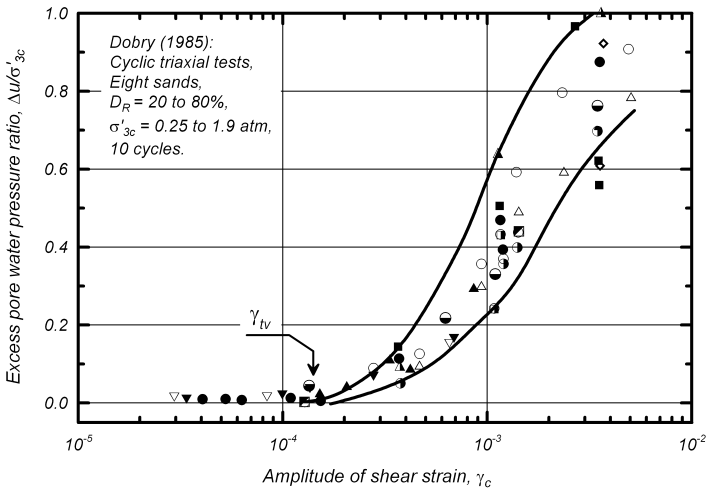

Figure 35. Excess pore water pressure generation versus shear strain amplitude in strain-controlled cyclic undrained triaxial tests on sand (NRC 1985).

0.3–1.0% would generally trigger $r_u = 100\%$. The volumetric cyclic threshold shear strain (γ_{tv}) is the shear strain amplitude below which there is no potential for volumetric strains or pore water pressure generation. The value of γ_{tv} for sand is typically about 0.01–0.02% (e.g., Ladd et al. 1989, Hsu and Vucetic 2004), as shown in Figure 35.

Energy-Based Evaluations of Undrained Cyclic Loading Behavior

The dissipated energy (or work) per unit volume of soil has also been shown to be useful in describing liquefaction behavior (e.g., Davis and Berrill 1978, Law et al. 1990, Cao and Law 1991, Figueroa et al. 1994). Experimental studies by these investigators have shown that the generation of excess pore water pressures in saturated sand or silt is strongly correlated with the dissipated energy during undrained cyclic loading. The subsequent application of energy-based approaches to the assessment of liquefaction in the field requires that the seismic loading be represented in terms of energy. One approach has been the use of Arias intensity (the integral of acceleration squared over time) to describe the energy in ground motions at different depths in a soil profile, as in studies by Egan and Rosidi (1991) and Kayen and Mitchell (1997). These initial studies suggested that energy-based approaches had promise, but this approach has not advanced further, because of (1) potentially large variations in Arias intensity versus

For more monographs, publications, or videos, visit http://www.eeri.org

depth in a soil profile and (2) questions about relating Arias intensity at a specific depth to that at the ground surface.

2.3 Laboratory Testing of Field Samples and the Effects of Sampling Disturbance

The most direct approach to estimating the cyclic strength of saturated sands is to obtain high-quality field samples and then test the specimens in cyclic laboratory tests. This approach requires knowledge of the effects of sampling disturbance (i.e., how the process of sampling the soil affects its subsequent loading behavior) and an understanding of the tests' limitations in approximating the cyclic loading that is induced in situ during an earthquake.

Cyclic triaxial devices and cyclic simple shear devices are the two laboratory test devices that are well suited for cyclic strength testing of undisturbed field samples. The loading conditions in a simple shear device approximate the one-dimensional consolidation conditions beneath level ground before an earthquake and the cyclic shear deformations that develop during vertical propagation of horizontal shear waves. The triaxial device commonly uses isotropic consolidation stresses, so the resulting CRR must be corrected for the differences in mean effective consolidation stresses (i.e., the correction for K_o conditions, as presented in Section 2.2, must be used). Triaxial devices and most simple shear devices are unidirectional in their loading, and thus the CRR must also be reduced by about 10% for the effects of two-directional shaking in the field.

Laboratory test results are also affected by nonuniformities of stress and strain that arise from imperfect boundary conditions, membrane compliance, and other experimental limitations. For example, Gilbert (1984) studied the effect of cyclic loading on specimen uniformity by subjecting $D_R = 40\%$ sand specimens to undrained cyclic loading and then dissecting the specimens in layers to measure the variation in D_R over the height of the specimen. The results in Figure 36 include one specimen that was cyclically loaded to an axial strain of about 11% and later found to have experienced dramatic loosening at its top. The effects of these experimental limitations may become more significant as the sand specimen becomes stronger, because the weakening effect of a stress concentration or interface slip can then become the controlling factor on the overall measurement of cyclic resistance. For this reason, some concerns remain about whether laboratory devices fully represent the cyclic

For more monographs, publications, or videos, visit http://www.eeri.org

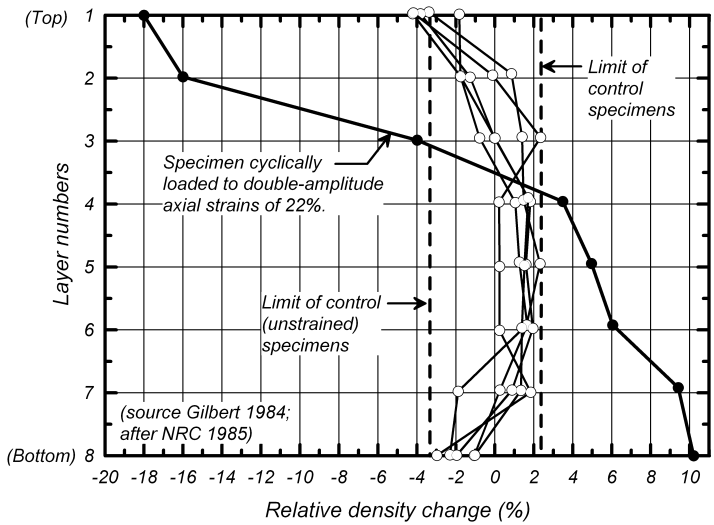

Figure 36. D_R values of various horizontal layers from cyclically loaded triaxial specimens of sand at an initial average D_R of 40% (after NRC 1985).

stress-strain behavior of dense sands under in-situ loading conditions. Nonetheless, careful laboratory testing can provide a valuable measure of a soil's cyclic stress-strain behavior, if the samples are truly undisturbed.

Sampling disturbance has, however, been established as an even greater concern when field samples are tested. This issue has been well illustrated by the comparison of laboratory measurements of the CRR for clean-sand samples that were obtained via high-quality tube sampling techniques versus the preferred "frozen sampling" technique. In frozen sampling, the sand is frozen in situ, and then samples are obtained by coring the frozen ground. The frozen samples are transported to the laboratory, mounted in a testing device, thawed, and tested. The freezing and thawing processes must be largely unidirectional, so that the expansion of the pore water upon freezing and its contraction upon thawing are accommodated by pore water flow rather than by volumetric straining of the soil skeleton. Frozen sampling, if done correctly, imposes very small net volumetric strain on the sand from the in-situ condition to the tested condition. In contrast, tube sampling invariably produces significant volumetric strains as well as partial or total destruction of the sand's fabric.

For more monographs, publications, or videos, visit http://www.eeri.org

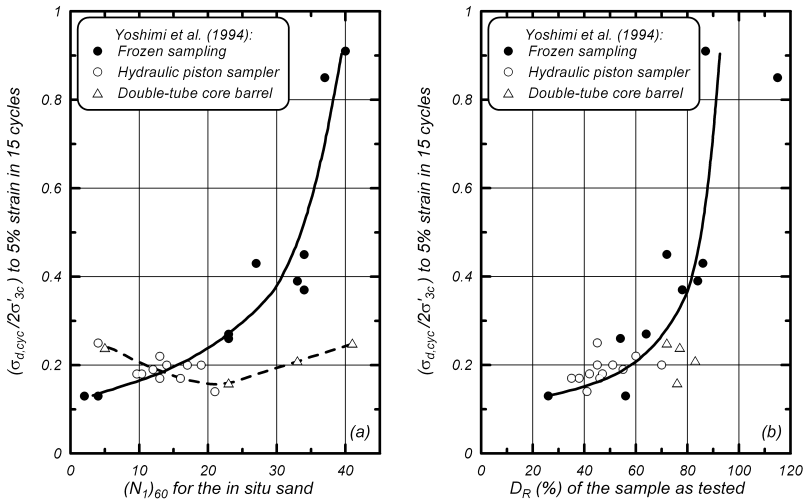

Figure 37. Comparison of CRRs from cyclic triaxial testing of samples obtained via tube sampling and frozen sampling techniques (after Yoshimi et al. 1994).

Figure 37 compares CRR values from cyclic triaxial tests on field samples of clean sands obtained via frozen sampling, hydraulic piston tube sampling, and double-tube core barrel sampling; the test data are from Yoshimi et al. (1994). Figure 37a plots the CRR values against the corrected SPT blow count of $(N_1)_{60}$ that was measured in the same sand deposit, and Figure 44b plots the CRR values against the D_R of the sand specimens as tested in the laboratory. The frozen sampling results show the expected trend of the CRR increasing with increasing values of D_R or $(N_1)_{60}$, whereas the conventional tube sampling results show a relatively low CRR even for the densest sand specimens. One major factor is that tube sampling caused the looser sands to densify and the denser sands to loosen over the course of sampling, transporting, handling, mounting, and reconsolidation. Another major factor is that tube sampling disturbs the sand fabric, which is believed to reduce the fabric's stability against cyclic loading and to particularly reduce any increases in fabric stability that may have been acquired in situ because of the processes of aging, prior stress and strain loading, overconsolidation, and cementation.

The experimental results of Singh et al. (1982) and Goto and Nishio (1988), as presented in Figures 38 and 39, illustrate both the effects of prior strain history and the efficacy of frozen sampling techniques. The cyclic triaxial tests by Singh et al. (1982) in

For more monographs, publications, or videos, visit http://www.eeri.org

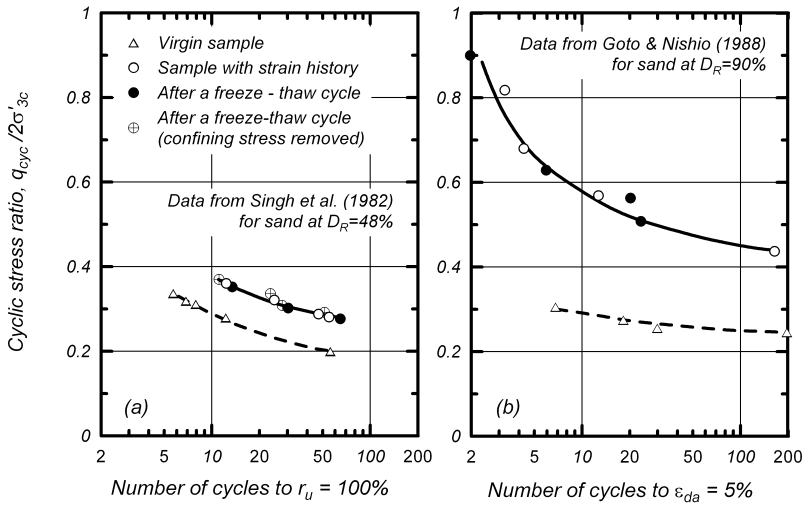

Figure 38. Effects of a freeze-thaw cycle on the cyclic resistance of saturated clean sand in undrained cyclic triaxial tests: (a) data from Singh et al. (1982) for sand at $D_R = 48\%$, and (b) data from Goto and Nishio (1988) for sand at $D_R = 90\%$ (after Yoshimi et al. 1994).

Figure 38a included tests on identical reconstituted sand specimens at $D_R = 48\%$, with one set having been subjected to a cyclic shear strain of relatively small amplitude. The cyclic strain history did not measurably change the specimens' D_R but nonetheless increased the specimens' CRR by 30–40%. The cyclic triaxial tests by Goto and Nishio (1988) on sand at $D_R = 90\%$ provides a similar comparison (Figure 38b), but with the "strain history" specimens having a far more extensive strain history (10,000 cycles with an axial strain amplitude of 0.05%). Again, the specimens' D_R was not significantly altered, but the CRR nonetheless increased by about 80–100%. The CRR's increase with prior strain history is attributed to the sand fabric's becoming more stable as a result of the cyclic straining, even without becoming measurably denser, and this increase is considered illustrative of how a natural sand deposit's CRR can be affected by the stress and strain it experiences over its geologic life.

The CRRs of the sand specimens with prior strain history were unaffected by the process of freezing and thawing, as shown in Figure 38, which indicates that the sand's fabric was not seriously disrupted by the freezing and thawing process. Disturbance during the frozen sampling process was further evaluated in the laboratory

For more monographs, publications, or videos, visit http://www.eeri.org

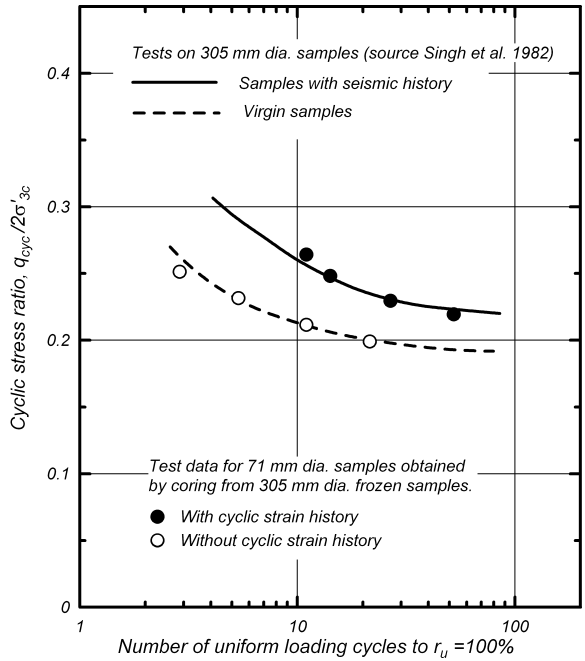

Figure 39. Cyclic resistance of samples obtained by freezing and coring sand at an initial D_R of 60% and effective confining stress of 55 kPa (after Yoshimi et al. 1994, data from Singh et al. 1982).

by Singh et al. (1982) by testing samples cored from two types of frozen reconstituted sands: those with a prior strain history and those with no such history. For both types, the samples obtained by frozen sampling techniques produced the same CRR as obtained for specimens that had not gone through the freezing and coring processes (i.e., reconstituted samples that were prepared directly in the laboratory test device), as shown in Figure 39. These results illustrate why frozen sampling techniques are believed to be capable of obtaining clean-sand samples that are sufficiently undisturbed to properly reflect the in-situ properties of a sand deposit.

The CRR of a dense sand sampled by frozen sampling and tube sampling techniques was also compared with the CRR obtained for specimens of the same sand reconstituted to the same D_R in the laboratory, as shown in Figure 40 (after Yoshimi et al. 1984). Reconstituted specimens were prepared by air pluviation and moist tamping. The CRR values for the tube samples and the reconstituted specimens

For more monographs, publications, or videos, visit http://www.eeri.org

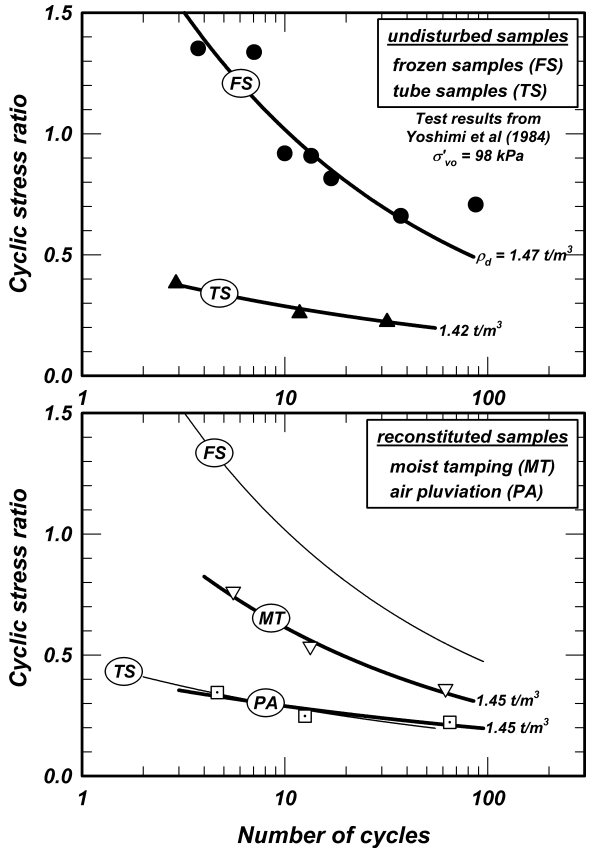

Figure 40. CSRs required to cause 5% double-amplitude axial strain of in-situ frozen samples (FS), conventional "undisturbed" tube samples (TS), samples reconstituted by air pluviation (PA), and samples reconstituted by moist tamping (MT) (after Yoshimi et al. 1984).

were all substantially smaller than those for the frozen samples, which shows that important characteristics of this sand, as they existed in situ, were destroyed or lost by the disturbance produced during tube sampling and were not recreated by the reconstitution of specimens in the laboratory. The greater CRR for the frozen samples is attributed to the in-situ environmental factors (e.g., age, cementation, and stress and strain history) that increase the sand's cyclic strength while not significantly affecting its density.

For more monographs, publications, or videos, visit http://www.eeri.org

Environmental factors can further affect the in-situ CRR through their influence on the in-situ lateral stress (i.e., through K_o). In most cases, the environmental factors of prior cyclic straining, overconsolidation, and aging would be expected to increase the in-situ K_o, with a corresponding increase in the in-situ CRR.

2.4 Field Processes Not Replicated in Laboratory Tests

The excess pore water pressures generated by an earthquake will dissipate over time as pore water seeps out of the zones of higher excess pore water head ($\Delta h = \Delta u/\gamma_w$) to zones of lower excess pore water head. The resulting pore water seepage that takes place both during and after earthquake shaking can greatly complicate the spatial occurrence of strength loss and deformation in a soil deposit. Laboratory element tests (e.g., triaxial or simple shear tests) do not replicate these effects, which have important implications for design practice, as discussed below.

The redistribution of pore water pressures within a layered soil profile is illustrated by the profile in Figure 41. A layer of loose sand 3–9 m deep is overlain by dense silty sand and underlain by stiff clay. The total and effective vertical stresses and the pore water pressures are shown for the conditions before earthquake shaking and after earthquake shaking has triggered "liquefaction" in the loose sand

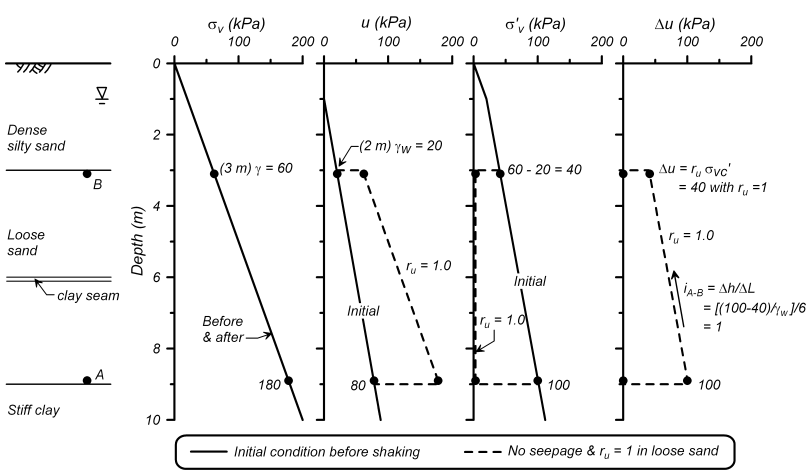

Figure 41. Stresses and pore pressures in a level-ground soil profile before earthquake shaking and for the condition in which $r_u = 100\%$ has been triggered in the loose sand but no significant seepage has occurred.

For more monographs, publications, or videos, visit http://www.eeri.org

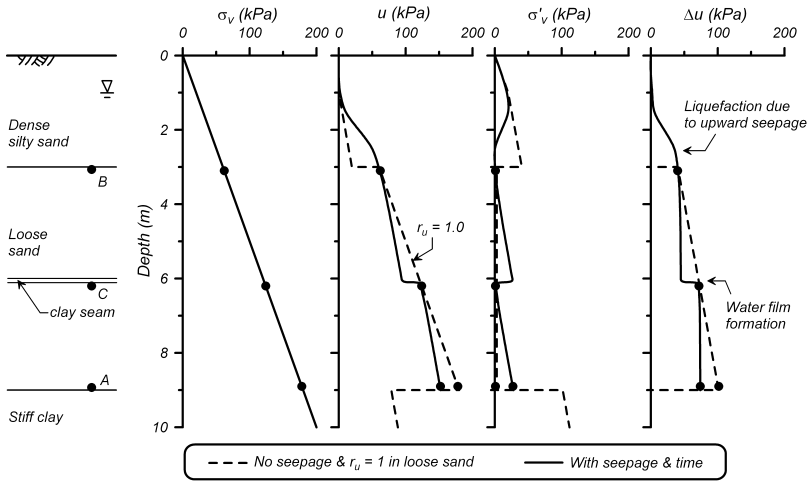

Figure 42. Two consequences of upward pore water seepage for a layered soil profile during and after earthquake shaking.

layer. This example further assumes that no excess pore pressures are generated in the overlying dense silty sand, that no significant pore water seepage has occurred, and that all soils weigh 20 kN/m^3. The σ'_v has dropped to zero throughout the loose sand, while Δu is now equal to σ'_{vc} at all depths. The Δu increases with depth because the vertical stresses increase with depth, and thus there is an upward hydraulic gradient ($i = \Delta h/\Delta L$) that initially is equal to unity throughout the loose sand layer. This condition of $i = 1$ upward in the loose sand layer is analogous to the conditions that can initiate piping erosion (or quicksand conditions) during steady seepage problems. The consequence of this upward hydraulic gradient is seepage of pore water up through the soil profile, often concentrated along cracks and localized channels and producing sand and water boils at the ground surface.

The complications that arise from the upward seepage of pore water during and after an earthquake are schematically illustrated in Figure 42, which is the same profile considered in Figure 41 but with the consequences of upward seepage included. The upward flow of pore water through the loose sand layer (i.e., from point A toward point B) can increase the excess pore pressures within the overlying dense silty sand layer (which has a slightly lower permeability than the clean loose sand) during or after shaking. This may lead to liquefaction of the overlying dense silty sand, which otherwise may have had a sufficiently large CRR to have precluded liquefaction during

For more monographs, publications, or videos, visit http://www.eeri.org

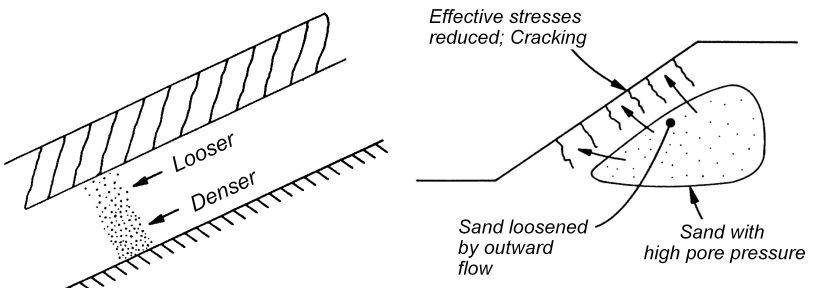

Figure 43. Two mechanisms by which void redistribution contributes to instability after earthquake-induced liquefaction (NRC 1985, Whitman 1985).

shaking if that sand had been perfectly undrained. A second possible complication of upward seepage can occur at even lower-permeability layers, such as the clay seam shown at a depth of 6 m (i.e., at point C). Upwardly seeping pore water can accumulate immediately below this interface, resulting in the formation of water films or water pockets under certain conditions. Note that the formation of a water film does not increase Δu, because the total u is already equal to the total overburden stress. Water films and water pockets may either slowly dissipate through the overlying layer or break through at concentrated cracks or piping channels that can extend up to the ground surface.

The trapping of seeping pore water at interfaces between lower- and higher-permeability soils can result in local void ratio changes without necessarily forming water films. Whitman (1985) used the term "void redistribution" to describe this process, which emphasizes the fact that zones can be getting denser locally while other zones are getting looser during the pore water pressure diffusion process. Figure 43 illustrates mechanisms by which void redistribution and upward seepage can contribute to deformations or instability of slopes. Figure 43a shows an infinite slope with liquefiable sand beneath a lower-permeability layer. Upward water seepage that is due to shaking-induced excess pore water pressures leads to a loosening (dilation) of sand at the top of the liquefied layer and densification (contraction) at the bottom. If the top of the layer becomes loose enough, then its critical-state strength can drop to a value less than that required for stability of the slope, after which deformations would develop along a localized shear plane at the top of the sand layer. Figure 43b is similar, but it also illustrates how the outward seepage can weaken overlying layers by increasing their pore pressures

For more monographs, publications, or videos, visit http://www.eeri.org

and/or facilitating the formation of cracks. Intermixing of finer- and coarser-grained layered soils along a shear zone may also contribute to progressive strength losses as deformations increase (Byrne and Beaty 1997, Naesgaard and Byrne 2005). Redistribution of excess pore water pressures, and any associated void redistribution, may explain delays between the end of shaking and the time of failure that have been observed in several case histories (e.g., Elorza and Machado 1929, Akiba and Semba 1941, Kawakami and Asada 1966, Seed et al. 1975, Seed 1979, Marcuson et al. 1979, Hamada 1992, Mejia and Yeung 1995, Harder and Stewart 1996, Berrill et al. 1997).

The major consequence of void redistribution is that the liquefied soil's shear strength and stress-strain response do not solely depend on the pre-earthquake material properties and state (e.g., relative density and effective confining stress); rather, they can also reflect the response of the entire system. The effects of void redistribution are poorly understood and are not explicitly incorporated in current engineering practice.

The formation of water films has been observed under level-ground conditions in physical model studies (Liu and Qiao 1984, Elgamal et al. 1989, Dobry and Liu 1992, Fiegel and Kutter 1994) and simple cylindrical column tests (Scott and Zuckerman 1972, Kokusho 1999, Kokusho and Kojima 2002). Figure 44 shows a water film that formed beneath a silt seam within a cylindrical column of saturated sand as a consequence of void redistribution after impact-induced liquefaction in the sand (Kokusho 1999). These studies have illustrated the importance of stratigraphy (layer thickness and sequence), permeability contrasts, and initial D_R on the thickness of water films.

For sloping ground conditions, numerous physical model tests have identified shear strain localizations at the interface between a liquefied sand layer and an overlying lower-permeability layer (e.g., Arulanandan et al. 1993, Fiegel and Kutter 1994, Balakrishnan and Kutter 1999, Brandenberg et al. 2001, Malvick et al. 2002, Kulasingam et al. 2004), including cases in which the majority of deformations were delayed until after shaking had ceased (e.g., Kokusho 1999, 2000; Kokusho and Kojima 2002; Malvick et al. 2004). For example, Figure 45 shows the postshaking deformed shape of a centrifuge model consisting of a uniform sand slope with embedded silt arcs and planes. The majority of the slope deformations were concentrated in a localized shear zone in the sand immediately beneath the silt arc, and this localization formed after the shaking had ceased. A

For more monographs, publications, or videos, visit http://www.eeri.org

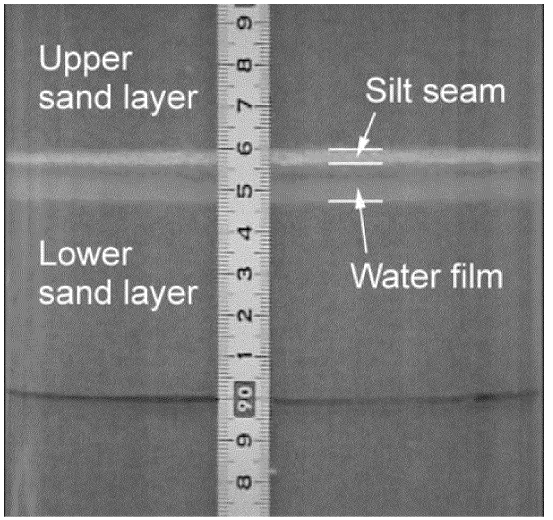

Figure 44. A water film that formed beneath a silt seam in a cylindrical column of saturated sand after liquefaction (Kokusho 1999, with permission from ASCE).

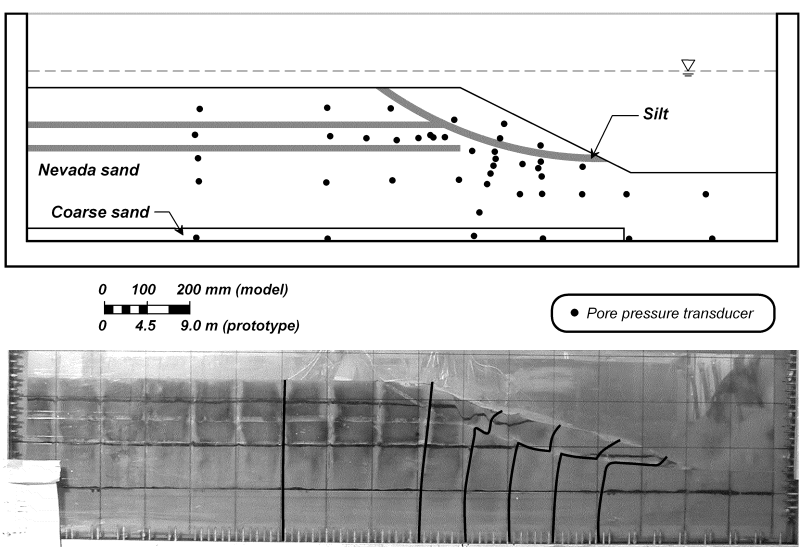

Figure 45. Localization of shear deformations along a lower-permeability interlayer within a saturated sand slope tested in a centrifuge (Malvick et al. 2008).

For more monographs, publications, or videos, visit http://www.eeri.org

dense array of pore pressure transducers showed that the onset of localized shear deformation was caused by the upward seepage of pore water being impeded by the lower-permeability silt arc (Malvick et al. 2008).

Void redistribution and localized shear deformations that are due to liquefaction-induced pore water seepage are complicated phenomena that are difficult to quantitatively predict, for a variety of reasons—such as heterogeneity of geologic deposits, formation of cracks and sand boils, and uncertainty in seismic shaking intensity and duration. However, the understanding of the basic void redistribution mechanism is increasing because of physical modeling studies and simple theoretical analyses. The results of physical modeling studies of liquefaction in layered soil profiles demonstrate that the residual shear strength of liquefied soil depends on all the factors that affect void redistribution and is therefore not uniquely related to pre-earthquake soil properties alone, as commonly represented by penetration resistances or by tests on "undisturbed" samples. The implications of these observations are addressed in Section 5.

For more monographs, publications, or videos, visit http://www.eeri.org

For more monographs, publications, or videos, visit http://www.eeri.org

3 TRIGGERING OF LIQUEFACTION

The assessment of potential liquefaction hazards involves two questions: (1) will liquefaction be triggered by the earthquake ground motions under consideration and (2) what are the potential consequences of liquefaction having been triggered? This section addresses the procedures used to evaluate liquefaction triggering, including a discussion of geologic considerations, the analysis framework, in-situ testing, liquefaction triggering correlations, and an example of an analysis.

3.1 Liquefaction Susceptibility of Soil Deposits

A study of local site geology is an essential part of characterizing the nature and possible extent of soils that are susceptible to liquefaction at a specific site. The extent or degree of liquefaction depends on the distribution of cohesionless sediments (gravels, sands, and very-low-plasticity silts) within the deposit and requires a sufficiently high water table for the sediments to be largely saturated. The most susceptible sediments are fills and alluvial, fluvial, marine, deltaic, and wind-blown deposits. In addition, sediments are most susceptible to liquefaction when they are recently deposited, becoming more resistant as they become older. These factors are represented in the criteria recommended by Youd and Perkins (1978), as shown in Table 1, for identifying the likely presence of soils susceptible to liquefaction. These types of criteria are commonly used with geologic maps to produce regional maps of liquefaction hazards for planning or zoning purposes.

Cohesive sediments (e.g., clays and plastic silts) can also develop significant strains and ground deformations during earthquake

For more monographs, publications, or videos, visit http://www.eeri.org

Table 1 Susceptibility of soil deposits to liquefaction during strong seismic shaking (Youd and Perkins 1978, with permission from ASCE).

Type of deposit	Distribution of cohesionless sediments in deposit	Likelihood that cohesionless sediments, when saturated, would be susceptible to liquefaction			
		< 500 years	Holocene	Pleistocene	Pre-Pleistocene
Continental					
River channel	Locally variable	Very high	High	Low	Very low
Floodplain	Locally variable	High	Moderate	Low	Very low
Alluvial fan and plains	Widespread	Moderate	Low	Low	Very low
Marine terraces and plains	Widespread	—	Low	Very low	Very low
Delta and fan delta	Widespread	High	Moderate	Low	Very low
Lacustrine and playa	Variable	High	Moderate	Low	Very low
Colluvium	Variable	High	Moderate	Low	Very low
Talus	Widespread	Low	Low	Very low	Very low
Dunes	Widespread	High	Moderate	Low	Very low
Loess	Variable	High	High	High	Unknown
Glacial till	Variable	Low	Low	Very low	Very low
Tuff	Rare	Low	Low	Very low	Very low
Tephra	Widespread	High	High	?	?
Residual soils	Rare	Low	Low	Very low	Very low
Sebkha	Locally variable	High	Moderate	Low	Very low

For more monographs, publications, or videos, visit http://www.eeri.org

Coastal zone					
Delta	Widespread	Very high	High	Low	Very low
Estuarine	Locally variable	High	Moderate	Low	Very low
Beach—high wave energy	Widespread	Moderate	Low	Very low	Very low
Beach—low wave energy	Widespread	High	Moderate	Low	Very low
Lagoonal	Locally variable	High	Moderate	Low	Very low
Foreshore	Locally variable	High	Moderate	Low	Very low
Artificial fill					
Uncompacted fill	Variable	Very high	—	—	—
Compacted fill	Variable	Low	—	—	—

For more monographs, publications, or videos, visit http://www.eeri.org

loading—particularly where the sediments are soft and sensitive, there is a significant driving shear stress (e.g., slope or foundation load), and the shaking levels are sufficiently strong. However, because cohesive soils differ in shear strength characteristics from cohesionless soils, different engineering procedures are required to evaluate how cohesive soils respond to seismic loading. For this reason, the term "liquefaction" is used in reference to the behavior of cohesionless soils (e.g., gravels, sands, and very-low-plasticity silts), whereas the term "cyclic softening" is used to describe the behavior of clays and plastic silts. Criteria and procedures for evaluating the potential for cyclic softening in cohesive soils are described in Section 6.

Surface evidence of liquefaction has most commonly been associated with liquefaction occurring at depths of less than about 15 m. This is related to the fact that the shallower deposits are typically the youngest and therefore most susceptible to liquefaction. Liquefaction at greater depths beneath level ground surfaces may not be manifested at the ground surface and thus may go undetected. Liquefaction at greater depths is, however, a concern in many situations, including earth embankments constructed of looser material (e.g., hydraulic fill) or constructed over younger sediments.

Historical records or geologic evidence of prior liquefaction at a site provides the most direct evidence that a soil deposit is susceptible to liquefaction, because soils that liquefy in one earthquake have often been observed to liquefy in subsequent earthquakes. Consequently, any evaluation of liquefaction hazards at a particular site would significantly benefit from a review of available historical records.

Local sedimentary processes and the historical construction of fills are often clearly evident in aerial photos. For example, Figure 46 shows an aerial photo of Moss Landing, California taken in 1952 and another taken in 1987. Both photos provide a good view of how beach, eolian, fluvial, and estuarine depositional processes all come together to produce a rather complex depositional environment. In addition, detailed comparison of these two photos shows that areas of the shoreline have been modified by port development (areas of filling and dredging) or changed by the natural deposition and erosion processes. The areas of very recent natural deposits and loosely placed fills would be considered highly susceptible to liquefaction, and in fact they closely corresponded to the areas of more severe ground deformations caused by liquefaction during the 1989 Loma Prieta earthquake.

For more monographs, publications, or videos, visit http://www.eeri.org

Figure 46. Aerial photos of Moss Landing, California, showing the geologic setting; the photo at left is from 1952, and the photo at right is from 1987. When compared, these photos can identify shoreline movements, artificial fills, and recent construction (photos: USGS).

3.2 Analysis Framework for Developing Liquefaction Triggering Correlations

Several approaches or frameworks have been proposed over the last 45 years for assessing the potential for triggering liquefaction. The most widely used approach has been the stress-based approach that compares the earthquake-induced cyclic stresses with the cyclic resistance of the soil. Strain-based and energy-based approaches are less common and are therefore not covered here.

Earthquake-induced cyclic stresses beneath level-ground sites are attributed primarily to the effects of horizontal shaking. Figure 47 schematically illustrates the stresses and pore pressures acting on an element of soil beneath a level ground surface before and during horizontal shaking by an earthquake. Vertical shaking of this profile would produce additional transient changes in the total vertical stress, total horizontal stress, and pore pressure, but the vertical and horizontal effective stresses would be unaffected. This is why the effects of vertical shaking are not considered in the analysis of level-ground profiles. The induced horizontal cyclic stresses are normalized by the vertical effective consolidation stress (σ'_{vc}) to arrive at a CSR, which is then compared with the soil's CRR, as shown in Figure 48. Liquefaction

For more monographs, publications, or videos, visit http://www.eeri.org

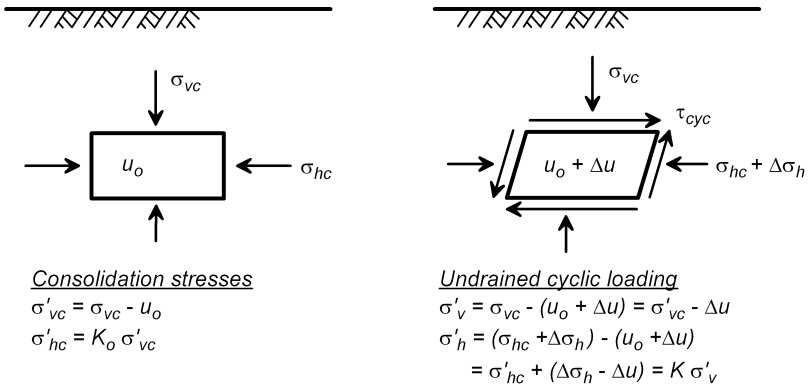

Figure 47. Cyclic stresses on a soil element beneath level ground during horizontal shaking.

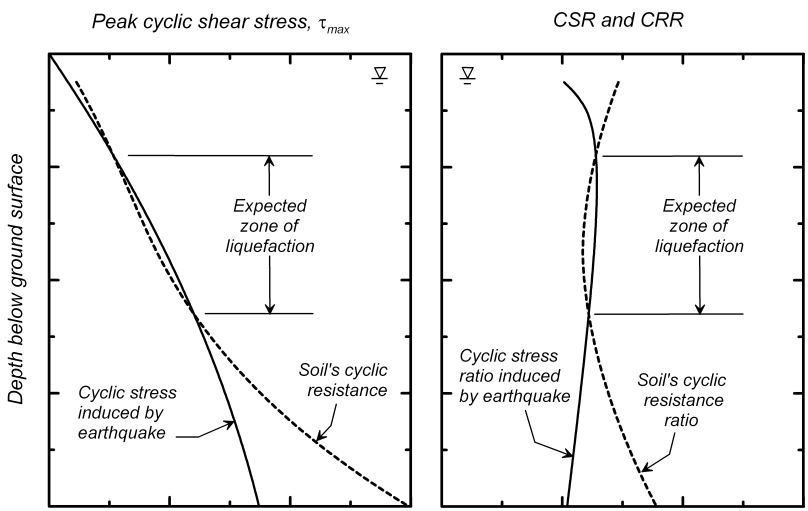

Figure 48. The expected zone of liquefaction is determined by comparing the earthquake-induced cyclic stresses with the cyclic resistances of the soil.

is expected at depths where the induced stresses exceed the cyclic resistances.

The development of design procedures therefore requires methods for estimating the earthquake-induced cyclic shear stresses (i.e., the CSR) and the in-situ CRR. The earthquake-induced CSR is often estimated via the Seed-Idriss simplified procedure described in Section 3.3.

For more monographs, publications, or videos, visit http://www.eeri.org

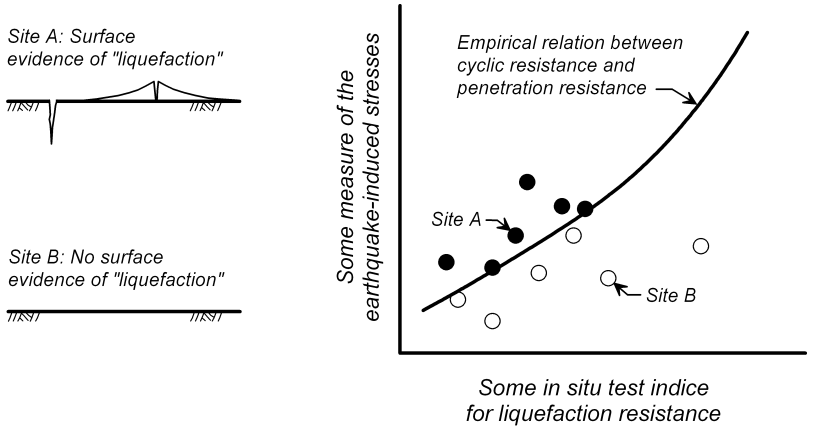

Figure 49. Schematic of the approach used to develop relationships between the in-situ CRR of sand and the results of in-situ tests.

The in-situ CRR of sands could be evaluated on the basis of laboratory testing of field samples, but this would require the use of frozen sampling techniques if meaningful results are to be obtained, as discussed in Section 2.3. The cost of frozen sampling techniques is prohibitive for the vast majority of projects.

Consequently, semi-empirical relationships are developed between the in-situ CRR of sands and the results of in-situ tests, on the basis of compilations of case histories in which evidence of liquefaction has or has not been observed, as schematically illustrated in Figure 49. For each site, the earthquake-induced CSR and in-situ test results (e.g., SPT and CPT results) are examined, and a critical layer is identified. A boundary line is then developed that separates the case histories in which "liquefaction" was observed (e.g., Site A in Figure 49) from case histories in which liquefaction was not observed (e.g., Site B in Figure 49). This boundary line is then adopted as providing the relationship between in-situ CRR and the in-situ test index.

The definition of "liquefaction" in this context refers to observations, mainly from the ground surface, that are interpreted as meaning that sand at some depths must have developed high excess pore water pressures and significant strains (shear or volumetric). The observed effects may include soil and water boils, ground cracking, ground deformations (lateral or vertical), upheaval of buried structures, and settlement or failures of structural foundations. The interpretation of field observations is complicated by the fact that surface observations can be inconclusive in identifying the depths at which liquefaction

For more monographs, publications, or videos, visit http://www.eeri.org

probably occurred or in identifying the absence of liquefaction at depth. For example, sands may liquefy within localized pockets or depth intervals that are not extensive or shallow enough to produce any surface manifestations.

The effectiveness of the resulting correlation also depends on the degree to which the in-situ test truly reflects the soil's resistance to cyclic loading. For example, Seed (1979b) explained that both the penetration resistance from an SPT or a CPT and the CRR of a sand would be expected to respond similarly (i.e., increase or decrease) to changes in factors such as D_R, K_o, age, cementation, or seismic history. This observation provides qualitative support for the expectation of a reasonable correlation between penetration resistance and CRR, although a more quantitative understanding of how these factors might affect the resulting correlation remains a desirable goal.

Our understanding of the cyclic loading behavior of saturated sands, on the basis of experimental findings, indicates that the in-situ CRR of sand also depends on the duration of shaking (i.e., this is analogous to the number of loading cycles), the effective overburden stress (i.e., σ'_{vc} and K_σ), and the presence of sloping ground (i.e., K_α). The case history database is not extensive enough to empirically define these individual effects, in part because they are correlated with other factors and relationships in the analyses, so these effects are instead accounted for by using relationships that are derived from our fundamental understanding of sand behavior. Relationships for these three effects are discussed in Sections 3.6–3.8.

The organization of case history data onto a single graph of CSR versus in-situ test measurement can then be achieved by adjusting the data points for each case history to a common reference condition (i.e., one duration, one overburden stress, and level-ground conditions). These adjustments are performed by using the same relationships that will be used in the final design procedure, and thus the final liquefaction correlation should strictly be used only in combination with the relationships that were used to process the case history database.

3.3 Simplified Procedure for Estimating Earthquake-Induced Stresses

The shear stresses induced at any depth in a soil deposit with a level ground surface during an earthquake appear to be due primarily to the vertical propagation of horizontal shear waves. Analytical

For more monographs, publications, or videos, visit http://www.eeri.org

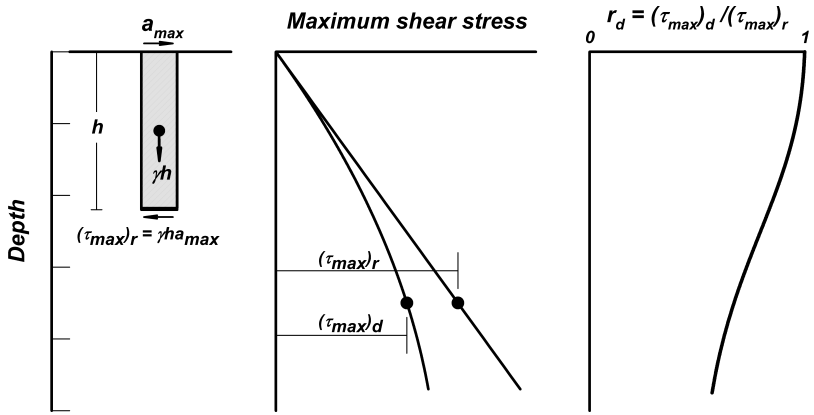

Figure 50. Schematic for determining maximum shear stress, $\tau_{\max}$, and the stress reduction coefficient, r_d.

procedures are available to calculate these stresses if the characteristics of the soils comprising this deposit and the input motions are known. Such information is not available for most of the "liquefaction/no liquefaction" case histories that have been used to develop correlations on the basis of field observations. In addition, borings drilled for most projects seldom extend to the depths needed to define the soil profile in sufficient detail for site response studies. For these reasons, the simplified liquefaction evaluation procedure (Seed and Idriss 1971) for calculating the induced shear stresses, and hence the CSR, continues to be widely used.

If the soil column above a depth z behaved as a rigid body (Figure 50), then the maximum shear stress on the base of that column can be computed as the product of its mass and maximum horizontal surface acceleration:

$$(\tau_{\max})_r = \frac{\gamma \cdot z}{g} a_{\max} = \sigma_v \frac{a_{\max}}{g} \tag{20}$$

where $a_{\max}$ is the maximum ground surface acceleration, γ is the average total unit weight of the soil above depth z, and σ_v is the total vertical stress at depth z. In reality, the soil column behaves as a deformable body, and hence the maximum shear stress will differ from the value for a rigid body with the same maximum ground surface acceleration. The maximum shear stress for a deformable body can be determined from dynamic site response analyses, and the results compare to the rigid body case as follows:

$$(\tau_{\max})_d = r_d (\tau_{\max})_r \tag{21}$$

For more monographs, publications, or videos, visit http://www.eeri.org

where r_d is a shear stress reduction coefficient. The variations of $(\tau_{\max})_r$ and $(\tau_{\max})_d$ will typically have the form shown in Figure 50, and thus the value of r_d will decrease from a value of 1 at the ground surface to lower values at large depths.

One-dimensional dynamic site response analyses have been used to develop simplified expressions for r_d. These analyses have shown that r_d is particularly dependent on the earthquake ground motion characteristics (e.g., intensity and frequency content), the shear wave velocity profile of the site, and the nonlinear dynamic soil properties (Seed and Idriss 1971, Golesorkhi 1989, Idriss 1999, Cetin et al. 2004).

Idriss (1999), in extending the work of Golesorkhi (1989), performed several hundred parametric site response analyses and concluded that, for the purpose of developing liquefaction evaluation procedures, the parameter r_d could be adequately expressed as a function of depth and earthquake magnitude (M). The following expressions were derived by using those results:

$$r_d = \exp(\alpha(z) + \beta(z)M) \tag{22}$$

$$\alpha(z) = -1.012 - 1.126 \sin\left(\frac{z}{11.73} + 5.133\right) \tag{23}$$

$$\beta(z) = 0.106 + 0.118 \sin\left(\frac{z}{11.28} + 5.142\right) \tag{24}$$

in which z is depth in meters, M is moment magnitude, and the arguments inside the sine terms are in radians. Equations 22–24 are mathematically applicable to a depth of $z \leq 34$ m. However, the uncertainty in r_d increases with increasing depth, so these equations should actually be applied only for depths that are less than about 20 m. Liquefaction evaluations at greater depths often involve special conditions for which more detailed analyses can be justified. For these reasons, it is recommended that the CSR (or equivalent r_d values) at depths greater than about 20 m be based on site response studies—provided, however, that a high-quality site response calculation can be completed for the site. Site response analyses for this purpose require sufficient subsurface characterization of the site and must account for variability in the possible input motions.

Figure 51 shows plots of r_d calculated by using the above recommended expressions for M values of 5.5, 6.5, 7.5, and 8. Also shown in this figure is the average of the range published by Seed and Idriss (1971). The information in Figure 51 indicates that the average of that

For more monographs, publications, or videos, visit http://www.eeri.org

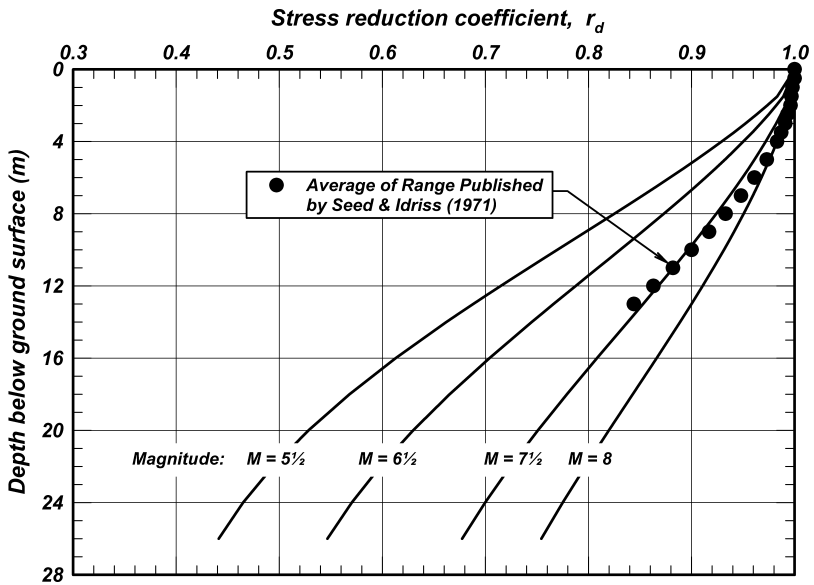

Figure 51. Variations of the stress reduction coefficient r_d with depth and earthquake magnitude (Idriss 1999).

range is comparable with the curve calculated by using the revised expressions with M = 7.5 for depths up to about 14 m. Cetin et al. (2004) proposed r_d values that are a function of depth, earthquake magnitude, level of shaking, and average shear wave velocity over the top 12 m of the site, whereas Kishida (2008) proposed r_d values that are a function of depth, a response spectra ratio (as a measure of frequency content), level of shaking, and shear wave velocity profile. The r_d values by Kishida are in good agreement with those in Figure 51 when the shear wave velocity profile corresponds to sandier soil deposits and are smaller than those in Figure 51 for depths greater than 6 m when the shear wave velocity profile corresponds to sites with predominantly soft fine-grained soils. The r_d values by Cetin et al. reduce more quickly with depth and are significantly smaller than those by Kishida or Idriss.

The earthquake-induced cyclic stress time series involves numerous cycles at different strengths, with the damaging effects of the irregular time series depending on the number of cycles and the stress magnitudes for each cycle. Various studies have shown that an irregular time series can be approximated by a uniform cyclic stress time

For more monographs, publications, or videos, visit http://www.eeri.org

series with an equivalent number of uniform cycles that depends on the uniform cyclic stress amplitude (as described in Section 3.5).

Consequently, Seed and Idriss (1971) chose to represent earthquake-induced cyclic stresses by using a representative value (or equivalent uniform value) equal to 65% of the peak cyclic stress. The corresponding earthquake-induced CSR is therefore computed as

$$\mathrm{CSR} = 0.65\frac{\tau_{\max}}{\sigma'_{vc}} = 0.65\frac{\sigma_{vc}}{\sigma'_{vc}}\frac{a_{\max}}{g}r_d \tag{25}$$

The choice of 0.65 to represent a reference stress level is somewhat arbitrary, but it was selected in the beginning of the development of liquefaction evaluation procedures in 1966 and has been in use ever since. More importantly, the overall liquefaction evaluation procedure would be essentially unaffected by the choice of a different reference stress ratio, provided that the adjustment factors for the duration of shaking and the empirically derived liquefaction correlations were all derived for that reference stress (see Section 3.5).

3.4 In-Situ Tests as Indices for Liquefaction Characteristics

The in-situ tests that have been most widely used as indices for evaluating liquefaction characteristics include the SPT, CPT, BPT, large penetrometer test (LPT), and shear wave velocity (V_s) test. The SPT was used first in developing liquefaction correlations and was the most common in practice up through the 1990s. The CPT has a number of advantages, however, that have made it the primary site characterization tool in certain geologic settings. The BPT, LPT, and V_s tests tend to be used in special situations and thus are used less often than the SPT and CPT in liquefaction evaluations. Each of these tests is discussed separately below, after which the complementary roles of site investigation techniques and the advantages of pairing techniques (e.g., CPT soundings and SPT borings) are discussed.

SPT

The SPT is a widely available sampling method that indicates a soil's compactness or strength. The SPT measures the number of blows (N) by a 140-pound hammer falling freely through a height of 30 in. that are required to drive a standard split-spoon sampling tube (2 in. outside diameter, $1^3/_8$ in. inside diameter) to a 12-in. depth after an initial seating drive of 6 in. The thick walls of the split-spoon sampler

For more monographs, publications, or videos, visit http://www.eeri.org

make it rugged enough to use in a wide range of soil conditions. The soil samples are too disturbed for meaningful engineering property tests but are nonetheless suitable for index testing (e.g., gradations and Atterberg limits). The SPT blow count or "*N* value" is low in soft or loose soils and increases with increasing stiffness or strength of the soil, and this value can thus be used as an index of the soil's in-situ strength or compactness. Because of its economical nature and ruggedness, this test is widely used to evaluate the spatial variability of a soil deposit, and consequently the *N* value has been correlated with a wide range of engineering characteristics (e.g., Kulhawy and Mayne 1990).

Satisfactory use of the SPT for liquefaction analyses requires that the apparatus and procedures conform with the ASTM D-6066 standard. The features of the procedure recommended by Seed et al. (1985) for liquefaction evaluations, as summarized in Table 2, meet this standard and continue to be followed in practice.

Among the most important variables is the amount of energy delivered to the drill rod stem by each impact of the SPT hammer. The

Table 2 Recommended features of SPT procedure for liquefaction evaluations (after Seed et al. 1985, with permission from ASCE).

Feature	**Description**
Borehole	Rotary borehole diameter of 4–5 in. with drilling mud for stability; the drilling mud should be kept thick enough, and the hole should always be full. Special care is required when pulling rods out of the hole, to avoid suction.
Drill bit	Upward deflection of drilling mud (e.g., tricone or baffled drag bit)
Sampler	O. D. = 2 in. I. D. = 1.38 in. (constant; i.e., no room for liners in barrel)
Drill rods	A or AW for depths < 50 ft N, BW, or NW for greater depths
Energy delivered to sampler	2,520 in.-lb. (i.e., 60% of theoretical maximum of 140 lbs. falling 30 in.)
Blow count rate	30–40 blows per minute
Penetration resistance count	Measured over a range of 6–18 in. of penetration into the ground

For more monographs, publications, or videos, visit http://www.eeri.org

range of delivered energy can be 30–90% of the theoretical maximum energy (the 140-lb hammer multiplied by its 30-in. drop height), depending on the amount of energy lost to frictional and mechanical resistances that depend on the type of equipment and its operating condition. The N value is essentially inversely proportional to the delivered energy (Schmertmann and Palacios 1979). In U.S. practice, the delivered energy is commonly about 55–60% of the theoretical maximum energy (Kovacs et al. 1983), and therefore Seed et al. (1984) recommended adopting N_{60} as a standard. The value of N_{60} is computed as

$$N_{60} = N_m \frac{ER_m}{60} \tag{26}$$

where N_m is the measured blow count, ER_m is the measured delivered energy ratio as a percentage, and N_{60} is the blow count for an energy ratio of 60%. The ratio of $ER_m/60$ is also referred to as an energy ratio correction factor, C_E. The energy ratio is one of the most important variables in obtaining reliable N_{60} values. Therefore, it is important that energy ratios be routinely measured as part of liquefaction evaluations.

Additional correction factors may be needed to arrive at a more standardized value of N_{60}. The resulting relationship is given by

$$N_{60} = C_E C_B C_R C_S N_m \tag{27}$$

in which C_E is the energy ratio correction factor described above, C_B is a correction factor for borehole diameter, C_R is a correction factor for rod length, and C_S is a correction factor for a sampler that had room for liners but was used without the liners. Suggested ranges for each factor are in Table 3. The borehole diameter and sampler correction factors can be important in interpreting older borings, but for future applications it is recommended that appropriate standards be followed so that the C_B and C_S factors are unnecessary (i.e., each is equal to unity).

The short rod correction factor C_R (Table 3) is intended to account for how the energy transferred to the sampling rods is affected by rod length (e.g., Schmertmann and Palacios 1979). The hammer-to-anvil impact sends a compressive stress wave down the sampling rods, which then reflects from the sampler as a tension wave. This tension wave returns to the anvil, where it causes the hammer to bounce off the anvil. Schmertmann and Palacios (1979) concluded that the energy imparted to the sampling rods during this primary impact

For more monographs, publications, or videos, visit http://www.eeri.org

Table 3 Correction factors for SPT N values.

Factor	Description
Energy ratio	Energy measurements are required to determine the delivered energy ratios or to calibrate the specific equipment being used. The correction factor is then computed as $$C_E = \frac{ER_m}{60}$$ where ER_m is the measured energy ratio as a percentage of the theoretical maximum. Empirical estimates of C_E (for rod lengths of 10 m or more) involve considerable uncertainty, as reflected by the following ranges: Doughnut hammer $C_E = 0.5$–1.0 Safety hammer $C_E = 0.7$–1.2 Automatic triphammer $C_E = 0.8$–1.3 (Seed et al. 1984, Skempton 1986, NCEER 1997)
Borehole diameter	Borehole diameter of 65–115 mm $C_B = 1.0$ Borehole diameter of 150 mm $C_B = 1.05$ Borehole diameter of 200 mm $C_B = 1.15$ (Skempton 1986)
Rod length	Where the ER_m is based on rod lengths of 10 m or more, the ER delivered with shorter rod lengths may be smaller. Recommended values from Youd et al. (2001) are as follows: Rod length < 3 m $C_R = 0.75$ Rod length 3–4 m $C_R = 0.80$ Rod length 4–6 m $C_R = 0.85$ Rod length 6–10 m $C_R = 0.95$ Rod length 10–30 m $C_R = 1.00$
Sampler	Standard split spoon without room for liners (the inside diameter is a constant $1^3/_8$ in.), $C_S = 1.0$. Split-spoon sampler with room for liners but with the liners absent (this increases the inside diameter to $1^1/_2$ in. behind the driving shoe): $C_S = 1.1$ for $(N_1)_{60} \leq 10$ $C_S = 1 + \frac{(N_1)_{60}}{100}$ for $10 \leq (N_1)_{60} \leq 30$ $C_S = 1.3$ for $(N_1)_{60} \geq 30$ (from Seed et al. 1984, equation by Seed et al. 2001)

For more monographs, publications, or videos, visit http://www.eeri.org

(before the arrival of the tension wave) was primarily responsible for sampler advancement and that any energy transferred in secondary impacts did not contribute to advancing the sampler. If the energy ratio (ER_m) for an SPT system is measured for rod lengths greater than about 10 m, then the energy ratio delivered with shorter rod lengths would be smaller. If the ER_m value is measured for a specific short rod length, however, then there is no need to apply a C_R correction, because the measured ER_m already accounts for the effects of the shorter rod. In developing liquefaction correlations, Seed et al. (1985) used $C_R = 0.75$ for rod lengths shorter than 3 m and $C_R = 1.0$ for longer rods. More recently, Youd et al. (2001) recommended C_R values that range from $C_R = 0.75$ for rod lengths shorter than 3 m to $C_R = 1.0$ at a rod length of 10 m.

The basis and need for short rod correction factors have been questioned in some recent studies (e.g., Daniel et al. 2005, Sancio and Bray 2005). Daniel et al. (2005) suggested that the energy transferred in secondary impacts may, in fact, contribute to sampler advancement. Sancio and Bray (2005) concluded that short rod lengths have only a small effect on the energy ratio calculated by the force-velocity method. The effect of these and other findings about the various analytical components of liquefaction procedures must be considered in future updates to liquefaction correlations.

The C_s correction is for SPTs performed via a sampler that has room for liners but uses no liners. In this case, the sampler is easier to drive, because the soil friction along the inside of the sampler is reduced. The effect on N values is relatively small for loose sands but increases to about 30% for dense sands.

The presence of large particles (coarse gravels and larger particles) in a sand can cause the SPT penetration resistance to be unreasonably high when the sampler strikes one of the particles. These influences have been evaluated on many projects by tracking the cumulative blow count for every 1-in. (or 0.1-ft) increment of penetration, as illustrated in Figure 52. A sharp increase in the blow count rate per inch of penetration indicates that a large particle was encountered, whereas a uniform rate of penetration indicates relatively uniform soil conditions over the sampling interval. In either case, the percent sample recovery and the type of soil returned provide additional information to consider. For example, striking a large particle may block soil from entering the spoon, thereby yielding a low sample recovery, or the soil sample that is recovered might contain coarse gravel particles, which indicates the general presence of gravels at

For more monographs, publications, or videos, visit http://www.eeri.org

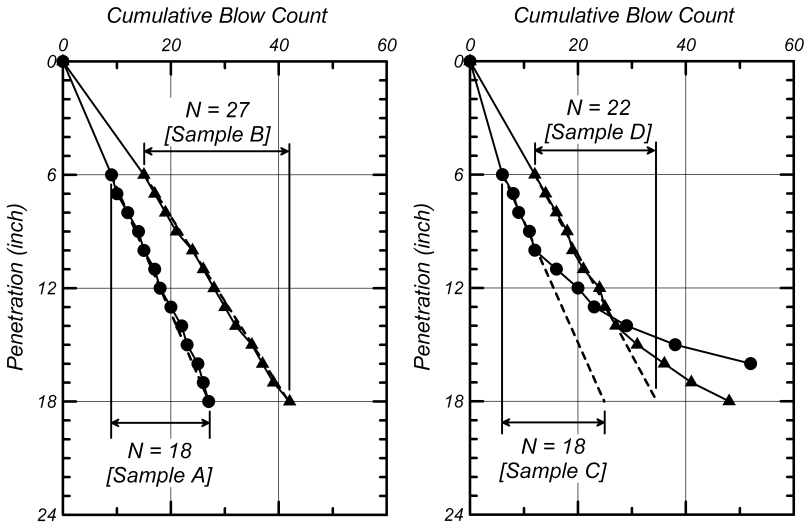

Figure 52. Examples of interpreting SPT blow counts on a per-inch basis: (a) smooth driving patterns that do not require corrections to N values and (b) strong increases in driving resistance that, along with sample recoveries, suggest that the sampler encountered large particles; this graph also shows the adjusted N value, based on extrapolating the pre-obstruction driving rate.

that depth. Where the driving record, sample recovery, and sample type are all consistent, it may be possible to extrapolate an SPT blow count that would be representative of the sand matrix if the large particle(s) had not been encountered, as illustrated in Figure 52. This approach to correcting for the presence of large particles is believed to be reasonable for gravel contents up to about 15–20% (Mejia 2007).

The presence of soft clay or silt interlayers in sand deposits can cause an SPT penetration resistance to be unreasonably low when the sampling interval is very close to the softer soil. These influences can sometimes be evidenced by (1) blow counts for the last six inches being substantially smaller than for the previous two six-inch intervals, (2) the logging of soft soils at the tip of the split spoon, or (3) a change in drilling fluid color or drilling effort immediately below that specific SPT sample depth. Figure 53 shows an example of this effect, in which SPT samples at depths of 6.4 m and 7.9 m were predominantly sand and sand with fine gravel, and yet the measured N_{60} values were much lower than expected on the basis of high

For more monographs, publications, or videos, visit http://www.eeri.org

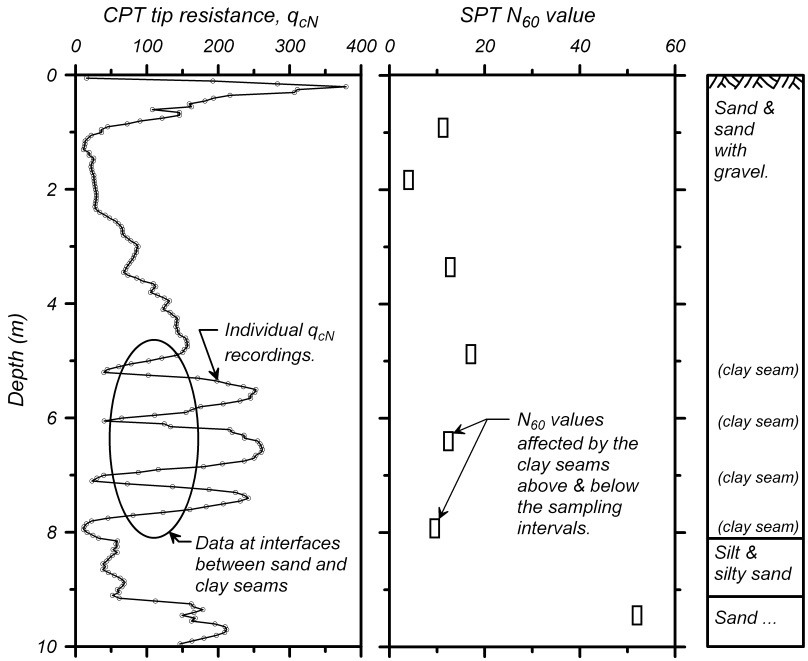

Figure 53. An adjacent SPT boring and CPT sounding that illustrate how thin clay seams can affect penetration resistances in sand (after Boulanger et al. 1995).

values of CPT tip resistance in an adjacent CPT sounding. The low N_{60} values were attributed to the presence of several thin, soft clay seams that are also clearly represented by the intervals of low CPT tip resistances.

SPT N_{60} values, after the various corrections and in the absence of any adverse effects, depend on the effective overburden stress as well as on the sand's relative density and other characteristics. Consequently, an additional correction of the N value for effective overburden stress is required, to arrive at a test result that is believed to primarily reflect the sand's properties and relative density. This correction for overburden stress is described in Section 3.7.

CPT

The CPT has proved to be a valuable tool for characterizing subsurface conditions and assessing various soil properties, including estimating the potential for liquefaction. A typical CPT involves

For more monographs, publications, or videos, visit http://www.eeri.org

pushing a 35.7-mm-diameter conical penetrometer into the ground at a standard rate of 2 cm/sec. while electronic transducers record (typically at 2-cm or 5-cm intervals) the force on the conical tip, the drag force on a short sleeve section behind the tip, the pore water pressure behind the tip (or sometimes at other locations), and other quantities (e.g., inclination and temperature). The tip force is divided by the cross-sectional area of the penetrometer to determine the tip resistance, q_c, and the sleeve drag force is divided by the sleeve surface area to determine the sleeve friction, f_s. The main advantages of the CPT are that it provides a continuous record of the penetration resistance and is less vulnerable to operator error than the SPT. The main disadvantages of the CPT are the difficulty in penetrating layers that have larger particles (e.g., gravels) or very high penetration resistance (e.g., strongly cemented soils) and the need to perform companion borings or soundings to obtain actual soil samples.

Empirical correlations have been developed between soil types and the various CPT measurements, so the soil profile can be approximately inferred even without direct soil sampling. For example, the empirical chart in Figure 54 categorizes soils into nine different soil behavior types on the basis of the dimensionless values for the normalized cone tip resistance (Q) and friction ratio (F). The value of Q is computed as

$$Q = \left(\frac{q_c - \sigma_{vc}}{P_a}\right)\left(\frac{P_a}{\sigma'_{vc}}\right)^n \tag{28}$$

where σ_{vc} is the total vertical stress, σ'_{vc} is the effective vertical stress, P_a is atmospheric pressure, and the exponent n varies from 0.5 in sands to 1.0 in clays (Olsen and Malone 1988, Robertson and Wride 1998). The value of F is computed as

$$F = \left(\frac{f_s}{q_c - \sigma_{vc}}\right) \cdot 100\% \tag{29}$$

Alternatively, the boundaries between soil types 2–7 in Figure 54 may be represented as a series of concentric circles whose common center is above the upper left corner of the plot. Any point on this chart can then be partly described by its radial distance from that center point, with the radial distance being referred to as the soil behavior type index (I_c). This approach was introduced by Jefferies and Davies (1993), but for a slightly different classification chart. For the chart in

For more monographs, publications, or videos, visit http://www.eeri.org

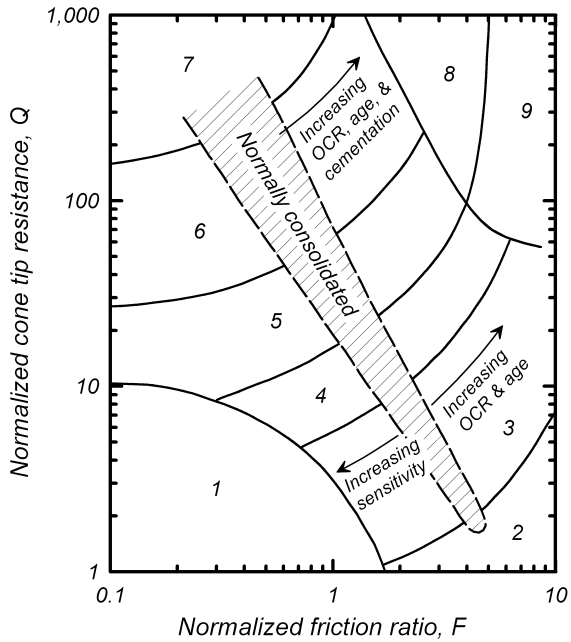

1. Sensitive, fine grained
2. Organic soils - peats
3. Clays - silty clay to clay
4. Silt mixtures - clayey silt to silty clay
5. Sand mixtures - silty sand to sandy silt
6. Sands - clean sand to silty sand
7. Gravelly sand to dense sand
8. Very stiff sand to clayey sand *
9. Very stiff, fine grained *

* Heavily overconsidated or cemented

Figure 54. Normalized CPT soil behavior type chart proposed by Robertson (1990).

Figure 54, an expression for I_c was derived by Robertson and Wride (1998) as

$$I_c = \left[(3.47 - \log(Q))^2 + (\log(F) + 1.22)^2\right]^{0.5} \tag{30}$$

For example, $I_c = 1.31$ is the approximate boundary between soil types 6 (clean sand to silty sand) and 7 (gravelly sand to dense sand), whereas $I_c = 2.60$ is the approximate boundary between soil types 4 (clayey silt to silty clay) and 5 (silty sand to sandy silt).

The I_c index has been correlated with the fines content (the percent passing a No. 200 sieve) and liquefaction resistance of sands (e.g., Suzuki et al. 1997, Robertson and Wride 1998, Suzuki et al.

For more monographs, publications, or videos, visit http://www.eeri.org

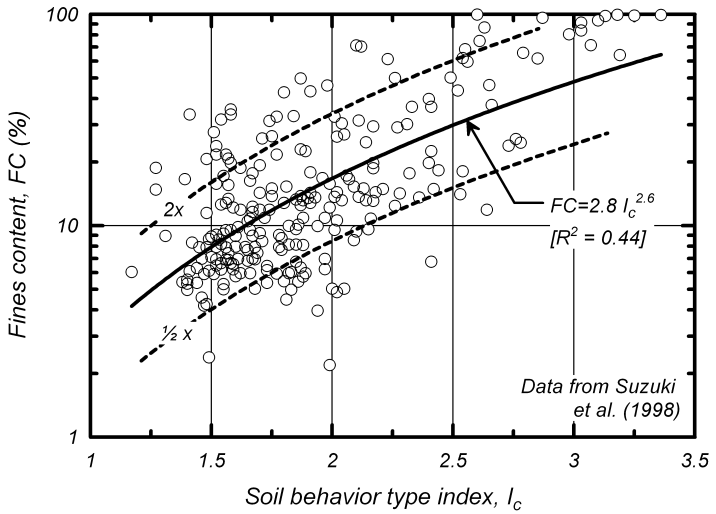

Figure 55. Correlation between fines content and the soil behavior type index, I_c (data from Suzuki et al. 1998).

1997). General correlations between I_c and fines content are poor, as illustrated by the large scatter in the Figure 55 plot and the low correlation coefficient. These data simply reflect the approximate nature of correlations between CPT measurements and soil type (e.g., Figure 54) that are developed for general application across a broad range of sites and geologic settings. The accuracy of CPT-based classification charts or I_c correlations can, however, be greatly improved by collecting, and calibrating against, site-specific data. Consequently, direct soil sampling should always be the primary means for determining soil characteristics, or for establishing site-specific correlations between soil characteristics and CPT measurements, for the purpose of liquefaction evaluations.

The penetration resistance from either a CPT or SPT is influenced by the strength and stiffness of the soils around the actual penetration interval. The zone of influence in sand may be 10–30 times the penetrometer's diameter, with the influence zone being larger for higher relative densities. Thus, the zone of influence may be about 20–50 cm for a CPT and about 50–150 cm for an SPT split-spoon sampler. In addition, the SPT penetration resistance is effectively integrated over a 30-cm-long interval, and thus the SPT blow count represents a much larger volume of soil than does a CPT tip resistance. The smaller zone

For more monographs, publications, or videos, visit http://www.eeri.org

of influence for the CPT enables it to identify stratigraphy in much greater detail, as illustrated in Figure 53 by the CPT's ability to identify the sharp transitions between the dense sands and soft clay seams at depths of 5–8 m. At the same time, it can be important to realize that even the CPT provides sufficiently smeared information that the discrete measurements taken near the interfaces between soils of significantly different strengths and stiffness may not be representative of either soil, as also noted in the CPT plot in Figure 53.

A related concern is the difficulty in characterizing thin sand layers that have softer soils above and below them. If the sand layer is too thin, then the cone tip may never be free of the influence of the softer soils, so the tip resistance in the sand is never representative of its relative density. This phenomenon can be partly accounted for by multiplying the measured tip resistance by a thin-layer correction factor (K_H), as illustrated in Figure 56 (Robertson and Fear 1995, Youd et al. 2001).

BPT and LPT

BPTs and LPTs have been used in soils with large particles (e.g., gravels and cobbles) that can interfere with the accuracy of SPTs and CPTs or even preclude their use. The BPT uses a double-acting diesel pile hammer to drive into the ground a 168-mm-diameter, 3-m-long double-walled casing with a closed bit. The BPT test provides a continuous driving record, from which the blow count is the number of hammer blows required to drive the casing each 300 mm (1 ft) into the ground. The LPT is similar to an SPT, except that it uses a larger split-spoon sampler and a larger hammer to drive it.

The BPT depends on a number of factors that affect the energy delivered to the casing tip, including the diesel hammer's energy efficiency and the friction along the entire casing. Correlations between BPT and SPT values in sand deposits are used to convert BPT blow counts into equivalent SPT N values for use in liquefaction analyses. Attempts have been made to further standardize the BPT and better understand its mechanics, but significant concerns remain about its repeatability and general interpretation. More details about the BPT procedures and related issues are provided by Harder (1997) and Sy (1997).

Several different LPTs have been developed around the world that have sampler outer diameters of 7.3–14 cm (as compared with 5.1 cm for the SPT) and hammer potential energies of 1.2–5.9 times the potential energy for the SPT hammer. Penetration resistances from

For more monographs, publications, or videos, visit http://www.eeri.org

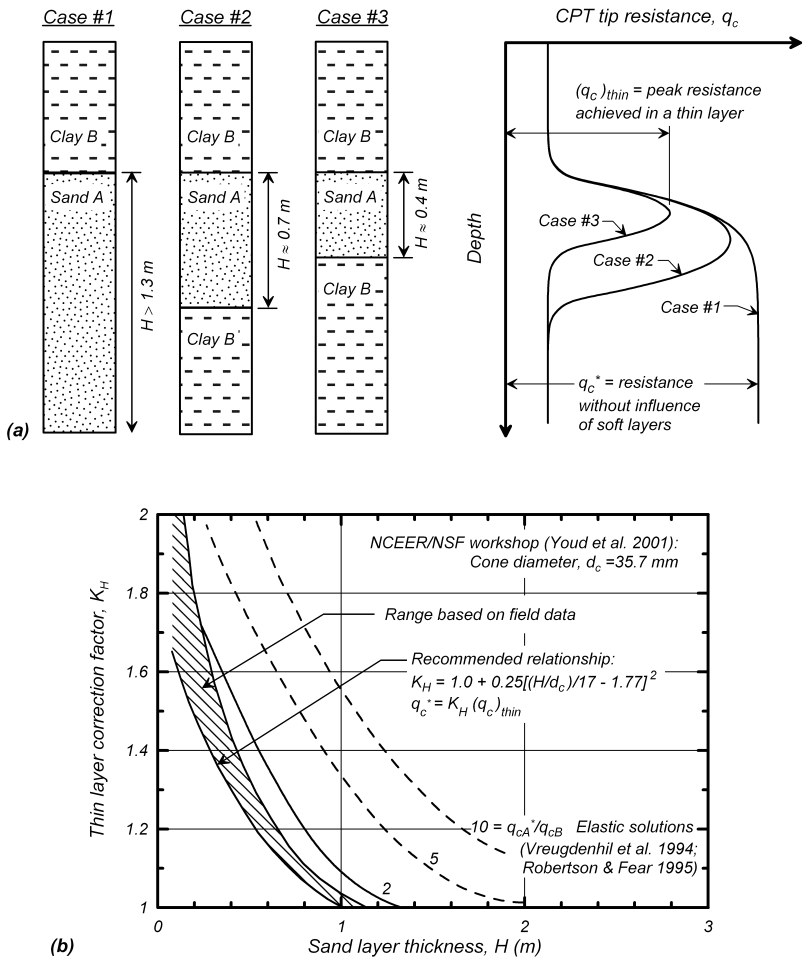

Figure 56. Thin-layer correction factor (K_H) for determining equivalent thick-layer CPT tip resistance: (a) a schematic of thin-layer effects and (b) the relationship recommended in Youd et al. (2001).

LPTs have been correlated with those from SPTs, so the LPT values can be converted into equivalent SPT N_{60} values for use in liquefaction evaluations. Daniel et al. (2003) showed that wave equation analyses of the different penetration tests provided a rational means for assimilating various empirical LPT-SPT correlations. They further noted the importance of energy measurements for obtaining reliable LPT penetration resistances.

For more monographs, publications, or videos, visit http://www.eeri.org

Shear Wave Velocity

Shear wave velocity tests measure the small-strain shear modulus (stiffness) of the soil, and thus they represent an engineering property measurement rather than an index test. There are several different methods for measuring V_s in situ (e.g., cross-hole, downhole, seismic CPT, and spectral analysis of surface waves (SASW)), each with particular advantages and disadvantages. A general advantage of V_s tests is that they can be used for sites underlain by soils that are difficult to penetrate or sample (e.g., gravels, cobbles, and boulders). The general disadvantages of V_s tests are that they provide very limited spatial resolution for characterizing site stratigraphy and heterogeneity (e.g., they measure an average velocity over relatively large volumes), they do not provide soil samples, and they are not a very sensitive measure of liquefaction resistance.

The Complementary Roles of Site Investigation Techniques

In-situ test results are useful as an index of liquefaction characteristics only if the overall site characterization has been reasonably complete and thorough. Site characterization efforts must include a thorough understanding of the geologic setting. This effort should include a study of geologic maps, aerial photos, and historical records of earthquake observations in the area. The interpretation of the geologic setting should include the identification of types of strata that are likely to exist, or may exist, and the type of detailed exploration that might—within reason—be needed to reasonably confirm their existence or nonexistence. More detailed site explorations may include borings, CPT soundings, and geophysical tests in various combinations and sequences, as best suited for the particular site.

It is perhaps useful to emphasize that the standard practice of SPT sampling does not provide a complete picture of the subsurface profile, and most engineering borehole log representations have been simplified. The photo in Figure 57 illustrates this fact. Clearly, SPT samples at a 1.5-m interval, which is a common sampling interval, provide only a limited view of the actual soil conditions. Careful logging of the drilling process can help identify changes in soil strata between sampling intervals and guide the need for more closely spaced samples. Nonetheless, most site exploration tools have a limited resolution at some spatial level, and thus the potential for missing a geologic feature should always be carefully considered as part of the overall interpretation of the site geology.

For more monographs, publications, or videos, visit http://www.eeri.org

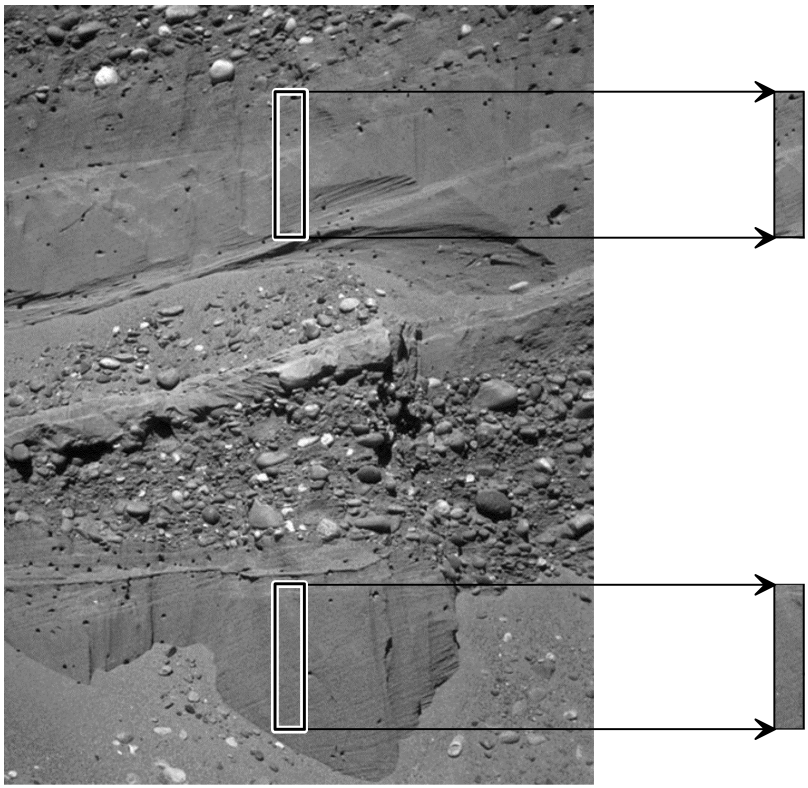

Figure 57. An excavation face showing the interlayering of sand, gravelly sand, and sandy gravel in an alluvial deposit and the portion of the deposit that would be observed via SPT samples at 1.5-m intervals.

Pairing CPT soundings and SPT borings can be extremely valuable, for several reasons. For example, it is often useful to complete a number of CPT soundings before selecting the optimal locations and depths for SPT or tube sampling. Another advantage of pairing SPT borings and CPT soundings is the ability to more clearly identify penetration resistance measurements that may have been affected by the proximity of softer soil layers, as illustrated in Figure 53. Paired CPT and SPT data can also be used to develop site-specific correlations between q_c and N_{60} for various strata of concern. Site-specific correlations can be valuable for interrelating the findings of CPT- and SPT-based liquefaction evaluations and for ground improvement control and evaluation purposes.

For more monographs, publications, or videos, visit http://www.eeri.org

3.5 Overburden Correction of in-Situ Test Results

Penetration Tests

SPT and CPT penetration resistances in sand increase with increasing confining stress, which means that N_{60} and q_c values from different depths, locations, or sites cannot be directly compared with each other unless they were measured at comparable vertical effective stresses. The progressive increase in penetration resistances with vertical effective stress is demonstrated in Figure 58. This figure shows the results of SPT calibration chamber tests on three different sands, with each sand prepared at three different relative densities (Marcuson and Bieganousky 1977a, 1977b). CPT calibration chamber tests show similar variations in q_c with vertical effective stress, and both SPT and CPT data from relatively uniform field deposits of sand also show the same variations.

Penetration resistances are corrected to the equivalent value that would have been obtained in the identical sand if the vertical effective stress had been 1 atm. The overburden corrected penetration resistances, $(N_1)_{60}$ and q_{c1}, are computed by using an overburden

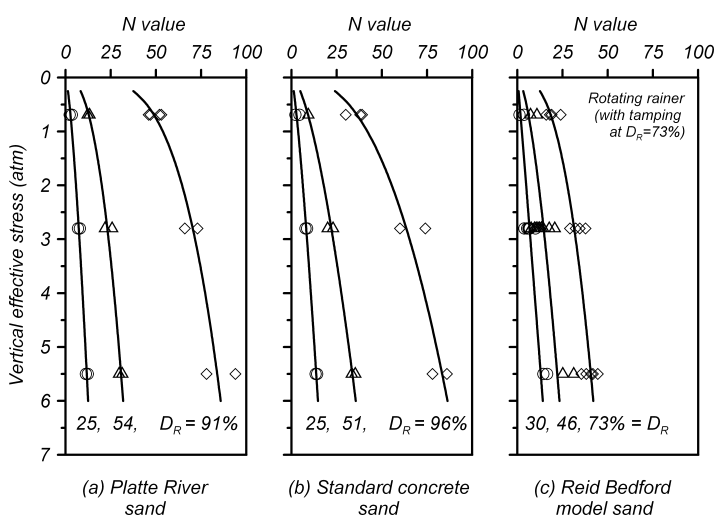

Figure 58. Variation of SPT N values with vertical effective stress for three different sands at three different relative densities (Idriss and Boulanger 2004; data from Marcuson and Bieganousky 1977a, 1977b).

For more monographs, publications, or videos, visit http://www.eeri.org

correction factor, C_N, as follows:

$$(N_1)_{60} = C_N N_{60} \tag{31}$$

$$q_{c1} = C_N q_c \tag{32}$$

The CPT is further normalized with respect to atmospheric pressure by dividing q_{c1} by P_a to obtain a corrected dimensionless tip resistance q_{c1N}, i.e., $q_{c1N} = q_{c1}/P_a$, as recommended by Robertson and Wride (1998).

The concept of C_N follows directly from experimental results like those in Figure 58, from which the C_N value for each σ'_v is determined by dividing the penetration resistance that was obtained in that sand at $\sigma'_v = 1$ atm by the penetration resistance in the same sand at $\sigma'_v \neq 1$ atm. The resulting $(N_1)_{60}$ and q_{c1} values are thus independent of vertical effective stress, making them an index of sand properties and relative density that can be more rationally compared within the same site or from one site to another.

C_N relationships can be derived from calibration chamber data for SPTs or CPTs such as those shown in Figure 58 for the SPT, from theoretical solutions for the CPT (e.g., Salgado et al. 1997a, 1997b), and from field data in relatively uniform sand deposits (e.g., Skempton 1986). A number of different relationships have been proposed for C_N. The following form is modified from that proposed by Liao and Whitman (1986):

$$C_N = \left(\frac{P_a}{\sigma'_{vc}}\right)^m \tag{33}$$

where m is a parameter that depends on the sand properties and relative density (Boulanger 2003b). For example, equation 33 was used to fit the SPT calibration chamber data in Figure 58, resulting in the m values that are summarized in Figure 59. Figure 59 also shows a relationship for m that fits CPT calibration chamber test results, illustrating how a single C_N relationship with

$$m = 0.784 - 0.521 \cdot D_R \tag{34}$$

provides a reasonable approximation for both penetration tests. Note that the larger m values (i.e., those closer to 1) at low relative densities correspond to a condition in which the plots of penetration resistance versus vertical effective stress in Figure 58 are closer to linear, whereas the smaller m values at higher relative densities correspond to a condition in which the plots are less linear.

For more monographs, publications, or videos, visit http://www.eeri.org

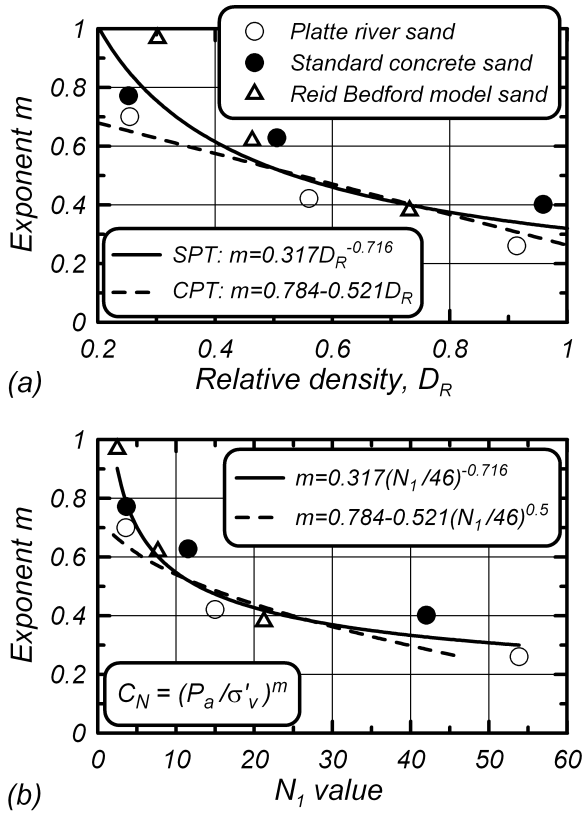

Figure 59. Overburden normalization factor exponent m versus (a) relative density and (b) N_1 value, for the three sands tested in SPT calibration chamber tests by Marcuson and Bieganousky (1977a, 1977b) (Boulanger 2003).

Implementation of the above expression in practice is facilitated by correlations between D_R and penetration resistance. A common expression for the SPT is

$$D_R = \sqrt{\frac{(N_1)_{60}}{C_d}} \tag{35}$$

where D_R is expressed as a ratio, rather than as a percentage. The original observations of Meyerhof (1957) indicated a C_d value of about 41. Skempton (1986) reviewed field and laboratory data and

For more monographs, publications, or videos, visit http://www.eeri.org

suggested that the best average C_d values for normally consolidated natural sand deposits were about 55 for fine sands and 65 for coarse sands. Skempton further noted that C_d varied significantly with the age of a deposit, and thus the typical C_d value for fine sands could be 35 in laboratory tests, 40 in recent fills, and 55 in natural deposits. Cubrinovski and Ishihara (1999) summarized data from high-quality undisturbed samples (obtained by in-situ freezing) that gave average C_d values of about 51 for clean-sand samples, about 26 for silty sand samples, and about 39 for all samples.

CPT tip resistances have also been correlated with D_R in various forms. The relationships by Salgado et al. (1997a, 1997b) for clean sands can be approximated as

$$D_R = 0.465 \left(\frac{q_{c1N}}{C_{dq}} \right)^{0.264} - 1.063 \tag{36}$$

where the term q_{c1N} is conveniently dimensionless. The factor C_{dq} is 0.64–1.55 for the range of sand properties studied by Salgado et al. (1997b).

These q_{c1N}-D_R and $(N_1)_{60}$-D_R correlations were used by Idriss and Boulanger (2003b) to check the consistency between SPT- and CPT-based liquefaction triggering correlations, as described in Section 3.10. A value of $C_d = 46$ was used for the SPT relationship, and $C_{dq} = 0.9$ was used for the CPT relationship. Thus, the following equations are obtained:

$$D_R = \sqrt{\frac{(N_1)_{60}}{46}} \tag{37}$$

$$D_R = 0.478\,(q_{c1N})^{0.264} - 1.063 \tag{38}$$

Substituting the above relationships into the expression for m (equation 34) gives the following expressions for determining C_N:

$$C_N = \left(\frac{P_a}{\sigma'_{vc}} \right)^{0.784 - 0.0768\sqrt{(N_1)_{60}}} \leq 1.7 \tag{39}$$

with $(N_1)_{60}$ limited to values ≤ 46 for use in this expression, and

$$C_N = \left(\frac{P_a}{\sigma'_{vc}} \right)^{1.338 - 0.249(q_{c1N})^{0.264}} \leq 1.7 \tag{40}$$

For more monographs, publications, or videos, visit http://www.eeri.org

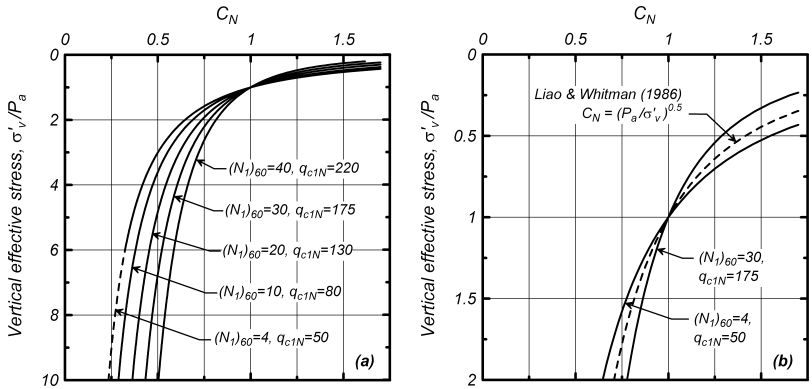

Figure 60. Overburden correction factor C_N for: (a) vertical effective stresses of up to 10 atm and (b) vertical effective stresses of up to 2 atm.

with q_{c1N} limited to values between 21 and 254 for use in this expression. The numerical limits on $(N_1)_{60}$ and q_{c1N} for use in equations 39 and 40 keep the exponent terms within the range of the available data.

C_N values computed via the above expressions are limited to maximum values of 1.7 because of practical considerations and the fact that these expressions were not derived for very low effective stresses. For example, the C_N expressions above produce very large values as the vertical effective stress approaches zero. Therefore, a limit must be imposed on the maximum value of C_N because of uncertainties in these equations at shallow depths (limits of 1.7–2.0 have been recommended by various researchers).

The resulting C_N curves are plotted in Figure 60, showing the importance of D_R with increasing depth (i.e., the role of D_R in this figure is represented by penetration resistances). Solving for C_N via the above expressions requires iteration, because $(N_1)_{60}$ depends on C_N, and C_N depends on $(N_1)_{60}$ (and similarly for the CPT, q_{c1N} depends on C_N, and C_N depends on q_{c1N}). This iteration can be easily accomplished by using a circular reference in most spreadsheet software.

The variation of C_N with D_R is of less importance when the vertical effective stress is 0.5–2.0 atm, which represents the range of stresses encountered in many practical situations (i.e., depths less than about 10–15 m). For this reason, past practice has often relied on C_N expressions that are independent of D_R. One of the most widely used

For more monographs, publications, or videos, visit http://www.eeri.org

of these C_N expressions was proposed by Liao and Whitman (1986):

$$C_N = \left(\frac{P_a}{\sigma'_{vc}}\right)^{0.5} \leq 1.7 \tag{41}$$

This expression matches the previously described expressions when $D_R \approx 54\%$, $(N_1)_{60} \approx 14$, and $q_{c1N} \approx 99$ and provides a simple and reasonable approximation of the available data at vertical effective stresses that do not vary substantially from $\sigma'_{vc} = 1$ atm.

Shear Wave Velocity

V_s values also increase with increasing effective confining stress, and thus they are also corrected to the equivalent value that would have been obtained in the identical sand if the vertical effective stress had been 1 atm. The overburden normalization for V_s values follows from the experimental observation that the maximum (low-strain) shear modulus, $G_{\max}$, in sand is approximately proportional to the square root of the effective confining stress. Since V_s is equal to the square root of $G_{\max}/\rho$ where ρ is the mass density, it follows that the sand's equivalent V_{s1} value can be obtained as

$$V_{s1} = V_s \left(\frac{P_a}{\sigma'_{vc}}\right)^{0.25} \tag{42}$$

This normalization is less sensitive to overburden stress than for penetration tests and can be considered independent of the sand's D_R.

3.6 Magnitude Scaling Factor

A magnitude scaling factor (MSF) is used to adjust the CSR and/or CRR to a common value of M (conventionally taken to be M = 7.5), because the CRR depends on the number of loading cycles, which correlates with M (Seed et al. 1975b). The basic definition of the MSF is

$$\text{MSF} = \frac{\text{CRR}_M}{\text{CRR}_{M=7.5}} \tag{43}$$

MSF relationships can be derived by combining (1) laboratory-based relationships between the CRR and the number of uniform stress cycles and (2) correlations of the number of equivalent uniform cycles with earthquake magnitude. These two relationships are interdependent, as described below, and thus must be developed in parallel to maintain compatibility and consistency.

For more monographs, publications, or videos, visit http://www.eeri.org

Converting Irregular Stress Time Series to Equivalent Uniform Time Series

Methods for converting an irregular time series to equivalent uniform cycles have involved concepts similar to those used in fatigue studies. First, the relationship between the CRR and the number of uniform stress cycles (N) is developed; as shown in Section 2, this relationship is reasonably approximated by using the form

$$\mathrm{CRR} = a \cdot N^{-b} \tag{44}$$

This power relation produces a straight line with a slope of $-b$ on a log(CRR) versus log(N) plot, with a b value of 0.34 being representative of clean sands. For two individual stress cycles having magnitudes CSR_A and CSR_B, the relative number of cycles to cause failure at these two stress ratios can be obtained as

$$\frac{N_A}{N_B} = \left(\frac{\mathrm{CSR}_B}{\mathrm{CSR}_A}\right)^{1/b} \tag{45}$$

The damage from one cycle of stress at CSR_B would then be equivalent to the damage from X_A cycles at CSR_A if their numbers of cycles are an equal fraction of the number of cycles to failure at their respective CSRs. This means that X_A can be computed as

$$\frac{X_A \text{ cycles}}{N_A} = \frac{1 \text{ cycle}}{N_B} \tag{46}$$

which leads to the expression

$$X_A = \left(\frac{\mathrm{CSR}_B}{\mathrm{CSR}_A}\right)^{1/b} (1 \text{ cycle at } \mathrm{CSR}_B) \tag{47}$$

This expression is used to convert individual stress cycles into an equivalent number of cycles at some reference stress level. Note that the above form of the CRR-N relationship is necessary for the conversion to produce a unique result, and the number of equivalent uniform cycles is controlled by the choice of the reference stress level.

The conversion of an irregular stress time series into an equivalent number of uniform stress cycles for saturated sand can be simply illustrated as follows. Suppose that undrained cyclic tests on a saturated sand indicate that 10 uniform cycles at CSR $= 0.45$ would cause liquefaction, whereas it would take 40 uniform cycles at CSR $= 0.30$ to cause liquefaction. Now suppose that this same sand is subjected to an irregular stress time series consisting of two cycles, one cycle having a CSR of 0.45 and the other cycle having a CSR of 0.30.

For more monographs, publications, or videos, visit http://www.eeri.org

This irregular time series can be converted into an equivalent uniform stress time series having 1.25 cycles (i.e., 1 cycle + 10/40 cycles) at a uniform CSR of 0.45, or 5 cycles (i.e., 40/10 cycles + 1 cycle) at a uniform CSR of 0.30.

Relating MSF, Number of Equivalent Uniform Stress Cycles, and Earthquake Magnitude

The number of equivalent uniform stress cycles (N) for a given earthquake time series depends on the specified reference stress level and the exponent b for the CRR versus N relationship. The reference stress is taken to be 65% of the peak earthquake-induced shear stress, as previously mentioned in the description of the Seed-Idriss simplified procedure for estimating earthquake-induced cyclic stresses. Note that the choice of reference level is largely arbitrary; selecting a different reference stress level would alter the values of certain parameters and relationships but would have no net effect on the final outcome of the derived liquefaction evaluation procedure, as long as this reference is used throughout.

N can then be computed for different earthquake time series, as illustrated in Figure 61, and the results can be correlated with various attributes of the earthquake. This process has been performed by using earthquake acceleration time series, with the subsequent approximation being that the number of equivalent uniform cycles of acceleration is about equal to that for cyclic shear stresses. The value

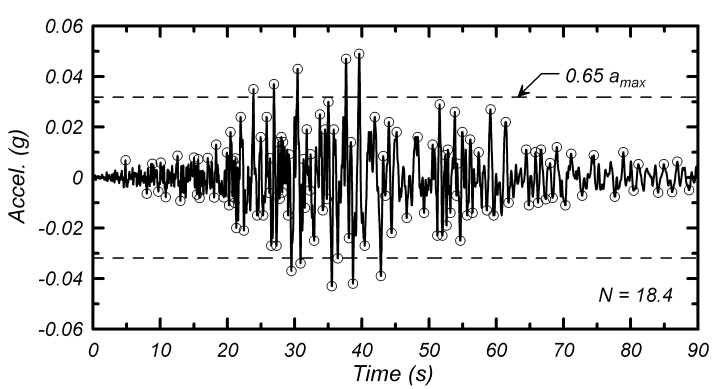

Figure 61. Example of a time series, showing the individual cycles that exceeded 10% of the record's peak acceleration and the equivalent number of uniform cycles at 65% of the peak.

For more monographs, publications, or videos, visit http://www.eeri.org

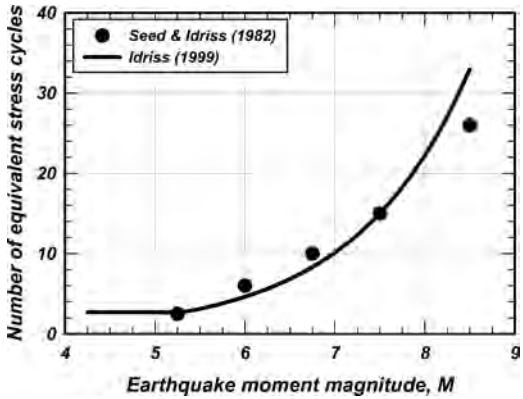

Figure 62. Mean number of equivalent uniform cycles at 65% of the peak stress versus earthquake magnitude.

of N has been found to depend most strongly on the earthquake magnitude, with a lesser dependence on the distance to the fault surface and the site conditions (Liu et al. 2001). Green and Terri (2005) evaluated the effects of an alternative method for computing equivalent numbers of cycles and concluded that they depend on earthquake magnitude, distance to the source, and depth in a soil profile. For simplicity, the trends of N may be expressed solely as a function of earthquake magnitude, as illustrated by the empirical correlation in Figure 62.

The MSF can then be derived from the N versus M relationship through the equation

$$\mathrm{MSF} = \frac{\mathrm{CRR}_M}{\mathrm{CRR}_{M=7.5}} = \left(\frac{N_{M=7.5}}{N_M}\right)^b \tag{48}$$

where $N_{M=7.5}$ is the number of uniform cycles for M = 7.5. An upper limit for the MSF is assigned to very-small-magnitude earthquakes for which a single peak stress can dominate the entire time series. Consider a time series dominated by single pulse of stress (i.e., $^1/_2$ to 1 full cycle, depending on its symmetry), with all other stress cycles being sufficiently small to neglect. If this limiting case is represented by $^3/_4$ of a cycle at the peak stress, then the equivalent number of uniform cycles at 65% of the peak stress would be

$$N_{\min} = \left(\frac{1.0}{0.65}\right)^{1/0.34} \left(\frac{3}{4}\ \text{cycle}\right) \approx 2.7 \tag{49}$$

For more monographs, publications, or videos, visit http://www.eeri.org

The upper limit for the MSF would then be computed as

$$(\mathrm{MSF})_{\mathrm{max,\ cohesionless}} = \left(\frac{15}{2.7}\right)^{0.34} \approx 1.8 \tag{50}$$

MSF values at different M values can be similarly computed by using the above expressions and the correlation between N and M in Figure 62. This approach was used by Idriss (1999) to arrive at the following relationships between the MSF and M:

$$\mathrm{MSF} = 6.9 \exp\left(\frac{-M}{4}\right) - 0.058 \tag{51}$$

$$\mathrm{MSF} \leq 1.8 \tag{52}$$

The MSF values obtained via the above recommended expressions are presented in Figure 63, together with those proposed by other researchers. These MSF values are somewhat greater (at $M < 7.5$) than those proposed by Seed and Idriss (1982), Tokimatsu and Yoshimi (1983), and Cetin et al. (2004). In contrast, the Idriss (1999) MSF values are significantly smaller than those proposed by Ambraseys (1988) and Arango (1996). The latter researchers had used different r_d relationships, along with empirical techniques that mixed the

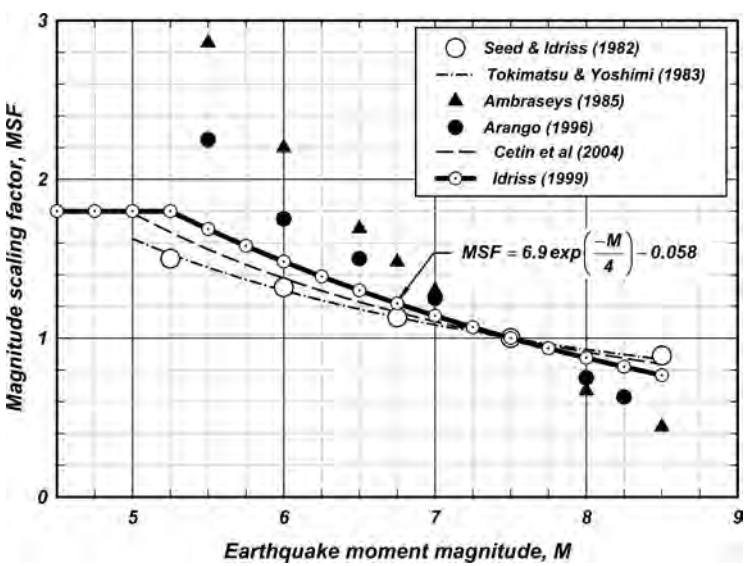

Figure 63. Magnitude scaling factor values proposed by various researchers.

For more monographs, publications, or videos, visit http://www.eeri.org

effects of the MSF and r_d; thus a direct comparison of their MSF values with the Idriss MSF values is not strictly appropriate.

3.7 Overburden Correction Factor, K_σ

The overburden correction factor (K_σ) was introduced by Seed (1983) to adjust the CSR and/or CRR to a common value of effective overburden stress, because the CRR of sand depends on the effective overburden stress. The definition of K_σ is

$$K_\sigma = \frac{\mathrm{CRR}_{\sigma'_{vc}}}{\mathrm{CRR}_{\sigma'_{vc}=1}} \tag{53}$$

where $\mathrm{CRR}_{\sigma'_{vc}}$ is the CRR of a soil under a specific value of σ'_{vc}, and $\mathrm{CRR}_{\sigma'_{vc}=1}$ is the CRR of the same soil when $\sigma'_{vc} = 1$ atm. Most K_σ relationships have been derived from laboratory test results, as described in the review by Harder and Boulanger (1997), whereas some K_σ relationships have also been guided by theoretical considerations (Hynes and Olsen 1998, Boulanger 2003b) or by regression against field case histories (Cetin et al. 2004).

Experimental studies with freshly reconstituted sands have shown that the CRR can be directly related to the relative state of the sand (e.g., Figure 24) so that the relationship between the CRR and ξ_R actually defines the K_σ relationship (as illustrated in Figure 25). This means that different K_σ relationships would be expected for sands that have different CRR versus D_R relationships for a given effective overburden stress (i.e., with p' constant, the CRR-D_R relationship fully defines the CRR-ξ_R relationship). CRR values, however, can be significantly different for freshly reconstituted sands than for field samples obtained via tube sampling techniques or for field samples obtained via frozen sampling techniques, as discussed in Section 2.3 and illustrated in Figures 37–40. These differences can be expected to lead to widely different K_σ values, which may partly explain the large scatter in results obtained by different researchers (e.g., Figure 22).

Consequently, Boulanger (2003b) derived K_σ relationships that are consistent with the semi-empirical correlations between the field CRR and penetration resistances (as presented in Section 3.8). This derivation involved relating penetration resistances to ξ_R so that the field CRR could be expressed as a function of ξ_R. This field CRR versus ξ_R relationship was then used to derive K_σ values via the procedure shown in Figure 25. The resulting K_σ relationships do not require the computing of ξ_R, because it was used only in the derivation process. Furthermore, the derived K_σ relationships are relatively

For more monographs, publications, or videos, visit http://www.eeri.org

insensitive to variations in the assumed relationships between ξ_R and penetration resistance, because the same relationships were used in mapping the field correlation to a CRR-ξ_R relationship and in mapping it back to K_σ relationships.

The recommended K_σ relationships are computed as

$$K_\sigma = 1 - C_\sigma \ln\left(\frac{\sigma'_{vc}}{P_a}\right) \leq 1.1 \tag{54}$$

where the coefficient C_σ can be expressed in terms of the sand's D_R or the overburden corrected penetration resistances as (Boulanger and Idriss 2004a)

$$C_\sigma = \frac{1}{18.9 - 17.3 D_R} \leq 0.3 \tag{55}$$

$$C_\sigma = \frac{1}{18.9 - 2.55\sqrt{(N_1)_{60}}} \leq 0.3 \tag{56}$$

$$C_\sigma = \frac{1}{37.3 - 8.27(q_{c1N})^{0.264}} \leq 0.3 \tag{57}$$

The coefficient C_σ may be restricted to its maximum value of 0.3 by restricting $(N_1)_{60}$ and q_{c1N} to values ≤ 37 and ≤ 211, respectively, in these expressions. Values of K_σ computed via equations 56 and 57 are shown in Figure 64 for a range of $(N_1)_{60}$ and q_{c1N} values. These plots

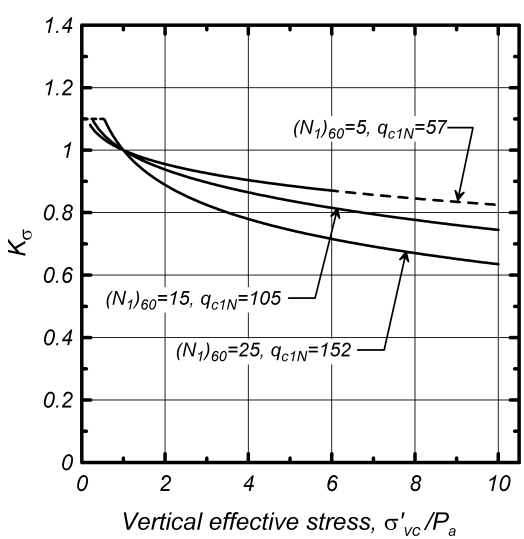

Figure 64. K_σ relationships derived from ξ_R relationships (Boulanger and Idriss 2004).

For more monographs, publications, or videos, visit http://www.eeri.org

show K_σ values slightly greater than 1.0 at low confining stresses, in accord with experimental findings, but the above regression equations slightly overestimate the derived K_σ values at these low stresses. Idriss and Boulanger (2006) chose to restrict the K_σ values computed via equations 56 and 57 to a maximum value of 1.0 for use with the semi-empirical liquefaction correlations. For this monograph, the K_σ values computed via the above expressions were instead restricted to a maximum value of 1.1, which better represents the experimental data.

3.8 Static Shear Stress Correction Factor, K_α

The CRR is affected by the presence of static shear stresses, such as exist within slopes or embankment dams, but the available case history data are not sufficient to empirically determine this effect. Seed (1983) introduced the correction factor K_α to adjust the CRR for the effects of static shear stresses. The definition of K_α is

$$K_\alpha = \frac{\mathrm{CRR}_\alpha}{\mathrm{CRR}_{\alpha=0}} \tag{58}$$

where α is the ratio of static shear stress to effective consolidation stress on the plane of interest, CRR_α is the CRR of a soil under a specific value of α, and $\mathrm{CRR}_{\alpha=0}$ is the CRR of the same soil when $\alpha = 0$. A number of K_α relationships have since been derived on the basis of laboratory test results, as reviewed by Harder and Boulanger (1997). The validity of these relationships for in-situ sands is difficult to assess, because there are insufficient empirical field data or laboratory data on field samples obtained via frozen sampling techniques.

Idriss and Boulanger (2003a) derived expressions that approximate the data in Figure 29, which are based primarily on simple shear tests and a failure criterion of 3% shear strain and which account for the principal effects of static shear stress ratio (α), relative density, and effective confining stress. These expressions use the ξ_R index in their functional form, as follows:

$$K_\alpha = a + b \cdot \exp\left(\frac{-\xi_R}{c}\right) \tag{59}$$

$$a = 1267 + 636\alpha^2 - 634\exp(\alpha) - 632 \cdot \exp(-\alpha) \tag{60}$$

$$b = \exp(-1.11 + 12.3\alpha^2 + 1.31 \cdot \ln(\alpha + 0.0001)) \tag{61}$$

$$c = 0.138 + 0.126\alpha + 2.52\alpha^3 \tag{62}$$

$$\alpha = \frac{\tau_s}{\sigma'_{vc}} \tag{63}$$

For more monographs, publications, or videos, visit http://www.eeri.org

The ξ_R index is computed from the penetration resistances as

$$\xi_R = \frac{1}{Q - \ln\left(\frac{100(1+2K_o)\sigma'_{vc}}{3P_a}\right)} - \sqrt{\frac{(N_1)_{60}}{46}} \tag{64}$$

and

$$\xi_R = \frac{1}{Q - \ln\left(\frac{100(1+2K_o)\sigma'_{vc}}{3P_a}\right)} - \left(0.478(q_{c1N})^{0.264} - 1.063\right) \tag{65}$$

with q_{c1N} limited to values ≥ 21 for use in this expression. In addition, α and ξ_R should be constrained within the following limits

$$\alpha \leq 0.35 \tag{66}$$

$$-0.6 \leq \xi_R \leq 0.1 \tag{67}$$

which correspond to the range of data that equations 59–65 were based on.

Examples of K_α values computed via the above expressions using $K_o = 0.45$ and $Q = 10$ are presented in Figure 65 for a range of penetration resistances and for σ'_{vc} values of 1 and 4 atm.

The parameter K_α is often omitted in analyses of lateral spreading at level or mildly sloping sites—which is reasonable, because K_α is approximately unity for small values of the initial static shear stress ratio. The inclusion of K_α can, however, be important for analyses of liquefaction within steeper slopes and embankment dams.

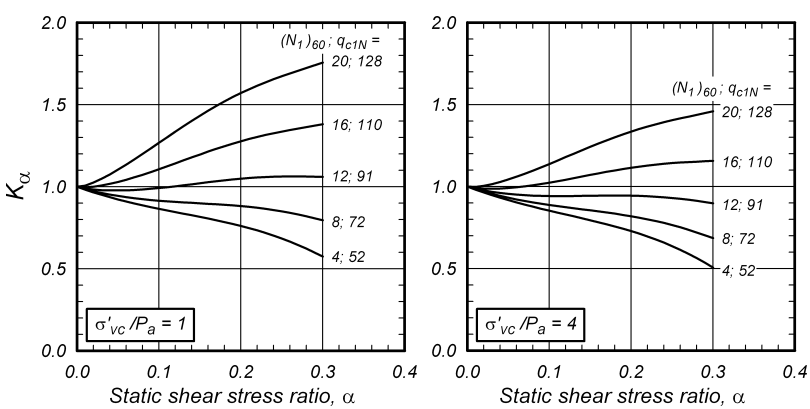

Figure 65. Variations of K_α with SPT and CPT penetration resistances at effective overburden stresses of 1 and 4 atm.

For more monographs, publications, or videos, visit http://www.eeri.org

3.9 Development of Liquefaction Triggering Correlations from Case Histories

The development of liquefaction correlations from case histories has progressed over the years through the efforts of countless researchers, particularly in the time-consuming investigations of individual case histories. The earliest efforts began in Japan with attempts to use SPT data to differentiate between liquefiable and nonliquefiable conditions in the 1964 Niigata earthquake (e.g., Kishida 1966). SPT procedures continued to evolve, with the SPT correlations recommended by Seed et al. (1984, 1985) being particularly noteworthy because they set the standard in engineering practice for the next two decades. The first CPT liquefaction correlations based directly on case histories were published by Zhou (1980), using observations from the 1978 Tangshan earthquake. Seed and Idriss (1981) as well as Douglas et al. (1981) proposed the use of correlations between the SPT and CPT to convert the available SPT-based charts for use with the CPT. The evolution of CPT procedures since then has included notable correlations by Shibata and Teparaksa (1988), Stark and Olson (1995), Suzuki et al. (1995, 1997), Robertson and Wride (1997, 1998), and Olsen (1997). A 1996–97 workshop by the National Center for Earthquake Engineering Research (NCEER 1997) and the National Science Foundation (NSF) provided a timely summary of most of the extant SPT-, CPT-, and V_s-based correlations and analytical procedures (Youd et al. 2001). The next few years produced a series of new case histories from several large earthquakes, with Cetin et al. (2000, 2004), Seed et al. (2001, 2003), Moss (2003), and Moss et al. (2006) producing valuable compilations of those data and associated revisions to the liquefaction procedures and correlations.

The compiled databases were reevaluated by using the updated framework (e.g., the revised r_d, MSF, K_σ, and C_N relationships) that was described in previous sections. This framework is the same as that used by Idriss and Boulanger (2004, 2006), except that K_σ is now allowed to exceed 1.0 at low confining stresses. The differences between the current and previous reevaluation of the database are sufficiently small that the liquefaction correlations by Idriss and Boulanger (2004, 2006) are still applicable.

Information for each case history was compiled by identifying the combination of the earthquake-induced CSR and in-situ penetration resistance that best represents the critical zone for each site. In compiling the case histories into a common data set, it is necessary to

For more monographs, publications, or videos, visit http://www.eeri.org

adopt some standard reference condition to which each case history can be adjusted. This was done by adopting the reference condition of an M = 7.5 earthquake and an effective overburden stress of $\sigma'_{vc} = 1$ atm. Most of the case histories involved relatively modest static shear stress ratios (α), so the resulting correlations are considered applicable for $\alpha = 0$. The earthquake-induced CSR at each site was then adjusted to the equivalent CSR for the reference values of M = 7.5 and $\sigma'_{vc} = 1$ atm, as

$$\mathrm{CSR}_{M=7.5,\sigma'_{vc}=1} = \mathrm{CSR}_{M,\sigma'_{vc}} \frac{1}{\mathrm{MSF}} \frac{1}{K_\sigma} \tag{68}$$

$$\mathrm{CSR}_{M=7.5,\sigma'_{vc}=1} = 0.65 \frac{a_{\max}}{g} \frac{\sigma_{vc}}{\sigma'_{vc}} r_d \frac{1}{\mathrm{MSF}} \frac{1}{K_\sigma} \tag{69}$$

The resulting $\mathrm{CSR}_{M=7.5,\sigma'_{vc}=1}$ values were plotted against the values of $(N_1)_{60}$ and q_{c1N}, with the remaining step being the development of a boundary line that separates cases of liquefaction from cases of nonliquefaction.

The development of these boundary lines was assisted by two additional considerations. First, the experimental results for in-situ sands obtained by frozen sampling techniques (Figure 37) were used to partially guide the form of the liquefaction correlation at high penetration resistance, because there are insufficient case histories to constrain the upper part of this correlation curve. Second, consistency between the SPT and CPT correlations was checked by mapping both sets of data onto a plot of CRR versus ξ_R (on the basis of the empirical relationships between D_R and penetration resistance presented in Section 3.5). Note that a common CRR versus D_R relationship at an effective overburden stress of $\sigma'_{vc} = 1$ atm is equivalent to requiring a common CRR-ξ_R relationship.

It is important to recognize that the resulting liquefaction correlations depend on the various relationships (e.g., r_d, MSF, K_σ, and C_N) that were used to interpret the case histories. Certain factors affect the case history interpretations through their influence on more than one relationship:

- Depth affects C_r, C_N, r_d, and K_σ.
- Earthquake magnitude affects the MSF and r_d.
- Fines content affects the CRR and has poorly defined effects on all the other relationships.

Therefore, the liquefaction correlations should be used only with the same relationships that were used in their development.

For more monographs, publications, or videos, visit http://www.eeri.org

3.10 SPT and CPT Correlations for Triggering of Liquefaction in Clean Sands

The compiled SPT and CPT data for clean sands are shown in Figures 66 and 67, respectively, along with the boundary lines derived by Idriss and Boulanger (2004) and those proposed by other researchers in earlier studies. The CRR-ξ_R relationships derived from the liquefaction correlations by Idriss and Boulanger are shown in Figure 68, which illustrates the consistency that was obtained between the two liquefaction correlations. These derived correlations between CRR and penetration resistances can be expressed via the following expressions for the SPT and CPT, respectively:

$$\mathrm{CRR}_{M=7.5,\sigma'_{vc}=1} = \exp\left(\frac{(N_1)_{60cs}}{14.1} + \left(\frac{(N_1)_{60cs}}{126}\right)^2 - \left(\frac{(N_1)_{60cs}}{23.6}\right)^3 + \left(\frac{(N_1)_{60cs}}{25.4}\right)^4 - 2.8\right) \quad (70)$$

$$\mathrm{CRR}_{M=7.5,\sigma'_{vc}=1} = \exp\left(\frac{q_{c1Ncs}}{540} + \left(\frac{q_{c1Ncs}}{67}\right)^2 - \left(\frac{q_{c1Ncs}}{80}\right)^3 + \left(\frac{q_{c1Ncs}}{114}\right)^4 - 3\right) \quad (71)$$

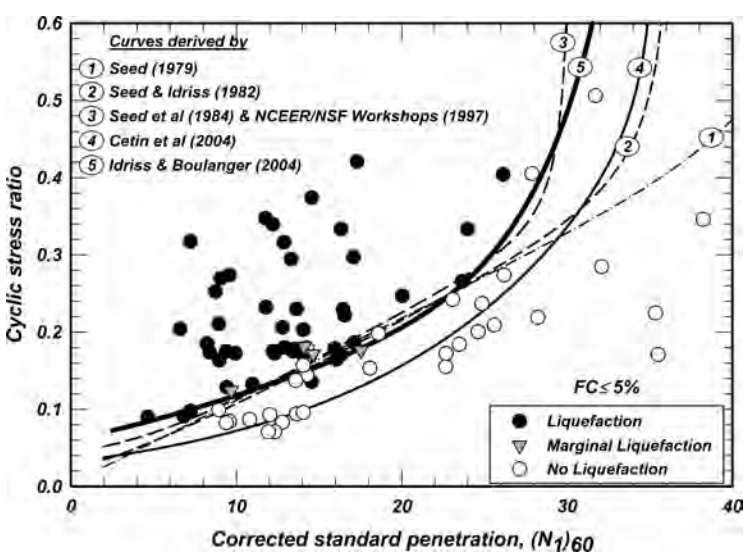

Figure 66. Curves relating the CRR to $(N_1)_{60}$ for clean sands with M = 7.5 and $\sigma'_{vc} = 1$ atm.

For more monographs, publications, or videos, visit http://www.eeri.org

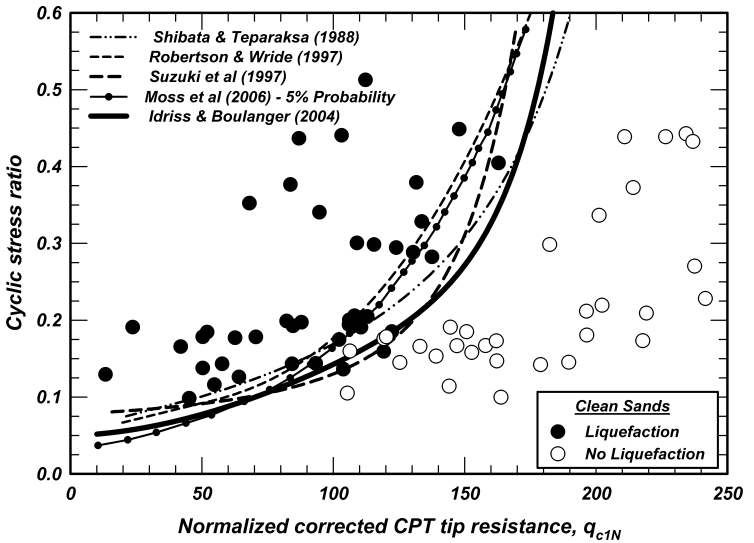

Figure 67. Curves relating the CRR to q_{c1N} for clean sands with M = 7.5 and σ'_{vc} = 1 atm.

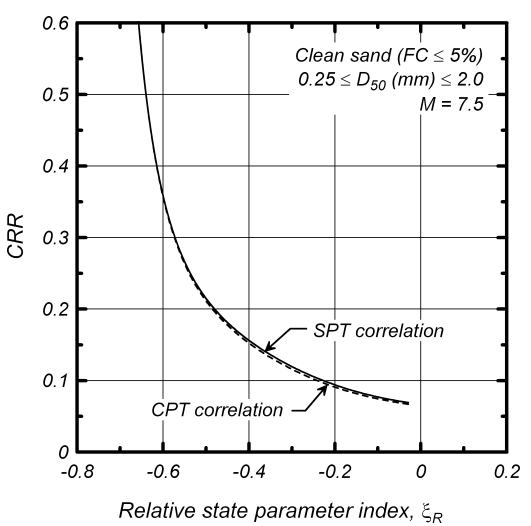

Figure 68. Field CRR-ξ_R relationships derived from the SPT- and CPT-based liquefaction correlations by Idriss and Boulanger (2004).

For more monographs, publications, or videos, visit http://www.eeri.org

In the terms $(N_1)_{60cs}$ and q_{c1Ncs}, the subscript cs indicates that their values pertain to clean sands. These correlations are applicable to M = 7.5 and an effective overburden stress of $\sigma'_{vc} = 1$ atm.

The above correlations for the CRR can be extended to other values of earthquake magnitude and effective overburden stress by using the same correction factors that were used to derive the correlations, namely

$$\mathrm{CRR}_{M,\sigma'_{vc}} = \mathrm{CRR}_{M=7.5,\sigma'_{vc}=1} \cdot \mathrm{MSF} \cdot K_\sigma \tag{72}$$

The factor of safety against the triggering of liquefaction can then be computed as the ratio of the sand's CRR to the earthquake-induced CSR, with both the CRR and CSR values pertaining to the design earthquake magnitude and the in-situ effective overburden stress:

$$FS_{liq} = \frac{\mathrm{CRR}_{M,\sigma'_{vc}}}{\mathrm{CSR}_{M,\sigma'_{vc}}} \tag{73}$$

Alternatively, it is algebraically equivalent to convert the earthquake-induced CSR into the reference condition presented in section 3.9 and compute the factor of safety as

$$FS_{liq} = \frac{\mathrm{CRR}_{M=7.5,\sigma'_{vc}=1}}{\mathrm{CSR}_{M=7.5,\sigma'_{vc}=1}} \tag{74}$$

Different liquefaction triggering correlations cannot be compared solely on the basis of their relative positions on plots like those in Figures 66 and 67, because this does not capture the differences in the various components of their respective analytical frameworks (C_N, K_σ, r_d, etc.). For example, the curve by Cetin et al. (2004) in Figure 66 is significantly lower than those of other researchers, in part because Cetin et al. use a different set of analytical relationships that result in the case-history data points and corresponding curve plotting lower. A more complete comparison of different liquefaction correlations can be made by comparing the CRR and FS_{liq} values that would be predicted on the basis of measured penetration resistances at different depths.

This type of comparison is illustrated in Figures 69 and 70 for depths of up to 20 m, using the SPT-based liquefaction correlations from the NCEER/NSF workshop (Youd et al. 2001) and the updates by Idriss and Boulanger (2006) and Cetin et al. (2004). These comparisons are for clean sands (FC = 5%), a water table depth of 1 m, and an earthquake magnitude of M = 7.5. Figure 69a shows contours of the ratio $\mathrm{CRR}_{IB}/\mathrm{CRR}_{NCEER}$, where CRR_{IB} is the CRR value from the

For more monographs, publications, or videos, visit http://www.eeri.org

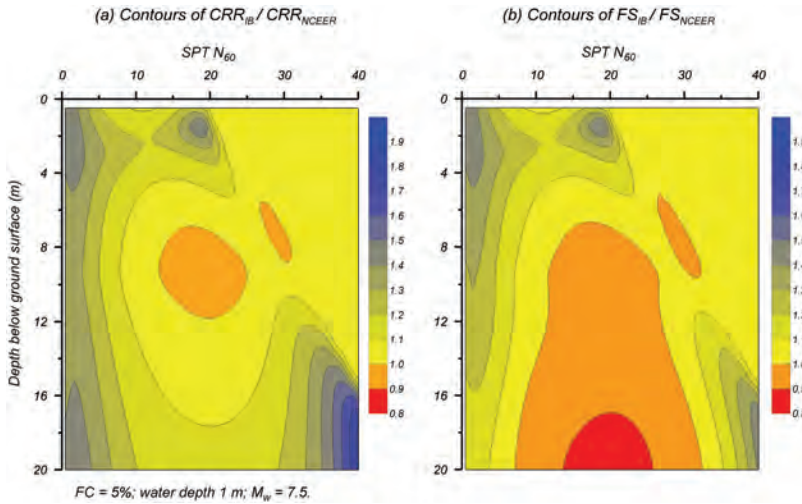

Figure 69. Comparison of liquefaction analysis procedures from Idriss and Boulanger (2006) with those from the NCEER/NSF workshop (Youd et al. 2001): (a) ratio of the CRR values and (b) ratio of FS_{liq}.

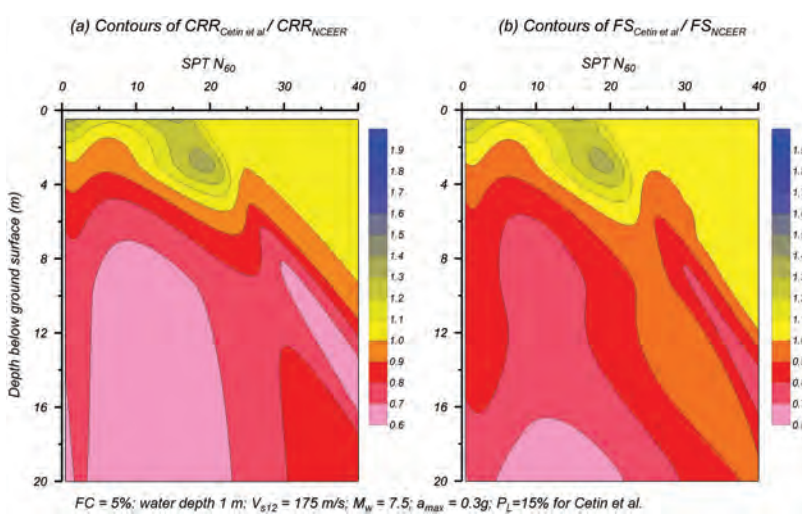

Figure 70. Comparison of liquefaction procedures from Cetin et al. (2004) with those from the NCEER/NSF workshop (Youd et al. 2001): (a) ratio of the CRR values and (b) ratio of FS_{liq}.

For more monographs, publications, or videos, visit http://www.eeri.org

Idriss and Boulanger (2006) procedures, and CRR_{NCEER} is the CRR value from the NCEER/NSF workshop procedures. Figure 69b shows contours of the ratio FS_{IB}/FS_{NCEER}, where FS_{IB} is the factor of safety against liquefaction obtained via the Idriss and Boulanger procedures, and FS_{NCEER} is the factor of safety from the NCEER/NSF workshop procedures. A similar comparison of the results obtained via the Cetin et al. (2004) procedures (i.e., $CRR_{Cetin\ et\ al.}$ and $FS_{Cetin\ et\ al.}$) and the NCEER/NSF procedures is shown in Figure 70. Note that Cetin et al. developed their procedures probabilistically, as described in Section 3.12, after which they recommended that deterministic analyses could use a curve that was equal to the curve for a probability of liquefaction (P_L) equal to 15% at $(N_1)_{60cs}$ values less than or equal to 32 and then became slightly higher than the $P_L = 15\%$ curve as $(N_1)_{60cs}$ values exceeded 32. For simplicity, the comparison shown in Figure 70 uses their $P_L = 15\%$ curve.

The comparisons in Figure 69 show that the CRR and FS_{liq} values obtained by the Idriss and Boulanger procedures are generally within ± 10% of the results obtained via the NCEER/NSF procedures for N_{60} values of 8–40 at depths of 4–14 m. The good agreement between the CRR and FS_{liq} values for this range of N_{60} values and depths is not surprising, given that the majority of the case history data fall in this range of conditions, and both procedures are constrained by largely the same data. Outside that range of N_{60} and depth values, the CRR_{IB} values are generally 10–40% larger than the CRR_{NCEER} values but become even larger for N_{60} values greater than 35 at depths greater than 16 m. The greatest contributors to these differences in the CRR values are the C_N and K_σ relationships in these two sets of procedures. The ratio FS_{IB}/FS_{NCEER} at depths greater than 12 m is smaller than the ratio CRR_{IB}/CRR_{NCEER}, because the r_d values used to compute the CSR at these depths are larger in the Idriss-Boulanger procedures than in the NCEER/NSF procedures. At depths close to 20 m, the FS_{IB} values are generally 88–140% of the FS_{NCEER} value.

The comparisons in Figure 70 show that the CRR and FS_{liq} values obtained by the Cetin et al. (2004) procedures are within ± 10% of those obtained by the NCEER/NSF procedures at depths close to 4 m, but the differences quickly become larger at other depths. At depths greater than about 8 m, the CRR values from the Cetin et al. procedures are generally 20–45% smaller than the CRR_{NCEER} values, and the $FS_{Cetin\ et\ al.}$ values are generally 10–45% smaller than the FS_{NCEER} values. The Cetin et al. procedures produce substantially lower estimates of the CRR and FS_{liq} at these depths for a number of reasons,

For more monographs, publications, or videos, visit http://www.eeri.org

including the differences in the r_d, C_N, and K_σ relationships and the effects those relationships have on the case history interpretations.

3.11 SPT and CPT Correlations for Triggering of Liquefaction in Silty Sands

SPT Correlations

The development of the SPT correlation for silty sands is illustrated in Figures 71–74. The case histories were compiled into bins of data with different fines contents and compared with the baseline liquefaction curve for clean sands. For example, Figure 71 shows the case history data points for cohesionless soils with FC $\geq$ 35%, along with the NCEER/NSF workshop curve (Youd et al. 2001) and the revised curve by Idriss and Boulanger (2004). The new curve is controlled by a few recent case history points that fell well below the FC $\geq$ 35% boundary curve agreed to at the NCEER/NSF workshop.

Similarly, the revised FC = 15% boundary curve is compared with the NCEER/NSF workshop curve in Figures 72 and 73. Figure 72 shows the case history data points for cohesionless soils with 5% $<$ FC $<$ 15%, and Figure 73 shows the case history data points for

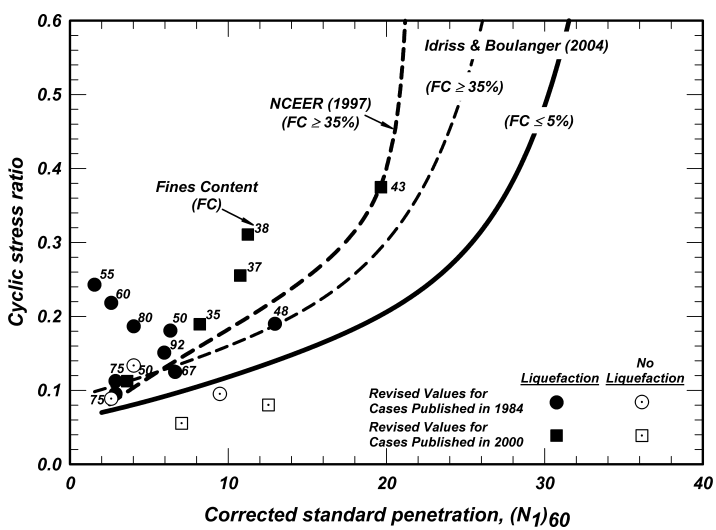

Figure 71. SPT case histories of cohesionless soils with FC $\geq$ 35%, the NCEER/NSF workshop curve (Youd et al. 2001), and the recommended curves for both clean sands and for FC $\geq$ 35% for M = 7.5 and σ'_{vc} = 1 atm.

For more monographs, publications, or videos, visit http://www.eeri.org

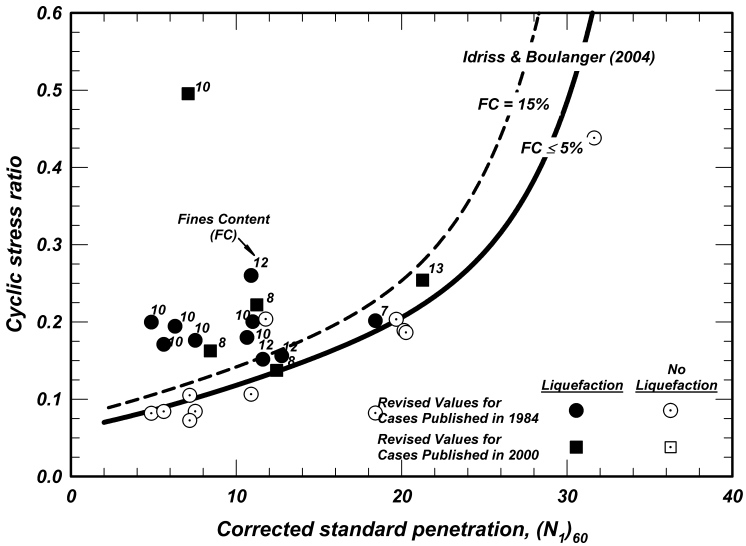

Figure 72. SPT case histories of cohesionless soils with 5% < FC < 15% and the recommended curves for both clean sands and for FC = 15% for M = 7.5 and σ'_{vc} = 1 atm.

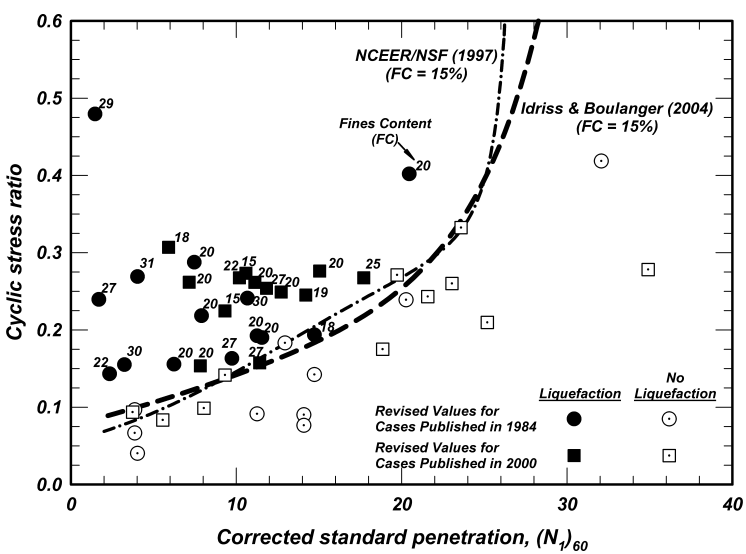

Figure 73. SPT case histories of cohesionless soils with 15% ≤ FC < 35% and the NCEER/NSF workshop curve (Youd et al. 2001) and the recommended curve for FC = 15% for M = 7.5 and σ'_{vc} = 1 atm.

For more monographs, publications, or videos, visit http://www.eeri.org

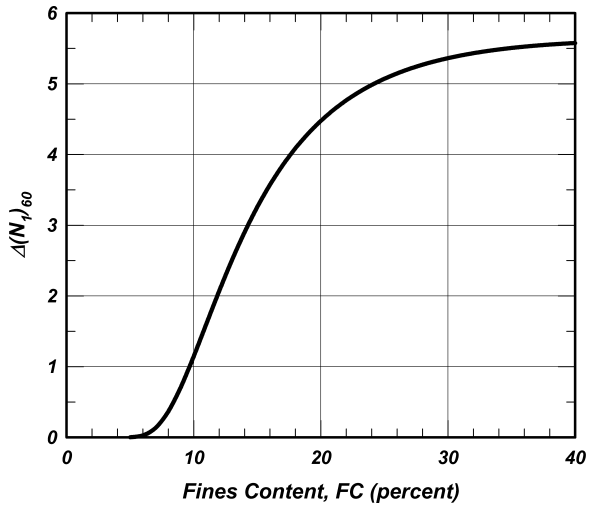

Figure 74. Variation of $\Delta(N_1)_{60}$ with fines content.

15% $\leq$ FC $<$ 35%. Again, the revised curve is lower than the NCEER/NSF workshop curve, and this reflects the influence of the recent SPT case history data set compiled by Cetin et al. (2000).

The revised boundary curves for silty sands are horizontal translations of the boundary curve for clean sand and can therefore be conveniently represented using an equivalent clean-sand SPT penetration resistance computed as

$$(N_1)_{60cs} = (N_1)_{60} + \Delta\,(N_1)_{60} \tag{75}$$

$$\Delta(N_1)_{60} = \exp\left(1.63 + \frac{9.7}{FC + 0.01} - \left(\frac{15.7}{FC + 0.01}\right)^2\right) \tag{76}$$

The variation of $\Delta(N_1)_{60}$ with FC, calculated via equations 75 and 76 (with FC in percent), is presented in Figure 74. Note that the correction for fines content is constant for FC values greater than about 35%, which is consistent with experimental observations that the behavior of silty sand with this level of fines content is largely governed by the matrix of fines, with the sand particles essentially floating within this matrix (e.g., Mitchell and Soga 2005). For silty sands with gravel contents of up to 15–20%, the liquefaction resistance is expected to depend primarily on the silty sand matrix. In those cases, SPT $(N_1)_{60}$ values should be carefully screened for the influence of the gravel particles (e.g., Figure 52), and then the FC used to compute the $\Delta(N_1)_{60}$ may be based on the soil fraction passing the No. 4 sieve.

For more monographs, publications, or videos, visit http://www.eeri.org

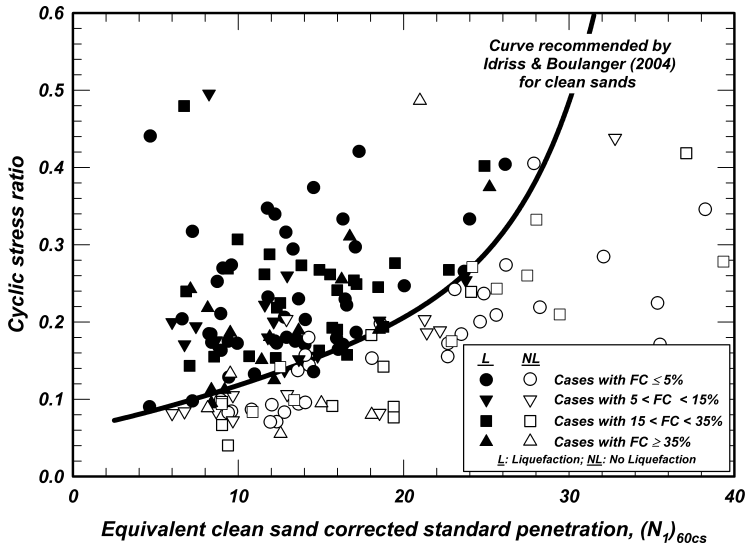

Figure 75. SPT case histories of liquefaction in cohesionless soils with various fines contents plotted versus their equivalent clean sand $(N_1)_{60cs}$ values for M = 7.5 and $\sigma'_{vc} = 1$ atm.

The SPT case histories of liquefaction in sands, silty sands, and sandy silts are replotted in Figure 75 against their equivalent $(N_1)_{60cs}$ values, with different symbols for different ranges of fines content. As expected, the boundary curve established for clean sands is seen to provide an equally good fit for any range of fines content. Consequently, the value of CRR for a magnitude M = 7.5 earthquake and an effective vertical stress of $\sigma'_{vc} = 1$ atm can be calculated on the basis of the $(N_1)_{60cs}$ value via the same expression presented above for clean sands.

Note that the C_N values for silty sands were computed via the equivalent clean-sand $(N_1)_{60cs}$ values; this appears to be a reasonable approximation, pending a better experimental definition of how fines content affects this relationship. This same approach is therefore applicable when this relationship is later used in practice.

The CRR values obtained for FC = 35% by using the correlations from the NCEER/NSF procedures (Youd et al. 2001) and the updates by Idriss and Boulanger (2006) and Cetin et al. (2004) are compared in Figure 76. These comparisons are for a water table depth of 1 m and an earthquake of M = 7.5. Figure 76a shows contours

For more monographs, publications, or videos, visit http://www.eeri.org

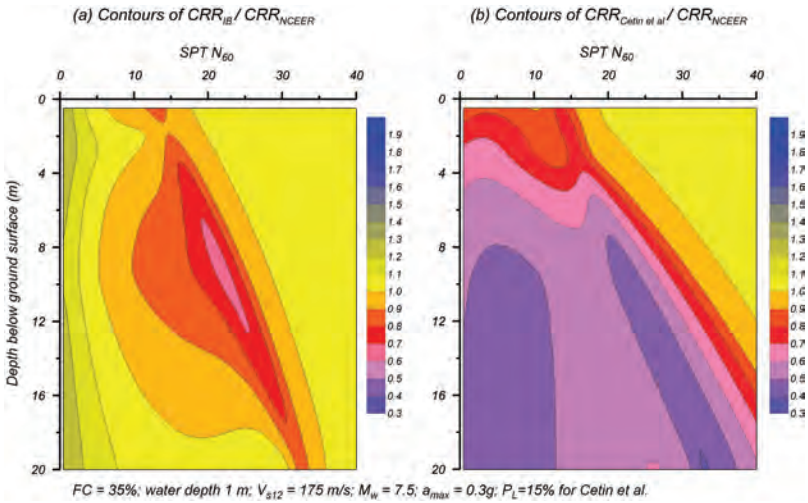

Figure 76. Comparison of liquefaction analysis procedures from Idriss and Boulanger (2006), Cetin et al. (2004), and NCEER/NSF (Youd et al. 2001) for FC = 35%.

of the ratio CRR_{IB}/CRR_{NCEER}, and Figure 76b shows contours of the ratio $CRR_{Cetin\ et\ al.}/CRR_{NCEER}$. The updates by Idriss and Boulanger and Cetin et al. both give CRR values that are generally smaller than those obtained via the NCEER/NSF procedures; this difference is a consequence of the recent earthquake case histories involving higher-FC sands. The Cetin et al. procedures produce CRR values that are significantly smaller than those obtained by the Idriss and Boulanger procedures; these differences generally increase with depth. The differences between the CRR_{IB} and $CRR_{Cetin\ et\ al.}$ values are a consequence of the same factors that affected their relative values for FC $\leq$ 5% sands (Figures 69 and 70).

CPT Correlations

Robertson and Wride (1997) and Suzuki et al. (1997) suggested the use of the "soil behavior type index," I_c (Jefferies and Davies 1993), which is a function of the tip resistance (q_c) and sleeve friction ratio (R_f), to estimate the values of the CRR for cohesionless soils with high fines content. The curve recommended by Robertson and Wride relating CRR-q_{c1N} at $I_c = 2.59$ (which they defined as corresponding to an "apparent" fines content of FC = 35%) is presented in Figure 77. Also shown in this figure are the CPT-based data points

For more monographs, publications, or videos, visit http://www.eeri.org

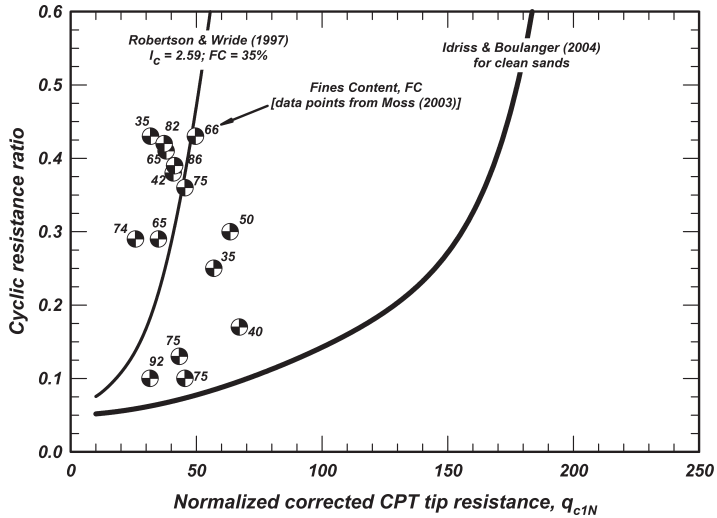

(a)

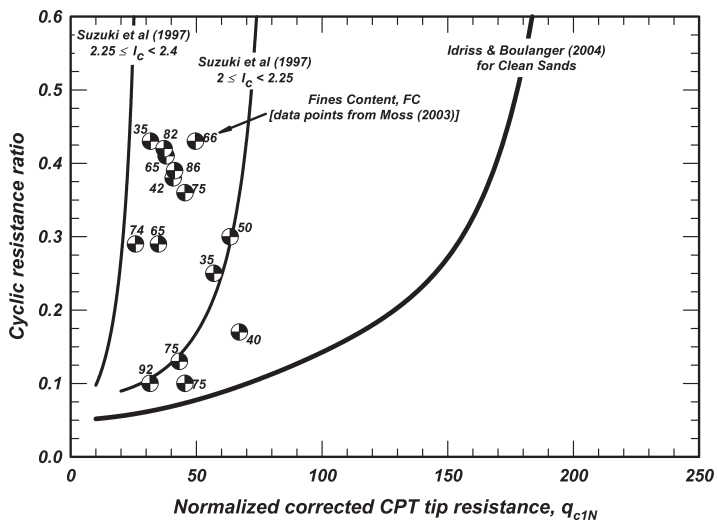

(b)

Figure 77. Comparison of field case histories for cohesionless soils with high fines content and the curves proposed by (a) Robertson and Wride (1997) for soils with $I_c = 2.59$ (apparent FC = 35%) and (b) Suzuki et al. (1997) for I_c values of 2.0–2.4.

For more monographs, publications, or videos, visit http://www.eeri.org

for the cases examined by Moss (2003) and Moss et al. (2006) for cohesionless soils (silty sands, sandy silts, and low-plasticity silts) with FC $\geq$ 35%. As the figure shows, the curve recommended by Robertson and Wride (1997) is unconservative in relation to these newer case history data points. The relationships by Suzuki et al. (1997) for cohesionless soils with high fines content are similarly unconservative in view of these new data.

The CPT-based approach can be modified to account for the effects of nonplastic fines content on the liquefaction resistance by using an approach similar to the one used for the SPT-based approach. Accordingly, an equivalent clean-sand value of the corrected tip resistance (q_{c1Ncs}) can be computed as

$$q_{c1Ncs} = q_{c1N} + \Delta q_{c1N} \tag{77}$$

The expression for Δq_{c1N} was derived to be consistent with the approximate effect that fines content has on the ratio q_{cN}/N_{60}. The resulting expression for Δq_{c1N} depends on both FC and q_{c1N}:

$$\Delta q_{c1N} = \left(5.4 + \frac{q_{c1N}}{16}\right) \cdot \exp\left(1.63 + \frac{9.7}{\mathrm{FC} + 0.01} - \left(\frac{15.7}{\mathrm{FC} + 0.01}\right)^2\right) \tag{78}$$

The variation of Δq_{c1N} with FC and q_{c1N} according to this relationship is illustrated in Figure 78.

Figure 79 compares the curve produced by this relationship for FC $\geq$ 35% with the cases examined by Moss et al. (2006) for cohesionless soils with FC $\geq$ 35%. Curves produced for other FC values are shown in Figure 80.

Influence of the Plasticity of the Fines

The plasticity of the fines also influences the cyclic loading behavior of soils. In examining this factor, it is useful to first consider the behavior of soils whose matrix is dominated by the fines fraction. This fraction is believed to dominate the matrix when the FC exceeds more than about 35–50% (e.g., Mitchell and Soga 2005).

The monotonic and cyclic loading behavior of fine-grained soils (or soils whose behavior is governed by a matrix of fines) appears to transition, over a fairly narrow range of plasticity indices, from soils that behave more fundamentally like sands ("sand-like" behavior) to soils that behave more fundamentally like clays ("clay-like"

For more monographs, publications, or videos, visit http://www.eeri.org

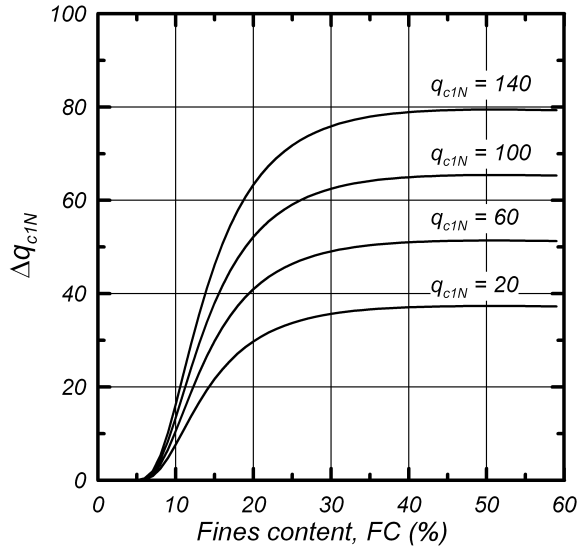

Figure 78. Variation of Δq_{c1N} with fines content and q_{c1N}.

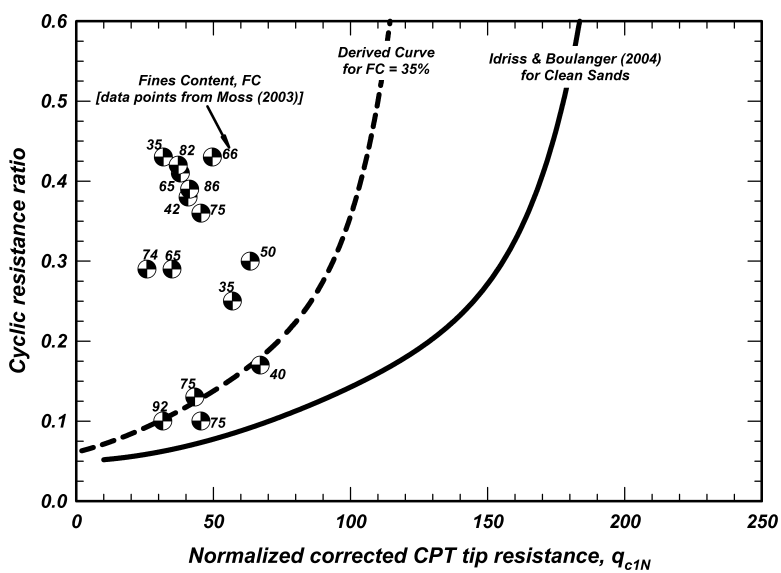

Figure 79. Comparison of field case histories for cohesionless soils with high fines content and a curve recommended for cohesionless soils with FC = 35%.

For more monographs, publications, or videos, visit http://www.eeri.org

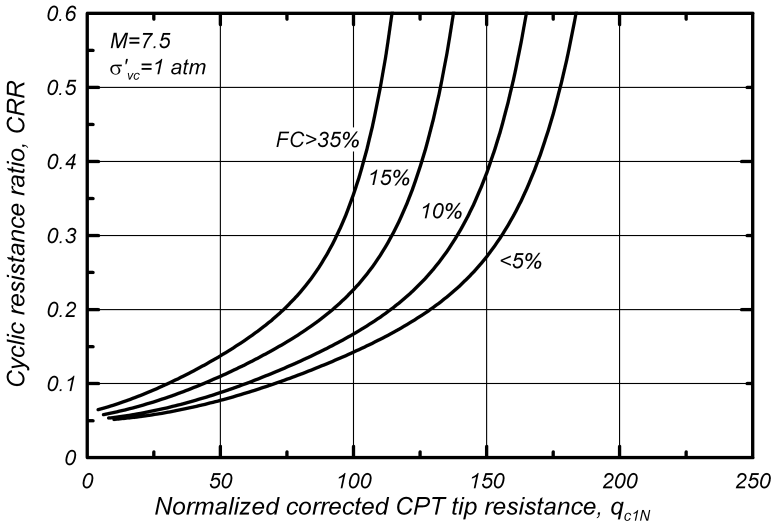

Figure 80. CPT relationships for cohesionless soils with various fractions of nonplastic fines.

behavior), with the distinction directly corresponding to the type of engineering procedures that are best suited to evaluating their seismic behavior. For practical purposes, Boulanger and Idriss (2004) suggest that sand-like behavior is observed for soils whose plasticity index (PI) is less than about 7, and clay-like behavior is observed for fine-grained soils with PI values greater than about 7. These boundaries are approximate, as the PI is only a proxy for the mineralogy and other factors that affect soil behavior. Fine-grained soils that are categorized as having clay-like behavior can still have the potential for earthquake-induced cyclic softening or failure, but the evaluation of that type of behavior requires the use of different engineering procedures. A more detailed discussion of criteria for categorizing soil behaviors, and of procedures for evaluating potential cyclic softening of clay-like soils, is in Section 6.

3.12 Probabilistic SPT and CPT Correlations for Triggering of Liquefaction

SPT- and CPT-based probabilistic correlations for the triggering of liquefaction in sands and silty sands have been developed by a number of researchers, including Liao et al. (1988), Liao and Lum (1998), Youd and Noble (1997), Toprak et al. (1999), Juang

For more monographs, publications, or videos, visit http://www.eeri.org

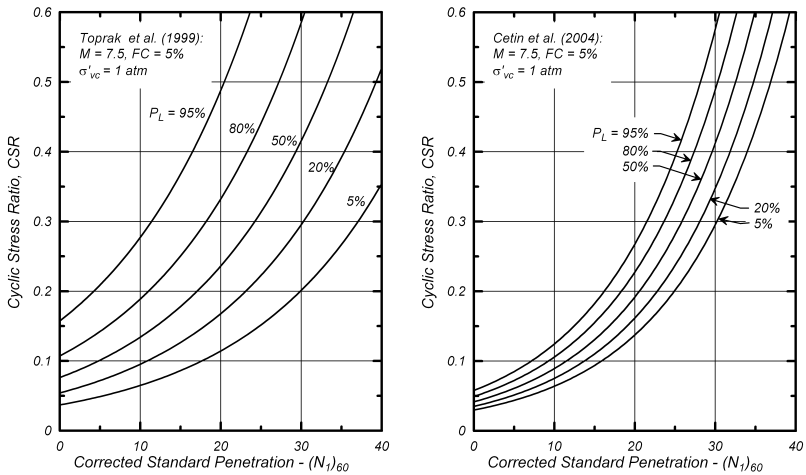

Figure 81. SPT-based probabilistic correlations for the CRR of clean sands for M = 7.5: (a) Toprak et al. (1999) and (b) Cetin et al. (2004, with permission from ASCE).

et al. (2002), Cetin et al. (2004), and Moss et al. (2006). For example, the SPT-based relationships by Toprak et al. (1999) and Cetin et al. (2004) are presented in Figure 81, which shows the contours of the CSR and $(N_1)_{60cs}$ corresponding to probabilities of liquefaction (P_L) whose range is 5–95%. The differences between these and other probabilistic relationships are partly due to the use of different statistical approaches, as well as to differences in the underlying case history databases and relevant parameters (e.g., C_N, MSF, r_d, K_σ, and $a_{\max}$). The relationships by Toprak et al. (1999) are typical of many probabilistic relationships, in that they show a very large difference between the contours for $P_L = 5\%$ and $P_L = 95\%$. In contrast, the relationships by Cetin et al. (2004) show a considerably smaller spread between the various contours of P_L (i.e., smaller uncertainty in cyclic strength). The smaller spread in the P_L contours from Cetin et al. (2004) is largely attributed to differences in the statistical approaches and is believed to be a more reasonable representation of the variance in cyclic strength at a given penetration resistance.

Comparisons of probabilistic and deterministic liquefaction triggering correlations by different investigators are, however, complicated by biases that arise from differences in their underlying databases and intermediate relationships (such as r_d, K_σ, C_N, etc). Thus improvements in methods of statistical analysis have produced a better

For more monographs, publications, or videos, visit http://www.eeri.org

estimate of variance in the liquefaction correlations, while the absolute positions continue to depend on the assumed analytical relationships.

The potential value of a probabilistic liquefaction correlation is its eventual use in a complete probabilistic evaluation of the performance of a structure or facility and the associated risks. This requires a probabilistic representation of ground motion hazards, site characteristics, liquefaction assessment, liquefaction consequences, and other applicable attributes that may be important to the specific structure or facility being evaluated. Fully probabilistic procedures for dealing with these types of problems are still at different stages of development (e.g., Kramer and Mayfield 2007) and, as they mature, they will be a valuable addition to engineering practice.

3.13 V_s-Based Correlations for Triggering of Liquefaction

The V_s-based procedure has advanced significantly in recent years, with improved correlations and more complete databases, as recently summarized by Andrus and Stokoe (2000) and Andrus et al. (2003). This procedure can be particularly useful for sites underlain by soils that are difficult to penetrate or sample (e.g., gravels, cobbles, and boulders). As such, V_s-based correlations provide a valuable tool that ideally is used in conjunction with SPT- or CPT-based liquefaction correlations, if possible. The question that arises, however, is which methodology should be given greater weight when parallel analyses by SPT, CPT, and V_s procedures produce significantly different results.

SPT, CPT, and V_s measurements each have particular advantages and disadvantages for liquefaction evaluations, but a particularly important point to consider is their respective sensitivity to the relative density, D_R, of the cohesionless soil under consideration. For example, changing the D_R of clean sand from 30% to 80% would be expected to increase the SPT blow count by a factor of about 7.1 (e.g., from an $(N_1)_{60}$ of 4 to 29) and the CPT tip resistance by a factor of about 3.3 (e.g., from a q_{c1N} of 53 to 173), as indicated by empirical relationships presented in Section 3.5. Note that the apparently greater sensitivity of the SPT to D_R is offset by the fact that there is normally greater uncertainty in SPT data than in CPT data. In contrast to both the SPT and CPT, the same change in D_R would be expected to change the V_s by a factor of roughly only 1.4 for clean sands, on the basis of published correlations (e.g., Harden and Drnevich 1972),

For more monographs, publications, or videos, visit http://www.eeri.org

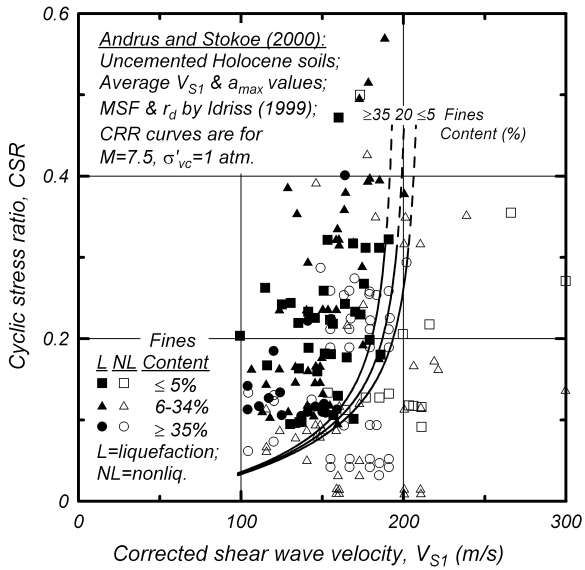

Figure 82. V_{s1}-based liquefaction correlation for clean uncemented sands (after Andrus and Stokoe 2000, with permission from ASCE).

and perhaps by a slightly greater factor for gravelly soils, on the basis of more recent findings (Stokoe 2007).

Given that D_R is known to have a strong effect on the cyclic and postcyclic loading behavior of saturated sand, it appears that V_s measurements would be the least sensitive for distinguishing among different types of behavior. It follows that a general correlation (as opposed to a soil-specific correlation) between small-strain stiffness and liquefaction behavior (which involves a larger range of strains) might be expected to have limited accuracy. This may partly explain why the correlation shown in Figure 82 has a large percentage of false positives (i.e., there are nonliquefaction case history points above the boundary line), as discussed by Liu and Mitchell (2006).

For this reason, it may be more appropriate to view the V_s case history database as providing bounds that identify conditions in which the likelihood of liquefaction is high, low, or uncertain. As such, a need remains for an improved understanding of V_s-based correlations and an assessment of their accuracy and usability in relation to SPT- and CPT-based correlations. In the meantime, it is recommended that greater weight be given to the results of SPT- or CPT-based liquefaction evaluations.

For more monographs, publications, or videos, visit http://www.eeri.org

3.14 Liquefaction Triggering Analyses—Examples and Discussion

General Considerations

The characterization of a site generally involves the synthesis of information from a variety of sources, from aerial photos to in-situ testing. The analysis of liquefaction triggering can proceed in a number of different ways, with the choice of an appropriate approach depending on each site's specific characteristics and the potential consequences of liquefaction that are of greatest concern. A key challenge is to structure the liquefaction triggering analysis in ways that appropriately consider the site's stratigraphy (e.g., the primary strata and spatial heterogeneity) and how it may relate to the potential consequences of liquefaction (e.g., liquefaction of isolated random pockets versus a continuous layer that could cause significant settlement or could lead to sliding toward a free face).

The influences that the spatial distribution of liquefied zones can have on the potential consequences of liquefaction are discussed in Section 4, after the various approaches for estimating potential deformations are presented. At this point, it is sufficient to note that some modes of deformation for a given structure may depend more on the average properties of specific strata, whereas other modes of deformation may depend more on the weakest zones within the strata.

Liquefaction Triggering Analyses for a Single SPT Boring and CPT Sounding

Examples of liquefaction triggering analyses are presented for a single SPT boring and single CPT sounding adjacent to each other at a site where liquefaction-induced lateral spreading was observed during the 1989 Loma Prieta earthquake. The extension of these analyses to an entire site must be guided by that site's specific characteristics and the mechanics of the potential deformation modes that are being considered, as was noted above and is discussed in greater detail in Section 4.

The liquefaction triggering analysis for the SPT data is plotted in Figure 83. The analysis was performed by using a spreadsheet, which, for ease of reference, is presented along with its cell equations in Appendix A.

The liquefaction triggering analysis for the adjacent CPT data is plotted in Figure 84. The analysis was also performed by using a spreadsheet, which is presented along with its cell equations in

For more monographs, publications, or videos, visit http://www.eeri.org

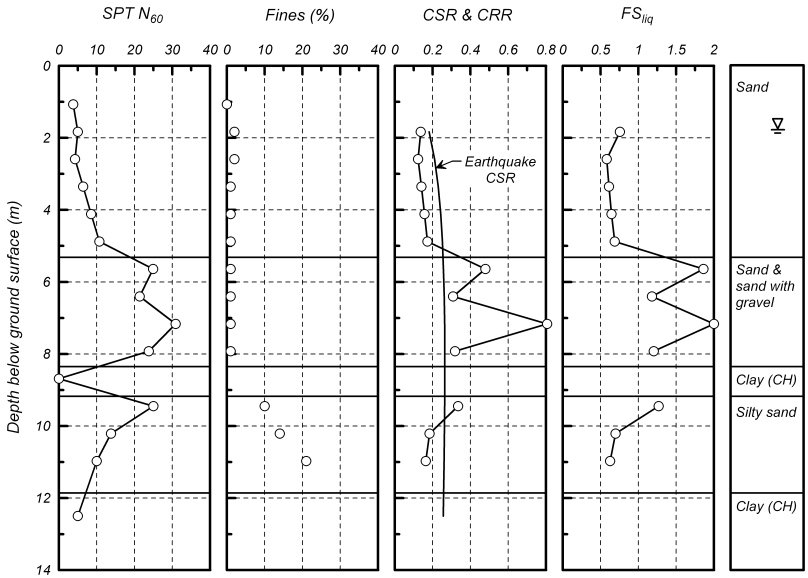

Figure 83. Example of a liquefaction triggering analysis for a single SPT boring.

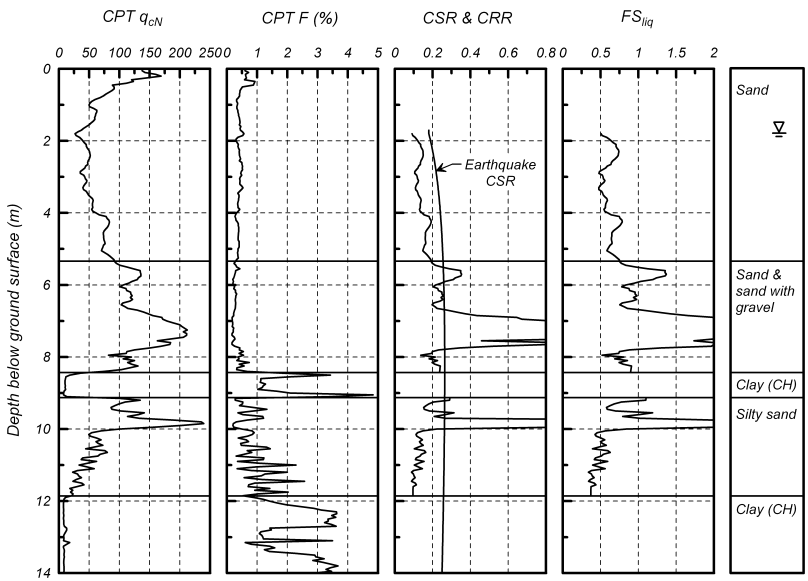

Figure 84. Example of a liquefaction triggering analysis for a single CPT sounding.

For more monographs, publications, or videos, visit http://www.eeri.org

Appendix B. One column of the spreadsheet specifies "interpreted q_{cN}" values in the sands near the contacts with softer clay layers; these interpreted values are taken to be the q_{cN} value in the sand at a distance of about 30 cm from the interface. The results of these analyses are compared with those for the adjacent SPT boring, from which it is clear that they are reasonably consistent for this site.

The CPT analysis requires specification of the fines content, which is information that is not directly provided by the CPT itself. For this example, it is fairly straightforward to obtain the appropriate fines contents from the laboratory test data on soil samples from the adjacent SPT boring. For a general site investigation, it is generally not necessary or feasible to have a boring beside every CPT sounding. Instead, SPT borings and CPT soundings may be paired beside each other in a few locations to establish the characteristics (including fines content) of the major strata and to establish the correlation between the CPT measurements and soil characteristics in the major strata. Additional CPT soundings may then be performed at other locations, with the fines contents estimated on the basis of the overall site characterization, provided that the CPT has encountered soil conditions comparable to those identified elsewhere at the site.

Various approaches may be used to establish a site-specific correlation between the CPT data and soil characteristics (e.g., fines content and/or plasticity), with the choice depending on the complexity of the site and other factors. For each major stratum at a site, the borehole data should be compiled, and the distributions of the fines content and other index characteristics should be determined. In some cases, it may be sufficient to simply determine the median values for fines content and other characteristics, especially when these values show relatively small spatial variations or the spatial variations do not affect the final results. For example, boring data at the site described in Figure 83 showed that the upper sand strata consisted of clean sands (hence, fines content can just be set as being $\leq 5\%$ in the analysis) and that the fine-grained soils of 8.4–9.1 m depth and below 11.9 m in depth consisted of high-plasticity clays (accordingly, their potential seismic behavior is not analyzed via these liquefaction correlations). In other strata, it may be advantageous to directly correlate variations in soil characteristics with the values of q_{cN}, R_f, or I_c. For example, the boring data at the site described in Figures 83 and 84 showed that the fines content in the silty sand stratum at a depth of 9.1–11.9 m increased with depth in the stratum (i.e., from 10% near the top to 21% near the bottom), which correlates directly with a progressive

For more monographs, publications, or videos, visit http://www.eeri.org

decrease in tip resistance, a progressive increase in sleeve friction ratio, and thus a progressive increase in the I_c index. Whether this trend warrants representation via a formal correlation or a simpler approximation depends on its importance to the specific project.

Automated Analysis Programs

Automated analytical procedures and computer software are widely available for performing liquefaction evaluations by using SPT or CPT data, but the user must be aware that such programs cannot perform the essential steps of screening SPT and CPT data quality or interpreting the overall site characteristics. The various difficulties that can be encountered in using automated calculations, and the steps needed to avoid such difficulties, were illustrated by Boulanger et al. (1999) and Kulasingam et al. (1999) for CPT soundings adjacent to the slope inclinometers at Moss Landing after the 1989 Loma Prieta earthquake. The three slope inclinometers were at different positions along a sloping shoreline that spread laterally toward the adjacent channel. The displacement profiles from the inclinometers identify the intervals over which significant shear strains, and hence liquefaction, appear to have developed. Automated analyses that used only the CPT data (i.e., point-by-point calculations with fines characteristics estimated from general correlations with the CPT measurements) resulted in erroneous predictions of strains and deformations versus depth (e.g., Kulasingam et al. 1999). For example, measurements of q_c and f_s near contacts between soils of greatly different penetration resistances and in finely interlayered soils were not representative of the actual soil conditions, and, as a result, the automated point-by-point liquefaction analysis of such data at Moss Landing predicted strains at several interfaces where no strains were observed. In addition, the default parameters for the CPT procedures by Robertson and Wride (1998) incorrectly predicted liquefaction of a high-plasticity silt layer. Fortunately, many of these types of common errors can be avoided by explicit consideration of soil sample data and site stratigraphy, along with careful inspection of the analytical results.

For more monographs, publications, or videos, visit http://www.eeri.org

4 CONSEQUENCES OF LIQUEFACTION

4.1 General Considerations

There is a wide range of possible consequences of liquefaction, which depends on the site conditions, the earthquake loading characteristics, and the nature of any structures on the site. Such consequences include deformation or instability of soil masses ranging from mildly sloping ground to embankment slopes, increased lateral pressures against retaining structures, loss of bearing support for shallow or deep foundations, loss of lateral support for embedded structures or piles, lurching of level ground, flotation of buried conduits or tunnels, and settlement caused by reconsolidation of the liquefied soils. Photos showing a number of these consequences are in Section 1.

Three consequences of liquefaction are discussed in this section:

- Loss of shear strength, leading to instability of slopes or embankments
- Lateral spreading of mildly sloping ground
- Settlement caused by reconsolidation of the liquefied soils

These three consequences were chosen because of their importance in practice and because they illustrate the range of concerns that are often involved and the approaches that are used to evaluate such concerns.

Factors that can significantly affect liquefaction-induced deformations are discussed in previous sections and are broadly grouped together as follows:

- Soil characteristics (e.g., relative density, gradation, fines content, age, degree of saturation, cementation, prior stress and strain history, K_o, and depositional environment)
- Earthquake ground motion characteristics (e.g., level of shaking, duration of shaking, and frequency content of shaking motions)

For more monographs, publications, or videos, visit http://www.eeri.org

- Site stratigraphy and topography, which affect site response, excess pore water pressure generation and diffusion, void redistribution, and deformation patterns (e.g., strata thickness and sequence, continuity of loose zones, water table elevation, hydraulic conductivities, sloping ground surface or strata, and proximity of a free face)
- Other complicating phenomena, such as (a) three-dimensional effects, whereby the lateral spreading mass may be partly restrained by the surrounding stable soils; (b) ground cracking that can vent water pressures and collapse water films that may have formed underneath lower-permeability layers; and (c) the influence of structural foundations or embedded structures

Current engineering analysis methods cannot reasonably account for the full range of these various factors or predict the complex deformation patterns observed in the field. Liquefaction analysis methods, both for triggering and consequences, must instead sacrifice some rigor, via various approximations or assumptions, in order to make the analysis tractable and then attempt to quantify the uncertainty in the predictions provided by the analysis method.

4.2 Instability and the Residual Shear Strength of Liquefied Soil

The most severe consequences with respect to ground deformations occur when a liquefied soil's shear strength is not sufficient to maintain stability under static loading alone (i.e., after the earthquake shaking is over). In this case, the static instability can result in deformations that are large enough to produce a deformed geometry that is statically stable, albeit with a much flatter slope than before. The slide in the upstream shell of the Lower San Fernando Dam shown in Figure 6 is a good example of such a consequence.

In discussing the shear strength of liquefied soils, it is essential to maintain clear distinctions among the different measures of strength that can be used in describing the in-situ stress-strain response of saturated soils during and after strong shaking. The ultimate shear resistance, or critical-state strength, which can be measured in an undrained monotonic laboratory element test, may be denoted as S_{CS}. The QSS shear resistance, which corresponds to a local minimum in the stress-strain curve from an undrained monotonic laboratory element test, may be denoted as S_{QSS}. Residual shear strength, denoted as S_r, refers to the shear resistance that a liquefied soil mobilizes in

For more monographs, publications, or videos, visit http://www.eeri.org

the field, which can be complicated by void redistribution, particle intermixing, and other field mechanisms that are not replicated in laboratory element tests.

Procedures for estimating the in-situ strength of liquefied sand on the basis of laboratory testing of field samples have included testing of field samples obtained via frozen sampling techniques (e.g., Robertson et al. 2000) as well as samples obtained via high-quality tube sampling techniques coupled with procedures for "correcting" the shear strength for the estimated volume changes that occur during sampling (e.g., Castro 1975, Castro and Poulos 1977, Poulos et al. 1985). Laboratory tests should approximate the field conditions as much as possible, because the measured shear resistance will depend on the consolidation stresses and direction of loading (e.g., see Figures 11 and 13). The values of S_{CS} or S_{QSS} obtained from the laboratory correspond to the soil's void ratio at the time of testing. If the diffusion of earthquake-induced excess pore water pressures causes the soil to become looser in some zone (e.g., Figure 43), then the in-situ S_{CS} of that zone would be reduced in relation to the value measured at the pre-earthquake void ratio. The potential changes in the in-situ S_{CS} that are due to void redistribution and particle intermixing are currently difficult to quantify, which makes it difficult to rely on the results obtained from laboratory testing of field samples.

Empirical approaches for estimating the in-situ S_r of liquefied sand have been developed by back-analyses of liquefaction flow slides, as first presented by Seed (1987) and since modified or amended by a number of researchers (e.g., Davis et al. 1988, Seed and Harder 1990, Ishihara 1993, Wride et al. 1999, Yoshimine et al. 1999, Olson and Stark 2002). The back-calculation procedure involves performing a post-earthquake static stability analysis of the earth structure, with each zone of nonliquefied soil assigned a best estimate of its shear strength, whereas the zone of suspected liquefaction is assigned an unknown shear strength S_r (with $\phi_u = 0$). This procedure is illustrated in Figure 85 for the Lower San Fernando Dam. An upper bound estimate for S_r is the value that gives a factor of safety against sliding equal to 1.0 for the undeformed geometry of the slope. Another estimate for S_r is similarly obtained for the final deformed geometry of the slope, if that deformed geometry is reasonably documented. Various procedures have been used to interpolate between these two estimates of S_r by accounting for the role of sliding inertia, evolving geometry, strength losses caused by intermixing with adjacent water bodies, and other factors. For the Lower San Fernando Dam,

For more monographs, publications, or videos, visit http://www.eeri.org

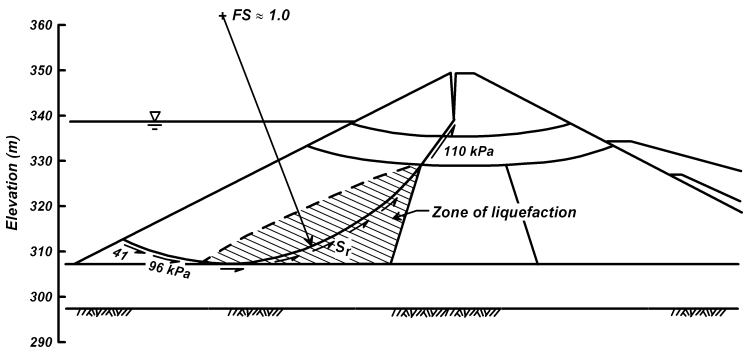

Figure 85. Back-calculation of the residual shear strength for the liquefied shell materials of the Lower San Fernando Dam, using limit equilibrium analyses (after Seed 1987, with permission from ASCE).

the analyses of Olson and Stark (2002) produced S_r values of about 36 kPa and 5 kPa for the undeformed geometry and the final deformed geometry estimates, respectively, and an interpolated best estimate of about 19 kPa. This illustrates how the interpolation of strengths between deformed and undeformed geometries is a significant step in the interpretation of the case histories, which adds considerably to the uncertainty in estimating S_r because of the very complex mechanisms involved.

Back-calculated S_r values for the liquefied soils have been correlated with the pre-earthquake or post-earthquake in-situ penetration resistance. The resulting correlations provide an implicit accounting of the various field processes that might have affected the mobilized shear strengths, such as void redistribution or particle intermixing (Seed 1987). The selection of a representative penetration resistance can be complicated by soil heterogeneity, as illustrated by the post-earthquake CPT and SPT data in Figures 86 and 87, respectively, that were obtained in the downstream shell of the Lower San Fernando Dam. The variability in the CPT tip resistance illustrates the thin stratification of coarser- and finer-grained soils in the hydraulic fill zones of the dam. In representing this case history, several researchers have used mean values from the suspected critical zone. For example, Seed and Harder (1990) selected a representative mean post-earthquake $(N_1)_{60}$ value of 14.5 for the cohesionless soils in the downstream shell from Figure 87 and then estimated that the representative mean $(N_1)_{60}$ value would have been about 11.5 for the soils in the upstream

For more monographs, publications, or videos, visit http://www.eeri.org

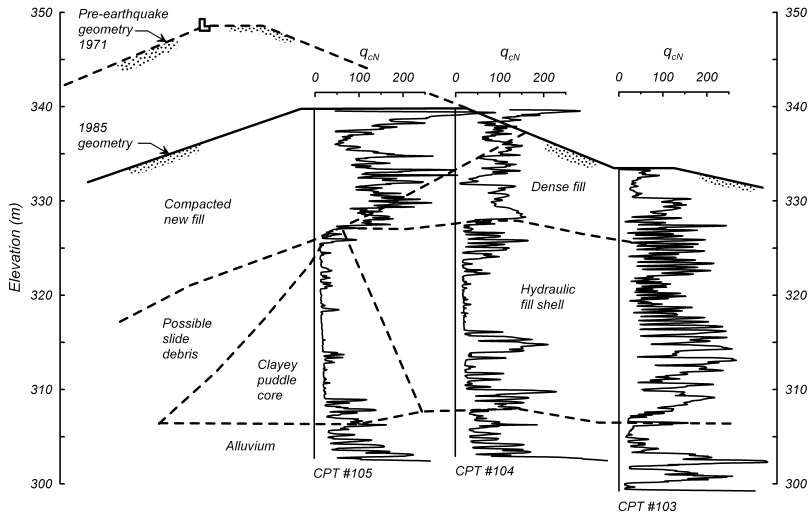

Figure 86. Post-earthquake CPT soundings in the downstream shell of the Lower San Fernando Dam in 1985 (section after Castro et al. 1989, CPT data from R. Olsen).

shell before the earthquake. Other researchers have chosen penetration resistances considerably smaller than the mean value, on the basis of arguments that the sliding may have been dominated by the weakest layers. Nevertheless, it is essential that the forward application of the resulting correlation be based on the same general approach to estimating representative penetration resistances that was used to develop the correlation.

Seed (1987) also suggested that the effects of fines content on S_r could be approximately accounted for by correcting the measured or estimated pre-earthquake SPT $(N_1)_{60}$ values to "equivalent clean-sand" $(N_1)_{60cs-Sr}$ values on the basis of the relationship

$$(N_1)_{60cs-Sr} = (N_1)_{60} + \Delta\,(N_1)_{60-Sr} \tag{79}$$

The values of $\Delta(N_1)_{60-Sr}$ recommended by Seed (1987), as listed in Table 4, were based primarily on engineering judgment because of the lack of physical data (experimental or empirical) from which a correction can be derived—a situation that persists today. Note, also, that these corrections for fines content are different from all previously adopted values for liquefaction triggering correlations.

For more monographs, publications, or videos, visit http://www.eeri.org

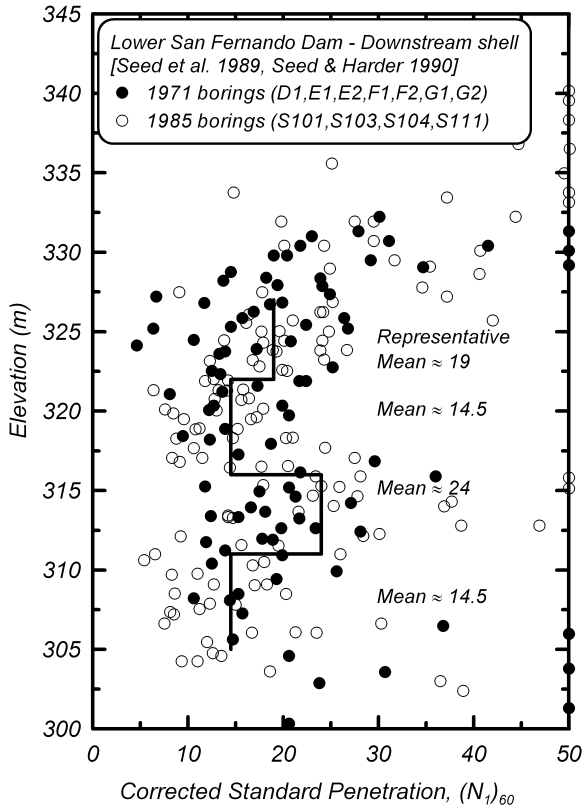

Figure 87. Summary of post-earthquake SPT data in predominantly cohesionless soils in the downstream shell of the Lower San Fernando Dam (after Seed et al. 1989 and Seed and Harder 1990).

Table 4 Values of $\Delta(N_1)_{60-Sr}$ recommended by Seed (1987).

Fines content (% passing No. 200 sieve)	$\Delta(N_1)_{60-Sr}$
10	1
25	2
50	4
75	5

For more monographs, publications, or videos, visit http://www.eeri.org

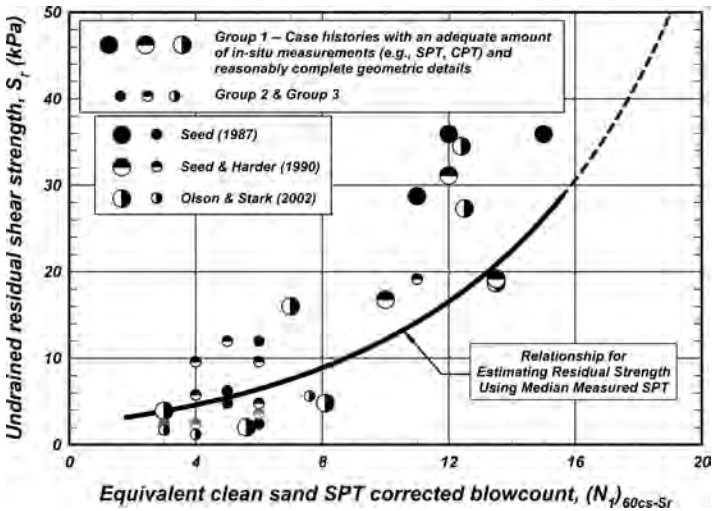

Figure 88. Residual shear strength of liquefied sand versus equivalent clean-sand SPT-corrected blow count, using the case histories published by Seed (1987), Seed and Harder (1990), and Olson and Stark (2002).

Eighteen case histories of flow slides attributed to liquefaction are summarized in Figure 88 by using S_r versus $(N_1)_{60cs-Sr}$ and in Figure 89 by using a normalized strength ratio S_r/σ'_{vc} versus $(N_1)_{60cs-Sr}$ (Idriss and Boulanger 2007). The soils for these case histories had fines content of 0–90%, and the SPT data were corrected for fines content on the basis of the values in Table 4. Figures 88 and 89 show the case history interpretations by three different researchers (Seed 1987, Seed and Harder 1990, Olson and Stark 2002) and categorize the individual case histories into one of three groups. Group 1, which includes 7 of the 18 case histories shown in these figures, has an adequate quantity of in-situ penetration test measurements (SPT or CPT) and reasonably complete geometric details. Group 2 case histories have an adequate quantity of in-situ penetration test measurements, but the geometric details are incomplete. Group 3 case histories have reasonably complete geometric details, but they have only estimated values for in-situ penetration resistances. These case histories illustrate the potentially severe strength loss associated with liquefaction, but the fact that so few are well documented contributes to the significant uncertainty in the resulting correlations for back-calculated shear strengths.

For more monographs, publications, or videos, visit http://www.eeri.org

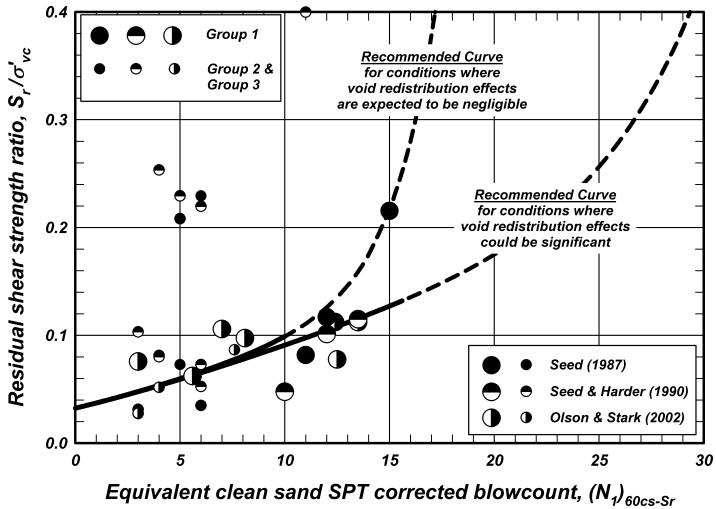

Figure 89. Normalized residual shear strength ratio of liquefied sand versus equivalent clean-sand SPT-corrected blow count for $\sigma'_{vc} < 400$ kPa, using the case histories published by Seed (1987), Seed and Harder (1990), and Olson and Stark (2002).

The idea of correlating S_r with $(N_1)_{60cs-Sr}$, as is done in Figure 88, was proposed by Seed (1987) and followed by Seed and Harder (1990). A direct correlation between S_r and $(N_1)_{60cs-Sr}$ was considered logical, on the basis of critical-state concepts (e.g., critical-state strength at large strains is a function of void ratio alone) and established correlations between the overburden corrected penetration resistance and in-situ relative density. Figure 88 also shows a design relationship that falls within the range recommended by Seed and Harder (1990) and has been widely used in practice during the last 10 years for estimating S_r on the basis of median penetration resistance.

There are a number of advantages, however, to expressing the S_r of liquefied soil as a normalized residual shear strength ratio, S_r/σ'_{vc}, a usage that has been adopted in several more recent studies (e.g., Vasquez-Herrera et al. 1990, Stark and Mesri 1992, Ishihara 1993, Vaid and Sivathayalan 1996, Wride et al. 1999, Yoshimine et al. 1999, Olson and Stark 2002, Idriss and Boulanger 2007). The use of S_r/σ'_{vc} rather than S_r is most commonly based on the fact that S_r/σ'_{vc} is more effective for describing undrained stress-strain behavior up

For more monographs, publications, or videos, visit http://www.eeri.org

to moderate strain levels in undrained monotonic laboratory element tests. In addition, the use of S_r/σ'_{vc} is believed to better reflect the potential effects of strength loss that is induced by void redistribution, because of the following considerations. The shear resistance in a loosening zone could locally diminish to zero if a water film forms, but the average shear resistance over a large area is unlikely to be zero, because water films can dissipate by piping into cracks that develop as the slope deforms, and the geologic interfaces where loosening develops are likely to be irregular enough to preclude continuous films of water over large areas. The potential for void redistribution to cause significant slope deformations decreases quickly with increasing D_R, because a greater D_R has the combined benefits of reducing the volume of water expelled by contracting zones and increasing the volume of water that can be absorbed by dilating zones. S_r/σ'_{vc} values can also be interpreted as representing small fractions of the pre-earthquake drained strength. For example, if is assumed that tan $\phi' \approx 0.6$ for loose sands, then the S_r/σ'_{vc} values of 0.05–0.12 obtained from most of these case histories are about 8–20% of the pre-earthquake drained strength (i.e., a strength loss of 80–92% because of liquefaction). For situations in which void redistribution is significant, it seems reasonable to expect that the shear strength will drop to a small fraction of the pre-earthquake drained shear strength, because the impeded pore water seepage allows the soil to shear at a sustained low value of σ'_v. Thus S_r/σ'_{vc} ratios are believed to provide a better representation of the potential effects of void redistribution than is provided by a direct correlation with S_r, while it is recognized that neither correlation fully accounts for the numerous factors that influence void redistribution processes.

Figure 89 shows two different relationships for estimating S_r/σ'_{vc} in design. They are essentially the same for $(N_1)_{60cs-Sr}$ values less than about 12, where they are both constrained by the available data. It is, however, necessary to estimate residual strengths for soils that have $(N_1)_{60cs-Sr}$ values greater than 14, and thus the extrapolation of the residual strength correlation beyond the limits of available data is unavoidable. The two relationships shown in Figure 89 provide guidance on this extrapolation for two conditions.

The upper relationship in Figure 89 corresponds to a condition in which the effects of void redistribution can be confidently judged to be negligible. This condition could include sites where the stratigraphy would not impede post-earthquake dissipation of excess pore

For more monographs, publications, or videos, visit http://www.eeri.org

water pressures, so the dissipation of excess pore pressures would be accompanied by densification of the soils at all depths. In this case, the available experimental data and correlations between D_R and $(N_1)_{60}$ for sands and silty sands indicate that the undrained shear resistance would increase rapidly as the $(N_1)_{60cs-Sr}$ value approaches 15. This relationship can be represented by the following equation:

$$\frac{S_r}{\sigma'_{vo}} = \exp\left(\frac{(N_1)_{60cs-Sr}}{16} + \left(\frac{(N_1)_{60cs-Sr} - 16}{21.2}\right)^3 - 3.0\right) \times \left(1 + \exp\left(\frac{(N_1)_{60cs-Sr}}{2.4} - 6.6\right)\right) \leq \tan\phi' \qquad (80)$$

The lower relationship in Figure 89 corresponds to conditions in which the effects of void redistribution can be significant. This would include sites with relatively thick layers of liquefiable soils that are overlain by lower-permeability soils that would impede the post-earthquake dissipation of earthquake-induced excess pore water pressures. In this case, the trapping of upwardly seeping pore water beneath the lower-permeability layer could lead to localized loosening, strength loss, and possibly even the formation of water films (Whitman 1985). This relationship can be represented by the following equation:

$$\frac{S_r}{\sigma'_{vo}} = \exp\left(\frac{(N_1)_{60cs-Sr}}{16} + \left(\frac{(N_1)_{60cs-Sr} - 16}{21.2}\right)^3 - 3.0\right) \leq \tan\phi' \qquad (81)$$

The potential role of void redistribution or other strength loss mechanisms in the case histories is not fully clear at this time. Physical and analytical models indicate that void redistribution is potentially most severe for loose sands and is likely to have played a role in many of the currently available case histories. This would suggest that the two design relationships should be somewhat different at the lower penetration resistances, but the current state of knowledge does not provide a basis for incorporating any difference at this time.

Similar relationships for a CPT-based evaluation of S_r/σ'_{vc} are shown in Figure 90, along with the same case histories that were used to develop the SPT-based relationship in Figure 89. For many of the case histories, it was necessary to convert available SPT data into CPT data via a combination of empirical correlations (e.g., Suzuki et al. 1998, Cubrinovski and Ishihara 1999, Salgado et al. 1997b),

For more monographs, publications, or videos, visit http://www.eeri.org

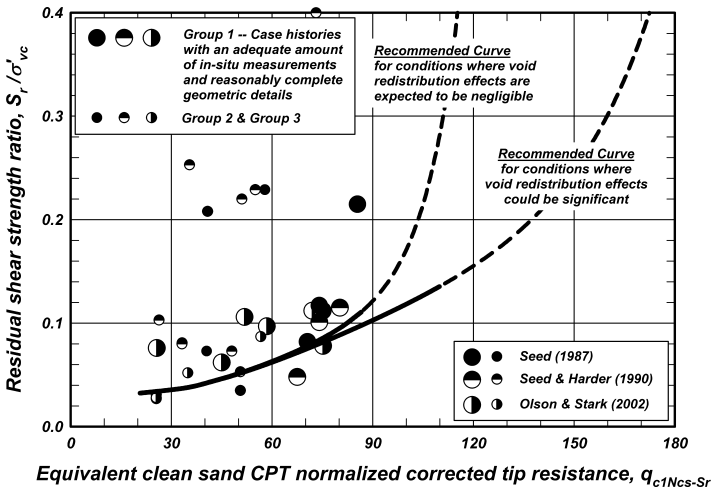

Figure 90. Correlation between the normalized residual shear strength ratio for liquefied soils and overburden-corrected CPT penetration resistance ($\sigma'_{vc} < 400$ kPa).

as described in Idriss and Boulanger (2007). CPT penetration resistances were then adjusted to equivalent clean-sand values by using the Δq_{c1N} values in Table 5, which were derived for consistency with the SPT corrections recommended by Seed (1987). The recommended relationships for S_r/σ'_{vc} can be calculated as

$$\frac{S_r}{\sigma'_{vo}} = \exp\left(\frac{q_{c1Ncs-Sr}}{24.5} - \left(\frac{q_{c1Ncs-Sr}}{61.7}\right)^2 + \left(\frac{q_{c1Ncs-Sr}}{106}\right)^3 - 4.42\right) \leq \tan\phi' \tag{82}$$

Table 5 Approximate values of Δq_{c1N-Sr} for CPT correlation with residual strengths.

Fines content (% passing No. 200 sieve)	Δq_{c1N-Sr}
10	10
25	25
50	45
75	55

For more monographs, publications, or videos, visit http://www.eeri.org

for a case in which void redistribution effects could be significant, and they can be calculated as

$$\frac{S_r}{\sigma'_{vo}} = \exp\left(\frac{q_{c1Ncs-Sr}}{24.5} - \left(\frac{q_{c1Ncs-Sr}}{61.7}\right)^2 + \left(\frac{q_{c1Ncs-Sr}}{106}\right)^3 - 4.42\right)$$
$$\times \left(1 + \exp\left(\frac{q_{c1Ncs-Sr}}{11.1} - 9.82\right)\right) \leq \tan\phi' \qquad (83)$$

for a case in which void redistribution effects are expected to be negligible.

The curves presented in Figures 89–90 are applicable to values of σ'_{vc} less than 400 kPa. The appropriate S_r/σ'_{vc} ratios for $\sigma'_{vc} > 400$ kPa are expected to be smaller than those recommended in Figures 89 and 90. For example, triaxial compression test results by Yoshimine et al. (1999) showed that S_r/σ'_{vc} ratios at a given D_R were relatively independent of σ'_{vc} up to σ'_{vc} values of about 500 kPa, but these ratios decreased at higher values of σ'_{vc}. This effect may be approximately accounted for by using the state-corrected penetration resistances, $(N_{1\xi})_{60cs-Sr}$ or $q_{c1\xi Ncs-Sr}$, in the above relationships (Boulanger and Idriss 2004a).

The selection of representative penetration resistances for determining the residual shear strengths of specific strata requires (1) consideration of the spatial variability in relation to the scale of the potential failure surface and (2) consistency with the way the empirical correlation was developed. Slope stability depends on the cumulative shear resistance along potential failure surfaces, so that the average shear strength can be used over some segments of the failure surface. For this reason, consideration must be given to whether the spatial heterogeneities are random or have systematic variations that produce weaker continuous layers or zones that could control slope stability.

The interpretation of the SPT data from the Lower San Fernando Dam by Seed et al. (1989) in Figure 87 illustrates how heterogeneity was considered in developing several of the common residual strength correlations (including those presented here). The $(N_1)_{60}$ values were first separated according to primary strata and soil type; that is, SPT data from the alluvium, hydraulic fill shell, clayey puddle core, and fill were not commingled, and the results from the clay and sand interlayers in the downstream shell were not commingled. The resulting data in Figure 87 are for only predominantly cohesionless soil samples from the downstream hydraulic fill shell. The pattern of $(N_1)_{60}$ values

For more monographs, publications, or videos, visit http://www.eeri.org

in the downstream hydraulic fill shell was then judged to be reasonably described by four elevation intervals, from which representative mean values of 19, 14.5, 24, and 14.5 were identified, and then ultimately a value of 14.5 was used by Seed et al. (1989) to represent the downstream hydraulic fill at the time of the explorations.

The effect that alternative interpretations would have on the selection of a representative $(N_1)_{60}$ can now be illustrated by reconsidering Figure 87. For example, indiscriminately grouping all the hydraulic fill shell data together would produce a mean value closer to 18, whereas further subdividing the shell into thinner elevation intervals would produce mean values as low as perhaps 12. If 30th percentile values were considered more appropriate than mean values, then the representative values would have been about 16, 12, 18, and 12 for the four elevation intervals, respectively; about 14 if the shell data were lumped together; and as low as about 11 if the shell were divided into significantly more elevation intervals. The approach, and the resulting representative values, used by Seed et al. (1989) and Seed and Harder (1990), as plotted in Figure 87, are considered more reasonable, given the scale of the subintervals in relation to the potential failure mechanism (i.e., Figure 85).

4.3 Lateral Spreading Deformations

Deformation Patterns and Spatial Heterogeneity

Liquefaction-induced lateral spreading can produce very complex deformation patterns, as illustrated by Figures 91 and 92 . Lateral spreading toward any open channel or face can occur in mildly sloping ground and extend to very large distances away from the open face. Displacement magnitudes within lateral spreads can exhibit strong spatial variations, both with distance from a free face and with position parallel to a free face.

Subsurface heterogeneity in soils has a strong influence on the magnitude and distribution of liquefaction-induced ground deformation. For example, Holzer and Bennett (2007) used several case histories to illustrate how the boundaries of lateral spreads are often determined by subsurface geologic or hydrogeologic conditions, such as abrupt changes in geologic facies (e.g., edges of buried channel sands or edges of fills) or transitional changes in soil characteristics (e.g., fines content). Similarly, variations in deformations within lateral spreads can often be related to observed variations in the subsurface soil and groundwater conditions.

For more monographs, publications, or videos, visit http://www.eeri.org

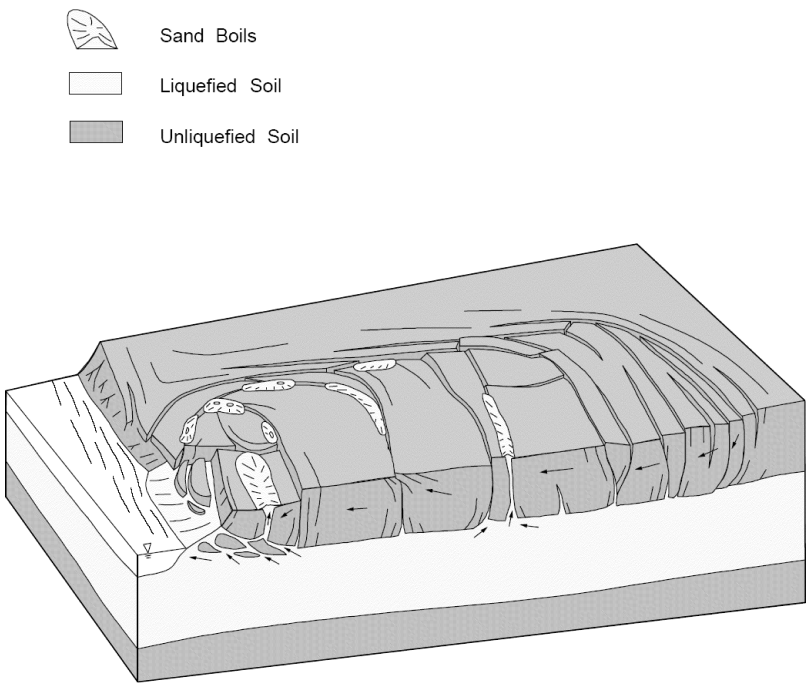

Figure 91. Complex deformation patterns in a lateral spread (Rauch 1997).

The importance of understanding the potential distribution of liquefied zones is illustrated by a simple example, shown in Figure 93. The simple building in Figure 93a is supported on spread footings over a deposit that is expected to develop liquefaction in scattered discontinuous pockets throughout the subsurface. In this case, the site would be more resistant to lateral spreading because the liquefied pockets are restrained by the surrounding nonliquefied soils, while individual footings may still experience significant amounts of vertical settlement. Figure 93b shows the same building, but with a continuous liquefied layer having been identified across the entire building footprint. The volume of liquefiable sand in Figures 93a and 93b may be about the same, but the fact that 93b has a continuous layer means that the soil is more susceptible to instability or lateral spreading toward the channel on the right. The example in Figure 93c is similar to that in Figure 93b, except that the liquefiable layer is bounded on the right by nonliquefiable soils rather than by an open channel. In this situation, the magnitude of transient and permanent

For more monographs, publications, or videos, visit http://www.eeri.org

Figure 92. Lateral spreading in Golcuk that occurred during the 1999 Kocaeli earthquake (photo: GeoEngineering Earthquake Reconnaissance Association).

lateral ground displacements caused by liquefaction would be expected to be smaller than when there is an adjacent open channel. Vertical settlement of the structure's footings would be expected to be more uniform for 93c than for 93a, because the liquefiable soils are deeper and are overlain by a thicker nonliquefiable layer. Vertical movements for 93b would include contributions from reconsolidation of the liquefied zones and the effects of lateral spreading or slumping along the channel, and thus the structure's footings could experience particularly uneven settlement. These types of considerations are important for the effective selection and use of analytical methods and are discussed further in subsequent sections.

Approaches for Estimating Lateral Spreading Displacements

A number of approaches have been proposed for estimating lateral spreading displacements. Four of these approaches are presented here, to illustrate both the range and types of approaches that can be useful in different situations:

- Estimate the permanent shear strains that are expected within the liquefied zones (and nonliquefied zones, if warranted) and

For more monographs, publications, or videos, visit http://www.eeri.org

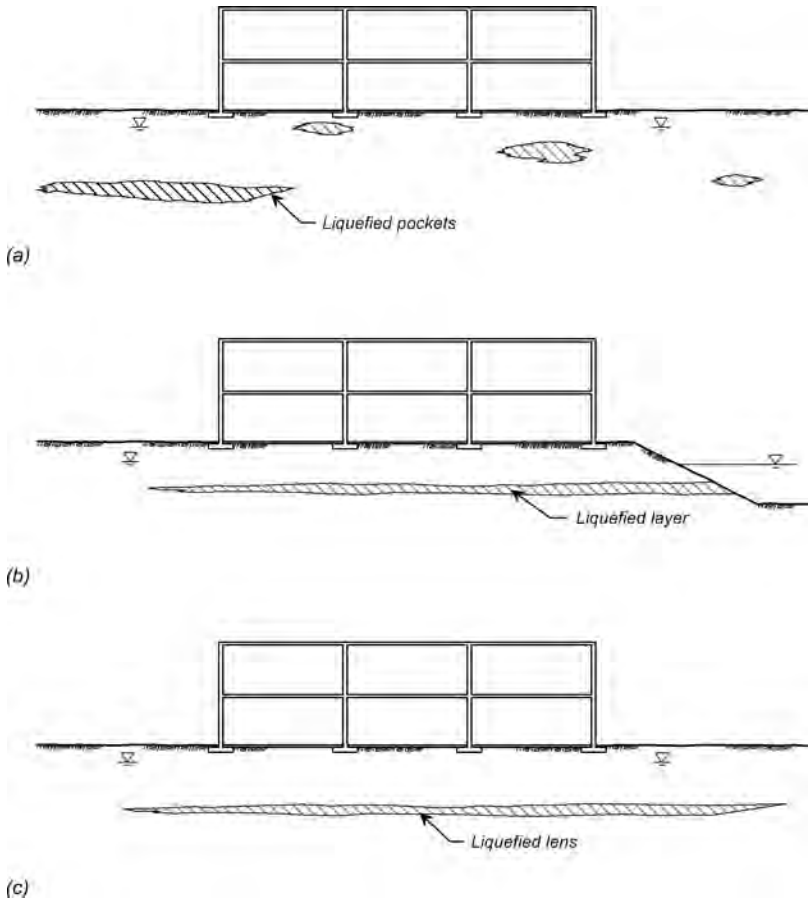

Figure 93. Spatial distribution of liquefied zones beneath a structure: (a) isolated pockets, (b) a layer with potential for lateral spreading toward a nearby free face, and (c) an isolated layer beneath level ground without the potential for lateral spreading.

then integrate those shear strains over depth to obtain an estimate of the potential lateral displacement at the ground surface. The estimated lateral displacement may also be empirically adjusted on the basis of calibration to case history observations.

- Estimate the permanent ground surface displacement via primarily empirical models that were derived by regression against past observations of ground displacements and which incorporate input parameters that appear to strongly influence the observed displacements.

For more monographs, publications, or videos, visit http://www.eeri.org

- Compute permanent ground surface displacements via a Newmark sliding block analysis, in which displacements are expected to occur whenever the inertial forces from shaking cause the factor of safety against instability to become temporarily less than unity.
- Perform detailed nonlinear dynamic analyses and postshaking nonlinear static analyses.

Each of these approaches involves significant simplifications whose result is that certain physical mechanisms of lateral spreading are not explicitly accounted for. These simplifications contribute to the uncertainty in the predicted lateral displacements, which is the price paid for arriving at a tractable means for exploring the likely range of expected ground displacements in engineering practice.

Estimated Shear Strain Potentials

Conceptually, the permanent lateral displacement (LD) at the ground surface can be computed by numerically integrating the expected shear strains (γ) versus depth, as

$$LD = \int_0^{z_{\max}} \gamma \cdot dz \tag{84}$$

This approach is a one-dimensional simplification of the strain potential procedure developed by Seed et al. (1975a) for estimating liquefaction-induced displacements in earth dams. This general approach has been used extensively in research and practice in a number of forms. Commonly, the relationships for predicting shear strains are based on laboratory test data, subject to certain modifications that are based on other considerations (e.g., Seed 1979). For lateral spreading problems, the computed ground displacement is then sometimes modified for the effects of other influencing factors (e.g., distance from the free face), which may be identified through comparisons with empirical field observations (e.g., Tokimatsu and Asaka 1998, Shamoto et al. 1998, Zhang et al. 2004, Faris 2004, Faris et al. 2006).

Maximum shear strains that develop during undrained cyclic loading in laboratory tests have been related to the factor of safety against the triggering of liquefaction by Ishihara and Yoshimine (1992). Their relationships are shown in Figure 94, along with the results of undrained cyclic simple shear tests by Nagase and Ishihara (1988) on clean reconstituted sand with no initial static shear stress and with irregular unidirectional and multidirectional loading. Figure 94

For more monographs, publications, or videos, visit http://www.eeri.org

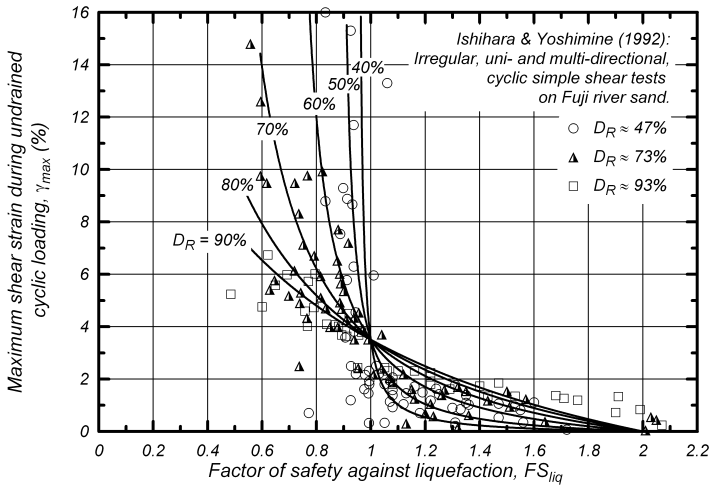

Figure 94. Relationship between the maximum shear strain and the factor of safety against liquefaction, on the basis of undrained cyclic simple shear tests on clean reconstituted sand at different relative densities (after Ishihara and Yoshimine 1992).

illustrates that the consequence of having a factor of safety of less than 1.0 against triggering "liquefaction" (i.e., $r_u = 100\%$ or a maximum shear strain of 3.5% in this plot) is much more severe for loose sands than for dense sands.

The maximum shear strains that occur at low factors of safety against liquefaction tend toward limiting values (for practical purposes) that decrease as the relative density of the sand increases. This relationship between limiting shear strains and $(N_1)_{60}$ values is given in the upper portion of Figure 95. The hatched zone in this figure represents the range estimated by Seed et al. (1984) for earthquake loading conditions. That range is based on the consideration of several sources of information, including laboratory test results for sand samples obtained via frozen sampling techniques (Yoshimi et al. 1994) and expert opinions about the influences of laboratory test limitations (e.g., natural versus reconstituted soils and stress and strain nonuniformities that cause unreasonably large strains in certain cases) (Seed 1979b).

The maximum shear strains that are expected for various combinations of earthquake-induced CSR and $(N_1)_{60cs}$ values can then be plotted alongside liquefaction correlations, as shown in Figure 95b

For more monographs, publications, or videos, visit http://www.eeri.org

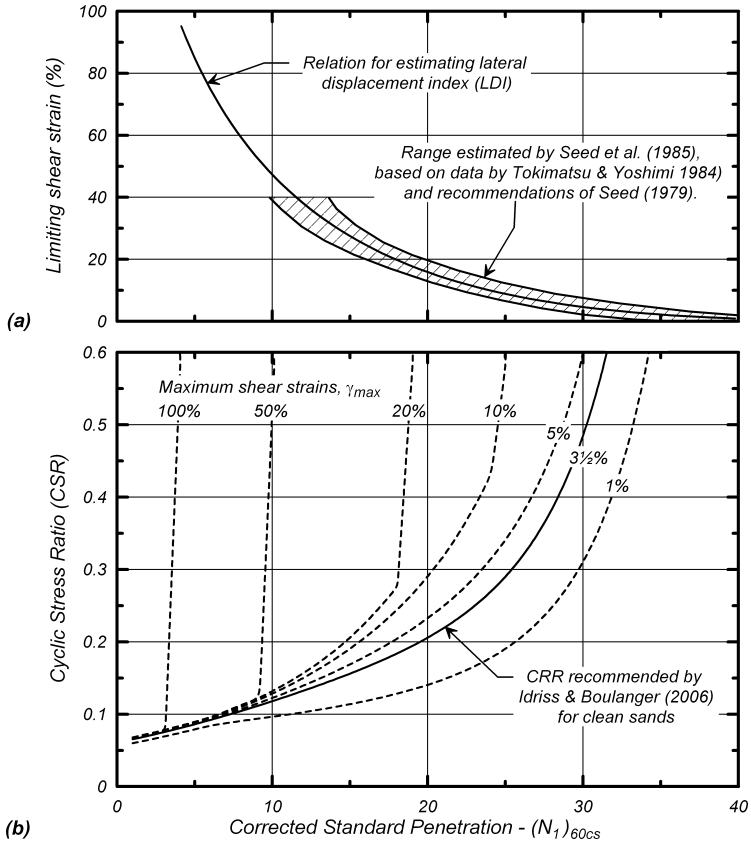

Figure 95. SPT-based liquefaction correlations for clean sands with M = 7.5 and $\sigma'_{vc} = 1$ atm: (a) limiting shear strains and (b) contours of maximum shear strains.

for the SPT and Figure 96 for the CPT. These figures were generated by combining the relationship from Figure 94, subject to the limiting strain values from Figure 95a, with the CRR-$(N_1)_{60cs}$ and CRR-q_{c1Ncs} relationships presented in Section 3. The use of these relationships for sands having a range of fines content has generally been assumed to be approximately accounted for by the use of the equivalent clean-sand penetration resistances. Shamoto et al. (1998) produced alternative SPT relationships for sands with 0%, 10%, and 20% fines, and the differences among these relationships are relatively minor when the overall accuracy of the methodology is considered. For practical

For more monographs, publications, or videos, visit http://www.eeri.org

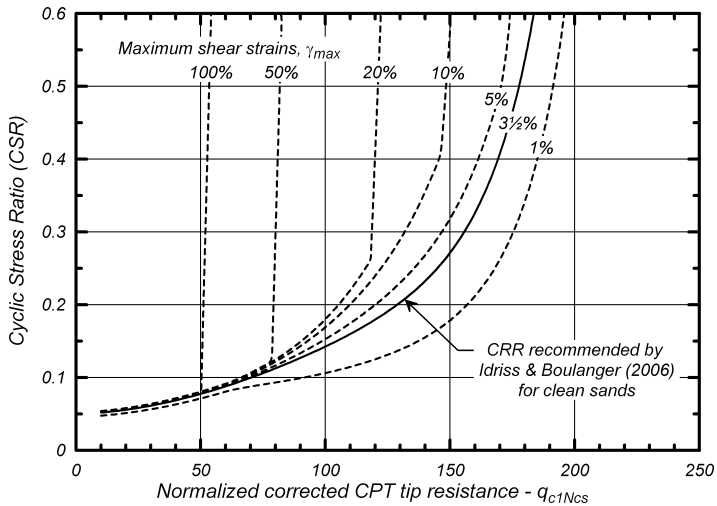

Figure 96. CPT-based liquefaction correlation for clean sands with M = 7.5 and $\sigma'_{vc} = 1$ atm, showing contours of maximum shear strains.

purposes, the use of a single CSR-$(N_1)_{60cs} - \gamma_{\max}$ (or CSR-$q_{c1Ncs} - \gamma_{\max}$) relationship for various fines content as shown in Figures 95 and 96 is considered a reasonable approximation.

The above relationship among maximum shear strain, CSR, and SPT $(N_1)_{60cs}$ is compared with similar relationships recommended by Tokimatsu and Asaka (1998) and Wu (2002) in Figure 97. Figure 97 compares the curves for maximum shear strains of 5%, 20%, and 50%. The spread among these different relationships, as well as the scatter in the Figure 94 data, indicate the uncertainty inherent in these types of generalized relationships.

The lateral spreading displacement that is calculated by integrating maximum shear strains versus depth represents a measure of the potential maximum displacement, for which Zhang et al. (2004) suggested the term "lateral displacement index" (LDI). The value of LDI is then computed as

$$\mathrm{LDI} = \int_0^{z_{\max}} \gamma_{\max} \cdot dz \tag{85}$$

where the maximum shear strains can be estimated by using the above relationships. A sample spreadsheet calculation of LDI is described

For more monographs, publications, or videos, visit http://www.eeri.org

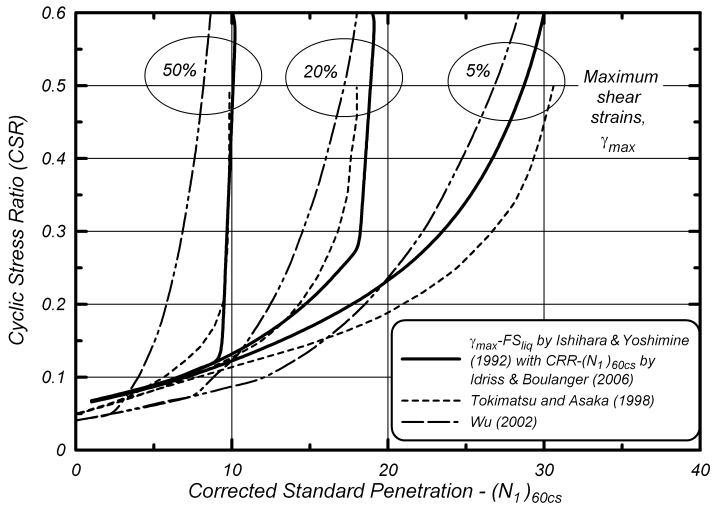

Figure 97. Comparison of the relationship among CSR, SPT $(N_1)_{60cs}$, and maximum shear strain for three levels of maximum shear strain.

in Section 4.5. Actual lateral displacements that occur will depend on several other factors, as previously noted (e.g., ground slope, spatial heterogeneity, distance from a free face, and restraint from embedded structures).

For spreadsheet calculations, the limiting shear strain (γ_{lim}) corresponding to about the midrange of the hatched zone in Figure 95 can be approximated as

$$\gamma_{\text{lim}} = 1.859 \left(1.1 - \sqrt{\frac{(N_1)_{60cs}}{46}}\right)^3 \geq 0 \tag{86}$$

This expression for γ_{lim} can also be expressed as a function of D_R or CPT penetration resistances by using the previously presented correlations between penetration resistances and D_R. The corresponding equations become

$$\gamma_{\text{lim}} = 1.859\,(1.1 - D_R)^3 \geq 0 \tag{87}$$

and

$$\gamma_{\text{lim}} = 1.859 \left(2.163 - 0.478\,(q_{c1Ncs})^{0.264}\right)^3 \geq 0 \tag{88}$$

For more monographs, publications, or videos, visit http://www.eeri.org

At very low relative densities, equations 86–88 indicate very large maximum shear strains consistent with the expectation that unlimited shear strains may develop if the residual shear strength is low enough that a flow slide (instability) develops. However, the effect of a single low $(N_1)_{60cs}$ value can be overstated by the one-dimensional approximation underlying the LDI calculation, and thus the value of γ_{lim} may also be limited to about 50% for computing LDI from individual borings or soundings. If loose sands are pervasive at a site, then the computed LDI will probably still be large, and the potential for instability must be checked separately.

The maximum shear strain for a given factor of safety against liquefaction can then be estimated by combining expressions that approximate the curves in Figure 94 (e.g., Yoshimine et al. 2006) with the additional constraint of a limiting shear strain (Figure 95).

$$F_\alpha = 0.032 + 4.7\, D_R - 6.0\, (D_R)^2 \tag{89}$$

$$\gamma_{\max} = 0 \quad \text{if} \quad FS_{liq} \geq 2 \tag{90}$$

$$\gamma_{\max} = \min\left(\gamma_{\text{lim}}, 0.035\,(2 - FS_{\text{liq}})\left(\frac{1 - F_\alpha}{FS_{\text{liq}} - F_\alpha}\right)\right)$$
$$\text{if} \quad 2 > FS_{\text{liq}} > F_\alpha \tag{91}$$

$$\gamma_{\max} = \gamma_{\text{lim}} \quad \text{if} \quad FS_{\text{liq}} \leq F_\alpha \tag{92}$$

The D_R should be limited to values ≥ 0.4 for use in equation 89. These expressions can similarly be used with SPT and CPT penetration resistances by substituting the correlations with D_R into the term F_α as

$$F_\alpha = 0.032 + 0.69\sqrt{(N_1)_{60cs}} - 0.13\,(N_1)_{60cs} \tag{93}$$

with $(N_1)_{60cs}$ limited to values ≥ 7 for use in this expression, and

$$F_\alpha = -11.74 + 8.34\,(q_{c1Ncs})^{0.264} - 1.371\,(q_{c1Ncs})^{0.528} \tag{94}$$

with q_{c1Ncs} limited to values ≥ 69 for use in this expression.

A key step in estimating lateral spreading displacements is accounting for the effects of site heterogeneity, especially in complex depositional environments or with limited site characterization data. For example, consider the schematic in Figure 98. It shows an existing building and pipeline along a shoreline, with the site having been characterized by eight borings around the building perimeter. The LDI may be computed for each of the borings individually and then depicted as vectors in the plan view, as shown in Figure 98a.

For more monographs, publications, or videos, visit http://www.eeri.org

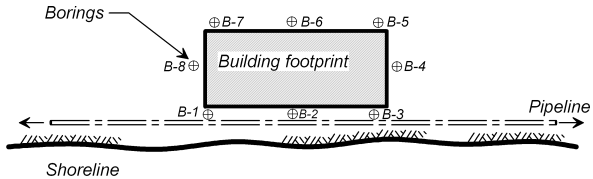

(a) Plan view of a building footprint and boring locations

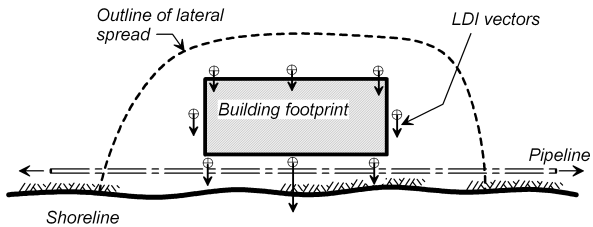

(b) Case I - liquefiable layer identified at all borings

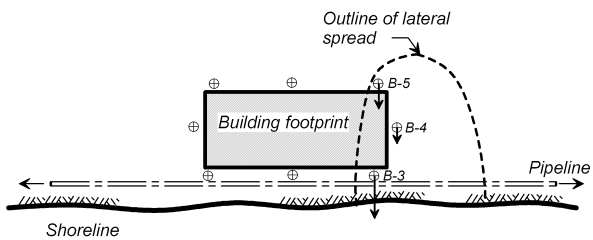

(c) Case II - liquefiable layer identified at borings 3, 4 and 5

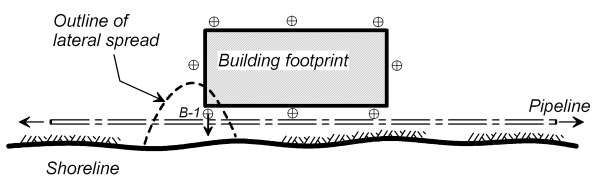

(d) Case III - liquefiable layer identified at boring 1 only

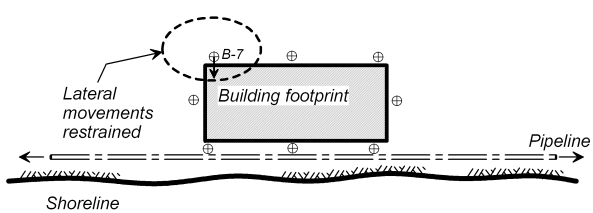

(e) Case IV - liquefiable layer identified at boring 7 only

Figure 98. Schematic of how the interpretation of LDI vectors at borings around an existing building may relate to potentially different extents of lateral spreading.

In Case I (Figure 98b), all the borings indicated a significant potential for lateral spreading (via their LDI values), and thus a lateral spread might be expected to encompass the entire building.

In Case II (Figure 98c), only borings 3, 4, and 5 along one side of the building indicated a significant potential for lateral spreading displacements, whereas the other borings indicated that no liquefaction would be expected. In this case, the lateral spreading may be more localized, but it may still damage the building. In characterizing the liquefiable layer, it could have been unconservative to have included data from the other borings. That is, if the data from all borings were plotted together and the profile were characterized via some percentile value of the penetration resistances, then the other borings would have given the impression of a denser representative condition.

In Case III (Figure 98d), only boring 1 identifies a potentially liquefiable layer and may identify the potential for an even more localized lateral spread that extends under the building corner. In this case, the lateral spread would be correctly characterized only by the single boring, and any averaging with other borings would clearly have been misleading. Case III is also an important situation to consider when evaluating the pipeline's vulnerability, because the prediction of liquefaction at any one boring along its alignment could indicate a localized lateral spread that could impair the pipeline.

In contrast, consider Case IV (Figure 98e), in which liquefaction is predicted only within a limited depth interval at boring 7 (on the landward side of the building) and not at any other boring location. It would be reasonable to conclude that liquefaction in a localized pocket at boring 7 may lead to building settlement but not significant lateral spreading at the site.

The variation of maximum shear strains with depth can also affect whether they are fully manifested as lateral spreading displacements at the ground surface. Chu et al. (2006) analyzed a number of case histories involving lateral spreading toward a free face of height H_{ff} (about 3 m) and concluded that the computation of LDI could be restricted to a maximum depth of $z_{\max} = 2H_{ff}$, because the soils at larger depths (e.g., more than H_{ff} below the bottom of the adjacent channel) would be sufficiently constrained against lateral movements that they would contribute relatively little to lateral movements at the ground surface. This can be a reasonable guideline for some situations, particularly when the loosest strata are included within the limits of $z_{\max}$. It may not be appropriate to fully rely on this guideline,

For more monographs, publications, or videos, visit http://www.eeri.org

however, when H_{ff} is small (e.g., less than about 3 m) or when its strict application causes a large reduction in the computed LDI (e.g., when a thick, loose stratum exists beneath $2H_{ff}$).

Lateral displacements within a laterally spreading mass will also generally decrease with distance from a free face, as has been observed in many case histories. The variation in LDs with distance from the free face (L) has been related to the ratio of L to the depth to the bottom of the liquefied layer (H) by Youd et al. (2002) and Zhang et al. (2004) and to the magnitude of the lateral displacement at the free face (LD_o), excluding the effects of any local instabilities at the free face, by Tokimatsu and Asaka (1998). Taken together, these data and relationships suggest that the LD may be expected to reduce to about half of the LD_o at a distance of $L/H \approx 5$–20 and to less than about 20% of the LD_o at a distance of $L/H \geq 20$, if the lateral spread is that large. Patterns of displacements at many sites are, however, more strongly controlled by local instabilities near the free faces, the influence of embedded structures, and the presence of geologic or hydrogeologic controls (e.g., Holzer and Bennett 2007). For these reasons, it is useful to map LDI values as illustrated in Figure 98 and interpret the expected pattern of displacements, after which the representative values of LDI may be adjusted for the effect of distance from a free face.

Empirical calibrations of LDI procedures against case histories have also been presented by Shamoto et al. (1998), Tokimatsu and Asaka (1998), Zhang et al. (2004), and Faris et al. (2006), in which adjustment factors were derived that depend primarily on geometric considerations (Shamoto et al.1998, Tokimatsu and Asaka 1998, Zhang et al. 2004) or static shear stress ratio and earthquake magnitude (Faris et al. 2006). The adjustment factors depend on the underlying procedures for computing LDI, and thus the adjustment factors derived with one set of procedures cannot be generalized for use with other procedures. In many situations, the uncertainty in estimating lateral displacements will be dominated by geologic heterogeneity, site characterization limitations, and the many other approximations inherent in the prediction of liquefaction triggering and computation of an LDI. Despite these uncertainties, the LDI values from a set of borings and soundings at a site provide valuable insight for judging the spatial distribution and progressive increase in ground displacements with varying levels of seismic demand, as are illustrated by examples in Section 4.5.

For more monographs, publications, or videos, visit http://www.eeri.org

Empirical Relationships

Empirical models for lateral spreading displacements have been developed by using regression techniques with compiled data from lateral spreading case histories. Table 6 summarizes the input variables used by three of these types of empirical models. The seismic loading is accounted for in all three models by including the

Table 6 Empirical models for lateral spreading displacements and their input variables.

Bartlett and Youd (1995), Youd et al. (2002)

M = earthquake moment magnitude
R = nearest horizontal distance from the site to the seismic energy source
T_{15} = cumulative thickness of saturated granular layers with $(N_1)_{60} < 15$
F_{15} = average fines content (% passing a No. 200 sieve) within the T_{15} soils
$D50_{15}$ = median grain size for granular soils within T_{15}
W = height of the free face (H) divided by the distance (L) from the base of the free face to the point of interest
S = ground slope for sites without a free face

Rauch and Martin (2000)

M = earthquake moment magnitude
R = nearest horizontal distance to the surface projection of a fault rupture or zone of seismic energy release
$a_{\max}$ = peak horizontal surface acceleration that would occur in the absence of excess pore pressures
T_d = duration between the first and last occurrence of surface acceleration ≥ 0.05 g
L_{slide} = maximum horizontal length of a lateral spread in the prevailing direction of movement
S_{top} = average slope across the surface of a lateral spread, from head to toe
H_{face} = height of the free face, measured vertically from the toe to the crest of the free face
$Z_{FS\min}$ = average depth to the minimum factor of safety in potentially liquefiable soil
Z_{liq} = average depth to the top of liquefied soil

Bardet et al. (2002a)

M = earthquake moment magnitude
R = nearest horizontal distance from the site to the seismic energy source
T_{15} = cumulative thickness of saturated granular layers with $(N_1)_{60} < 15$
W = height of the free face (H) divided by the distance (L) from the base of the free face to the point of interest
S = ground slope for sites without a free face

For more monographs, publications, or videos, visit http://www.eeri.org

earthquake moment magnitude and a measure of distance to the earthquake source as input variables, whereas the model by Rauch and Martin (2000) also includes the peak ground surface acceleration and shaking duration. The topographic conditions are accounted for in all three models by including measures of the ground surface slope, height of a free face, and length of the lateral spread (or distance from the free face to the point of interest). Subsurface soil conditions are accounted for differently by the three models: Bardet et al. (2002a) use only the cumulative thickness (T_{15}) of saturated granular layers with $(N_1)_{60}$ less than 15, Bartlett and Youd (1995) and Youd et al. (2002) use T_{15} along with the average fines content and median grain size within the T_{15} soils, and Rauch and Martin (2000) use the average depth to the top of the liquefied soil and the average depth to the minimum factor of safety against liquefaction.

The accuracy of these empirical models, which are roughly comparable, is illustrated by the results for the Youd et al. (2002) model in Figure 99, which shows measured versus computed lateral spreading displacements. The majority of the data fall within a factor of 2 from

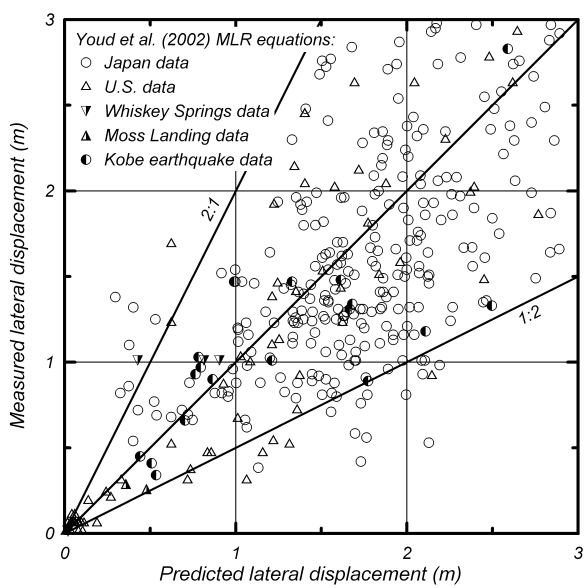

Figure 99. Measured versus predicted displacements for the empirical multilinear regression model by Youd et al. (2002).

For more monographs, publications, or videos, visit http://www.eeri.org

the predicted values, although there are numerous cases with much larger differences.

These current empirical models are based on databases that do not cover the full range of conditions encountered in practice, and the forms of the models are not constrained by any theoretical basis for extrapolation beyond that database. The use of these models therefore requires full awareness of the limits of the supporting case history database.

Newmark Sliding Block Analysis

Ground surface displacements may also be computed by using a Newmark sliding block type of analysis, wherein the soil mass is assumed to incrementally slide (displace) when the shaking-induced inertial forces cause the total shear stress to exceed the available shear strengths (Newmark 1965, Goodman and Seed 1966). The slide mass will slip in relation to the underlying base soils whenever the total shear forces (static plus inertial forces) exceed the available shear resistances from the soils. The inertial force at yield (the onset of sliding) is described by the yield acceleration (a_y), which is simply the inertial force at yield divided by the slide mass. The sample Newmark sliding block type of analysis in Figure 100 is for a case in which the yield acceleration was modeled as decreasing during the process of shaking.

There are coupled and decoupled methods for performing the sliding block calculation, and each is suited to different types of applications. The coupled method explicitly includes the effects of sliding on the dynamic response of the soil mass above the slip surface, and it directly solves for the relative slip along the slip surface. In the coupled analysis, the shear stress (static plus dynamic) on the slip surface is limited by the soil's shear strength, and the maximum inertial force (or equivalent average acceleration) of the sliding mass is limited by the yield acceleration. The decoupled method computes the dynamic response of the soil column without including slip along the failure surface, and therefore the computed maximum inertial force (or equivalent average acceleration) can exceed the value at the yield acceleration. In a decoupled analysis, the relative slip (normally constrained to one direction only) is then computed by double-integrating the difference between the computed acceleration for the slide mass and its yield acceleration. The decoupled method has been used, for example, in combination with equivalent-linear dynamic finite element analyses that cannot directly model permanent deformations.

For more monographs, publications, or videos, visit http://www.eeri.org

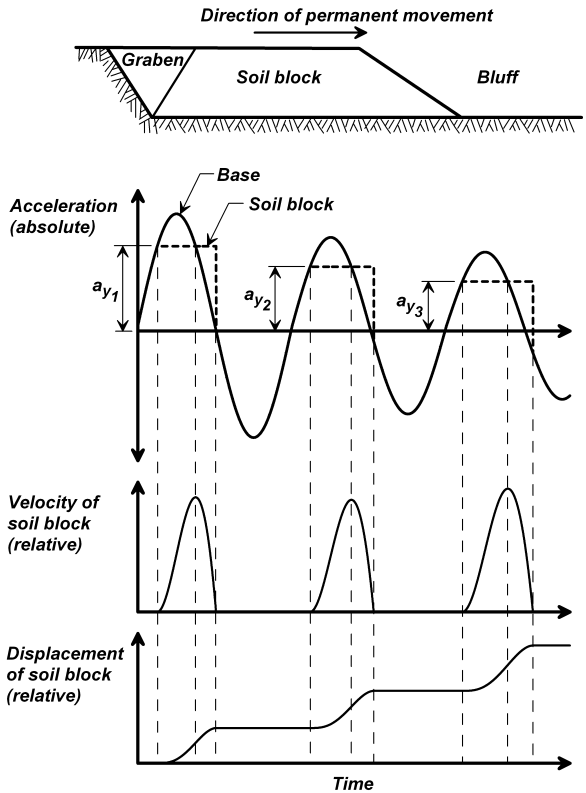

Figure 100. Schematic of a Newmark sliding block analysis, with the soil's shear strength and corresponding yield acceleration decreasing during shaking (after Idriss 1985, adapted from Goodman and Seed 1966, with permission from ASCE).

Differences in the displacements computed via coupled and decoupled methods depend on the characteristics of the soil mass and ground motions (e.g., Lin and Whitman 1983, Gazetas and Uddin 1994, Kramer and Smith 1997, Rathje and Bray 2000). The decoupled method produces reasonable estimates of displacements for many practical situations, given the uncertainties in other aspects of the analysis. Note that the coupled and decoupled methods produce identical results if the slide mass is considered to behave rigidly.

A number of researchers have developed regression models for the magnitude of the sliding block displacement when the yield

For more monographs, publications, or videos, visit http://www.eeri.org

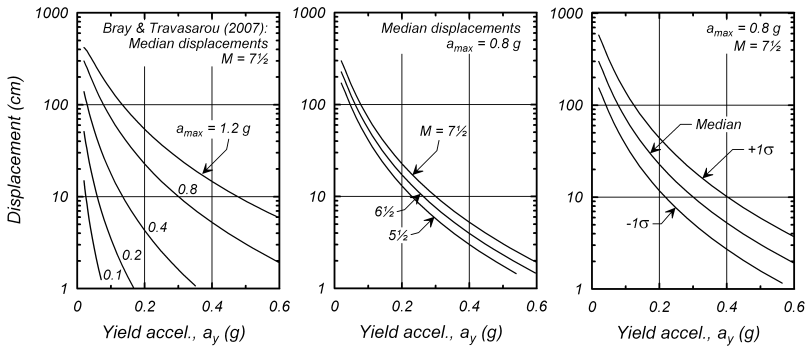

Figure 101. Sliding displacements for an essentially rigid block, on the basis of the regression model of Bray and Travasarou (2007).

acceleration and certain characteristics of the ground motion are given. Ground motion characteristics play a dominant role in these computations, which means that the various relationships proposed over the years depend considerably on the database of ground motion recordings that were available at the time. The model by Bray and Travasarou (2007), which was based on a very large set of ground motion records, was used to generate the plots in Figure 101, which shows the influence of various parameters on the computed displacements for one-way sliding of an essentially rigid soil mass. Figure 101a shows median displacements for an M = 7.5 earthquake for a range of peak accelerations and yield accelerations. Figure 101b shows that, for the same peak acceleration and yield acceleration, the slip displacements increase with increasing earthquake magnitude (which reflects the influence of earthquake magnitude on duration and frequency content). Figure 101c shows that variability in ground motion characteristics, even at the same earthquake magnitude and peak ground acceleration, has a very large effect on sliding displacements. For example, the $\pm 1\sigma$ results correspond to displacements that are 1.93 and 0.52 times the median value.

Sliding block models are a crude approximation of the deformation processes that occur as a consequence of liquefaction. The underlying assumptions of rigid-plastic shear resistance and slip along a discrete sliding surface have little resemblance to the actual deformation mechanisms in most situations. Lateral spreading problems are particularly challenging, with additional complications arising from

For more monographs, publications, or videos, visit http://www.eeri.org

the low levels of driving shear stress beneath mildly sloping ground and the sensitivity of analytical results to the assumed residual shear strengths. For these and other reasons, it is not very common to use sliding block models for lateral spreading problems. Sliding block models do, however, have the advantage of being easily extended to the analysis of slopes or embankments where failure surfaces may pass through both liquefied and nonliquefied soils and may also be influenced by restraining forces from structural elements (e.g., pile foundations). Newmark sliding block models are useful for obtaining an approximate estimate of the expected deformations.

Nonlinear Analyses

Nonlinear dynamic analyses, using finite element or finite difference methods, provide a powerful tool for evaluating the effects of liquefaction on structures. These types of analyses require a high level of expertise with computational methods and considerable effort to perform, but they are often invaluable for addressing complex problems and are increasingly being used on larger projects. Coverage of this important aspect of liquefaction analysis is, however, beyond the scope of this monograph.

The accuracy of any nonlinear analysis depends directly on the site characterization, its simplified representation for analysis, the correlations used to derive soil properties from in-situ test data, the details of the constitutive models and their numerical implementation, the importance of phenomena that are not included in the numerical model (e.g., ground cracking or water films), and the selection of input ground motions. For these reasons, the sophistication of a nonlinear analysis does not necessarily translate into a high degree of accuracy in predicting deformations.

Nonetheless, nonlinear analyses make it possible to investigate complex interaction mechanisms that are otherwise difficult to assess. For example, nonlinear analyses can assess the sensitivity of earth dam deformations to varying extents of ground improvement in the dam's foundation or assess the dynamic interaction between pile foundations and laterally spreading ground. Nonlinear analyses are particularly valuable for identifying likely patterns of deformation and how they might affect the performance of a structure. In such cases, nonlinear analyses, which should always include appropriate sensitivity studies, can provide valuable insight for more refined decision making, even if the final estimates of ground deformations are still uncertain.

For more monographs, publications, or videos, visit http://www.eeri.org

Judgment in Estimating Lateral Spreading Displacements

None of our available analytical methods capture or account for all the physical mechanisms that influence lateral spreading, and undoubtedly this further limits such methods' ability to accurately predict displacements. Using a more rigorous model does not guarantee more accuracy, because the practical limitations in our ability to accurately characterize natural deposits, the complexity of localization processes (e.g., water film formation and ground cracking), and the inherent uncertainty in ground motion characteristics may dominate the overall uncertainty in any lateral spreading prediction.

The final estimation of ground surface displacements in an area or earth structure affected by liquefaction can benefit from calculating the expected displacements via more than one approach, evaluating the computed displacements' sensitivity to the input parameters, considering how the limitations of each method relate to the situation at hand, considering the site's similarity to case histories, and exercising appropriate engineering judgment. The final estimate of ground surface displacement should be conveyed to all affected parties as being unavoidably approximate. The ground displacement consequences for any overlying or embedded structures will affect the degree of conservatism that is required in dealing with the uncertainty in the estimated ground surface displacements.

4.4 Post-liquefaction Reconsolidation Settlement

Vertical displacements can develop in two primary ways: (1) settlement caused by reconsolidation of the liquefied soil and (2) vertical displacements caused by shear deformation of the soil associated with lateral spreading. This section addresses only settlement caused by reconsolidation. The potential effect of vertical displacements caused by shear deformation of the soil, however, must be recognized as potentially dominating in areas of lateral spreading.

The post-liquefaction reconsolidation strains are computed by using relationships that are largely derived from laboratory studies but which have been found to provide reasonably good agreement with field observations (Lee and Albaisa 1974, Tokimatsu and Seed 1987, Ishihara 1996). One approach was developed by Ishihara and Yoshimine (1992), who observed that the volumetric strains that occur during post-liquefaction reconsolidation of sand samples were directly related to the maximum shear strains that developed during undrained cyclic loading and to the initial relative density of the

For more monographs, publications, or videos, visit http://www.eeri.org

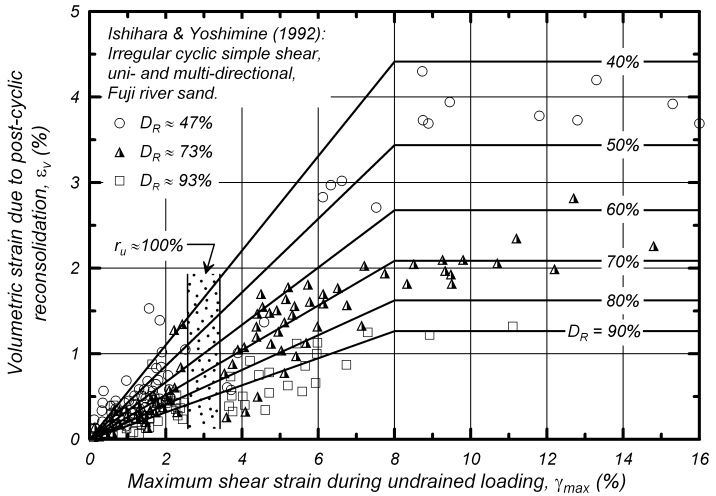

Figure 102. Relationship between post-liquefaction volumetric strain and the maximum shear strain induced during undrained cyclic loading of clean sand (after Ishihara and Yoshimine 1992).

sand, as illustrated in Figure 102. Their recommended relationships can be reasonably approximated by using the following expression (Yoshimine et al. 2006):

$$\varepsilon_v = 1.5 \cdot \exp\left(-2.5 D_R\right) \cdot \min\left(0.08, \gamma_{\max}\right) \tag{95}$$

in which both D_R and shear strain are in decimal. This equation can also be expressed in terms of SPT and CPT penetration resistances, as follows:

$$\varepsilon_v = 1.5 \cdot \exp\left(-0.369\sqrt{(N_1)_{60cs}}\right) \cdot \min\left(0.08, \gamma_{\max}\right) \tag{96}$$

or

$$\varepsilon_v = 1.5 \cdot \exp\left(2.551 - 1.147\left(q_{c1Ncs}\right)^{0.264}\right) \cdot \min\left(0.08, \gamma_{\max}\right) \tag{97}$$

with q_{c1Ncs} limited to values ≥ 21 for use in this expression.

These results can be coupled with those in Figure 94 to arrive at a relationship between post-liquefaction volumetric strains and the factor of safety against liquefaction for different initial relative densities. The plot in Figure 103 was produced this way by Ishihara and Yoshimine (1992), although it should be noted that the strict coupling

For more monographs, publications, or videos, visit http://www.eeri.org

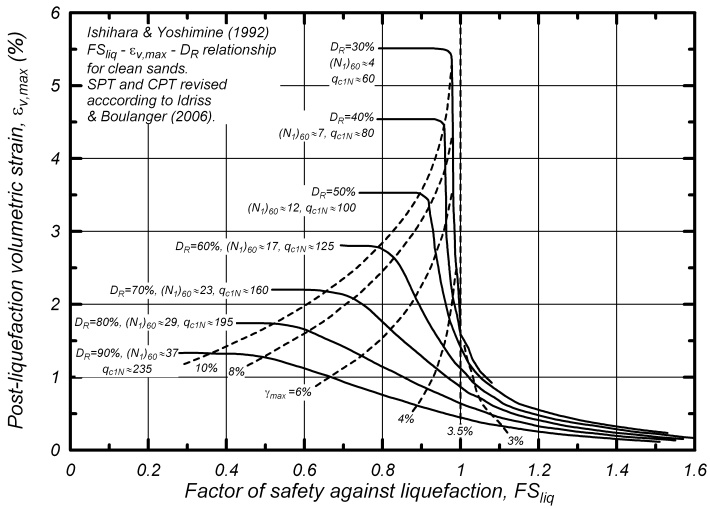

Figure 103. Post-liquefaction volumetric strains versus the factor of safety against triggering of liquefaction (r_u = 100%) for clean sands of different initial relative densities (after Ishihara and Yoshimine 1992).

of the prior two relationships would produce sets of curves that cross over each other near a factor of safety of unity. Correlations with relative density were used to assign SPT and CPT penetration resistances to each curve.

The post-liquefaction volumetric strains (ε_v) for various combinations of earthquake-induced CSR and $(N_1)_{60cs}$ values can now be plotted along with the liquefaction correlations, as shown in Figure 104 for the SPT and Figure 105 for the CPT. These figures were generated by combining the relationships from Figure 94 and Figure 102 with the CRR-$(N_1)_{60cs}$ and CRR-q_{c1Ncs} relationships presented in Section 3.10. As discussed for shear strains, the use of these relationships for sands having a range of fines contents is approximately taken into account by the use of the equivalent clean sand penetration resistances. This approximation is considered reasonable for practical purposes.

The above relationship among post-liquefaction volumetric strains, CSR, and SPT $(N_1)_{60cs}$ is compared with similar relationships recommended by Shamoto et al. (1998) and Wu (2002) in Figure 106. Figure 106 compares the curves for post-liquefaction volumetric strains of 1%, 3%, and 5%. The spread among these

For more monographs, publications, or videos, visit http://www.eeri.org

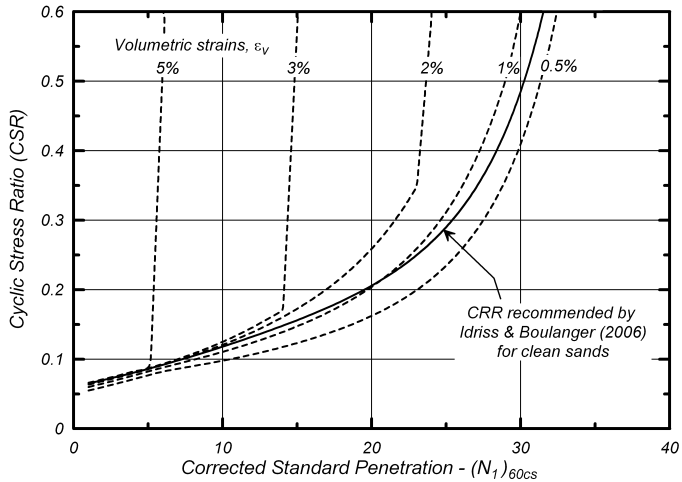

Figure 104. SPT-based liquefaction correlation for clean sands with M = 7.5 and $\sigma'_{vc} = 1$ atm, showing the computed variation of volumetric strains during reconsolidation.

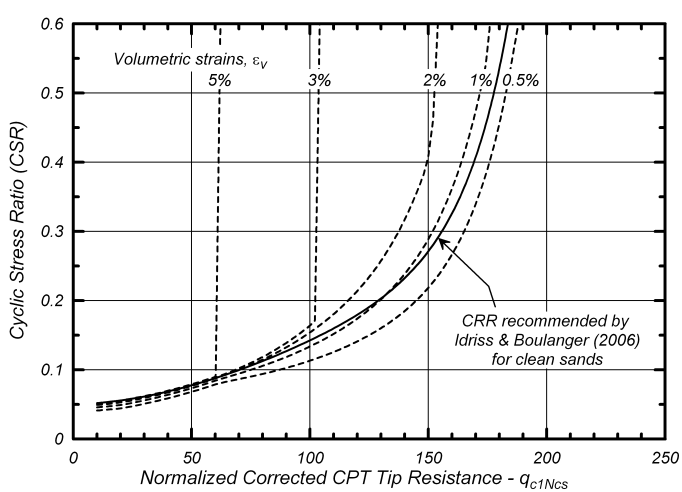

Figure 105. CPT-based liquefaction correlation for clean sands with M = 7.5 and $\sigma'_{vc} = 1$ atm, showing the computed variation of volumetric strains during reconsolidation.

For more monographs, publications, or videos, visit http://www.eeri.org

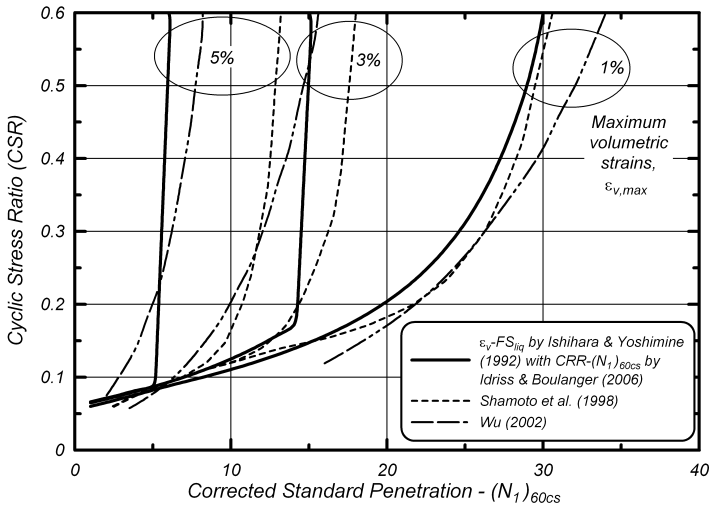

Figure 106. Comparison of the relationships among CSR, SPT $(N_1)_{60cs}$, and maximum volumetric strain for three levels of maximum volumetric strain.

different relationships, as well as the scatter in the Figure 103 data, indicate the uncertainty inherent in these types of generalized relationships.

The ground surface settlement for one-dimensional reconsolidation (i.e., no lateral spreading movements) is then computed by equating the vertical strains to the volumetric strains (as is appropriate for one-dimensional reconsolidation) and then integrating the vertical strains over the depth interval of concern:

$$S_{v-1D} = \int_0^{z_{\max}} \varepsilon_v \cdot dz \tag{98}$$

The consequences of one-dimensional post-liquefaction reconsolidation settlement depend on the spatial distribution of liquefied zones and the type of structure being evaluated. For example, the discontinuous pockets of liquefied sand beneath the building on spread footings in Figure 93a could cause an erratic pattern of ground surface settlement. The worst scenario in this case is the occurrence of a liquefied pocket immediately below one spread footing that subsequently settles significantly (perhaps aggravated by a bearing failure instability) while an adjacent spread footing hardly settles at all. Such a scenario produces the worst estimate of differential settlement for the

For more monographs, publications, or videos, visit http://www.eeri.org

structure's spread footings, which is what most affects the structure's performance, and the potential for such settlement must be considered in design.

The consequences of one-dimensional settlement may, however, be largely mitigated by the presence of a thick nonliquefied layer above the liquefied soils (e.g., Ishihara 1985, Naesgaard et al. 1998, Bouckovalas and Dakoulas 2007). For example, consider the building in Figure 93c; the limited lateral extent of the liquefiable layer and the absence of a nearby free face or channel limits the potential for lateral spreading displacements. A thick nonliquefied layer between the building's footings and the liquefied stratum may act as a bridging layer that arches or redistributes stresses and therefore results in more uniform ground surface settlement. In this manner, a well-constructed building on shallow foundations may settle slightly but not suffer any damage, because the differential settlement is small.

Figure 107 indicates the benefit of a thick nonliquefied surface layer overlying the expected interval of liquefaction, as postulated by Ishihara (1985) by using a number of post-earthquake observations of ground surface damage patterns. Figure 107 distinguishes between ground surface damage and the absence of such damage. As such, the information in this figure can be used to examine the reduction in

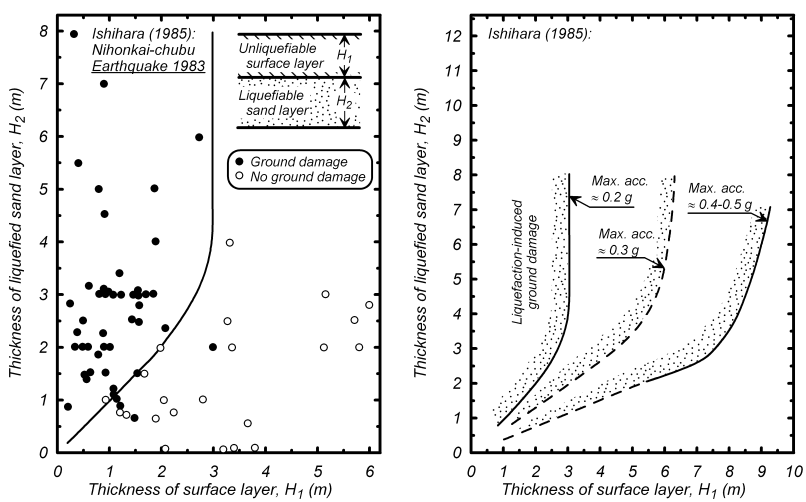

Figure 107. Combinations of nonliquefied surface layer thickness, liquefied layer thickness, and peak ground surface acceleration that distinguish between ground surface damage and the absence of such damage (Ishihara 1985).

For more monographs, publications, or videos, visit http://www.eeri.org

consequences associated with one-dimensional reconsolidation settlement and ground surface distress in areas where there is no lateral spreading. The content of this figure is not applicable where lateral spreading or instability can develop along underlying liquefied strata, such as in Figure 93b, or where transient lateral displacements (lurching) of the overlying crust may impose loads on pile foundations or embedded structures.

The effects of post-liquefaction ground surface settlement are different for structures supported on pile foundations than for structures on shallow foundations. As an example, Figure 108 shows post-liquefaction ground surface settlement around the pile foundations of a rail viaduct on Port Island after the 1995 Kobe earthquake. Ground surface settlement was 30–60 cm in the area shown in the photo, and yet the settlement was sufficiently uniform that no ground surface ruptures or distortions were evident away from the piles. The relative uniformity of settlement is attributable to the approximately 4-m-thick nonliquefied surface layer overlying the relatively uniform loose fill materials that liquefied. Settlement caused by liquefaction in other earthquakes, however, has generally been far less uniform and hence potentially more damaging than at this site.

Figure 108. Liquefaction-induced ground surface settlement around pile-supported viaduct bents on Port Island after the 1995 Kobe earthquake.

For more monographs, publications, or videos, visit http://www.eeri.org

Light buildings supported by shallow foundations on Port Island appeared to be relatively undamaged by the ground settlement. The uniformity of the ground surface settlement produced relatively small differential settlement or angular distortions for these buildings, which explains the absence of significant damage to the buildings.

Larger buildings supported on sufficiently strong pile foundations also appeared to experience relatively small settlement and thus did not suffer any structural damage induced by differential settlement. Nonetheless, the differential ground settlement in the vicinity of buildings caused extensive damage to utility connections and disrupted them. In addition, it is suspected that the settling ground would have induced significant down-drag loads on the piles, which is an aspect that should be considered in designing piles for use in areas of liquefaction.

4.5 Examples of Lateral Displacement and Settlement Calculations

Sample Calculations for Single SPT Borings or CPT Soundings

A sample calculation of the LDI and reconsolidation settlement is presented for the same SPT boring from Moss Landing State Beach that was used in the sample liquefaction analysis shown in Figure 83 and Appendix A. The analytical steps include computing the maximum shear strains and volumetric strains, which makes it possible to compute the LDI and one-dimensional reconsolidation settlement (S_{v-1D}) at the same time. The spreadsheet computation of these quantities is in Appendix C, showing primarily the steps that must be added to those in Appendix A. The computed strains are then plotted versus depth in Figure 109. For this example, the interval at depths of 1.8–5.2 m has an average volumetric strain of about 4%, the interval at depths of 10.0–11.9 m has an average volumetric strain of about 3%, and the other intervals have considerably smaller expected strains. Thus the expected one-dimensional reconsolidation settlement of 0.22 m is largely due to the computed changes in thickness for these two depth intervals—that is, $(0.04)(3.4\text{ m}) + (0.03)(1.9\text{ m}) = 0.19\text{ m}$.

The sensitivity of the predicted ground deformations to various parameters should be evaluated as part of the analysis. For example, the effect of peak horizontal ground surface acceleration ($a_{\max}$) on the computed LDI and one-dimensional reconsolidation settlement (S_{v-1D}) is shown in Figure 110 for two locations at the Moss Landing State Beach during the 1989 Loma Prieta earthquake. The results for

For more monographs, publications, or videos, visit http://www.eeri.org

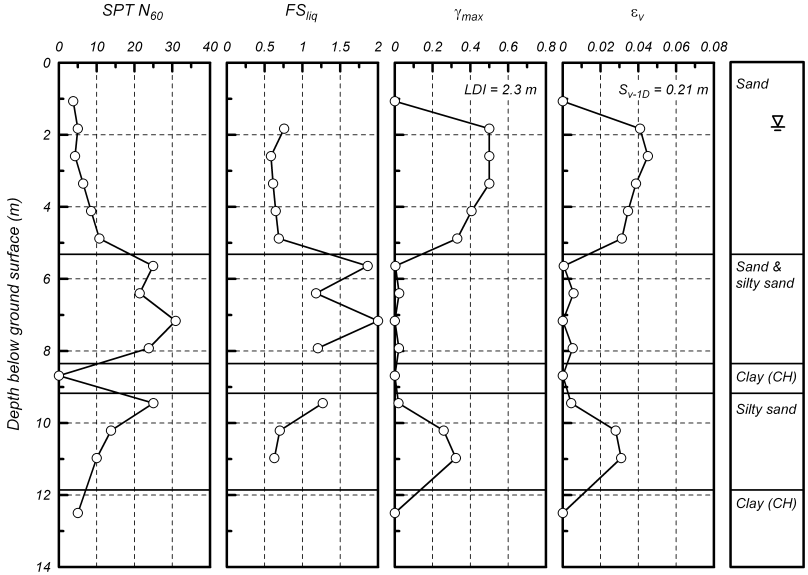

Figure 109. Sample analysis of LDI and one-dimensional reconsolidation settlement for a single SPT boring.

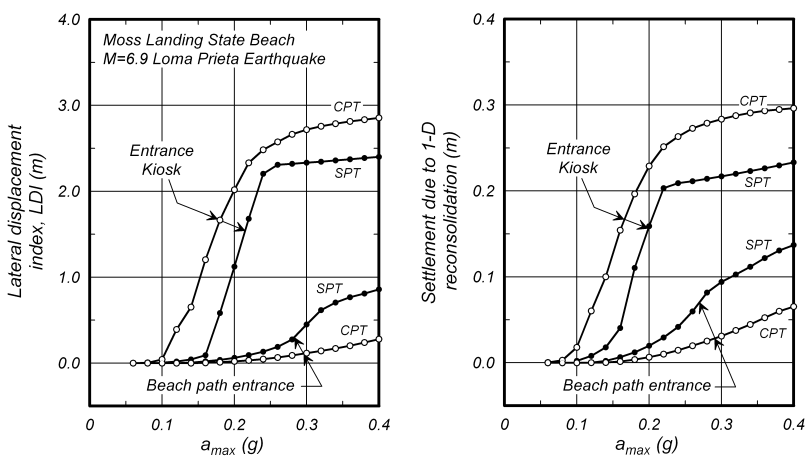

Figure 110. Effect of peak ground acceleration on the computed LDI and S_{v-1D} at two locations along the Moss Landing State Beach access road during an M = 6.9 earthquake.

For more monographs, publications, or videos, visit http://www.eeri.org

the entrance kiosk are for the same SPT boring in Figure 109 and the adjacent CPT sounding in Figure 84. The results for this CPT are slightly more conservative in predicting larger displacements for similar levels of shaking, but overall both the SPT and CPT analyses show that displacements are negligible for $a_{max} < 0.12$ g and that the potential displacements become less sensitive to the shaking level for a_{max} values greater than about 0.25 g at this site. Both the SPT and CPT results at the beach path entrance show substantially smaller potential displacements and settlement than at the entrance kiosk, and the SPT results are more conservative than the CPT in this case. At this site, the earthquake produced peak ground accelerations of about 0.25–0.30 g and caused substantially greater ground displacements at the entrance kiosk than at the beach path entrance, as shown in Figure 111. The calculated indices of displacement potential (LDI and S_{v-1D}) provide a reasonable estimate of both the observed magnitudes of displacements and the differences in displacements observed at these two locations, which are near each other.

Computed LDI Values from SPT Borings and CPT Soundings across a Site

The Moss Landing Marine Laboratory, which experienced liquefaction-induced lateral spreading displacements of 1–2 m during the 1989 Loma Prieta earthquake, provides an illustrative example of the use of computed LDI values. The laboratory was on a spit between Monterey Bay and the Old Salinas River slough, as shown in Figure 112. Subsurface conditions across the southern side of the building, with penetration resistances from SPT borings and CPT soundings, are shown in Figure 113. The building foundation experienced 1.0–1.3 m of extension perpendicular to the spit, and lateral displacements along the Old Salinas River shoreline side of the building were 0.6–1.4 m. The measured displacements and the computed LDI values for individual SPT borings and CPT soundings across the site are shown as vectors in Figure 112 (the direction of a computed LDI vector is presumed to be toward the closest shoreline). Computed LDI values ranged from very small (0.04 m) near the northwest corner of the building to very large (4.3 m) near the midpoint of the southern side of the building, with about two-thirds of the LDI values being 0.6–2.2 m.

Interpreting these computed LDI values requires consideration of the spatial distribution of the liquefied zones, as schematically illustrated in Figures 93 and 98. The analytical results for the various SPT

For more monographs, publications, or videos, visit http://www.eeri.org

(a)

(b)

Figure 111. Liquefaction-induced ground deformations caused by the 1989 Loma Prieta earthquake at two locations along the Moss Landing State Beach access road: (a) entrance kiosk and (b) beach path entrance.

For more monographs, publications, or videos, visit http://www.eeri.org

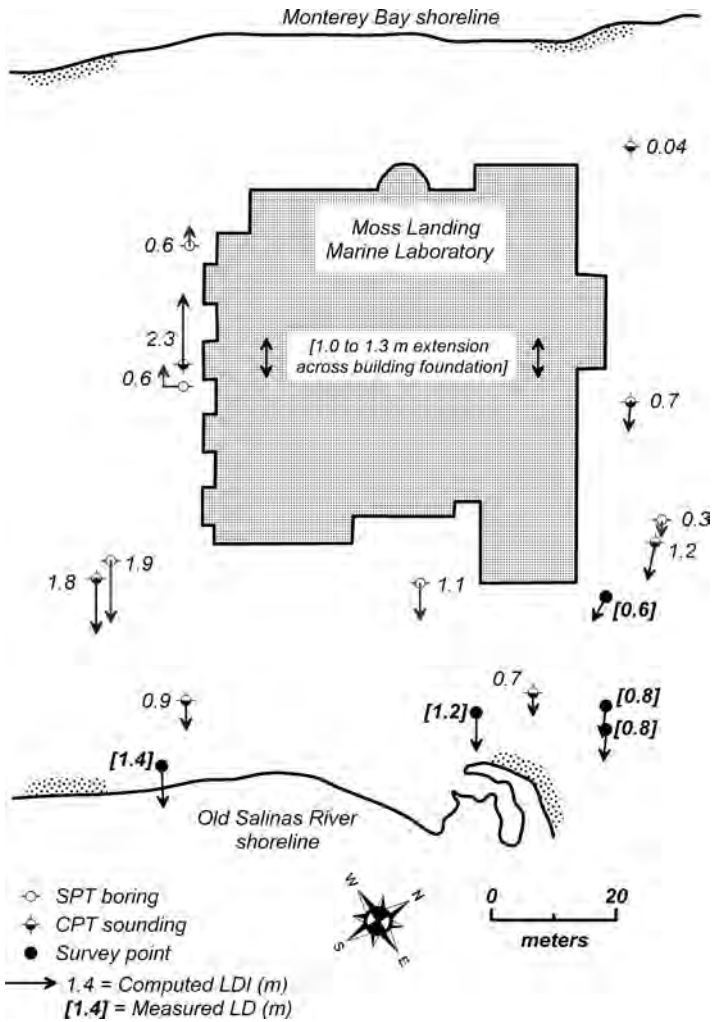

Figure 112. Computed LDI and measured lateral displacements at the Moss Landing Marine Laboratory for the 1989 Loma Prieta earthquake.

borings and CPT soundings showed that liquefaction was expected in the same major strata and thus formed layers that were continuous enough to facilitate lateral spreading across the site. The building is about 25 m from the bay shoreline and 40 m from the Old Salinas River shoreline, and the expected depth of liquefaction is about

For more monographs, publications, or videos, visit http://www.eeri.org

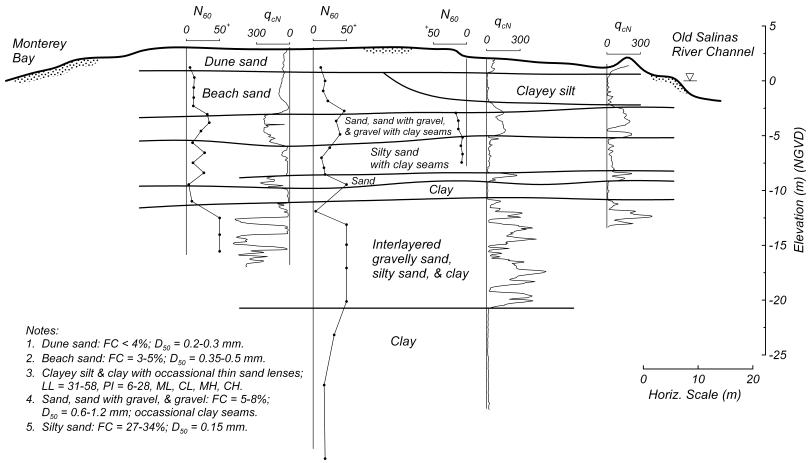

Figure 113. Subsurface profile across the southern side of the Moss Landing Marine Laboratory (Boulanger et al. 1997).

12 m, which gives L/H ratios of about 2.0–3.3. For this site, lateral spreading displacements can be expected to decrease with distance from the shorelines and must, in fact, become zero at the point where the direction of spreading switches from eastward to westward. An adjustment to the LDI values for distance from the free faces does not seem warranted, however, given the relatively small L/H ratios and the difficulty in confidently predicting displacement directions across the building foundation. The computed LDI vectors without any adjustments provide a reasonable representation of the observed pattern of lateral spreading at the site and the 1.0–1.3 m of building foundation extension in the east-west direction (Figure 112).

4.6 Margin of Safety

The desired margin of safety against unacceptable performance from liquefaction depends on the uncertainty in the estimated performance, the consequences of unacceptable performance, and the acceptable level of risk. With regard to the expected performance, ground deformations are often a primary concern.

Different types of liquefaction problems dictate that the margin of safety be addressed in slightly different ways. For example, a distinction may be made between (1) cases involving ground improvements in which the designer can modify the expected ground behavior and

For more monographs, publications, or videos, visit http://www.eeri.org

(2) cases in which the designer accepts the existing ground conditions and instead may modify the structure or its foundation. In the former case, it is possible to directly specify the target ground conditions that are expected to produce a desired performance, and thus the margin of safety against unacceptable performance may be provided by the degree or extent of the ground improvements. The latter case focuses more on evaluating an expected behavior (deformation or instability), and thus the margin of safety against unacceptable performance is accommodated through a conservative estimate of the expected ground behavior and/or the design of the structure and its foundation.

For cases involving liquefaction-induced ground deformations such as settlement or lateral spreading, the ground deformation specifications to be used in designing or evaluating supported structures must include allowances for the inaccuracies in the analytical methods and the uncertainties in site characterization. The level of uncertainty in the various analytical methods is difficult to define rigorously, because there are many other considerations, but a factor of two for computed displacements is a prudent starting point, in view of the various comparisons in the literature between predicted and measured displacements induced by liquefaction. The influence of site characterization uncertainties is similarly difficult to generalize, but useful insight can be obtained from (1) the variability in computed displacements among individual borings and soundings, such as those illustrated in Figure 112, and (2) how sensitive the computed displacements for individual borings and soundings are to the ground motions, as illustrated in Figure 110.

For cases involving potential instability of earth structures, allowances must be made for uncertainties in the estimated shear strengths of soils that are expected to liquefy and the uncertainties in site characterization. The stability of an earth structure may be expressed as a factor of safety against instability, such as may be obtained from a limit equilibrium slope stability analysis, but this factor of safety is also usually accompanied by some estimate of potential deformations. In evaluating such problems, it is important to quantify how sensitive the computed factors of safety and deformations are to the assumed strength parameters and site characterization.

Liquefaction triggering analyses include the calculation of a factor of safety against liquefaction (FS_{liq}) at different points within the subsurface. The FS_{liq} clearly relates to the potential development of significant strains and excess pore water pressures at different points within the subsurface, but an estimate of overall ground displacements

For more monographs, publications, or videos, visit http://www.eeri.org

requires more information than is provided by the FS_{liq}. However, if the FS_{liq} is greater than 1.2–1.3 at all depths at a relatively level ground site, then the potential shear strains would be less than 1–2% (e.g., Figure 94), potential volumetric strains would be less than about 0.5% (Figure 103), and residual excess pore water pressure ratios would be less than about 0.5. Where such conditions are known to correspond to acceptable levels of ground deformations, the margin of safety against unacceptable performance may be alternatively expressed in terms of the minimum FS_{liq}.

Some other uncertainties in estimating liquefaction-related performance, whether the focus is on ground deformations or instability, are partly accounted for by other components of the engineering analyses. For example, uncertainty in site characterization is often partly accounted for by conservative assumptions about groundwater levels or representative penetration resistances. Uncertainty in the correlation between liquefaction resistance and in-situ test measurements is accounted for by a conservative interpretation of case histories and the derivation of correlations that generally envelop the observed cases of liquefaction. Uncertainty in the ground motions is accounted for in the selection of design hazard levels. Uncertainty in the amount of deformation that any given structure can tolerate is often accounted for by a conservative specification of the acceptable deformation levels.

The final margin of safety against unacceptable performance from liquefaction for a given project depends on the degree of conservatism that is incorporated at each step in the analyses. Conservatism at each of the numerous analytical steps can quickly accumulate into a higher margin of safety than may be required, thus leading to more expensive conclusions than are necessary. Probabilistic methods can provide a means for understanding how the uncertainties (or instances of conservatism) in the individual steps propagate through to decisions, but these methods do require considerable effort and judgment in their application. In all situations, reasonable judgment is necessary in understanding how the performance of a system is affected by uncertainties in each step of the evaluations, along with recognition that the simultaneous occurrence of low-probability conditions for each step in an analysis has an even lower probability of occurring.

For more monographs, publications, or videos, visit http://www.eeri.org

5 MITIGATION OF LIQUEFACTION HAZARDS

5.1 Evaluating and Selecting Possible Mitigation Strategies

The successful design of liquefaction mitigation for a given structure or system requires a thorough understanding of the liquefaction hazard, the potential consequences of liquefaction for the structure, the performance objectives, and the available construction materials and methods. The final selection of a mitigation scheme depends on the approach to managing risk and may range from a heuristic evaluation to a very formal risk evaluation. The different mitigation strategies can include the following:

- Doing nothing and accepting the potential damage and risk
- Abandoning the project or choosing another site
- Improving the ground so that the damage is precluded or is reduced to acceptable levels
- Modifying the design so that liquefaction of the ground does not damage the structure, or the damage is reduced to acceptable levels

For networks or systems of structures, the mitigation strategy may include a mix of different approaches that best manages the overall risk—such as maintaining functionality for portions of the system while requiring only life safety for the other portions during a given design earthquake. The overall objective is to develop options for mitigating liquefaction hazards so that the relative benefits versus costs for different levels of mitigation effort can be evaluated.

This section briefly introduces some of the more common methods of ground improvement for mitigating liquefaction. To evaluate the appropriateness of a ground improvement method for a specific site, it is important to (1) understand the basic mechanisms of the improvement so that the engineering design procedures and

For more monographs, publications, or videos, visit http://www.eeri.org

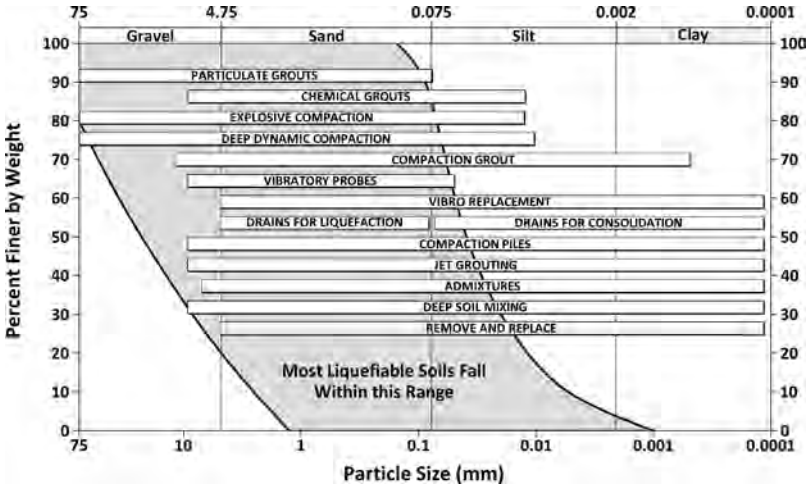

Figure 114. General applicability of ground improvement methods for soils of various grain-size distributions (Mitchell 2008, with permission from ASCE).

the quality control or verification criteria are reasonable and (2) be familiar with constructibility issues so that the selected method is constructible and cost-effective. Possibilities for design modification strategies are not covered here, because they are beyond the scope of this monograph.

5.2 Methods of Ground Improvement

Some of the more common ground improvement methods are listed in Figure 114, which shows the range of soil grain sizes in which the methods are likely to be reasonably effective (Mitchell 2008). While approximate in its guidance, this figure illustrates that the first criterion is selection of a ground improvement method that is well suited to the soils to be treated.

Vibro Methods

Vibro methods encompass a variety of different construction processes whereby a vibrating probe repetitively penetrates the ground to densify the liquefiable soils. There are numerous kinds of equipment and procedures, which are known by a range of generic and proprietary names (e.g., PHRI 1997, Mosely and Kirsch 2004, Kitazume 2005). The simplest categorization of vibro methods is as follows:

- Vibro-rod: vertical vibration is applied to the top of a penetrating probe or rod.

For more monographs, publications, or videos, visit http://www.eeri.org

- Vibroflotation: a horizontally vibrating motor is housed in the tip of the penetrating probe.
- Vibro-replacement: the probe cavity is filled with imported materials, such as crushed stone, gravel, sand, or sometimes concrete.

Figure 115 shows the process of constructing a vibro-replacement stone column, and Figure 116 shows typical construction equipment.

Vibro-replacement methods can improve liquefiable soil deposits by (1) densifying the in-situ soils, (2) increasing the in-situ lateral stress, (3) reinforcing the soil mass with the stiffer columns of fill material, and (4) providing increased drainage of earthquake-induced excess pore water pressures from the in-situ soils. Factors that control, and can severely limit, the ability of the columns to provide rapid drainage during shaking are discussed later in this section, along with other drainage techniques.

Vibro methods have been widely used because they are the most effective and economical choice in many situations, provided that the grain-size distribution of the soils to be improved is within the range shown in Figure 114. Two of the widely available methods are the sand composer technique (common in Japan) and vibro-replacement stone columns (common in the United States).

The constructibility and effectiveness of vibro-replacement stone columns can be limited in certain site conditions. They are often

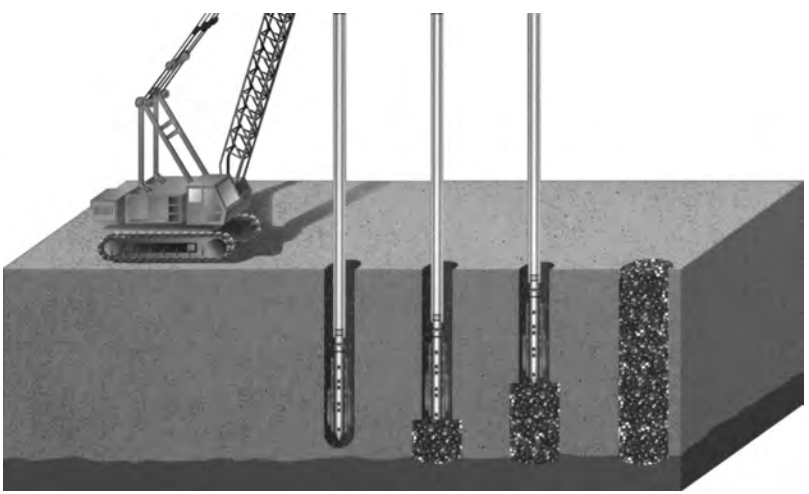

Figure 115. Process for constructing a vibro-replacement stone column (Hayward Baker, Inc.).

For more monographs, publications, or videos, visit http://www.eeri.org

Figure 116. Vibroflotation with a water jet to assist ground penetration during construction of a vibro-replacement stone column.

ineffective for densifying soils that have high fines content (e.g., greater than about 20%), although the installation of wick drains before the vibro-replacement work at some sites has facilitated a more rapid dissipation of the excess pore water pressures generated by the vibrator, thereby increasing the degree of densification that was achieved in soils having much higher fines content (Luehring et al. 2001). If the liquefiable strata are of limited thickness at some significant depth, then vibro-replacement may be an inefficient choice, because it must penetrate the entire depth and penetrate any harder or denser overlying strata. In the latter case, cemented strata or strata with large cobbles or boulders can be difficult to penetrate as well. Vibro methods can cause settlement of surrounding ground, which can damage existing structures unless special precautions are taken. Completed stone columns can also provide a vertical conduit for the transport of environmental contaminants from one stratum to another.

Deep Dynamic Compaction

In deep dynamic compaction, a crane repetitively drops a large tamper mass from a significant height onto the ground surface, as shown in Figure 117. Crawler cranes can drop tamper masses weighing up to 33 tons from heights of up to 30 m, and specially constructed

For more monographs, publications, or videos, visit http://www.eeri.org

Figure 117. Deep dynamic compaction, showing the pattern of primary impact points (photo: DGI-Menard, Inc.).

For more monographs, publications, or videos, visit http://www.eeri.org

machines can drop even larger masses (Mosely and Kirsch 2004). The impact of the tamper on the ground surface produces a crater, whose depth depends on the strength of the surface soils, and propagates dynamic stress waves through the subsurface soils. These dynamic stresses can be large enough to liquefy or at least generate high excess pore water pressures in the soils beneath the impact point. Dissipation of these excess pore water pressures densifies the soil, with associated ground surface settlement.

Deep dynamic compaction improves liquefiable soil deposits primarily by densifying the in-situ soils and increasing the in-situ lateral stress. The advantages of deep dynamic compaction include the following: it is relatively economical in treating large areas under certain conditions, the equipment and procedures are relatively simple, and it does not require insertion of any equipment into the subsurface. The latter advantage can be important in trying to densify deposits that contain large particles, debris, or contaminants. In many cases, however, the presence of large boulders can impede the densification of the soil around the boulders.

Deep dynamic compaction also has limitations. One is that this method is often effective only in the upper 10 m of soil. Another is that the effectiveness decreases with decreasing permeability of the subsurface soils, because the slower rate of pore pressure dissipation reduces the densification that can occur between tamper drops spaced at reasonable time intervals. For this reason, the method's effectiveness starts to lessen as the fines content becomes greater than about 20%. Interlayers or lenses of soft soils (e.g., normally consolidated clays) at shallower depths can dampen the transmission of dynamic shear stresses to the underlying soils, thereby reducing the treatment effectiveness beneath the soft soils. Vibrations from the tamper impacts can be disturbing to existing structures or their occupants, which can limit the use of this method in the vicinity of existing structures or facilities.

Compaction Grouting

Compaction grouting involves injecting thick, mortar-like grout that displaces, rather than penetrates, the surrounding soil. Figure 118 shows the process of compaction grouting via the bottom-up approach, in which injection starts at the bottom and progresses as the grout rods are incrementally pulled up in stages.

Compaction grouting can improve liquefiable soils by (1) densifying the in-situ soils, (2) increasing the in-situ lateral stress, and

For more monographs, publications, or videos, visit http://www.eeri.org

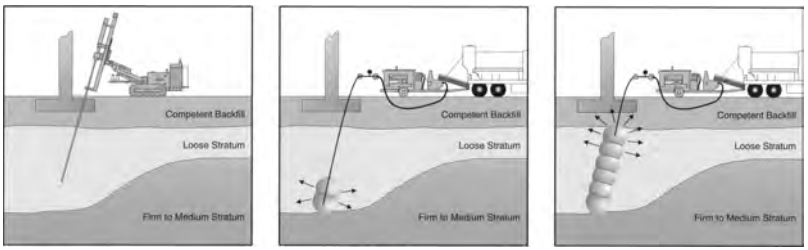

Figure 118. Compaction grouting via the bottom-up approach (Hayward Baker, Inc.).

(3) providing some reinforcement of the soil mass. The growth of a grout bulb shears the surrounding soil as it is displaced outward, which causes the soil to move toward its critical state under the confining stresses imposed by the expanding cavity. The advantages of compaction grouting are that it can work in low-overhead and constricted spaces (e.g., inside a building basement or under a bridge deck) and can target a specific depth interval without having to treat all the overlying soils. This method has also been relatively effective in soils with high fines content and in soils containing larger particles or debris that can impede penetration by larger equipment components such as vibrators or deep soil mixing augers.

Compaction grouting also has disadvantages. One is that this method is not very effective at depths of less than about 6 m, because the confining stresses are too low, and the grouting pressures can heave the ground surface rather than densifying the soil. The reinforcing effects of the compaction grout bulbs/columns may be minimal, because the grout bulb/column will be relatively brittle in bending and will be weak once it has cracked. In some cases, steel reinforcing bars have been inserted into the grout hole before the grout has set, thereby providing some increased tensile and shear capacity and thus improving the integrity of the column.

Deep soil mixing

Deep soil mixing involves the mixing, and sometimes partial replacement, of in-situ soils with cementitious materials or grout. Deep soil mixing uses various mixing augers or combinations of augers, as illustrated in Figure 119 and described in Mosely and Kirsch (2004). The mixing augers are advanced to the target depth, and then cementitious materials or grout are injected through the auger stems as they continue to rotate and mix the injected matter with the native

For more monographs, publications, or videos, visit http://www.eeri.org

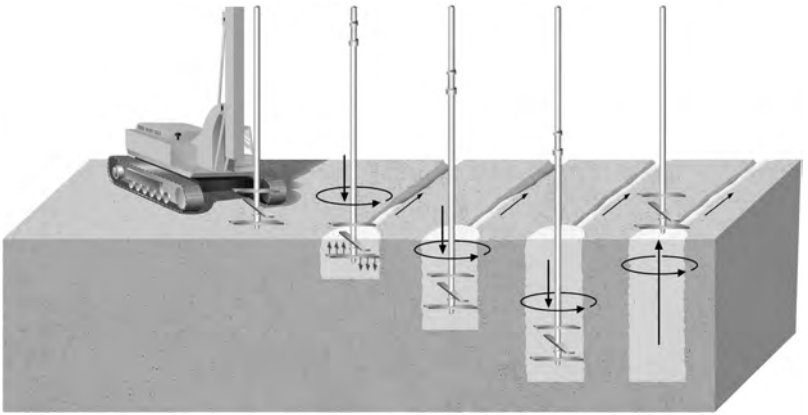

Figure 119. The deep soil mixing process (Hayward Baker, Inc.).

soils. This process produces excess material or spoil that is collected at the ground surface and disposed of. The soil cement materials in the mixed columns can have a wide range of unconfined compressive strengths (e.g., 0.1–7 MPa), depending on the native soil characteristics and the amount of cementitious material that is used.

Deep soil mixing can be used to construct in-ground shear walls by overlapping the soil cement columns. A grid of in-ground shear walls can improve a liquefiable soil deposit in three ways (e.g., Babasaki et al. 1991, O'Rourke and Goh 1997): (1) reducing the earthquake-induced shear strains in the treatment zone, thereby limiting the generation of excess pore water pressures in the enclosed native soil; (2) structurally restraining the enclosed soil from deforming if it does liquefy, thus contributing to the composite shear strength of the treated zone; and (3) acting as a barrier to the migration of excess pore water pressures from the adjacent untreated zones into the treatment area. In-ground walls reduce the earthquake-induced shear strains, because they are stiffer in shear than the enclosed soil, and hence they attract a greater share of the horizontal inertial forces during shaking.

An advantage of deep soil mixing and its use as in-ground shear walls is that such walls can generally be constructed in a wide range of soil types, including soils with high fines content. This is a considerable advantage, given that many of the other ground improvement methods are less effective in such soils. The equipment does require significant overhead clearance, which can limit its use around some existing structures. Also, the augers must penetrate from the ground

For more monographs, publications, or videos, visit http://www.eeri.org

surface to the full target depth, which can be a disadvantage when treatment is required only for liquefiable layers of limited thickness at some significant depth or when harder or denser overlying strata impede the augers.

A concern that often arises with deep soil mixing is that the unreinforced soil-cement materials may be brittle and have low tensile strength, and thus they may develop excessive cracking during earthquake shaking, with an associated reduction in their effectiveness. Recent experiences have shown good field performance, however (Hamada and Wakamatsu 1996). For example, the Oriental Hotel in Kobe, Japan was founded on piles that were protected by a grid of deep soil-mixed walls, and this building performed exceptionally well during the 1995 Kobe earthquake, despite liquefaction and extensive deformations around the perimeter of the pier that the hotel was on.

Jet Grouting

Jet grouting involves mixing and partial replacement of in-situ soils with cementitious grouts, but the mixing is accomplished by high-pressure jets of air, water, and/or grout (e.g., Mosely and Kirsch 2004). The different kinds of jets are combined by using single-, double-, or triple-tube grouting techniques. Figure 120 illustrates how jet grouting can produce overlapping soil-cement columns.

Jet grouting can also be used to construct in-ground shear walls, as mentioned in the discussion of deep soil mixing. The mechanisms

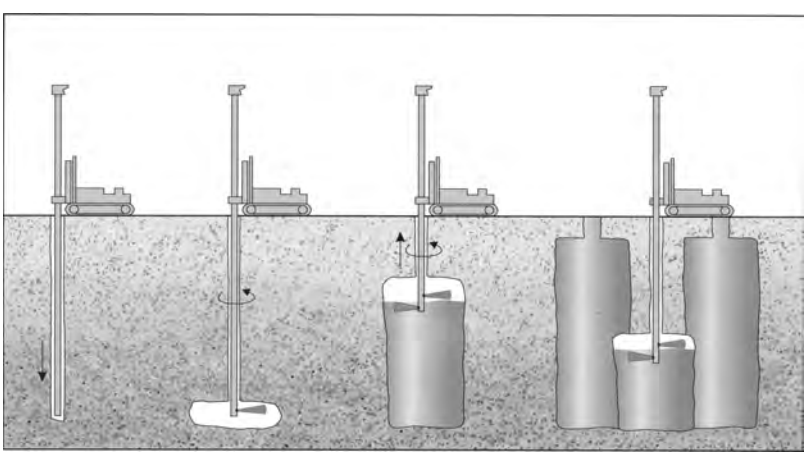

Figure 120. Using jet grouting to produce overlapping columns (Hayward Baker, Inc.).

For more monographs, publications, or videos, visit http://www.eeri.org

of improvement and the concerns about the potential brittle behavior of such walls are similar to those cited for deep soil mixing.

An advantage of jet grouting is that it can be performed in low-overhead areas, such as around existing facilities, and it can target liquefiable layers of limited thickness at some significant depth.

Drainage

Drainage systems generally consist of individual vertical drain elements constructed in a closely spaced grid or curtain (line) patterns. The drain elements may consist of coarse aggregates or geosynthetic composites, and whether their installation is accompanied by some degree of densification depends on the installation technique.

Drainage can increase dissipation rates for the excess pore water pressures that are generated during shaking, or it can modify the dissipation patterns and thus alleviate potential damage from pore pressure redistribution. A clear distinction must be made between these two intended functions, because they directly affect the design considerations.

Drains can sometimes increase the rate of pore water pressure dissipation by amounts that are sufficient to maintain the excess pore pressures at acceptably low levels throughout the duration of shaking. In this case, the drains may be installed in a closely spaced grid pattern, as illustrated in Figure 121a. Design charts for drains to control maximum r_u levels were first developed by Seed and Booker (1977), but more recent analytical methods and design charts (e.g., Onoue 1988, Iai and Koizumi 1986, Pestana et al. 2000) provide a more complete accounting of the hydraulic resistance of the drains and other factors. The effectiveness of drains during earthquake shaking decreases with decreasing soil permeability, increasing soil compressibility, longer drainage path lengths, thicker soil layers, higher hydraulic resistance in the drain (or lower-permeability drain material), a lower factor of safety against the triggering of liquefaction if there are no drains, and a longer duration of shaking. Designing drains to control the maximum r_u levels is often complicated by concerns about the uncertainties in the spatial distribution of hydraulic conductivities in the field, the ability to ensure that certain types of drains are as permeable as intended, and the nature of the ground motions. As a consequence, the applicability of drains for controlling pore pressure generation is limited to relatively high-permeability soil deposits.

Drains can also control the dissipation patterns of earthquake-induced excess pore pressures, both during and after shaking. The

For more monographs, publications, or videos, visit http://www.eeri.org

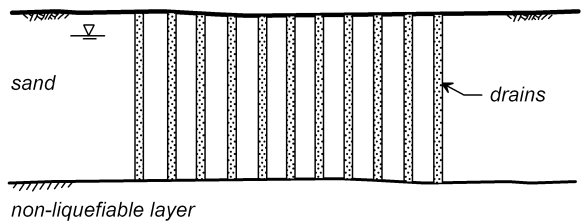

(a)

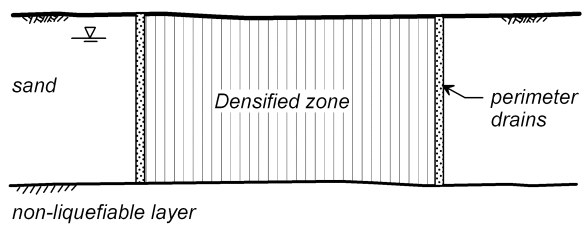

(b)

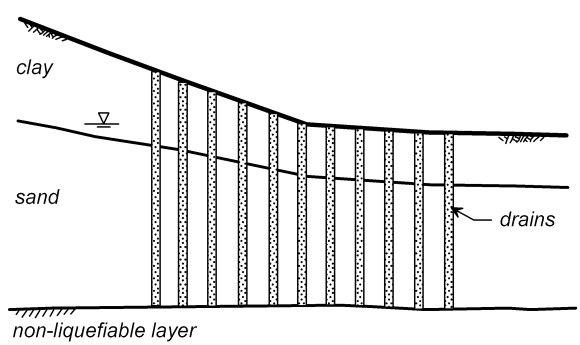

(c)

Figure 121. Gravel drains for liquefaction mitigation: (a) a grid of drains for controlling maximum r_u levels during earthquake shaking, (b) perimeter drains to prevent migration of high excess pore pressures from untreated zones into a densified zone, and (c) a grid of drains to prevent void redistribution or water film generation beneath a lower-permeability capping layer.

For more monographs, publications, or videos, visit http://www.eeri.org

intent might be to prevent the migration of high excess pore water pressures from untreated liquefied zones into a densified (treated) zone where the shaking-induced excess pore pressures are lower, such as in Figure 121b. The migration of the pore pressures into a treated zone can weaken it and result in ground deformations and/or foundation settlement. Another possible function would be to minimize or prevent the accumulation of pore water at the interface between an overlying low-permeability stratum and an underlying sand layer in which high excess pore water pressures have been generated by earthquake shaking (Figure 121c). In this case, the upward seepage of pore water can be trapped by the overlying low-permeability stratum, leading to the formation of water films or void-redistribution-induced weakening of the soils at the interface (Figure 43). Recent centrifuge modeling studies (Naesgaard et al. 2005) have shown that drains can reduce the hydraulic impedance of the interface and mitigate the potential loss of strength along the interface during or after shaking.

Permeation Grouting

Permeation grouting involves injecting a grout that permeates the pore space of the surrounding soil before the grout begins to harden, or "set." The hardened grout improves the soil primarily by cementing the soil particles together and by filling the void spaces (thus reducing the potential for contraction during cyclic shearing). There is a wide range of grouting materials (e.g., microfine cement grouts and chemical grouts), with the choice of material depending primarily on the pore sizes of the soil to be grouted, required setting time, required strengths, environmental constraints, and cost. The injection process is conceptually simple, with the grout injected under pressure through pipes installed in the ground. The actual construction process is quite complex, however. Computerized automation of the grout injection procedures (pressures, volumes, rates, and intervals) and grout mixing processes (grout concentrations, admixtures, and setting times) is commonly used to optimize the construction process and provide quality control. Figure 122 shows exposed bulbs of ground that had been treated by injecting a silica gel substance via permeation grouting at a site in Japan (Yamazaki et al. 2005).

Permeation grouting can be particularly advantageous where it is important to avoid disturbing the native soil because of concerns about associated settlements or distress to an existing foundation or structure. Grouting equipment can work in constricted spaces and

For more monographs, publications, or videos, visit http://www.eeri.org

Figure 122. Soil that had been treated by permeation grouting before being exposed by excavation (Yamazaki et al. 2005).

target specific zones or intervals, and it can do so with minimal disturbance to the native soil (if done properly). However, the use of such equipment is limited to relatively clean sands (Figure 114), because the ability to permeate a soil decreases rapidly with increasing fines content. Permeation grouting may also be more expensive than other ground improvement methods, hence its use is generally limited to special situations.

Explosive Compaction

Explosive compaction or blasting involves detonating explosive charges placed at various depths in boreholes across the site. The explosions propagate dynamic shear stresses through the subsurface that can liquefy the subsurface soils (e.g., Narin van Court and Mitchell 1998). The drainage of these excess pore water pressures is accompanied by densification of the soils, with associated ground surface settlement and sometimes the formation of sediment boils (Figure 123) similar to those observed at liquefied sites after earthquakes.

Explosive compaction can be economical for conditions in which it is effective and acceptable, such as the presence of deeper deposits of cleaner loose sands that will experience relatively large and rapid

For more monographs, publications, or videos, visit http://www.eeri.org

Figure 123. Sand boil and ejected water caused by blasting-induced liquefaction (photo: S. Ashford).

reconsolidation strains (e.g., Solymar 1984). It is not effective for densification at shallow depths, it may be less effective if the fines content exceeds about 15–20%, and the vibrations from the explosions can limit how close to existing buildings the blasting can be. The amount of densification that can be achieved is generally not as great or as uniform as is possible with some other methods, and thus the usefulness of this method depends on the design levels of shaking. Obtaining permits can also be a significant obstacle to the use of this method in some areas.

Removal and Replacement

The most direct method for improving a loose soil is to excavate it and then replace it as a compacted fill. An advantage of this method is that it affords a high degree of confidence in the final product and uses construction equipment and practices that are widely available and easily tested. It is usually most economical where the liquefiable soils do not extend to large depths, where the excavation does not affect or limit the use of existing structures or facilities, and where the groundwater levels can be controlled.

For more monographs, publications, or videos, visit http://www.eeri.org

Combinations of Ground Improvement Methods

The optimal approach to ground improvement can involve using two or more ground improvement methods, with the specific combination depending on the unique circumstances of the given project. Some examples from past projects include the following:

- Explosive compaction was used to densify the lower portion of a liquefiable soil layer to depths of up to 45 m at Jebba Dam, Nigeria, and vibro-compaction was used to densify the upper 25 m (Solymar 1984).
- Compaction grouting was used to densify the lower portion of a liquefiable soil layer to depths of about 15 m at a submarine facility in Georgia, and deep dynamic compaction was used to densify the upper portion (Hussin and Ali 1987).
- Vibro-replacement stone columns were used to treat about 5,500 m^2 of Mole B at King Harbor in Redondo Beach, California, and compaction grouting was used to treat about 1,900 m^2 behind a seawall and near a sewage lift station that were considered sensitive to the vibrations that would be induced by vibro-replacement work (Kerwin and Stone 1997).
- Remedial work at Seymour Falls Dam, Canada included pre-excavating the upper 10 m of soil, performing explosive compaction from depths of 10–20 m below the excavation base, performing deep dynamic compaction on the base of the excavation, and then replacing the excavated soils as compacted fill (Siu et al. 2004).

For large sites, it is possible that different ground improvement methods might be used in different areas because of changes in the soil profile (e.g., the thickness and depth of liquefiable soils), changes in the types of existing structures (e.g., overhead restrictions or sensitivity to vibrations), or constraints on the work schedule and equipment availability. These are just a few examples of the countless combinations that have been effectively used in construction.

5.3 General Design and Construction Considerations

The design and construction of ground improvements for seismic risk mitigation are affected by a broad range of considerations, such as those discussed by Mitchell et al. (1998) and PHRI (1997). A few of the more general considerations are summarized below.

The final selection of a ground improvement method may depend on the designer's confidence in the reliability of the available

For more monographs, publications, or videos, visit http://www.eeri.org

technologies and their supporting design methodologies. Confidence in a given technology can depend on a wide range of factors, such as confidence in the mechanisms of improvement, the demonstrated ability to measure and quantify the effectiveness of treatment, the rigor of and basis for the design methodologies, and the availability of physical modeling or case history experiences that demonstrate the technology's effectiveness in mitigating the effects of earthquake shaking. For these reasons, it can take several years for a newly developed ground improvement technology to gain broad acceptance and use.

For professionals to gain confidence in various techniques and sometimes learn the limitations of certain practices, the observed performance of improved sites during past earthquakes has been very important. Compilations of such case histories (e.g., Mitchell et al. 1995, Hausler and Sitar 2001) provide examples of good performance and a few examples of poor performance. The overall record of improved sites in past earthquakes is quite good. The few cases of poor performance are attributable to practices or procedures that would no longer be acceptable or to shaking intensities that exceeded those at which the improved ground would be expected to perform well. In any case, the record of performance must be considered with respect to the level of site improvement and the robustness of design in relation to current standards.

The effectiveness of a ground improvement method for a specific site can be very difficult to predict reliably. Thus it is very common to require a trial or demonstration section before final design and construction bidding. A trial section in an appropriately representative area of the site allows both the designer and the contractor to identify potential difficulties with construction and/or the quality control procedures and to optimize or verify the construction parameters required to achieve the desired improvement. For some ground improvement methods and soils, the post-treatment penetration resistances can exhibit significant changes over periods ranging from weeks to many months. Evaluating these temporal effects may require repeating the in-situ testing over several time intervals to assess the long-term improvements (e.g., Mitchell and Solymar 1984). Experience from the trial section reduces uncertainty for the contractors who are bidding on the project, and this usually translates into an overall saving through lower bids from the contractors. In some cases, the trial section may show that the proposed method cannot achieve the desired improvement, which has the advantage of avoiding the very

For more monographs, publications, or videos, visit http://www.eeri.org

costly change orders that would have arisen if the contract had been let without the benefit of a trial section.

The successful execution of a ground improvement project strongly depends on the engineer's development of clear, reasonable, feasible, and enforceable specifications and quality control procedures. The specifications and quality control procedures should allow for the nuances of the construction practices and how they might be adjusted to meet changing site conditions. It is important to be familiar with the limits of what can reasonably be constructed via current technologies and then design the ground improvement project in accordance with those limits.

For more monographs, publications, or videos, visit http://www.eeri.org

For more monographs, publications, or videos, visit http://www.eeri.org

6 CYCLIC SOFTENING IN CLAYS AND PLASTIC SILTS

6.1 Behavior of Saturated Clays and Plastic Silts during Earthquakes

Ground failures in deposits of clays and plastic silts (i.e., "cohesive" soils) have been observed during earthquakes, but such failures are considerably less common than in deposits of saturated sands and other cohesionless soils. The Fourth Avenue slide in Anchorage during the 1964 Prince William Sound, Alaska earthquake occurred in the Bootlegger Cove clay and produced lateral and vertical movements of several meters (Idriss 1985), as shown in Figure 124. Five- and six-story buildings in Wufeng, Taiwan experienced foundation failures during the 1999 Chi-Chi earthquake (Figure 125) that are attributed to failure and strength loss in underlying clays and clayey silts (Chu et al. 2004, Boulanger and Idriss 2004b, Chu et al. 2007). Other instances of ground and foundation failure in clays and plastic silts include those in the 1985 Michoacan earthquake in Mexico (Mendoza and Auvinet 1988, Zeevaert 1991), the 1999 Kocaeli earthquake in Turkey (Bray et al. 2004, Martin et al. 2004, Yilmaz et al. 2004), and the 2001 Bhuj earthquake in India (Bardet et al. 2002b).

The potential for cyclic loading to produce the onset of rapidly increasing strains in saturated clays is illustrated by the cyclic triaxial test results for normally consolidated Cloverdale clay in Figure 126 (Zergoun and Vaid 1994). These tests were performed sufficiently slowly to ensure reliable measurements of pore water pressure, as opposed to the more common seismic loading rates of 1 Hz, at which pore pressure measurements can be unreliable for clay samples. The results were similar to those shown in Section 2.2 for clean sand: the undrained cyclic loading of this clay sample caused a progressive

For more monographs, publications, or videos, visit http://www.eeri.org

Figure 124. Ground failure along Fourth Avenue, Anchorage after the 1964 Prince William Sound, Alaska earthquake (photo: W. Hansen).

increase in excess pore water pressure to some limiting level (r_u = 80% for this sample), at which time the sample developed rapidly increasing strains with each subsequent loading cycle. The stress-strain loops after this limiting r_u had been reached dissipated considerably more energy than is observed for clean sand (i.e., the hysteretic loops were broader). Furthermore, the stress-strain loops for clay generally did not develop the very flat middle portions (where the shear stiffness is essentially zero) that are observed for sands after they temporarily develop r_u = 100%. Nonetheless, this type of stress-strain behavior could lead to significant ground deformations during earthquake shaking, which in many respects can be difficult to differentiate from ground displacements observed at sites where liquefaction of sands has caused the ground deformations.

The characteristics of clays and plastic silts are quite different from sands and other cohesionless soils in ways that have led to the development of very different engineering procedures for characterizing their static and dynamic strengths (e.g., Ishihara 1996; Boulanger and Idriss 2004b, 2007). The term "cyclic softening" is used in reference to strength loss and deformation in clays and plastic silts, while

For more monographs, publications, or videos, visit http://www.eeri.org

Figure 125. Bearing failure and settlement of spread footings under the front columns and the mat foundation under the rear portion of a six-story building in Wufeng, Taiwan caused by the 1999 Chi-Chi earthquake (photo: R. Seed). The thin concrete slab between the mat and column footings was damaged by the soil heaving in relation to the footings and mat.

the term "liquefaction" is used in reference to strength loss and deformation in saturated sands and other cohesionless soils. As such, the terms "cyclic softening" and "liquefaction" can also be used in reference to the engineering procedures that have been developed for these respective soil types.

The remainder of this section addresses three issues: (1) evaluation of the cyclic strength of clays and plastic silts, (2) soil characteristics that correspond to the transition from sand-like to clay-like behavior in fine-grained soils, and (3) consequences of cyclic softening in clay-like fine-grained soils.

6.2 Relating Monotonic and Cyclic Undrained Shear Strengths

The undrained cyclic strength of saturated clays and plastic silts can be expressed as a relatively unique function of the soil's undrained monotonic shear strength, as illustrated by the experimental results summarized in Figure 127 for different natural fine-grained soils and

For more monographs, publications, or videos, visit http://www.eeri.org

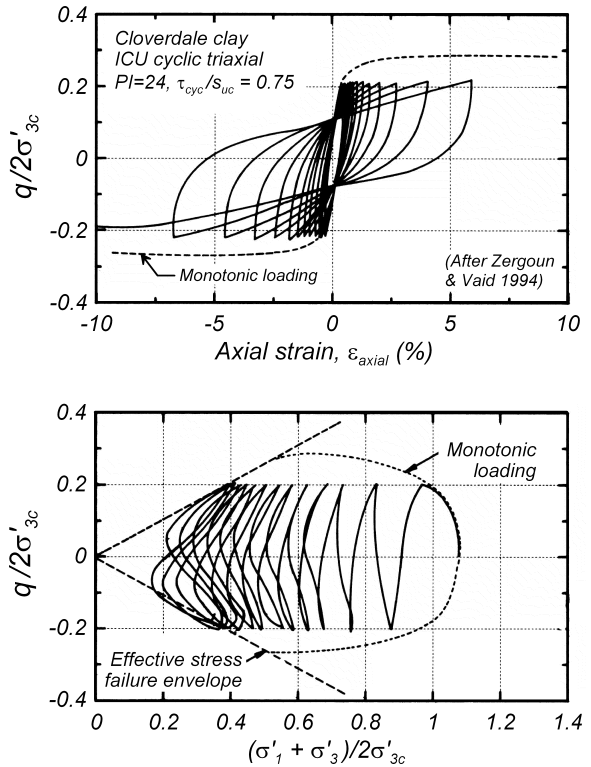

Figure 126. Stress-strain response and effective stress paths for Cloverdale clay during undrained slow cyclic loading (after Zergoun and Vaid 1994).

tailings materials with overconsolidation ratios (OCRs) of 1-4, in which OCR is defined as

$$\mathrm{OCR} = \frac{\sigma'_{vp}}{\sigma'_{vc}} \tag{99}$$

where σ'_{vp} equals the vertical effective preconsolidation stress (the maximum past vertical effective stress), and σ'_{vc} equals the current vertical effective consolidation stress. These results show the CSRs, $q_{cyc}/2s_u$ for triaxial shear and τ_{cyc}/s_u for direct simple shear, required to generate peak (single-amplitude) shear strains of 3% during uniform cyclic loading; s_u in these expressions is the undrained shear strength of the soil under monotonic loading conditions. The CSRs have all been adjusted to an equivalent uniform cyclic loading

For more monographs, publications, or videos, visit http://www.eeri.org

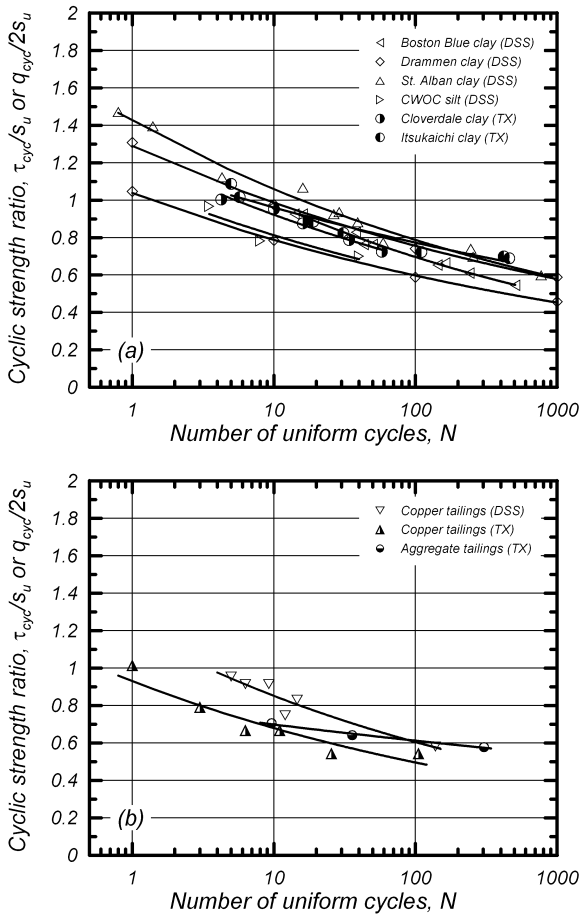

Figure 127. CSRs required to cause cyclic failure (3% strain) versus the number of uniform loading cycles at a frequency of 1 Hz: (a) samples from natural deposits (Andersen et al. 1988, Azzouz et al.1989, Hyodo et al. 1994, Lefebvre and Pfendler 1996, Woodward-Clyde 1992a, Zergoun and Vaid 1994) and (b) samples from tailings deposits (Moriwaki et al. 1982; Romero 1995; Woodward-Clyde 1992b).

frequency of 1 Hz, which is based on the observation that cyclic strengths increase about 9% per log cycle of loading rate (e.g., Lefebvre and LeBouef 1987, Zergoun and Vaid 1994, Lefebvre and Pfendler 1996, Boulanger et al. 1998). The influence of loading rate is further illustrated in these results by the fact that the cyclic shear

For more monographs, publications, or videos, visit http://www.eeri.org

stresses for failure in one loading cycle exceed s_u, because the reference value of s_u is for the much slower conventional monotonic loading rates. The results for these clays and plastic silts fall within relatively narrow ranges, although the cyclic strengths for the tailings materials are somewhat lower than for the naturally deposited soils. It is also worth noting that Seed and Chan (1966) observed similar cyclic strength ratios for compacted sandy clay and compacted silty clay specimens, which suggests that the cyclic strength ratios shown in these figures may also be applicable to compacted clays as well as natural sedimentary clays.

A key feature of the stress-strain behavior of many saturated clays and plastic silts is that the monotonic undrained shear strength can be closely expressed as a function of consolidation stress history, as illustrated by the experimental results shown in Figure 128 for Boston Blue clay (Ladd and Foott 1974). These and other results discussed in Ladd (1991) illustrate that normalizing shear stresses by the effective vertical consolidation stress can result in relatively unique normalized stress-strain behavior for the same OCR. These data also illustrate how the undrained shear strength (s_u) can be expressed in the form (Ladd and Foott 1974)

$$\frac{s_u}{\sigma'_{vc}} = \mathrm{S} \cdot \mathrm{OCR}^m \tag{100}$$

where S is the value of s_u/σ'_{vc} for OCR = 1, and m is the slope of the s_u/σ'_{vc} versus OCR relationship on a log-log plot. Ladd (1991) provided detailed recommendations about appropriate values for S and m to be used in analyses of staged embankment construction, on the basis of a review of experimental data and field experiences. The value of S was 0.16–0.28 for direct simple shear loading, with the values depending on the PI of the soil, whether it plotted above the A-line (the USCS classifications of CL or CH) or below the A-line (USCS classifications of ML or MH) on an Atterberg limit chart, and whether the soil was varved or not. The value of m was typically close to 0.80. Thus, in estimating s_u on the basis of the above expression, the most important term to determine is often the OCR, followed by the value of S.

Procedures for evaluating the cyclic strength of saturated clays and plastic silts follow directly from the above two observations and can be presented in different forms. The following sections develop relationships for CRRs that can be compared with the earthquake-induced CSRs computed via the same Seed-Idriss simplified procedure that was used for sands.

For more monographs, publications, or videos, visit http://www.eeri.org

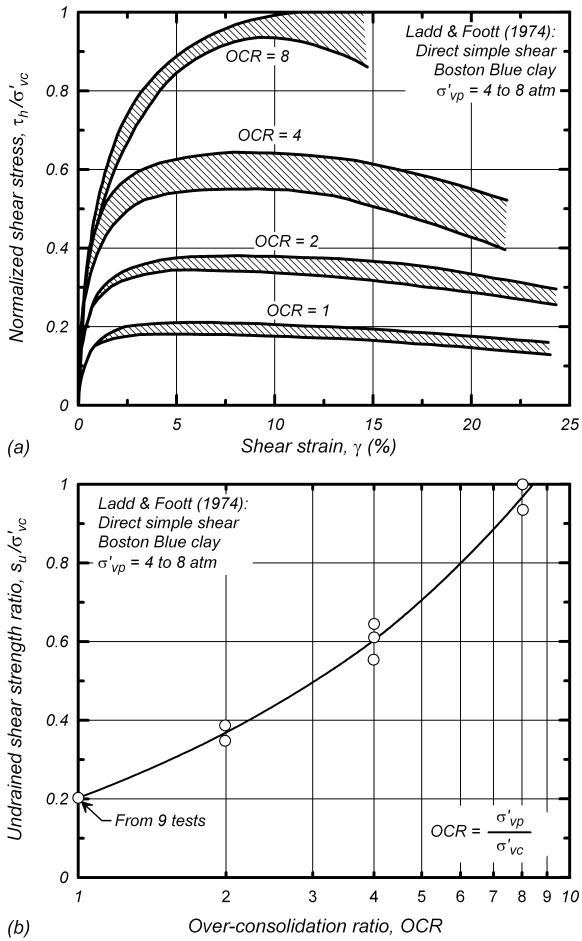

Figure 128. Response of Boston Blue clay in undrained direct simple shear tests on samples with preconsolidation stresses of 400–800 kPa and OCRs of 1, 2, 4, and 8 (after Ladd and Foott 1974): (a) normalized shear stress versus shear strain and (b) normalized shear strength versus OCR.

6.3 Number of Equivalent Uniform Loading Cycles and MSF

The number of equivalent uniform loading cycles that an earthquake may represent for clays depends on both the reference stress level (i.e., the percentage of the peak shear stress) and the relationship

For more monographs, publications, or videos, visit http://www.eeri.org

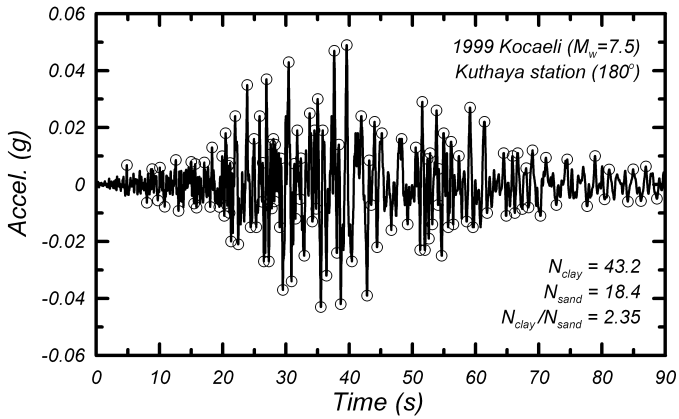

Figure 129. Comparison of the equivalent number of uniform loading cycles for clay and sand for the same earthquake time series (Boulanger and Idriss 2004b).

between the CSR and the number of uniform loading cycles to failure (e.g., Figure 127). For consistency with the procedures previously adopted for sands, the reference stress can be taken to be 65% of the peak shear stress in the time series. The relationship between the CSR and the number of uniform loading cycles to failure can be approximately fitted with a power relation, as described in Section 3.6, with the exponent typically being about 0.135 for clays versus about 0.34 for sands (i.e., the relationship for clay is much flatter than for sands). The effect of this difference in exponents on the equivalent number of uniform loading cycles is illustrated in Figure 129, where a time series from the 1999 Kocaeli earthquake (M = 7.5) would be equivalent to 18 and 43 uniform loading cycles in sand and clay, respectively (Boulanger and Idriss 2004b). This computation has been repeated for a large of number of earthquake time series, with the results indicating that the loading of clay by M = 7.5 earthquakes can be represented by an average of about 30 uniform loading cycles at 65% of the peak stress, as opposed to an average of about 15 cycles previously determined in Section 3.6 for sands.

The choice of reference stress level (i.e., 65% of the peak stress) is arbitrary and is worth commenting on briefly. If the reference stress had instead been taken to be 100% of the peak stress, then the equivalent number of uniform loading cycles for an M = 7.5 earthquake would have been about 4.2 for sands and only 1.23 for clays. The calculated factor of safety against failure would be independent of the

For more monographs, publications, or videos, visit http://www.eeri.org

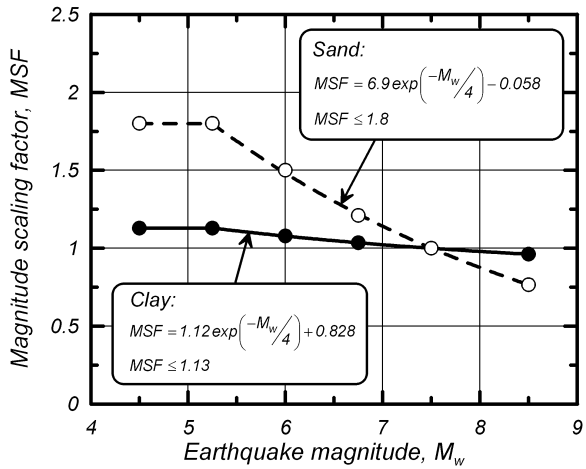

Figure 130. MSF relationship for clays and plastic silts (Boulanger and Idriss 2007, with permission from ASCE).

reference stress level, as long as the same reference stress level is used in computing the earthquake-induced CSR and determining the number of equivalent uniform loading cycles that will define the cyclic strengths. This algebraic equivalence is discussed in Section 6.6, after the relationships for cyclic strengths are further developed.

The average number of equivalent uniform loading cycles varies with earthquake magnitude, distance, and site conditions, as mentioned in Section 3.6 for sands. For practical purposes, this effect is approximately accounted for by an MSF. The MSF relationship for clays, namely,

$$\mathrm{MSF} = 1.12 \exp\left(\frac{-M}{4}\right) + 0.828 \tag{101}$$

is flatter than for sands, as shown in Figure 130, because the relationship between the CSR and the number of loading cycles to failure is flatter for clays.

6.4 Static Shear Stress Correction Factor

The effects of an initial static shear stress on the cyclic strength of clay can be expressed as a K_α relationship, as described for sands in Section 3.8, where K_α is simply the ratio of the cyclic strength

For more monographs, publications, or videos, visit http://www.eeri.org

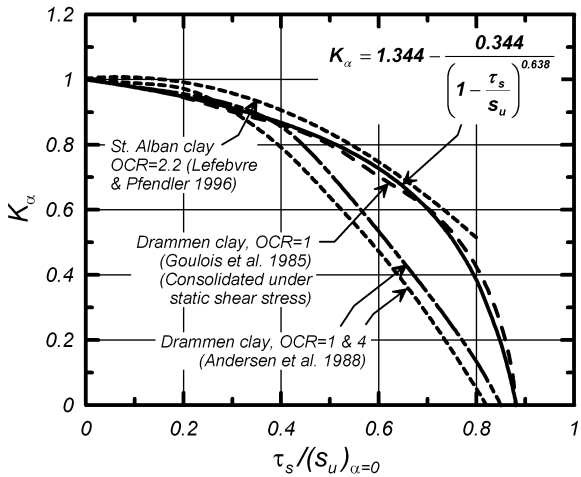

Figure 131. K_α versus $(\tau_s/s_u)_{\alpha=0}$ relationships for clays (Boulanger and Idriss 2007, with permission from ASCE). Note that the specimens were not consolidated under the applied static shear stresses, except as otherwise labeled.

with some initial static shear stress (CRR_α) to the cyclic strength without any initial static shear stresses ($\mathrm{CRR}_{\alpha=0}$). K_α relationships for Drammen clay (OCRs of 1 and 4; Goulois et al. 1985, Andersen et al. 1988) and St. Alban clay (an OCR of 2.2., Lefebvre and Pfendler 1996) are shown in Figure 131, with the initial static shear stress expressed in terms of τ_s/s_u instead of $\alpha = \tau_s/\sigma'_{vc}$. This figure was generated for 10 loading cycles to failure (defined as 3% peak shear strain, and not including strains induced by the static shear stresses), but the results are relatively unaffected by the choice of the number of loading cycles or the failure strain. The resulting K_α curves fall within a relatively narrow band, particularly for $\tau_s/(s_u)_{\alpha=0}$ values less than about 0.5.

The K_α results for the Drammen clay with consolidation under the static shear stress are reasonably representative of the overall results and are perhaps more applicable to situations of interest in seismic design. In particular, most designs for seismic loading would assume that the clay-like soils had sufficient time to consolidate under the sustained loading of some structure or embankment before

For more monographs, publications, or videos, visit http://www.eeri.org

the seismic design event. The following expression,

$$K_\alpha = 1.344 - \frac{0.344}{\left(1 - \frac{\tau_s}{s_u}\right)^{0.638}} \tag{102}$$

was derived to approximate the Drammen clay results. Other test results for Drammen clay by Andersen et al. (1988) showed very similar relationships for OCRs of 1, 4, and 40 when the specimens were not consolidated under the static shear stress. Consequently, it appears reasonable to tentatively assume that equation 102 is applicable over a wide range of OCRs.

The above expression for K_α can also be recast as a function of the initial static shear stress ratio (α) as used for sand-like soils. This is accomplished by dividing both the numerator and denominator of the τ_s/s_u term by σ'_{vc} and then replacing the resulting s_u/σ'_{vc} term with an appropriate empirical relationship (equation 100), as follows:

$$\frac{\tau_s}{s_u} = \frac{\tau_s}{s_u} \cdot \frac{1/\sigma'_{vc}}{1/\sigma'_{vc}} = \frac{\alpha}{s_u/\sigma'_{vc}} = \frac{\alpha}{0.22 \cdot \mathrm{OCR}^{0.8}} \tag{103}$$

which then produces the expression

$$K_\alpha = 1.344 - \frac{0.344}{\left(1 - \frac{\alpha}{0.22 \cdot \mathrm{OCR}^{0.8}}\right)^{0.638}} \tag{104}$$

This equation may be used where an estimate of α can be more readily made, and it allows K_α relationships for clay-like and sand-like soils to be directly compared.

The K_α versus α relationship for saturated clays and plastic silts, computed via equation 104, is plotted in Figure 132 for OCRs of 1, 2, 4, and 8. The K_α values are lowest for normally consolidated soils, and these values increase with increasing OCRs at a given value of α. These curves show how the cyclic strength of normally consolidated clay-like soils may be negligible if they are already sustaining a static shear stress that is close to their undrained shear strength. Conversely, the cyclic strength of an OCR = 8 clay-like soil is reduced only slightly by an α as high as 0.30. This pattern is consistent with that observed for sand-like soils, in that an increasing OCR reduces the contractive tendencies of a clay-like soil in shear. Thus the results for both clay-like and sand-like soils show that, for a given static shear stress ratio, the effect of the static shear stress on cyclic strength is most detrimental for contractive soils.

For more monographs, publications, or videos, visit http://www.eeri.org

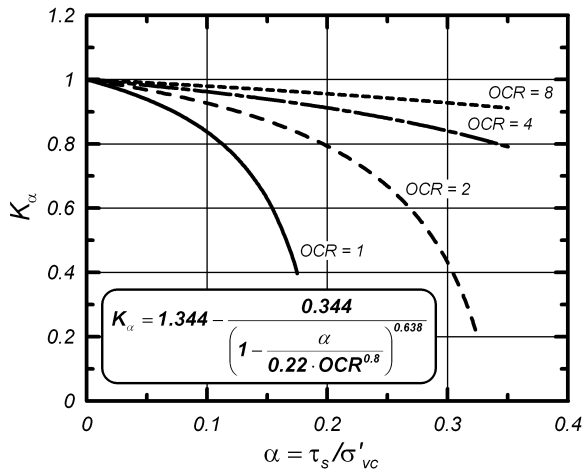

Figure 132. The K_α versus τ_s/σ'_{vc} relationship for clay at different overconsolidation ratios.

6.5 Estimating CRRs

The CRR of saturated clays and plastic silts can be estimated via three different approaches:

- Directly measuring the CRR by cyclic laboratory testing
- Measuring s_u by in-situ or laboratory testing and then multiplying it by an empirical factor to estimate the CRR
- Empirically estimating the CRR on the basis of the stress history profile and the estimated values for the normalized cyclic strength ratios

The successful application of these procedures requires careful attention to the various techniques and issues involved in obtaining s_u profiles from laboratory and in-situ testing programs, as described in Ladd (1991) and Ladd and DeGroot (2003), for example. These various options provide the opportunity to evaluate a site with progressively increasing levels of confidence while considering the potential benefits that additional information may provide, given the uncertainties in the current level of analysis.

Empirically Estimating CRR by Using an Undrained Shear Strength Profile

Values of the CSR for $N = 30$ cycles are plotted against PI in Figure 133a for the soils summarized in Figure 127. The different

For more monographs, publications, or videos, visit http://www.eeri.org

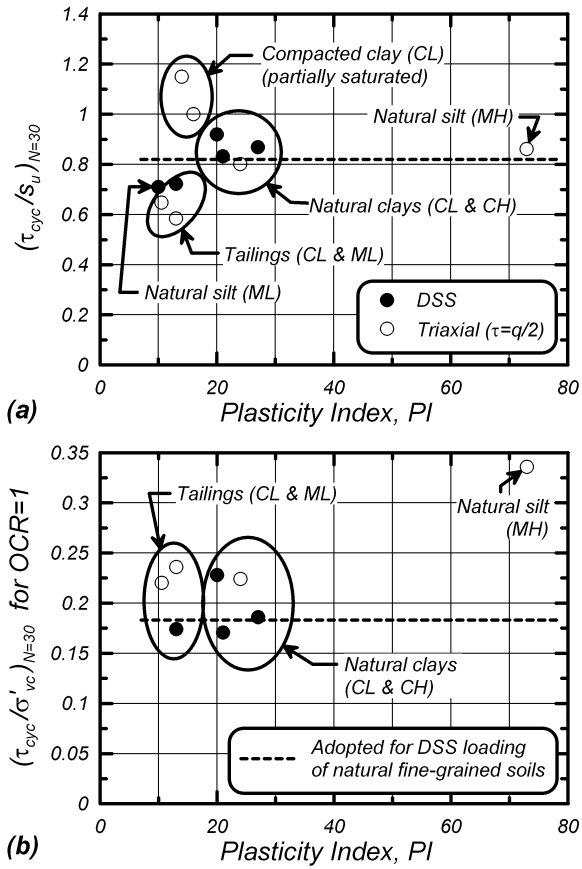

Figure 133. Cyclic strengths for cohesive fine-grained soils and proposed relationships for design: (a) cyclic strength ratios, $(\tau_{cyc}/s_u)_{N=30}$, versus PI and (b) CSRs, $(\tau_{cyc}/\sigma'_{vc})_{N=30}$, for normally consolidated soils versus PI.

types of soils and test conditions are highlighted in this figure, from which the following observations can be made. The tailings materials gave the lowest ratios of τ_{cyc}/s_u, being perhaps about 20% lower than the natural silts and clays. The tailings materials cover a lower range of PIs (10–13) than the natural silts and clays (10–73) and are much younger than the natural silts and clays. Consequently, it is not clear how much of this difference in τ_{cyc}/s_u ratios is due to differences in PI or age. The compacted silty clay and compacted sandy clay by

For more monographs, publications, or videos, visit http://www.eeri.org

Seed and Chan (1966) gave the highest ratios of τ_{cyc}/s_u. These specimens were partially saturated and tested in unconsolidated-undrained conditions, so their state of effective stress was not known.

The triaxial and direct simple shear (DSS) tests gave comparable τ_{cyc}/s_u ratios for the natural silts and clays, whereas the triaxial tests on tailings materials appeared to give τ_{cyc}/s_u ratios that were about 15–20% lower than those obtained in DSS tests on tailings materials. It is clear that the data summarized in Figure 133a are insufficient to clearly define all the various factors that may affect the τ_{cyc}/s_u ratio, such as age, PI, soil type, OCR, and test type. Despite these uncertainties, the data for natural soils do tend to fall within relatively narrow ranges, with $(\tau_{cyc}/s_u)_{N=30} = 0.83$ representing a reasonable average for natural clay-like soils subjected to direct simple shear loading conditions.

The CRR for clay-like fine-grained soils beneath level-ground sites can then be estimated as

$$\mathrm{CRR}_{M=7.5} = C_{2D} 0.83 \cdot \frac{s_u}{\sigma'_{vc}} \tag{105}$$

where C_{2D} is an adjustment factor for the effects of two-directional cyclic loading, as produced by the two horizontal components of earthquake shaking. The value of C_{2D} was estimated to be 0.96 for clays, versus the value of 0.90 recommended for sands by Seed (1979b). These relative C_{2D} values reflect the fact that the second direction of cyclic loading is less damaging for clays than for sands, which is directly related to the fact that the CSR versus the number of cycles to failure relationship is flatter for clays than for sands. With this value for C_{2D}, the $\mathrm{CRR}_{M=7.5}$ for clays can then be estimated as

$$\mathrm{CRR}_{M=7.5} = 0.80 \cdot \frac{s_u}{\sigma'_{vc}} \tag{106}$$

For tailings materials, the above CRR estimate should tentatively be reduced by about 20%, as suggested by the data in Figure 133a.

In many situations, the uncertainty in the s_u profiles will be greater than the uncertainty in the $(\tau_{cyc}/s_u)_{M=7.5}$ ratio, but when the uncertainty in the $(\tau_{cyc}/s_u)_{M=7.5}$ ratio is important, a detailed cyclic laboratory testing program would be beneficial.

For more monographs, publications, or videos, visit http://www.eeri.org

Empirically Estimating CRR by Using a Consolidation Stress History Profile

Cyclic strengths may be similarly computed by combining the empirical $(\tau_{cyc}/s_u)_{M=7.5}$ relationships with the empirical relationships previously described (Section 6.2) that relate s_u to consolidation stress history. The resulting expression for $\mathrm{CRR}_{M=7.5}$ is

$$\mathrm{CRR}_{M=7.5} = 0.80 \cdot S \cdot \mathrm{OCR}^m \tag{107}$$

For homogenous sedimentary clays (CL and CH), the simplest representation may be to use $S = 0.22$ and $m = 0.8$ (Ladd 1991), so that the $\mathrm{CRR}_{M=7.5}$ is estimated as

$$\mathrm{CRR}_{M=7.5} = 0.18 \cdot \mathrm{OCR}^{0.8} \tag{108}$$

Measured values of $(\tau_{cyc}/\sigma'_{vc})_{N=30}$ for the several normally consolidated soils from Figure 127 are plotted versus PI in Figure 133b, from which the following observations can be made. The tailings materials had $(\tau_{cyc}/\sigma'_{vc})_{N=30}$ values that are similar to those for the natural clays, despite their differences in PI and age. The cyclic DSS tests appear to give $(\tau_{cyc}/\sigma'_{vc})_{N=30}$ values that are about 20% smaller than those obtained in cyclic triaxial tests. The monotonic and cyclic shear stresses in triaxial tests were computed as $\tau_{cyc} = q_{cyc}/2$, which means that, if the shear stresses were instead computed for the eventual shear plane as $\tau_{cyc} = (q/2) \cdot \cos(\phi')$, then the $(\tau_{cyc}/\sigma'_{vc})_{N=30}$ values for triaxial tests would have been about 15% smaller (i.e., $\phi' \approx 32°$), and the difference between the DSS and triaxial test results in Figure 133b would have been very small (note that the ratio τ_{cyc}/s_u for triaxial tests is the same for either interpretation of shear stresses). The one natural silt (MH) had the highest $(\tau_{cyc}/\sigma'_{vc})_{N=30}$ value, which may be attributable to its very high PI. However, the other data show no apparent trend with PI.

For practical purposes at this time, the $(\tau_{cyc}/\sigma'_{vc})_{N=30}$ ratio might reasonably be estimated as 0.183, independent of PI, for normally consolidated clay-like fine-grained soils subjected to one-dimensional direct simple shear loading (as shown in Figure 133b). The corresponding $\mathrm{CRR}_{M=7.5}$ value for two-dimensional shaking would then be approximately 0.18, independent of PI. This value is consistent with the above derivation based on $S = 0.22$, $(\tau_{cyc}/s_u)_{N=30} = 0.83$, and $C_{2D} = 0.96$.

For sedimentary deposits of plastic silts and organic soils that plot below the A-line on the Atterberg limits chart, Ladd (1991) suggested that S would more typically be about 0.25, rather than the 0.22 value

For more monographs, publications, or videos, visit http://www.eeri.org

for homogenous sedimentary clays. These S values imply that silts and organic soils that plot below the A-line would have a 14% higher CRR if the $(\tau_{cyc}/s_u)_{N=30}$ ratio were the same for both soil types. The data in Figure 133 are, however, not yet complete enough to clearly define the dependence of CRR values on the various factors of concern, including any potential differences among silts, organic soils, and clays. It is therefore suggested that the CRR of silts and organic soils that plot below the A line but still have a PI $\geq$ 7 may be estimated by using the same expressions previously given for CL and CH soils.

Continued compilations of cyclic laboratory test data on silts and clays can be expected to lead to improved relationships among cyclic strength, consolidation stress history, and soil characteristics.

6.6 Factors of Safety and Choice of Reference Stress

It is instructive to revisit choosing 65% of the peak stress as the reference stress level (i.e., r_e = 0.65) at which both the earthquake-induced CSR and the soil's CRR were determined. For $r_e = 0.65$, the CSR for a given earthquake of magnitude M is

$$\mathrm{CSR}_M = 0.65\frac{\tau_{peak}}{\sigma'_{vc}} \tag{109}$$

where τ_{peak} is the peak shear stress induced by the earthquake. The CRR, based on $r_e = 0.65$ and the empirical relationship between cyclic and monotonic undrained shear strengths, is computed as

$$\mathrm{CRR}_M = 0.80\frac{s_u}{\sigma'_{vc}}\mathrm{MSF} \cdot K_\alpha \tag{110}$$

The factor of safety against cyclic softening (3% shear strain), for cases in which the static shear stress correction factor is unity ($K_\alpha = 1$), can then be expressed as

$$FS_{\gamma=3\%} = \frac{\mathrm{CRR}_M}{\mathrm{CSR}_M} \tag{111}$$

$$FS_{\gamma=3\%} = \frac{0.80\frac{s_u}{\sigma'_{vc}}\mathrm{MSF}}{0.65\frac{\tau_{peak}}{\sigma'_{vc}}} \tag{112}$$

$$FS_{\gamma=3\%} = 1.23\ \mathrm{MSF}\frac{s_u}{\tau_{peak}} \tag{113}$$

For more monographs, publications, or videos, visit http://www.eeri.org

The MSF is limited to a maximum value of 1.13 for small-magnitude earthquakes that can be dominated by a single cycle of loading. In that case, the peak shear stress induced by the earthquake must exceed 139% of the monotonic undrained shear strength to trigger cyclic softening (for shear strains exceeding 3%). This ratio of 1.39 is simply the effect of the loading rate, whereby the shear resistance of cohesive soils is significantly greater during the rapid loading of an earthquake, compared with the very slow loading rates at which the monotonic undrained shear strengths are determined.

For M = 7.5 earthquakes (MSF = 1), the peak shear stress induced by the earthquake must still exceed 123% of the monotonic undrained shear strength to trigger peak strains of 3%. In this case, the ratio of 1.23 represents the combined effects of the loading rate and cyclic degradation from numerous loading cycles.

The procedures for evaluating the potential for cyclic softening in saturated clays and plastic silts may be expressed in a number of different formats, as illustrated by the above equations. In certain applications, the potential for yielding and deformations in cohesive soils may be evaluated by combining stability and Newmark sliding block types of analyses. In other applications, there are advantages to comparing the cyclic resistance of cohesive soils with those of cohesionless soils in a common framework. The procedures presented in this section and in Section 6.5 serve this latter purpose, as well as illustrating the common features and differences of behavior between sands (cohesionless soils) and clays/plastic silts (cohesive soils).

6.7 Transition from Sand-Like to Clay-Like Behavior in Fine-Grained Soils

Fine-grained soils appear to transition from behavior that is more fundamentally like sands to behavior that is more fundamentally like clays over a fairly narrow range of Atterberg limits. On one end of this transition are fine-grained soils that are essentially nonplastic and behave very similarly to sands in most respects. These soils are difficult to sample, are strongly affected by sampling disturbance, and do not exhibit unique stress-history normalized strength properties. The cyclic strengths of these sand-like soils are more appropriately estimated within the framework of liquefaction correlations that are based on in-situ tests. On the other end of the transition are clays and plastic silts that are more easily sampled, are less affected by sampling disturbance, and exhibit stress-history normalized strength

For more monographs, publications, or videos, visit http://www.eeri.org

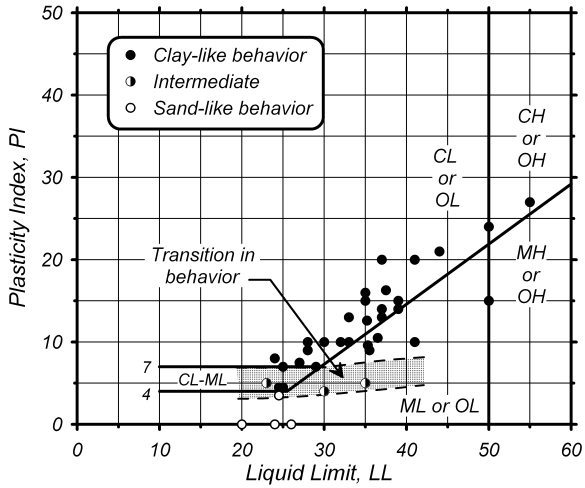

Figure 134. Atterberg limits chart, showing representative values for each soil that exhibited cohesive, cohesionless, or intermediate behavior.

properties. The cyclic strengths of these soils are more appropriately estimated on the basis of information from in-situ testing, laboratory testing, and empirical correlations that are similar to, or that build upon, established procedures for evaluating the monotonic undrained shear strengths of such soils. Thus, the transition from more sand-like to more clay-like behavior has a direct correspondence to the types of engineering procedures that are best suited to evaluating their seismic behavior.

Atterberg limits for fine-grained soils exhibiting a range of behaviors in monotonic and cyclic undrained loading were compiled from the literature and summarized by Boulanger and Idriss (2004b, 2006). Each soil was categorized as exhibiting sand-like, clay-like, or intermediate behavior in the context of the classic behaviors described in Sections 2.1–2.2 and 6.1–6.2. The Atterberg limits for all three groups of soils are plotted together in Figure 134, with a focus on the low-plasticity portion of the chart. The soils exhibiting clay-like behavior included some ML soils with PI values as low as 9 and some CL-ML soils with PI values as low as 4. Intermediate behavior was observed for samples classified as CL-ML and ML with PI values of 4–5. Sand-like behavior was observed only for ML soils (below the A-line) with PI values of 3.5 or smaller.

For more monographs, publications, or videos, visit http://www.eeri.org

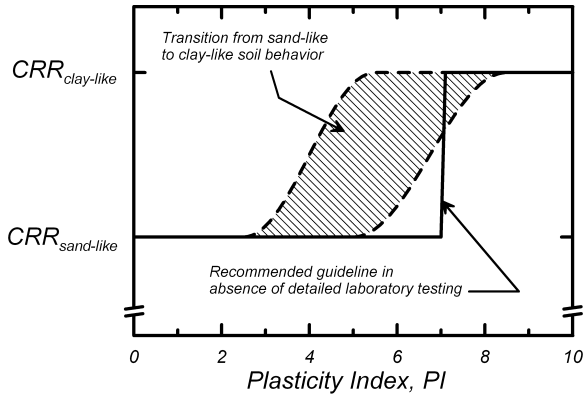

Figure 135. Schematic of the transition from sand-like to clay-like behavior for fine-grained soils with increasing PI, and the recommended guideline for practice.

The transition between sand-like and clay-like behavior in fine-grained soils undoubtedly spans a range of Atterberg limits, both because the actual soil behavior would smoothly transition with increasing plasticity (or clay content) and because a simple index test like the Atterberg limits cannot be expected to provide a perfect correlation with a soil's complex stress-strain characteristics. This transition is schematically illustrated in Figure 135, which shows how the cyclic strength of a soil may reasonably transition as the PI increases from about 3 to 8. In addition, the data in Figure 134 seem to suggest that CL-ML soils would transition more toward the left side of the plotted transition zone, whereas ML soils would transition more toward the right side of that zone. Note that the liquid limit, LL, by itself would not be able to distinguish among the observed behaviors.

In engineering practice, fine-grained soils can reasonably be expected to exhibit clay-like behavior if they have a PI $\geq$ 7. This criterion provides a slightly conservative interpretation of the likely transition interval (Figure 135) and includes all CL soils by definition. If a soil plots as CL-ML, then the PI criterion may be reduced by 1–2 points and still be consistent with the data in Figure 134. The cyclic strengths of these soils should be estimated on the basis of information from in-situ testing, laboratory testing, and empirical correlations that are similar to, or that build upon, established procedures for evaluating the monotonic undrained shear strengths of such soils.

For more monographs, publications, or videos, visit http://www.eeri.org

Fine-grained soils that do not meet the above criteria should be considered soils that probably exhibit sand-like behavior (i.e., they are liquefiable), unless shown to be otherwise through detailed in-situ or laboratory testing. The cyclic strengths of these soils should currently be estimated within the framework of liquefaction correlations that are based on in-situ tests.

Fine-grained soils with PI values of 3–6 may exhibit intermediate behavior, including cyclic strengths that may be greater than those for nonplastic fine-grained soils at the same SPT or CPT penetration resistance. In this case, laboratory testing of low-plasticity silts and clayey silts may provide significant benefits that cannot be attained by relying solely on existing liquefaction correlations. Thus, the above criteria provide a reasonable screening guide, after which the additional possible benefits from more detailed laboratory testing can be assessed with due consideration for the site heterogeneity, level of seismic hazard, and other project-specific conditions.

The above criteria differ from other published liquefaction susceptibility criteria for a number of reasons, as discussed in Boulanger and Idriss (2006). The criteria recommended by Seed and Idriss (1982) were based primarily on case history data from China (Wang 1979), whereas more recent criteria have been guided by combinations of findings from case histories and laboratory testing (e.g., Koester 1992, Pollito 1999, Andrews and Martin 2000, Seed et al. 2003, Bray and Sancio 2006). These other criteria provide envelopes for the characteristics of silts and clays that have been found to develop high excess pore pressures and significant strains in cyclic laboratory tests and/or experience ground failure during earthquakes. The criteria depicted in Figure 134 were instead developed to provide guidance in choosing engineering procedures, with the recognition that soft clays and loose sands can exhibit similar deformation behaviors in the laboratory and the field under certain conditions, but that these behaviors are best analyzed via different procedures.

Fines Content at Which the Fines Fraction Constitutes the Soil Matrix

The preceding discussions have focused on fine-grained soils (i.e., silts and clays) for which the fines content is greater than 50% by definition, but in certain cases the same findings may be extended to soils with slightly lower fines content. The key issue is whether or not the fines fraction constitutes the stress-carrying matrix or skeleton for the soil mass, with the larger sand-sized (or larger) particles

For more monographs, publications, or videos, visit http://www.eeri.org

essentially floating (because they are isolated from each other) within the matrix. For many soils, it is likely that the fines fraction forms the load-carrying matrix when the fines fraction exceeds roughly 35%, but the transition may occur at higher or lower fines content in any specific soil, depending on factors such as the soil's full gradational characteristics, mineralogical composition, particle shapes, and depositional environment or fabric (e.g., Mitchell and Soga 2005). For projects in which this transition point is of critical importance, it would be prudent to perform an appropriate program of in-situ and laboratory testing to evaluate the soil's behavior characteristics before extending these criteria to fines content that is less than 50%.

6.8 Consequences of Cyclic Softening in Clays and Plastic Silts

The consequences of cyclic softening in clay-like fine-grained soils, with respect to potential deformations or instability, depends on the soil's sensitivity (S_t), which is defined as

$$S_t = \frac{s_u}{s_{ur}} \tag{114}$$

where s_u is the intact undrained shear strength, and s_{ur} is the fully remolded undrained shear strength. The sensitivity of natural clay-like soils can be related to the effective consolidation stress and liquidity index:

$$\mathrm{LI} = \frac{w_n - \mathrm{PL}}{\mathrm{LL} - \mathrm{PL}} \tag{115}$$

where w_n is the natural water content, as shown in Figure 136. Soft, normally consolidated or lightly overconsolidated clays will generally have higher natural water content, higher liquidity index (LI) values, and higher sensitivities and will therefore be most prone to strength loss during earthquakes. Well-compacted and heavily overconsolidated clays will have lower natural water content, have lower LI values, and be generally insensitive to remolding. Consequently, with all else being equal, potential ground deformations that arise from cyclic softening may range from relatively severe in natural quick clays (i.e., $S_t > 8$) to relatively minor in well-compacted or heavily overconsolidated clays.

This aspect of behavior is analogous to the fact that the consequences of liquefaction in sands are much more severe for loose sands than for medium-to-dense sands, as reflected in the correlations that

For more monographs, publications, or videos, visit http://www.eeri.org

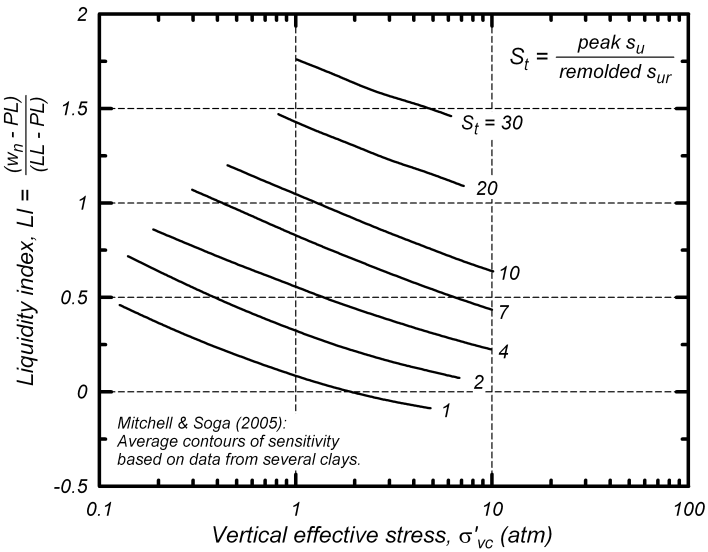

Figure 136. The relationship among sensitivity, LI, and effective consolidation stress (after Mitchell and Soga 2005).

show residual shear strengths increasing and potential shear strains decreasing as the SPT $(N_1)_{60}$ value increases. Thus cyclic softening of clay-like soils should not necessarily be assumed to imply that a major problem exists, but rather that the potential deformations must be evaluated.

Potential deformations in clay-like fine-grained soils may be estimated by a Newmark sliding block type of analysis, by integrating estimated shear or volumetric strains over the thickness of the deforming strata, or by nonlinear dynamic analyses. Factors affecting one-dimensional settlement caused by postshaking reconsolidation of clay layers are discussed in Ohara and Matsuda (1988), Matsuda and Ohara (1991), and Fiegel et al. (1998). The analytical method chosen depends on the specific problem and the expected mode of deformations. In some cases, the parallel application of both methods may provide valuable insights. In this regard, the future development of relationships among the factor of safety against cyclic softening, shear strains, reconsolidation strains, sensitivity, and eventual strength loss would be beneficial.

The magnitude of strain or ground displacement that will reduce the clay's undrained shear strength to its fully remolded value

For more monographs, publications, or videos, visit http://www.eeri.org

is currently difficult to assess. It is generally recognized that it would take less ground displacement to fully remold a very brittle soil (e.g., quick clay) than to remold a more ductile soil (i.e., relatively insensitive clay), but defining the transition from peak to remolded shear strengths is complicated by limitations in our experimental methods and our ability to predict shear localizations in the field. Experiences from case histories provide only limited guidance about this issue, and thus additional research is needed to reliably define this aspect of behavior.

Determining the stress history and determining the sensitivity of clay-like fine-grained soils are therefore two key tasks for evaluating both the potential for cyclic softening and the potential consequences of cyclic softening. Increasing the OCR has a very strong effect on the cyclic behavior of natural clay-like soils, because the OCR affects both the resistance to cyclic softening (i.e., the CRR) and the potential consequences of cyclic softening. For example, clay with an OCR of 8.0 versus 1.0 would have more than five times the cyclic strength, would be far less affected by the presence of static shear stresses such as those in slopes, and would generally be much less sensitive to remolding.

For more monographs, publications, or videos, visit http://www.eeri.org

For more monographs, publications, or videos, visit http://www.eeri.org

REFERENCES

Akiba, M., and Semba, H., 1941. The earthquake and its influence on reservoirs in Akita prefecture, *J. Agric. Eng. Soc.* Japan **13**(1), 31–59.

Ambraseys, N. N., 1988. Engineering seismology, *Earthquake Eng. and Structural Dynamics* **17**(1), 1–105.

Andersen, K, Kleven, A., and Heien, D., 1988. Cyclic soil data for design of gravity structures, *J. Geotechnical Eng. Div.,* ASCE **114**(5), 517–39.

Andersen, K. H., 1976. Behavior of clay subjected to undrained cyclic loading, in *Proceedings, Conference on Behavior of Off-Shore Structures,* Trondheim, Norway, Vol. 1, pp. 392–403.

Andrews, D. C. A., and Martin, G. R., 2000. Criteria for liquefaction of silty soils, in *Proceedings, 12th World Conference on Earthquake Engineering,* Auckland, New Zealand.

Andrus, R. D., and Stokoe, K. H., 2000. Liquefaction resistance of soils from shear-wave velocity, *J. Geotechnical and Geoenvironmental Eng.,* ASCE **126**(11), 1015–025.

Andrus, R. D., Stokoe, K. H., Chung, R. M., and Juang, C. H., 2003. *Guidelines for Evaluating Liquefaction Resistance Using Shear Wave Velocity Measurements and Simplified Procedures,* NIST GCR 03-854, National Institute of Standards and Technology, Gaithersburg, MD.

Arango, I., 1996. Magnitude scaling factors for soil liquefaction evaluations, *J. Geotechnical Eng.,* ASCE 122(11), 929–36, 1996.

Arulanandan, K., Seed, H. B., Yogachandran, C., Muraleetharan, K., and Seed, R. B., 1993. Centrifuge study on volume changes and dynamic stability of earth dams., *J. Geotech. Eng.,* ASCE **119**(11), 1717–731.

Azzouz, A. S., Malek, A. M., and Baligh, M. M., 1989. Cyclic behavior of clays in undrained simple shear, *J.Geotechnical Eng. Div*., ASCE **115**(5): 637–57.

For more monographs, publications, or videos, visit http://www.eeri.org

Babasaki, R., Suzuki, K., Saitoh, S., Suzuki, Y., and Tokitoh, K., 1991. *Construction and Testing of Deep Foundation Improvement Using the Deep Cement Mixing Method,* Deep Foundation Improvements: Design, Construction, and Testing, ASTM STP 1089, Esrig and Bachus, eds., Philadelphia, PA.

Balakrishnan, A., and Kutter, B. L., 1999. Settlement, sliding, and liquefaction remediation of layered soil, *J. Geotech. Eng.,* ASCE **125**(11), 968–78.

Bardet, J.-P., Rathje, E. M., and Stewart, J. P., principal authors, 2002b. Chapter 8: Ports. *Bhuj, India Earthquake of January 26, 2001 Reconnaissance Report,* Jain, S. K., Lettis, W. R., Murty, C. V. R., and Bardet, J. P., eds., *Earthquake Spectra,* Supplement A to vol. **18**, 101–30.

Bardet, J.-P., Tobita, T., Mace, N., and Hu, J., 2002a. Regional modeling of liquefaction-induced ground deformation, *Earthquake Spectra,* EERI **18**(1), 19–46.

Bartlett, S. F., and Youd, T. L., 1995. Empirical prediction of liquefaction-induced lateral spread, *J. Geotechnical Eng.,* ASCE **121**(4), 316–29.

Been, K., and Jefferies, M. G., 1985. A state parameter for sands, *Geotechnique* **35**(2), 99–112.

Berrill, J. B., Christensen, S. A., Keenan, R. J., Okada, W., and Pettinga, J. R., 1997. Lateral-spreading loads on a piled bridge foundation, in *Proceedings, Seismic Behavior of Ground and Geotechnical Structures,* Balkema, Rotterdam, pp. 173–83.

Bolton, M. D., 1986. The strength and dilatancy of sands, *Geotechnique* **36**(1), 65–78.

Bouckovalas, G., and Dakoulas, P., 2007. Liquefaction performance of shallow foundations in presence of a soil crust, in *Earthquake Geotechnical Engineering, 4th International Conference on Earthquake Geotechnical Engineering–Invited Lectures,* K. D. Pitilakis, ed., Springer, Netherlands, 245–76.

Boulanger, R. W., 2003a. Relating K_α to relative state parameter index, *J. Geotechnical and Geoenvironmental Eng.,* ASCE **129**(8), 770–73.

Boulanger, R. W., 2003b. High overburden stress effects in liquefaction analyses, *J. Geotechnical and Geoenvironmental Eng.,* ASCE **129**(12), 1071–082.

Boulanger, R. W. and Idriss, I. M., 2004a. State normalization of penetration resistances and the effect of overburden stress on liquefaction resistance, in *Proceedings, 11th International Conference on*

For more monographs, publications, or videos, visit http://www.eeri.org

Soil Dynamics and Earthquake Engineering, and 3rd International Conference on Earthquake Geotechnical Engineering, D. Doolin et al., eds., Stallion Press, Vol. 2, pp. 484–91.

Boulanger, R. W., and Idriss, I. M., 2004b. *Evaluating the Potential for Liquefaction or Cyclic Failure of Silts and Clays,* Report No. UCD/CGM-04/01, Center for Geotechnical Modeling, Department of Civil and Environmental Engineering, University of California, Davis.

Boulanger, R. W., and Idriss, I. M., 2006. Liquefaction susceptibility criteria for silts and clays, *J. Geotechnical and Geoenvironmental Eng.,* ASCE **132**(11), 1413–426.

Boulanger, R. W., and Idriss, I. M., 2007. Evaluation of cyclic softening in silts and clays, *J. Geotechnical and Geoenvironmental Eng.,* ASCE **133**(6), 641–52.

Boulanger, R. W., Idriss, I. M., and Mejia, L. H., 1995. *Investigation and Evaluation of Liquefaction Related Ground Displacements at Moss Landing during the 1989 Loma Prieta Earthquake,* Report No. UCD/CGM-95/02, Center for Geotechnical Modeling, Department of Civil and Environmental Engineering, University of California, Davis, May.

Boulanger, R. W., Mejia, L. H., and Idriss, I. M.,1999. Closure to liquefaction at Moss Landing during Loma Prieta earthquake, *J. Geotechnical and Geoenvironmental Eng.,* ASCE **125**(1), 92–96.

Boulanger, R. W., Mejia, L. H., and Idriss, I. M., 1997. Liquefaction at Moss Landing during Loma Prieta earthquake, *J. Geotechnical and Geoenvironmental Eng,* ASCE **123**(5), 453–67.

Boulanger, R. W., Meyers, M. W., Mejia, L. H., and Idriss, I. M., 1998. Behavior of a fine-grained soil during Loma Prieta earthquake, *Canadian Geotechnical J.* **35**, 146–58.

Boulanger, R. W., Seed, R. B., Chan, C. K., Seed, H. B., and Sousa, J. B., 1991. *Liquefaction Behavior of Saturated Sands under Uni-Directional and Bi-Directional Monotonic and Cyclic Simple Shear Loading,* Geotechnical Engineering Report No. UCB/GT/91-08, University of California, Berkeley, August.

Boulanger, R. W., and Truman, S. P., 1996. Void redistribution in sand under post-earthquake loading, *Canadian Geotechnical J.* **33**, 829–34.

Brandenberg, S. J., Singh, P., Boulanger, R. W., and Kutter, B. L., 2001. *Behavior of Piles in Laterally Spreading Ground During Earthquakes,* Centrifuge data report for SJB02, UCD/CGMDR-01/06, Center for Geotechnical Modeling, University of California, Davis.

For more monographs, publications, or videos, visit http://www.eeri.org

Bray, J. D., and Sancio, R. B., 2006. Assessment of the liquefaction susceptibility of fine-grained soils, *J. Geotechnical and Geoenvironmental Eng.,* ASCE **132**(9), 1165–177.

Bray, J. D., Sancio, R. B., Durgunoglu, T., Onalp, A., Youd, T. L., Stewart, J. P., Seed, R. B., Cetin, O. K., Bol, E., Baturay, M. B., Christensen, C., and Karadayilar, T., 2004. Subsurface characterization at ground failure sites in Adapazari, Turkey, *J. Geotechnical and Geoenvironmental Eng.,* ASCE **130**(7), 673–85.

Bray, J. D., and Travasarou, T., 2007. Simplified procedure for estimating earthquake-induced deviatoric slope displacements, *J. Geotechnical and Geoenvironmental Eng.,* ASCE **133**(4), 381–92.

Byrne, P. M., and Beaty, M. H., 1997. Post-liquefaction shear strength of granular soils: theoretical/conceptual issues, in *Proceedings, Workshop on Post-Liquefaction Shear Strength of Granular Soils,* Urbana-Champaign, IL, April 17–18, pp. 16–45.

Cao, Y. L., and Law, K. Y., 1991. Energy approach for liquefaction of sandy and clayey silts, Paper 3.38, in *Proceedings, 2nd International Conference on Recent Advances in Geotechnical Earthquake Engineering and Soil Dynamics,* University of Missouri, Rolla, MO.

Casagrande, A., 1976. *Liquefaction and Cyclic Deformation of Sands–a Critical Review,* Harvard Soil Mechanics Series No. 88, Harvard University, Cambridge, MA.

Castro, G., 1975. Liquefaction and cyclic mobility of saturated sands, *J. Geotechnical Eng. Div.,* ASCE **101**(GT6), 551–69.

Castro, G., 2008. Personal communication.

Castro, G., Keller, T. O., and Boynton, S. S., 1989. *Re-evaluation of the Lower San Fernando Dam–Report 1: an Investigation of the February 9, 1971 Slide,* Contract Report GL-89-2, Vols. 1–2, U.S. Army Engineer Waterways Experiment Station, Vicksburg, MS.

Castro, G., and Poulos, S. J., 1977. Factors affecting liquefaction and cyclic mobility, *J. Geotechnical Eng. Div.,* ASCE **103**(GT6), 501–06.

Cetin, K. O., Seed, R. B., Der Kiureghian, A., Tokimatsu, K., Harder, L. F., Kayen, R. E., and Moss, R. E. S., 2004. Standard penetration test-based probabilistic and deterministic assessment of seismic soil liquefaction potential, *J. Geotechnical and Geoenvironmental Eng.,* ASCE **130**(12), 1314–340.

Cetin, K. O., Seed, R. B., Moss, R. E. S., Der Kiureghian, A. K., Tokimatsu, K., Harder, L. F., and Kayen, R. E., 2000. *Field Performance Case Histories for SPT-Based Evaluation of Soil*

For more monographs, publications, or videos, visit http://www.eeri.org

Liquefaction Triggering Hazard, Geotechnical Engineering Research Report No. UCB/GT-2000/09, Geotechnical Engineering, Department of Civil Engineering, University of California at Berkeley.

Chu, D. B., Stewart, J. P., Lee, S., Tsai, J. S., Lin, P. S., Chu, B. L., Seed, R. B., Hsu, S. C., Yu, M. S., Wang, M. C. H., 2004. Documentation of soil conditions at liquefaction and nonliquefaction sites from 1999 Chi-Chi (Taiwan) earthquake, *Soil Dynamics and Earthquake Eng.* **24**(9–10), 647–57.

Chu, D. B., Stewart, J. P., Lin, P. S., and Boulanger, R. W., 2007. Cyclic softening of low-plasticity clay and its effect on seismic foundation performance, *Earthquake Geotechnical Engineering, 4th International Conference on Earthquake Geotechnical Engineering–Conference Presentations,* Springer, Netherlands, paper 1490.

Chu, D. B., Stewart, J. P., Youd, T. L., and Chule, B. L., 2006. Liquefaction-induced lateral spreading in near-fault regions during the 1999 Chi-Chi, Taiwan earthquake, *J. Geotechnical and Geoenvironmental Eng.,* ASCE **132**(12), 1549–565.

Cubrinovski, M., and Ishihara, K., (1999). Empirical correlation between SPT N-value and relative density for sandy soils, *Soils and Foundations,* Japanese Geotechnical Society **39**(5), 61–71.

Daniel, C. R., Howie, J. A., Jackson, R. S., and Walker, B., 2005. Review of standard penetration test short rod corrections, *J. Geotechnical and Geoenvironmental Eng.,* ASCE **131**(4), 489–97.

Daniel, C. R., Howie, J.A., and Sy, A., 2003. A method for correlating large penetration test (LPT) to standard penetration test (SPT) blow counts, *Canadian Geotechnical J.* **40**, 66–77.

Davis, A. P., Poulos, S. J., and Castro, G., 1988. Strengths back figured from liquefaction case histories, in *Proceedings, 2nd International Conference on Case Histories in Geotechnical Engineering,* St. Louis, MO, pp.1693–701.

Davis, R. O., and Berrill, J. B., 1978. Energy dissipation and seismic liquefaction in sands, *Earthquake Eng. and Structural Dynamics,* **10**, 598.

DeAlba, P., Seed, H. B., and Chan, C. K., 1976. Sand liquefaction in large scale simple shear tests, *J. Geotechnical Eng. Div.,* ASCE **102**(GT9), 909–27.

Desrues, J., Chambon, R., Mokni, M., and Mazerolle, F., 1996. Void ratio evolution inside shear bands in triaxial sand specimens studied by computed tomography, *Geotechnique,* London **46**(2), 529–46.

Dobry, R., 1985. Personal communication.

For more monographs, publications, or videos, visit http://www.eeri.org

Dobry, R., and Liu, L., 1992. Centrifuge modeling of soil liquefaction, in *Proceedings, 10th World Conference on Earthquake Engineering,* Madrid, Spain, pp. 6801–809.

Douglas, B. J., Olson, R. S., and Martin, G. R., 1981. Evaluation of the cone penetrometer test for SPT liquefaction assessment, Preprint 81 544, *Session on In Situ Testing to Evaluate Liquefaction Susceptibility, ASCE National Convention,* St. Louis, MO, October.

Duku, P. M., Stewart, J. P., and Whang, D. H., 2008. Volumetric strains of clean sands subject to cyclic loads, *J. Geotechnical and Geoenvironmental Eng.,* ASCE, in press.

Egan, J. A., and Rosidi, D., 1991. Assessment of earthquake-induced liquefaction using ground-motion energy characteristics, in *Proceedings, Pacific Conference on Earthquake Engineering,* New Zealand.

Elgamal, A. W., Dobry, R., and Adalier, K., 1989. Study of effect of clay layers on liquefaction of sand deposits using small-scale models, in *Proceedings, 2nd U.S.-Japan Workshop on Liquefaction, Large Ground Deformation and Their Effects on Lifelines*. NCEER, SUNY-Buffalo, Buffalo, NY, pp. 233–45.

Elorza, O., and Machado, M. R., 1929. Report on causes of failure of Barahona Dam, *Boletin del Museo Nacional de Chile* (in Spanish).

Faris, A. T., 2004. *Probabilistic Models for Engineering Assessment of Liquefaction-Induced Lateral Spreading Displacements,* Ph.D. thesis, University of California at Berkeley, 436 pp.

Faris, A. T., Seed, R. B., Kayen, R. E., and Wu, J., 2006. A semi-empirical model for the estimation of maximum horizontal displacement due to liquefaction-induced lateral spreading, *8th National Conference on Earthquake Engineering,* EERI, San Francisco, CA.

Fiegel, G. L., and Kutter B. L., 1994. Liquefaction-induced lateral spreading of mildly sloping ground, *J. Geotechnical Eng.,* ASCE **120**(12), 2236–243.

Fiegel, G. L., Kutter, B. L., and Idriss, I. M., 1998. Earthquake-induced settlement of soft clay, in *Proceedings, Centrifuge 98,* Balkema, Rotterdam (1), pp. 231–36.

Figueroa, J. L., Saada, A. S., Liang, L, and Dahisaria, N. M., 1994. Evaluation of soil liquefaction by energy principles, *J. Geotechnical and Geoenvironmental Eng.,* ASCE **120**(9), 1554–569.

Finn, W. D. L., 1981. Liquefaction potential: developments since 1976, in *Proceedings, International Conference on Recent*

For more monographs, publications, or videos, visit http://www.eeri.org

Advances in Geotechnical Earthquake Engineering and Soil Dynamics, University of Missouri, Rolla, MO, pp. 655–81.

Finn, W. D. L., Bransby, P. L., Pickering, D. J., 1970. Effect of strain history on liquefaction of sand, *J. Soil Mechanics and Foundations Div.,* ASCE **96**(SM6), 1917–934.

Finn, W. D. L., Pickering, D. J., and Bransby, P. L., 1971. Sand liquefaction in triaxial and simple shear tests, *J. Soil Mechanics and Foundations Div.,* ASCE **97**(SM4), 639–59.

Finno, R. J., and Rechenmacher, A. L., 2003. Effects of consolidation history on critical state of sand, *J. Geotechnical and Geoenvironmental Eng.,* ASCE **129**(4), 350–60.

Frost, J. D., and Jang, D.-J., 2000. Evolution of sand microstructure during shear, *J. Geotechnical and Geoenvironmental Eng.,* ASCE **126**(2), 116–30.

Gazetas, G., and Uddin, N., 1994. Permanent deformation on pre-existing sliding surfaces in dams, *J. Geotechnical Eng.,* ASCE **120**(11), 2041–061.

Gilbert, P.A., 1984. *Investigation of Density Variation in Triaxial Test Specimens of Cohesionless Soil Subjected to Cyclic and Monotonic Loading,* Technical Report No. GL-84-10, U.S. Army Corps of Engineers, Waterways Experiment Station, Vicksburg, MS, September.

Golesorkhi, R., 1989. *Factors Influencing the Computational Determination of Earthquake-Induced Shear Stresses in Sandy Soils,* Ph.D. thesis, University of California at Berkeley, 395 pp.

Goodman, R. E., and Seed, H. B., 1966. Earthquake-induced displacements in sand embankments, *J. Soil Mechanics and Foundations Div.,* ASCE **92**(SM2), 125–46.

Goto, S., and Nishio, S., 1988. Influence of freeze thaw history on undrained cyclic strength of sandy soils (in Japanese), in *Proceedings, Symposium on Undrained Cyclic Tests on Soils, Japanese Society for Soil Mechanics and Foundation Engineering,* pp. 149–54.

Goulois, A. M., Whitman, R. V., and Hoeg, K., 1985. *Effects of sustained Shear Stresses on the Cyclic Degradation of Clay,* Strength Testing of Marine Sediments: Laboratory and In-Situ Strength Measurements, ASTM STP 883, R. C. Chaney and K. R. Demars, eds., ASTM, Philadelphia, PA, pp. 336–51.

Green, R. A., and Terri, G. A., 2005. Number of equivalent cycles concept for liquefaction evaluations—revisited, *J. Geotechnical and Geoenvironmental Eng.,* ASCE **131**(4), 477–88.

For more monographs, publications, or videos, visit http://www.eeri.org

Hamada, M., 1992. *Large ground Deformations and Their Effects on Lifelines: 1964 Niigata Earthquake,* Case Studies of Liquefaction and Lifeline Performance During Past Earthquakes. Vol. 1: Japanese Case Studies, Technical Report NCEER-92-0001, pp. 3.1–3.123.

Hamada, M., and Wakamatsu, K., 1996. *Liquefaction, Ground Deformation and Their Caused Damage to Structures,* The 1995 Hyogoken-Nanbu earthquake–Investigation into Damage to Civil Engineering Structures, Committee of Earthquake Engineering, Japan Society of Civil Engineers, pp. 45–92.

Hansen, W. R., 1971. Effects at Anchorage, the Great Alaska earthquake of 1964, *Geology,* Part A, National Academy of Sciences, 5–43.

Harden, B. O., and Drnevich, V. P., 1972. Shear modulus and damping in soils. *J. Soil Mechanics and Foundations Division,* ASCE **98**(7), 667–692.

Harder, L. F., 1997. Application of the Becker Penetration test for evaluating the liquefaction potential of gravelly soils, in *Proceedings, NCEER Workshop on Evaluation of Liquefaction Resistance of Soils,* National Center for Earthquake Engineering Research, Buffalo, NY, 129–48.

Harder, L. F., and Boulanger, R. W., 1997. Application of K_σ and K_α correction factors, in *Proceedings, NCEER Workshop on Evaluation of Liquefaction Resistance of Soils,* T. L. Youd and I. M. Idriss, Eds., Technical Report NCEER-97-0022, National Center for Earthquake Engineering Research, SUNY, Buffalo, NY, pp. 167–90.

Harder, L. F., and Stewart, J. P., 1996. Failure of Tapo Canyon Tailings Dam, *J. Performance of Constructed Facilities* **10**(3), 109–14.

Hausler, E. A., and Sitar, N., 2001. Performance of soil improvement techniques during earthquakes, *4th International Conference on Recent Advances in Geotechnical Earthquake Engineering and Soil Dynamics,* Paper 10.15.

Holzer, T. L., and Bennett, M. J., 2007. Geologic and hydrogeologic controls of boundaries of lateral spreads: lessons from USGS liquefaction case histories, *First North American Landslide Conference,* Vail, CO, June 3–8.

Hsu, C., and Vucetic, M., 2004. Volumetric threshold shear strain for cyclic settlement, *J. Geotechnical and Geoenvironmental Eng.,* ASCE **130**(1), 58–70.

For more monographs, publications, or videos, visit http://www.eeri.org

Hussin, J. D., and Ali, S., 1987. *Soil Improvement at the Trident Submarine Facility,* Soil improvement–a ten year update; Geotechnical Special Publication No. 12, J. P. Welsh, ed., ASCE, 215–31.

Hynes, M. E., and Olsen, R., 1998. Influence of confining stress on liquefaction resistance, in *Proceedings, International Symposium on the Physics and Mechanics of Liquefaction,* Balkema, Rotterdam, pp. 145–52.

Hyodo, M., Yamamoto, Y., and Sugiyama, M., 1994. Undrained cyclic shear behavior of normally consolidated clay subjected to initial static shear stress, *Soils and Foundations,* Japanese Society of Soil Mechanics and Foundation Engineering **34**(4), 1–11.

Iai, S., and Koizumi, K., 1986. Estimation of earthquake induced excess pore water pressure for gravel drains, in *Proceedings, 7th Japan Earthquake Engineering Symposium,* pp. 679–84.

Idriss, I. M., 1985. Evaluating seismic risk in engineering practice, in *Proceedings, 11th International Conference on Soil Mechanics and Foundation Engineering,* San Francisco, Balkema, Rotterdam, pp. 265–320.

Idriss, I. M., 1999. An update to the Seed-Idriss simplified procedure for evaluating liquefaction potential, in *Proceedings, TRB Workshop on New Approaches to Liquefaction,* Publication No. FHWA-RD-99-165, Federal Highway Administration, January.

Idriss, I. M., and Boulanger, R. W., 2003a. Estimating K_α for use in evaluating cyclic resistance of sloping ground, in *Proceedings, 8th US-Japan Workshop on Earthquake Resistant Design of Lifeline Facilities and Countermeasures against Liquefaction,* Hamada, O'Rourke, and Bardet, eds., Report MCEER-03-0003, MCEER, SUNY Buffalo, NY, pp. 449–68.

Idriss, I. M., and Boulanger, R. W., 2003b. Relating K_α and K_σ to SPT blow count and to CPT tip resistance for use in evaluating liquefaction potential, in *Proceedings of the 2003 Dam Safety Conference,* ASDSO, September 7–10, Minneapolis, MN.

Idriss, I. M., and Boulanger, R. W., 2004. Semi-empirical procedures for evaluating liquefaction potential during earthquakes, in *Proceedings, 11th International Conference on Soil Dynamics and Earthquake Engineering, and 3rd International Conference on Earthquake Geotechnical Engineering,* D. Doolin et al., eds., Stallion Press, Vol. 1, pp. 32–56.

Idriss, I. M., and Boulanger, R. W., 2006. Semi-empirical procedures for evaluating liquefaction potential during earthquakes, *J. Soil Dynamics and Earthquake Eng.* **26**, 115–30.

For more monographs, publications, or videos, visit http://www.eeri.org

Idriss, I. M., and Boulanger, R. W., 2007. SPT- and CPT-based relationships for the residual shear strength of liquefied soils, *Earthquake Geotechnical Engineering, 4th International Conference on Earthquake Geotechnical Engineering–Invited Lectures,* K. D. Pitilakis, ed., Springer, Netherlands, pp.1–22.

Ishibashi, I. and Sherif, M., 1974. Soil liquefaction by torsional simple shear device, *J. Geotechnical Eng. Div.,* ASCE **100**(GT8), 871–88.

Ishihara, K., 1985. Stability of natural deposits during earthquakes, in *Proceedings, 11th International Conference on Soil Mechanics and Foundation Engineering,* San Francisco, A. A. Balkema, Rotterdam, pp. 321–376.

Ishihara, K., 1993. Liquefaction and flow failure during earthquakes, *Geotechnique* **43**(3), 351–415.

Ishihara, K., 1996. *Soil Behavior in Earthquake Geotechnics,* The Oxford Engineering Science Series, No. 46.

Ishihara, K., Iwamoto, S., Yasuda, S., and Takatsu, H., 1977. Liquefaction of anisotropically consolidated sand, in *Proceedings, 9th International Conference on Soil Mechanics and Foundation Engineering,* Japanese Society of Soil Mechanics and Foundation Engineering, Tokyo, Japan **2,** pp. 261–64.

Ishihara, K., and Nagase, H., 1980. Cyclic simple shear tests on saturated sand in multi-directional loading, in Ishihara, K., and Yamazaki, A., *Soils and Foundations,* Japanese Society of Soil Mechanics and Foundation Engineering, **20**(1), March, closure to discussion.

Ishihara, K., and Takatsu, H., 1979. Effects of overconsolidation and K_0 conditions on the liquefaction characteristics of sands, *Soils and Foundations,* Japanese Society of Soil Mechanics and Foundation Engineering **19**(4), 59–68.

Ishihara, K, Tatsuoka, F., and Yasuda, S., 1975. Undrained deformation and liquefaction of sand under cyclic stresses, *Soils and Foundations* **15**, 29–44.

Ishihara, K., Verdugo, R. L., and Acacio, A. A., 1991. Characterization of cyclic behavior of sand and post-seismic stability analyses, in *Proceedings, 9th Asian Regional Conference on Soil Mechanics and Foundation Engineering,* Bangkok, Thailand, Vol. 2, pp. 45–70.

Ishihara, K, Yamazaki, A, and Haga, K., 1985. Liquefaction of *Ko*-consolidated sand under cyclic rotation of principal stress direction with lateral constraint, *Soils and Foundations,* Japanese Society of Soil Mechanics and Foundation Engineering **5**(4), 63–74.

For more monographs, publications, or videos, visit http://www.eeri.org

Ishihara, K., and Yoshimine, M., 1992. Evaluation of settlements in sand deposits following liquefaction during earthquakes, *Soils and Foundations* **32**(1), 173–88.

Jefferies, M. G., and Davies, M. P., 1993. Use of CPTu to estimate equivalent SPT N_{60}, *ASTM Geotechnical Testing J.* **16**(4), 458–67.

Juang, C. H., Jiang, T. J., and Andrus, R. D., 2002. Assessing probability-based methods for liquefaction potential evaluation, *J. Geotechnical and Geoenvironmental Eng.* **128**(7), 580–589.

Kawakami, F., and Asada, A., 1966. Damage to the ground and earth structures by the Niigata earthquake of June 16, 1964, *Soils and Foundations* **1**, 14–30.

Kawasumi, Hirosi, ed., 1968. *General report on the Niigata earthquake of 1964.* Tokyo: Electrical Engineering College Press, 550 pp.

Kayen, R. E., and Mitchell, J. K., 1997. Assessment of liquefaction potential during earthquakes by Arias intensity, *J. Geotechnical and Geoenvironmental Eng.* **123**(12), 1162–174.

Kerwin, S. T., and Stone, J. J., 1997. Liquefaction failure and remediation: King Harbor Redondo Beach, California, *J. Geotechnical and Geoenvironmental Eng.* **123**(8), 760–69.

Kishida, H., 1966. Damage to reinforced concrete buildings in Niigata City with Special reference to foundation engineering, *Soils and Foundations,* Japanese Society of Soil Mechanics and Foundation Engineering, **6**(1),71–86.

Kishida, T., 2008. Seismic site effects for the Sacramento-San Joaquin Delta, Ph.D. dissertation, University of California, Davis, 261 pp.

Kitazume, M., 2005. *The Sand Pile Compaction Method,* Taylor and Francis, London, UK, 271 pp.

Koester, J. P., 1992. The influence of test procedure on correlation of Atterberg limits with liquefaction in fine-grained soils, *Geotechnical Testing J.*, ASTM **15**(4), 352–60.

Kokusho, T., 1999. Water film in liquefied sand and its effect on lateral spread, *J. Geotechnical Eng.,* ASCE **125**(10), 817–26.

Kokusho, T., 2000. Mechanism for water film generation and lateral flow in liquefied sand layer, *Soils and Foundations* **40**(5), 99–111.

Kokusho., T and Kojima, T., 2002. Mechanism for postliquefaction water film generation in layered sand, *J. Geotechnical Eng.,* ASCE **128**(2), 129–37.

Konrad, J.-M., 1988. Interpretation of flat plate dilatometer tests in sands in terms of the state parameter, *Geotechnique* **38**(2), 263–77.

For more monographs, publications, or videos, visit http://www.eeri.org

Kovacs, W. D., Salomone, L. A., and Yokel, F. Y., 1983. *Comparison of energy Measurements in the Standard Penetration Test Using the Cathead and Rope Method,* National Bureau of Standards Report to the U.S. Nuclear Regulatory Commission, November.

Kramer, S. L., and Mayfield, R. T., 2007. Return period of soil liquefaction, *J. Geotechnical and Geoenvironmental Eng.,* ASCE **133**(7), 802–13.

Kramer, S. L., and Smith, M. W., 1997. Modified Newmark model for seismic displacements of compliant slopes, *J. Geotechnical Eng.,* ASCE **123**(7), 635–44.

Kulasingam, R., Boulanger, R. W., and Idriss, I. M., 1999. Evaluation of CPT liquefaction analysis methods against inclinometer data from Moss Landing, in *Proceedings, 7th US-Japan Workshop on Earthquake Resistant Design of Lifeline Facilities and Countermeasures against Liquefaction,* Technical Report MCEER-99-0019, MCEER, SUNY, Buffalo, NY, pp. 35–54.

Kulasingam, R., Malvick, E. J., Boulanger, R. W., Kutter, B. L., 2004. Strength loss and localization at silt interlayers in slopes of liquefied sand, *J. Geotechnical and Geoenvironmental Eng.,* ASCE **130**(11), 1192–1202.

Kulhawy, F. H., and Mayne, P. W., 1990. *Manual on Estimating Soil Properties for Foundation Design,* Report EPRI EL-6800, Electric Power Research Institute, Palo Alto, CA.

Ladd, C. C., 1991. Stability evaluation during staged construction, *J. Geotechnical Eng.,* ASCE **117**(4), 540–615.

Ladd, C. C., and DeGroot, D. J., 2003. Recommended practice for soft ground site characterization: Arthur Casagrande Lecture, in *Proceedings, Soil and Rock America,* P. J. Culligan, H. H. Einstein, and A. J. Whittle, eds., Verlag Gluckauf GMBH, Essan, Germany, Vol. 1, pp. 3–57.

Ladd, C. C., and Foott, R., 1974. New design procedure for stability of soft clays, *J. Geotechnical Eng. Div.,* ASCE **100**(7), 763–86.

Ladd, C. C., Foott, R., Ishihara, K., Schlosser, F., and Poulos, H. G., 1977. Stress-deformation and strength characteristics: SOA report, in *Proceedings, 9th International Conference on Soil Mechanics and Foundation Engineering,* 2, pp. 421–94.

Ladd, R. S., 1974. Specimen preparation and liquefaction of sands, *J. Geotechnical Eng. Div.,* ASCE **100**(10), 1180–184.

Ladd, R. S., 1977. Specimen preparation and cyclic stability of sands, *J. Geotechnical Eng. Div.,* ASCE **103**(6), 535–47.

For more monographs, publications, or videos, visit http://www.eeri.org

Ladd, R. S., Dobry, R., Dutko, P., Yokel, F. Y., and Chung, R. M., 1989. Pore-water pressure buildup in clean sands because of cyclic straining, *Geotechnical Testing J.*, ASTM **12**(1), 77–86.

Law, K. T., Cao, Y. L., and He, G. N., 1990. An energy approach for assessing seismic liquefaction potential, *Canadian Geotechnical J.* **27**(3), 320–29.

Lee, K. L., and Albaisa, A., 1974. Earthquake induced settlements in saturated sands, *J. Soil Mechanics and Foundations Div.,* ASCE **100**(4), 387–406.

Lee, K. L., and Focht, J. A., 1975. Liquefaction potential at Ekofisk Tank in North Sea, *J. Geotechnical Eng. Div.,* ASCE **101**(GT1), 1–18.

Lee, K. L., and Seed, H. B., 1967. Drained strength characteristics of sands, *J. Soil Mechanics and Foundations Div.,* ASCE **93**(SM6), 117–41.

Lefebvre, G., and LeBouef, D., 1987. Rate effects and cyclic loading of sensitive clays, *J. Geotechnical Eng.,* ASCE **113**(5), 476–89.

Lefebvre, G., and Pfendler, P., 1996. Strain rate and preshear effects in cyclic resistance of soft clay, *J. Geotechnical and Geoenvironmental Eng.,* ASCE **122**(1), 21–26.

Liao, S. S. C., and Lum, K. Y., 1998. Statistical analysis and application of the magnitude scaling factor in liquefaction analysis, in *Proceedings, ASCE 3rd Specialty Conf. in Geotechnical Earthquake Engineering and Soil Dynamics,* ASCE Vol. 1, pp. 410–421.

Liao, S. S. C., Veneziano, D., and Whitman, R. V., 1988. Regression models for evaluating liquefaction probability, *J. Geotechnical Engineering Div.,* ASCE **114**(4), 389–411.

Liao, S. C., and Whitman, R. V., 1986. Overburden correction factors for SPT in sand, *J. Geotechnical Eng.,* ASCE **112**(3), 373–77.

Lin, J.-S., and Whitman, R. V., 1983. Decoupling approximation to the evaluation of earthquake-induced plastic slip in earth dams, *Earthquake Eng. and Structural Dynamics,* **11**, 667–78.

Liu, A. H., Stewart, J. P., Abrahamson, N. A., and Moriwaki, Y., 2001. Equivalent number of uniform stress cycles for soil liquefaction analysis, *J. Geotechnical and Geoenvironmental Eng.,* ASCE **127**(12), 1017–026.

Liu, N., and Mitchell, J. K., 2006. Effect of nonplastic fines on shear wave velocity based liquefaction procedure, *J. Geotechnical and Geoenvironmental Eng.,* ASCE **132**(8), 1091–097.

Liu, H., and Qiao, T., 1984. Liquefaction potential of saturated sand deposits underlying foundation of structure, in *Proceedings, 8th*

For more monographs, publications, or videos, visit http://www.eeri.org

World Conf. Earthquake Engineering, Vol. III, San Francisco. pp. 199–206.

Luehring, R., Snortland, N., Stevens, M., and Mejia, L. H., 2001. *Liquefaction Mitigation of a Silty Dam Foundation Using Vibro-Stone Columns and Drainage Wicks: a Case History at Salmon Lake Dam,* Bureau of Reclamation Water Operation and Maintenance Bulletin, No. 198, 1–15.

Malvick, E. J., Feigenbaum, H. P., Boulanger, R. W., and Kutter, B. L., 2004. Post-shaking failure of sand slope in centrifuge test, in *Proceedings, 11th International Conference on Soil Dynamics and Earthquake Engineering, and 3rd International Conference on Earthquake Geotechnical Engineering,* Doolin, D. et al., (eds.), Stallion Press, Vol. 2, pp. 447–55.

Malvick, E. J., Kulasingam, R., Kutter, B. L., and Boulanger, R. W., 2002. Void redistribution and localized shear strains in slopes during liquefaction, in *Proceedings, International Conference on Physical Modeling in Geotechnics,* ICPMG '02, St. John's, Newfoundland, Canada, pp. 495–500.

Malvick, E. J., Kutter, B. L., and Boulanger, R. W., 2008. Postshaking shear strain localization in a centrifuge model of a saturated sand slope. *J. Geotechnical and Geoenvironmental Engineering,* ASCE, **134**(2), 164–174.

Marcuson, W. F., Ballard, R. F., and Ledbetter, R. H., 1979. Liquefaction failure of tailings dams resulting from the Near Izu Oshima earthquake, 14 and 15 January 1978, in *Proceedings, 6th Panamerican Conference on Soil Mechanics and Foundation Engineering,* Vol. II, pp. 69–80.

Marcuson, W. F., and Bieganousky, W. A., 1977a. Laboratory standard penetration tests on fine sands, *J. Geotechnical Eng. Div.,* ASCE **103**(GT6), 565–88.

Marcuson, W. F., and Bieganousky, W. A., 1977b. SPT and relative density in coarse sands, *J. Geotechnical Eng. Div.,* ASCE **103**(GT11), 1295–309.

Marcuson, W. F., Hynes, M. E., and Franklin, A. G., 1990. Evaluation and use of residual strength in seismic safety analysis of embankments, *Earthquake Spectra,* **6**(3), 529–72.

Martin, J. R., Olgun, C. G., Mitchell, J. K., Durgunoglu, H. T., 2004. High modulus columns for liquefaction mitigation, *J. Geotechnical and Geoenvironmental Eng.,* ASCE **130**(6), 561–71.

Matsuda, H. and Ohara, S., 1991. Settlement calculations of clay layers induced by earthquake, in *Proceedings, 2nd International*

For more monographs, publications, or videos, visit http://www.eeri.org

Conference on Recent Advances in Geotechnical Earthquake Engineering and Soil Dynamics, March 11–15, St. Louis, MO, Paper No. 3.35, pp. 473–79.

Mejia, L. H., 2007. Personal communication.

Mejia, L. H., and Yeung, M. R., 1995. *Liquefaction of Coralline Soils During the 1993 Guam Earthquake,* Earthquake-induced Movements and Seismic Remediation of Existing Foundations and Abutments, Geotechnical Special Publication No. 55, ASCE, 33–48.

Mendoza, M. J., and Auvinet, G., 1988. The Mexico earthquake of September 19, 1985–behavior of building foundations in Mexico City, *Earthquake Spectra,* **4**(4), 139–60.

Meyerhof, G. G., 1957. Discussion on research on determining the density of sands by spoon penetration testing, in *Proceedings, 4th International Conference on Soil Mechanics and Foundation Engineering,* London, Vol. 3, p. 110.

Mitchell, J. K., 2008. Mitigation of liquefaction potential of silty sands, in *From Research to Practice in Geotechnical Engineering,* Laier, J.E., Crapps, D.K., Hussein, M.H., (eds.), Geotechnical Special Publication 180, ASCE, Reston, VA.

Mitchell, J. K., Baxter, C. D. P., and Munson, T. C., 1995. Performance of improved ground during earthquakes, in *Proceedings, Soil Improvements for Earthquake Hazard Mitigation,* Geotechnical Special Publication No. 49, ASCE, pp. 1–36.

Mitchell, J. K., Cooke, H. G., and Schaeffer, J. A., 1998. *Design Considerations in Ground Improvement for Seismic Risk Mitigation,* Geotechnical Earthquake Engineering and Soil Dynamics III, Geotechnical Special Publication No. 75, P. Dakoulas, M. Yegian, and R. D. Holtz, eds., Vol. 1, 580–613.

Mitchell, J. K., and Soga, K., 2005. *Fundamentals of Soil Behavior,* 3rd edition, John Wiley and Sons, Hoboken, NJ, 577 p.

Mitchell, J. K., and Solymar, Z. V., 1984. Time-dependent strength gain in freshly deposited or densified sand, *J. Geotechnical Eng.,* ASCE **110**(11), 1559–576.

Mohamad, R., and Dobry, R., 1986. Undrained monotonic and cyclic triaxial strength of sand, *J. Geotechnical Eng.,* ASCE **112**(10), 941–58.

Moriwaki, Y., Akky, M. R., Ebeling, R., Idriss, I. M., and Ladd, R. S., 1982. Cyclic strength and properties of tailing slimes, in *Proceedings, Specialty Conference on Dynamic Stability of Tailings Dams,* ASCE.

For more monographs, publications, or videos, visit http://www.eeri.org

Moseley, M. P. and Kirsch, K., 2004. *Ground Improvement*. 2nd edition, Spon Press, New York, NY, 288 pp.

Moss, R., 2003. *CPT-Based Probabilistic Assessment of Seismic Soil Liquefaction Initiation,* Ph.D. thesis, University of California at Berkeley.

Moss, R. E. S., Seed, R. B., Kayen, R. E., Stewart, J. P., Der Kiureghian, A., and Cetin, K. O., 2006. CPT-based probabilistic and deterministic assessment of in situ seismic soil liquefaction potential, *J. Geotechnical and Geoenvironmental Eng.,* ASCE **132**(8), 1032–051.

Mulilis, J. P., Seed, H. B., Chan, C. K., Mitchell, J. K., and Arulanandan, K., 1977. Effect of sample preparation on sand liquefaction, *J. Geotechnical Eng. Div.,* ASCE **103**(GT2), 91–108.

Naesgaard, E., and Byrne, P. M., 2005. Flow liquefaction due to mixing of layered deposits, in *Proceedings, Geotechnical Earthquake Engineering Satellite Conference,* TC4 Committee, ISSMGE, Osaka, Japan, September.

Naesgaard, E., Byrne, P. M., Seid-Karbasi, M., and Park, S. S., 2005. Modeling flow liquefaction, its mitigation, and comparison with centrifuge tests, in *Proceedings, Performance Based Design in Earthquake Geotechnical Engineering: Concepts and Research, Geotechnical Earthquake Engineering Satellite Conference,* Osaka, Japan, September 10, pp. 95–102.

Naesgaard, E., Byrne, P. M., and Ven Huizen, G., 1998. *Behaviour of Light Structures Founded on Soil Crust over Liquefied Ground,* Geotechnical Earthquake Engineering and Soil Dynamics III, Geotechnical Special Publication No. 75, P. Dakoulas, M. Yegian, and R. D. Holtz, eds., ASCE, 422–33.

Nagase, H., and Ishihara, K., 1988. Liquefaction-induced compaction and settlement of sand during earthquakes. Soils and Foundations, Tokyo, Japan, **28**(1):66–76.

Narin van Court, W. A., and Mitchell, J. K., 1998. *Investigation of Predictive Methodologies for Explosive Compaction,* Geotechnical Earthquake Engineering and Soil Dynamics III, Geotechnical Special Publication No. 75, P. Dakoulas, M. Yegian, and R. D. Holtz, eds., ASCE, 639–53.

National Center for Earthquake Engineering Research (NCEER), 1997. *Proceedings of the NCEER Workshop on Evaluation of Liquefaction Resistance of Soils,* T. L. Youd and I. M. Idriss, editors, Technical Report NCEER-97-022, 41–88

For more monographs, publications, or videos, visit http://www.eeri.org

National Research Council (NRC), 1985. *Liquefaction of Soils During Earthquakes,* National Academy Press, Washington, DC, 240 pp.

Newmark, N., 1965. Effects of earthquakes on dams and embankments, *Geotechnique,* London, England **15**(2), 139–60.

Ohara, S. and Matsuda, H., 1988. Study on the settlement of saturated clay layer induced by cyclic shear, *Soil and Foundations,* Japanese Society for Soil Mechanics and Foundation Engineering **28**(3), 103–13.

Olsen, R. S., 1997. Cyclic liquefaction based on the cone penetrometer test, in *Proceedings, NCEER Workshop on Evaluation of Liquefaction Resistance of Soils,* National Center for Earthquake Engineering Research, State University of New York at Buffalo, Report No. NCEER-97-0022, pp. 225–76.

Olsen, R. S. and Malone, P. G., 1988. *Soil Classification and Site Characterization Using the Cone Penetrometer Test,* Penetration Testing 1988, ISOPT-1, De Ruiter (ed.), Rotterdam, the Netherlands, Vol. 2, 887–93.

Olson, S. M., and Stark, T. D., 2002. Liquefied strength ratio from liquefaction flow case histories, *Canadian Geotechnical J.* **39**, 629–47.

Onoue, A., 1988. Diagrams considering well resistance for designing spacing ratio of gravel drains, *Soils and Foundations* **28**(3), 160–68.

O'Rourke, T. D., and Goh, S. H., 1997. Reduction of liquefaction hazards by deep soil mixing, in *Proceedings, Workshop on Earthquake Engineering Frontiers in Transportation Facilities,* National Center for Earthquake Engineering Research, Buffalo, NY, pp. 87–105.

Pestana, J. M., Hunt, C. E. and Goughnour, R. R., 1997. *FEQDrain: a Finite Element Computer Program for the Analysis of the Earthquake Generation and Dissipation of Pore Water Pressure in Layered Sand Deposits with Vertical Drains,* Report No. EERC 97-17, Earthquake Engineering Res. Ctr., University of California at Berkeley.

Port and Harbour Research Institute (PHRI), 1997. *Handbook on Liquefaction Remediation of Reclaimed Land*. A. A. Balkema, Rotterdam, 312 pp.

Poulos, S. J., Castro, G., and France, J. W., 1985. Liquefaction evaluation procedure, *J. Geotechnical Eng.,* ASCE **111**(6), 772–91.

For more monographs, publications, or videos, visit http://www.eeri.org

Pyke, R. M., Chan, C. K., and Seed, H. B., 1974. *Settlement and Liquefaction of Sands under Multi-Directional Shaking,* Report No. EERC 74-2, Earthquake Engineering Research Center, University of California at Berkeley.

Rathje, E. M., and Bray, J. D., 2000. Nonlinear coupled seismic sliding analyses of earth structures, *J. Geotechnical and Geoenvironmental Eng.,* ASCE **126**(11), 1002–014.

Rauch, A. F., 1997. *EPOLLS: an Empirical Method for Predicting Surface Displacements Due to Liquefaction-Induced Lateral Spreading in Earthquakes,* Ph.D. dissertation, Virginia Polytechnic Institute and State University, VA.

Rauch, A. F., and Martin, J. R., 2000. EPOLLS model for predicting average displacements on lateral spreads, *J. Geotechnical and Geoenvironmental Eng.,* ASCE **126**(4), 360–71.

Riemer, M. F., and Seed, R. B., 1997. Factors affecting apparent position of steady-state line, *J. Geotechnical and Geoenvironmental Eng.,* ASCE **123**(3), 281–88.

Robertson, P. K., 1990. Soil classification using the cone penetration test, *Canadian Geotechnical J*. **27**(1), 151–58.

Robertson, P. K., and Fear, C. E., 1995. Liquefaction of sands and its evaluation, keynote lecture, IS Tokyo 95, in *Proceedings of the 1st International Conference on Earthquake Geotechnical Engineering,* Ishihara, K. (ed.)., A. A. Balkema, Amsterdam.

Robertson, P. K., and Wride, C. E., 1997. Cyclic liquefaction and its evaluation based on SPT and CPT, in *Proceedings, NCEER Workshop on Evaluation of Liquefaction Resistance of Soils.*

Robertson, P. K., and Wride, C. E., 1998. Evaluating cyclic liquefaction potential using the cone penetration test, *Canadian Geotechnical J*. **35**(3), 442–59.

Robertson, P. K., Wride, C. E., List, B. R., Atukorala, U., Biggar, K. W., Byrne, P. M., Campanella, R. G., Cathro, C. D., Chan, D. H., Czajewski, K., Finn, W. D. L., Gu, W. H., Hammamji, Y., Hofmann, B. A., Howie, J. A., Hughes, J., Imrie, A. S., Konrad, J.-M., Kupper, A., Law, T., Lord, E. R. F., Monahan, P. A., Morgenstern, N. R., Phillips, R., Piche, R., Plewes, H. D., Scott, D., Sego, D. C., Sobkowicz, J., Stewart, R. A., Watts, B. D., Woeller, D. J., Youd, T. L., and Zavodni, Z., 2000. The Canadian liquefaction experiment: an overview, *Canadian Geotechnical J*. **37**, 499–504.

Romero, S., 1995. *The Behavior of Silt As Clay Content Is Increased,* Master's thesis, University of California at Davis, 108 pp.

For more monographs, publications, or videos, visit http://www.eeri.org

Salgado, R., Boulanger, R. W., and Mitchell, J. K., 1997. Lateral stress effects on CPT liquefaction resistance correlations, *J. Geotechnical and Geoenvironmental Eng.,* ASCE **123**(8), 726–35.

Salgado, R., Mitchell, J. K., and Jamiolkowski, M., 1997. Cavity expansion and penetration resistance in sands, *J. Geotechnical and Geoenvironmental Eng.,* ASCE **123**(4), 344–54.

Sancio, R. B., and Bray, J. D., 2005. An assessment of the effect of rod length on SPT energy calculations based on measured field data, *Geotechnical Testing J.,* ASTM **28**(1), 1–9.

Schmertmann, J. S., and Palacios, A., 1979. Energy dynamics of SPT, *J. Soil Mechanics and Foundations Div.,* ASCE **105**(GT8), 909–26.

Schofield, A., and Wroth, P., 1968. *Critical State Soil Mechanics,* McGraw-Hill, New York, NY, 310 p.

Scott, R. F., and Zuckerman K. A., 1972. Sandblows and liquefaction, in *Proceedings, The Great Alaska Earthquake of 1964,* Engineering Publication 1606, National Academy of Sciences, Washington, DC, pp. 179–89.

Seed, H. B., 1979a. Considerations in the earthquake-resistant design of earth and rockfill dams, *Geotechnique,* **29**(3).

Seed, H. B., 1979b. Soil liquefaction and cyclic mobility evaluation for level ground during earthquakes, *J. Geotechnical Eng. Div,* ASCE **105**(GT2), 201–55.

Seed, H. B., 1983. Earthquake resistant design of earth dams, in *Proceedings, Symposium on Seismic Design of Embankments and Caverns, Pennsylvania,* ASCE, NY, pp. 41–64.

Seed, H. B., 1987. Design problems in soil liquefaction, *J. Geotechnical Eng.,* ASCE **113**(8), 827–45.

Seed, H. B. and Booker, J. R., 1977. Stabilization of potentially liquefiable sand deposits using gravel drains, *J. Geotechnical Eng. Div.,* ASCE **103** (GT7), 757–68.

Seed, H. B., and Chan, C. K.,1966. Clay strength under earthquake loading conditions, *J. Soil Mechanics and Foundations Div.,* ASCE **92**(SM2), 53–78.

Seed, H. B., and Idriss, I. M., 1971. Simplified procedure for evaluating soil liquefaction potential, *J. Soil Mechanics and Foundations Div.,* ASCE **97**(SM9), 1249–273.

Seed, H. B., and Idriss, I. M., 1981. *Evaluation of Liquefaction Potential of Sand Deposits Based on Observations of Performance in Previous Earthquakes,* Preprint 81 544, Session on In Situ Testing to Evaluate Liquefaction Susceptibility, ASCE National Convention, St. Louis, MO, October.

For more monographs, publications, or videos, visit http://www.eeri.org

Seed, H. B., and Idriss, I. M., 1982. *Ground Motions and Soil Liquefaction During Earthquakes,* Earthquake Engineering Research Institute, Oakland, CA, 134 pp.

Seed, H. B., Idriss, I. M., Makdisi, F., and Banerjee, N., 1975b. *Representation of Irregular Stress Time Histories by Equivalent Uniform Stress Series in Liquefaction Analyses,* Report No. EERC 75-29, Earthquake Engineering Research Center, University of California at Berkeley, CA, October.

Seed, H. B., and Lee, K. L., 1966. Liquefaction of saturated sands during cyclic loading, *J. Soil Mechanics and Foundations Div.,* ASCE **92**(SM6), 105–34.

Seed, H. B., Lee, K. L., Idriss, I. M., and Makdisi, F., 1975a. The slides in the San Fernando dams during the earthquake of February 9, 1971, *J. Geotechnical Eng.,* ASCE **101**(7), 651–88.

Seed, H. B., Martin, P. P., and Lysmer, J., 1976. Pore-water pressure changes during soil liquefaction, *J. Geotechnical Eng. Div.,* ASCE **102**(4), 323–46.

Seed, H. B., Mori, K., and Chan, C. K., 1975c. *Influence of Seismic History on the Liquefaction Characteristics of Sands,* Report No. EERC 75-25, Earthquake Engineering Research Center, University of California at Berkeley, August.

Seed, H. B., Mori, K., and Chan, C. K., 1977. Influence of seismic history on liquefaction of sands, *J. Geotechnical Eng. Div.,* ASCE **103**(GT4), 257–70.

Seed, H. B., and Peacock, W. H., 1971. Test procedures for measuring soil liquefaction characteristics, *J. Soil Mechanics and Foundations Div.,* ASCE **97**(SM8), Proceedings Paper 8330, August, pp. 1099–119.

Seed, H. B., Seed, R. B., Harder, L. F., and Jong, H.-L., 1989. *Re-evaluation of the Lower San Fernando Dam–Report 2: Examination of the Post-Earthquake Slide of February 9, 1971,* Contract Report GL-89-2, U.S. Army Engineer Waterways Experiment Station, Vicksburg, MS.

Seed, H. B., Tokimatsu, K., Harder, L. F. Jr., and Chung, R., 1985. Influence of SPT procedures in soil liquefaction resistance evaluations, *J. Geotechnical Eng.,* ASCE **111**(12), 1425–445.

Seed, H. B., Tokimatsu, K., Harder, L. F. Jr., and Chung, R., 1984. *The Influence of SPT Procedures on Soil Liquefaction Resistance Evaluations,* Report No. UCB/EERC-84/15, Earthquake Engineering Research Center, University of California at Berkeley.

For more monographs, publications, or videos, visit http://www.eeri.org

Seed, R. B., Cetin, K. O., Moss, R. E. S., Kammerer, A., Wu, J., Pestana, J., Riemer, M., 2001. Recent advances in soil liquefaction engineering and seismic site response evaluation, in *Proceedings, 4th International Conference and Symposium on Recent Advances in Geotechnical Earthquake Engineering and Soil Dynamics,* University of Missouri, Rolla, MO, Paper SPL-2.

Seed, R. B., Cetin, K. O., Moss, R. E. S., Kammerer, A., Wu, J., Pestana, J., Riemer, M., Sancio, R. B., Bray, J. D., Kayen, R. E., and Faris, A., 2003. *Recent Advances in Soil Liquefaction Engineering: a Unified and Consistent Framework,* Keynote presentation, 26th Annual ASCE Los Angeles Geotechnical Spring Seminar, Long Beach, CA.

Seed, R. B, and Harder, L. F., 1990. SPT-based analysis of cyclic pore pressure generation and undrained residual strength, in *Proceedings, Seed Memorial Symposium,* J. M. Duncan, ed., BiTech Publishers, Vancouver, British Columbia, pp. 351–76.

Shamoto, Y., and Zhang, J.-M., 1998. Evaluation of seismic settlement potential of saturated sandy ground based on concept of relative compression, Special Issue on Geotechnical Aspects of the January 17, 1995 Hyogoken-Nambu Earthquake, No. 2, *Soils and Foundations,* Japanese Geotechnical Society, pp. 57–68.

Shamoto, Y., Zhang, J.-M., and Tokimatsu, K., 1998. Methods for evaluating residual post-liquefaction ground settlement and horizontal displacement, Special Issue on Geotechnical Aspects of the January 17, 1995 Hyogoken-Nambu Earthquake, No. 2, *Soils and Foundations,* Japanese Geotechnical Society, pp. 69–84.

Shibata, T., and Teparaksa, W., 1988. Evaluation of liquefaction potentials of soils using cone penetration tests, *Soils and Foundations,* Tokyo, Japan, **28**(2), 49–60.

Silver, M. L., and Seed, H. B., 1971. Volume changes in sand during cyclic loading, *J. Soil Mechanics and Foundations Div.,* ASCE **97**(SM9), 1171–182.

Singh, S., Seed, H. B., and Chan, C. K., 1982. Undisturbed sampling of saturated sands by freezing, *J. Geotechnical Engineering Division,* ASCE **108**(GT2), 247–64.

Siu, D., Huber, F., Murray, L., and Lozinski, W., 2004. Seismic upgrade of the Seymour Falls Dam: Design phase, *13th World Conference on Earthquake Engineering,* Vancouver, British Columbia, August 1–6, paper no. 994.

For more monographs, publications, or videos, visit http://www.eeri.org

Skempton, A. W., 1986. Standard penetration test procedures and the effects in sands of overburden pressure, relative density, particle size, aging and overconsolidation, *Geotechnique,* **36**(3), 425–47.

Solymar, Z. V., 1984. Compaction of alluvial sands by deep blasting, *Canadian Geotechnical J.* **21**, 305–21.

Stark, T. D., and Mesri, G., 1992. Undrained shear strength of sands for stability analysis, *J. Geotechnical Eng. Div.,* ASCE **118**(11), 1727–747.

Stark, T. D., and Olson, S. M., 1995. Liquefaction resistance using CPT and field case histories, *J. Geotechnical Eng.,* ASCE **121**(12), 856–69.

Stokoe, K. H., 2007. Personal communication.

Suzuki, T., and Toki, S., 1984. Effects of preshearing on liquefaction characteristics of saturated sand subjected to cyclic loading, *Soils and Foundations,* Japanese Society of Soil Mechanics and Foundation Engineering **24**(2), 16–28.

Suzuki, Y., Koyamada, K., and Tokimatsu, K., 1997. Prediction of liquefaction resistance based on CPT tip resistance and sleeve friction, in *Proceedings, 14th International Conference on Soil Mechanics and Foundation Engineering,* Hamburg, Germany, Vol. 1, pp. 603–06.

Suzuki Y., Sanematsu, T., and Tokimatsu, K., (1998) Correlation between SPT and seismic CPT. In: Robertson PK, Mayne PW (eds.), in *Proceedings, Conference on Geotechnical Site Characterization,* Balkema, Rotterdam, pp. 1375–380.

Suzuki, Y., Tokimatsu, K., Taya, Y., and Kubota, Y., 1995. Correlation between CPT data and dynamic properties of in situ frozen samples, in *Proceedings, 3rd International Conference on Recent Advances in Geotechnical Earthquake Engineering and Soil Dynamics,* Vol. I, St. Louis, MO.

Sy, A., 1997. Twentieth Canadian Geotechnical Colloquium: recent developments in the Becker penetration test: 1986–1996, *Canadian Geotechnical J*. **34**, 952–73.

Tokimatsu, K., and Asaka, Y., 1998. Effects of liquefaction-induced ground displacements on pile performance in the 1995 Hyogoken-Nambu earthquake, *Soils and Foundations,* Special Issue, Japanese Geotechnical Society, pp.163–77.

Tokimatsu, K., and Seed, H. B., 1987. Evaluation of settlements in sands due to earthquake shaking, *J. Geotechnical Eng.,* ASCE **113**(GT8), 861–78.

For more monographs, publications, or videos, visit http://www.eeri.org

Tokimatsu, K., and Yoshimi, Y., 1983. Empirical correlation of soil liquefaction based on SPT *N*-value and fines content, *Soils and Foundations,* Japanese Society of Soil Mechanics and Foundation Engineering **23**(4), 56–74.

Toprak, S., Holzer, T. L., Bennett, M. J., and Tinsley, J. C., III., 1999. CPT- and SPT-based probabilistic assessment of liquefaction, in *Proceedings, 7th U.S.–Japan Workshop on Earthquake Resistant Design of Lifeline Facilities and Countermeasures against Liquefaction, Seattle,* August, Multidisciplinary Center for Earthquake Engineering Research, Buffalo, NY, pp. 69–86.

Vaid, Y. P., and Chern, J. C., 1985. *Cyclic and Monotonic Undrained Response of Saturated Sands,* Advances in the Art of Testing Soils under Cyclic Conditions, ASCE, NY, 120–47.

Vaid, Y. P., and Eliadorani, A., 1998. Instability and liquefaction of granular soils under undrained and partially drained states, *Canadian Geotechnical J.* **35**(6), 1053–062.

Vaid, Y. P., and Finn, W. D. L., 1979. Static shear and liquefaction potential, *J. Geotechnical Div.,* ASCE **105**(GT10), 1233–246.

Vaid, Y. P., and Sivathayalan, S., 1996. Static and cyclic liquefaction potential of Fraser Delta sand in simple shear and triaxial tests, *Canadian Geotechnical J.* **33**, 281–89.

Vasquez-Herrera, A., Dobry, R., and Baziar, M. H., 1990. Re-evaluation of liquefaction triggering and flow sliding in the Lower San Fernando Dam during the 1971 earthquake, in *Proceedings, 4th U.S. National Conference on Earthquake Engineering,* Earthquake Engineering Research Institute, **3**, pp. 783–92.

Wang, W. S., 1979. *Some Findings in Soil Liquefaction,* Water Conservancy and Hydroelectric Power Scientific Research Institute, Beijing, China.

Whitman, R. V., 1985. On liquefaction, in *Proceedings, 11th International Conference on Soil Mechanics and Foundation Engineering,* San Francisco, CA, A.A. Balkema, pp. 1923–926.

Woodward-Clyde Consultants, 1992a. *California Water Operations Center–Site Evaluation and Remediation–Conceptual Design, Appendix E: CWOC Site Characterization Memo,* Oakland, CA.

Woodward-Clyde Consultants, 1992b. *Seismic Stability Evaluation and Piezometer Installation, Tailing Pond No. 7,* Denver, CO.

Wride, C. E., McRoberts, E. C., and Robertson, P. K., 1999. Reconsideration of case histories for estimating undrained shear strength in sandy soils, *Canadian Geotechnical J.* **36**, 907–33.

For more monographs, publications, or videos, visit http://www.eeri.org

Wu, J., 2002. *Liquefaction triggering and post-liquefaction deformations of Monterey 0/30 sand under uni-directional cyclic simple shear loading,* Ph.D. thesis, University of California at Berkeley, 509 pp.

Yamazaki, H., Hayashi, K., and Zen, K., 2005. New liquefaction countermeasure based on pore water replacement, in *Proceedings, 16th International Conference on Soil Mechanics and Geotechnical Engineering,* Millpress Science Publishers, Rotterdam, Vol. 4, pp. 2741–746.

Yilmaz, M. T., Pekcan, O., and Bakir, B. S., 2004. Undrained cyclic and shear deformation behavior of silt-clay mixtures of Adapazari, Turkey, *Soil Dynamics and Earthquake Eng.* **24**(7), 497–507.

Yoshimi, Y., Tokimatsu, K., Kaneko, O., and Makihara, Y., 1984. Undrained cyclic shear strength of a dense Niigata sand, *Soils and Foundations,* Japanese Society of Soil Mechanics and Foundation Engineering **24**(4), 131–45.

Yoshimi, Y., Tokimatsu, K., and Ohara, J., 1994. In situ liquefaction resistance of clean sands over a wide density range, *Geotechnique,* **44**(3), 479–94.

Yoshimine, M., Nishizaki, H., Amano, K., and Hosono, Y., 2006. Flow deformation of liquefied sand under constant shear load and its application to analysis of flow slide in infinite slope, *Soil Dynamics and Earthquake Eng*. **26**, 253–264.

Yoshimine, M., Robertson, P. K., and Wride, C. E., 1999. Undrained shear strength of clean sands to trigger flow liquefaction. *Canadian Geotechnical J*. **36**, 891–906.

Youd, T. L., 1972. Compaction of sands by repeated straining, *J. Soil Mechanics and Foundations Div.,* ASCE **98(**SM7), 709–25.

Youd, T. L., Hansen, C. M., and Bartlett, S. F., 2002. Revised multilinear regression equations for prediction of lateral spread displacement, *J. Geotechnical and Geoenvironmental Eng.* **128**(12), 1007–017.

Youd, T. L., Idriss, I. M., Andrus, R. D., Arango, I., Castro, G., Christian, J. T., Dobry, R., Finn, W. D. L., Harder, L. F., Hynes, M. E., Ishihara, K., Koester, J. P., Liao, S. S. C., Marcuson, W. F., Martin, G. R., Mitchell, J. K., Moriwaki, Y., Power, M. S., Robertson, P. K., Seed, R. B., and Stokoe, K. H., 2001. Liquefaction resistance of soils: summary report from the 1996 NCEER and 1998 NCEER/NSF workshops on evaluation of liquefaction resistance of soils, *J. Geotechnical and Geoenvironmental Eng.,* ASCE **127**(10), 817–33.

For more monographs, publications, or videos, visit http://www.eeri.org

Youd, T.L., and Noble, S.K., 1997. Liquefaction criteria based on probabilistic analyses, in NCEER Workshop on Evaluation of Liquefaction Resistance of Soils, National Center for Earthquake Engineering Research Technical Report NCEER-97-0022, 201–216.

Youd, T. L., and Perkins, M., 1978. Mapping liquefaction-induced ground failure potential, *J. Geotechnical Eng. Div.,* ASCE **104**(GT4), 433–46.

Zeevaert, L., 1991. Seismosoil dynamics of foundations in Mexico City earthquake, September 19, 1985, *J. Geotechnical Eng.* **117**(3), 376–428.

Zergoun, M., and Vaid, Y. P., 1994. Effective stress response of clay to undrained cyclic loading, *Canadian Geotechnical J.* **31**, 714–27.

Zhang, G., Robertson, P. K., and Brachman, R. W. I., 2004. Estimating liquefaction-induced lateral displacements using the standard penetration test or cone penetration test, *J. Geotechnical and Geoenvironmental Eng.,* ASCE **130**(8), 861–71.

Zhou, S., 1980. Evaluation of the liquefaction of sand by static cone penetration test, in *Proceedings, 7th World Conference on Earthquake Engineering,* Istanbul, Turkey, Vol. 3, 156–162.

For more monographs, publications, or videos, visit http://www.eeri.org

For more monographs, publications, or videos, visit http://www.eeri.org

APPENDICES

APPENDIX A: Example of SPT-based liquefaction triggering analysis for a single boring

APPENDIX B: Example of CPT-based liquefaction triggering analysis for a single sounding

APPENDIX C: Example of SPT-based calculation of lateral displacement index (LDI) and 1-D reconsolidation settlement

APPENDIX A: Example of SPT-based liquefaction triggering analysis for a single boring

	A	B	C	D	E	F	G	H	I	J	K	L	M	N	O	P	Q	R	S	T	U	V	W	X	Y
3	Input parameters:																								
4	Peak ground accel (g) =			0.280																					
5	Earthquake magnitude, M =			6.9																					
6	Water table depth (m) =			1.8																					
7	Average γ above water table (kN/m^3) =				19.0																				
8	Average γ below water table (kN/m^3) =				20.0																				
9	Borehole diameter (mm) =			100																					
10	Requires correction for sampler liners (YES/NO):					NO																			
11	Rod lengths assumed equal to the depth plus 1.5 m (for the above ground extension).																								
12																									
13	SPT sample number	Depth (m)	Measured N	Soil type (USCS)	Flag "Clay" "Unsaturated" "Unreliable"	Fines content (%)	Energy ratio, ER (%)	C_E	C_B	C_R	C_S	N_{60}	σ_{vc} (kPa)	σ_{vc}' (kPa)	C_N	$(N_1)_{60}$	ΔN for fines content	$(N_1)_{60\text{-}cs}$	Stress reduct. coeff, r_d	CSR	MSF for sand	K_σ for sand	CRR for M=7.5 & σ_{vc}'=1atm	CRR	Factor of Safety
14																									
15	1	1.1	4	SP	Unsaturated	0	75	1.25	1	0.75	1.00	3.8	20	20	1.70	6.4	0.0	6.38	1.00	0.181	1.16	1.10	0.094	n.a.	n.a.
16	2	1.8	5	SP		2	75	1.25	1	0.8	1.00	5.0	35	34	1.70	8.5	0.0	8.50	0.99	0.181	1.16	1.09	0.108	0.137	0.76
17	3	2.6	4	SP		2	75	1.25	1	0.85	1.00	4.3	50	42	1.66	7.0	0.0	7.05	0.98	0.211	1.16	1.07	0.098	0.123	0.58
18	4	3.4	6	SP		1	75	1.25	1	0.85	1.00	6.4	65	50	1.47	9.4	0.0	9.37	0.97	0.230	1.16	1.06	0.114	0.141	0.61
19	5	4.1	8	SP		1	75	1.25	1	0.85	1.00	8.5	80	58	1.34	11.4	0.0	11.39	0.96	0.243	1.16	1.05	0.128	0.157	0.65
20	6	4.9	9	SP		1	75	1.25	1	0.95	1.00	10.7	96	66	1.24	13.3	0.0	13.29	0.95	0.252	1.16	1.05	0.142	0.173	0.69
21	7	5.6	21	SP		1	75	1.25	1	0.95	1.00	24.9	111	73	1.13	28.1	0.0	28.14	0.93	0.257	1.16	1.06	0.389	0.479	1.86
22	8	6.4	18	SP		1	75	1.25	1	0.95	1.00	21.4	126	81	1.09	23.4	0.0	23.40	0.92	0.261	1.16	1.03	0.257	0.308	1.18
23	9	7.2	26	SP		1	75	1.25	1	0.95	1.00	30.9	141	89	1.05	32.3	0.0	32.28	0.91	0.263	1.16	1.03	0.674	0.806	2.00
24	10	7.9	20	SP		1	75	1.25	1	0.95	1.00	23.8	157	97	1.02	24.2	0.0	24.18	0.90	0.264	1.16	1.01	0.272	0.318	1.20
25	11	8.7	0	CH	Clay		75	1.25	1	1	1.00	0.0	172	104	0.99	n.a.	n.a.	n.a.	0.88	0.264	1.16	0.99	n.a.	n.a.	n.a.
26	12	9.4	20	SP-SM		10	75	1.25	1	1	1.00	25.0	187	112	0.96	24.0	1.1	25.13	0.87	0.264	1.16	0.98	0.293	0.335	1.27
27	13	10.2	11	SM		14	75	1.25	1	1	1.00	13.8	202	120	0.92	12.7	2.9	15.57	0.85	0.262	1.16	0.98	0.161	0.183	0.70
28	14	11.0	8	SM		21	75	1.25	1	1	1.00	10.0	218	128	0.89	8.9	4.6	13.52	0.84	0.261	1.16	0.98	0.144	0.163	0.63
29	15	12.5	4	CH	Clay		75	1.25	1	1	1.00	5.0	248	143	0.91	n.a.	n.a.	n.a.	0.81	0.256	1.16	0.90	n.a.	n.a.	n.a.

Equations in the cells of row 15:

C_E	=G15/60	C_B	=IF(D$9<115.1,1,IF(D$9<150.1,1.05,1.15))
C_R	=IF((B15+1.5)<3,0.75, IF((B15+1.5)<4, 0.8,IF((B15+1.5)<6,0.85,IF((B15+1.5)<10,0.95,1))))	C_S	=IF(F10="NO",1,IF(P15<10,1.1,IF(P15>30,1.3,1+P15/100)))
N_{60}	=C15*H15*I15*J15*K15	σ_{vc}	=IF(B15<D6,B15*E7,D6*E7+(B15-D6)*E$8)
σ'_{vc}	=M15-MAX(B15-D6,0)*9.81	C_N	=MIN(1.7,(101/N15)^(0.784-0.0768*SQRT(MIN(R15,46))))
$(N_1)_{60}$	=IF(E15="Clay","n.a.",L15*O15)	ΔN	=IF(E15="Clay","n.a.",EXP(1.63+9.7/(F15+0.01)-(15.7/(F15+0.01))^2))
$(N_1)_{60-cs}$	=IF(E15="Clay","n.a.",P15+Q15)	r_d	=EXP(-1.012-1.126*SIN(B15/11.73+5.133) +D$5*(0.106+0.118*SIN(B15/11.28+5.142)))
CSR	=0.65*D$4*(M15/N15)*S15	MSF	=MIN(1.8,6.9*EXP(-D$5/4)-0.058)
K_σ	=MIN(1.1,1-(1/(18.9-2.55*SQRT(MIN(R15,37)))* LN(N15/101)))	$CRR_{M7.5,\sigma vc'=1}$	=IF(E15="Clay","n.a.",IF(R15<37.5,EXP(R15/14.1+(R15/126)^2-(R15/23.6)^3+(R15/25.4)^4-2.8),2))
CRR	=IF(E15="Clay","n.a.",IF(E15="Unsaturated","n.a.", IF(E15="Unreliable","?", MIN(2,W15*V15*U15))))	FS	=IF(E15="Clay","n.a.",IF(E15="Unsaturated","n.a.", IF(E15="Unreliable","?", IF(X15/T15>2,2, X15/T15))))

APPENDIX B: Example of CPT-based liquefaction triggering analysis for a single sounding

	A	B	C	D	E	F	G	H	I	J	K	L	M	N	O	P	Q	R	S	T	U	V	W
3	Input parameters:													Computed constants:									
4	Peak ground accel (g) =				0.28									Magnitude scaling factor, MSF =				1.16					
5	Earthquake magnitude, M =				6.9																		
6	Water table depth (m) =				1.8																		
7	Average γ above water table (kN/m					19.0																	
8	Average γ below water table (kN/m					20.0																	
9																							
10	Depth (m)	Tip q_{cN}	F_{sN}	σ_{vc} (kPa)	σ_{vc}' (kPa)	Q	F	I_c	Layer	Flag "Clay" or "Unsaturated"	Fines (%)	Interpreted q_{cN} near interfaces	Thin layer factor	Interpreted q_{cN}	C_N	q_{c1N}	q_{c1N-cs}	Stress reduct. coeff, r_d	CSR	K_σ for sand	CRR for M=7.5 & σ_{vc}'=1atm	CRR	Factor of Safety
11																							
12	0.05	137.3	0.8	1	1	14599.3	0.59	1.21	1	Unsaturated	1			137	1.70	233.5	233.5	1.00	0.182	1.10	2.000	n.a.	n.a.
13	0.10	142.1	1.0	2	2	7554.3	0.72	1.15	1	Unsaturated	1			142	1.70	241.6	241.6	1.00	0.182	1.10	2.000	n.a.	n.a.
14	0.15	159.6	1.0	3	3	5656.1	0.62	1.05	1	Unsaturated	1			160	1.70	271.4	271.4	1.00	0.182	1.10	2.000	n.a.	n.a.
15	0.20	169.0	1.1	4	4	4490.3	0.62	1.03	1	Unsaturated	1			169	1.70	287.3	287.3	1.00	0.182	1.10	2.000	n.a.	n.a.
16	0.25	144.9	0.9	5	5	3079.0	0.65	1.03	1	Unsaturated	1			145	1.70	246.2	246.2	1.00	0.182	1.10	2.000	n.a.	n.a.
17	0.30	120.0	0.7	6	6	2125.8	0.58	0.99	1	Unsaturated	1			120	1.70	204.1	204.1	1.00	0.182	1.10	1.382	n.a.	n.a.
18	0.35	123.1	1.1	7	7	1867.9	0.93	1.20	1	Unsaturated	1			123	1.70	209.2	209.2	1.00	0.182	1.10	1.812	n.a.	n.a.
⋮																							
40	1.45	57.0	0.2	28	28	207.9	0.43	1.43	1	Unsaturated	1			57	1.70	96.9	96.9	0.99	0.181	1.10	0.137	n.a.	n.a.
41	1.50	53.0	0.2	29	29	186.9	0.43	1.47	1	Unsaturated	1			53	1.70	90.2	90.2	0.99	0.180	1.10	0.127	n.a.	n.a.
42	1.55	50.0	0.2	29	29	170.5	0.41	1.49	1	Unsaturated	1			50	1.70	85.0	85.0	0.99	0.180	1.10	0.120	n.a.	n.a.
43	1.60	45.3	0.2	30	30	149.6	0.46	1.57	1	Unsaturated	1			45	1.70	77.1	77.1	0.99	0.180	1.10	0.109	n.a.	n.a.
44	1.65	40.5	0.2	31	31	129.4	0.44	1.61	1	Unsaturated	1			40	1.70	68.8	68.8	0.99	0.180	1.10	0.098	n.a.	n.a.
45	1.70	36.9	0.2	32	32	114.3	0.45	1.66	1	Unsaturated	1			37	1.70	62.7	62.7	0.99	0.180	1.09	0.091	n.a.	n.a.
46	1.75	31.3	0.2	33	33	94.1	0.52	1.76	1	Unsaturated	1			31	1.70	53.2	53.2	0.99	0.180	1.08	0.081	n.a.	n.a.
47	1.80	26.5	0.1	34	34	77.2	0.56	1.86	1		1			26	1.70	45.0	45.0	0.99	0.180	1.07	0.073	0.091	0.51
48	1.85	28.5	0.1	35	35	81.8	0.52	1.82	1		1			28	1.70	48.4	48.4	0.99	0.182	1.07	0.076	0.095	0.52
49	1.90	34.0	0.1	36	35	96.6	0.36	1.68	1		1			34	1.70	57.9	57.9	0.99	0.185	1.08	0.086	0.107	0.58
50	1.95	37.1	0.1	37	36	103.8	0.30	1.61	1		1			37	1.70	63.1	63.1	0.99	0.187	1.08	0.091	0.115	0.61
51	2.00	39.6	0.1	38	36	109.2	0.30	1.59	1		1			40	1.70	67.3	67.3	0.99	0.189	1.08	0.096	0.121	0.64
52	2.05	42.1	0.1	39	37	114.7	0.34	1.60	1		1			42	1.70	71.6	71.6	0.99	0.191	1.09	0.102	0.128	0.67
53	2.10	45.1	0.2	40	37	121.1	0.38	1.60	1		1			45	1.70	76.6	76.6	0.98	0.193	1.09	0.108	0.137	0.71
⋮																							

166	7.75	150.5	0.6	153	95	158.7	0.43	1.53	2		1			151	1.03	154.3	154.3	0.90	0.264	1.01	0.293	0.344	1.30
167	7.80	125.0	0.5	154	95	130.8	0.41	1.59	2		1			125	1.03	128.2	128.2	0.90	0.264	1.01	0.198	0.232	0.88
168	7.85	112.3	0.6	155	96	116.8	0.54	1.70	2		1			112	1.02	115.1	115.1	0.90	0.264	1.01	0.170	0.198	0.75
169	7.90	111.4	0.4	156	96	115.2	0.40	1.63	2		1			111	1.02	113.9	113.9	0.90	0.264	1.01	0.167	0.195	0.74
170	7.95	81.8	0.4	157	97	83.6	0.55	1.82	2		1			82	1.02	83.6	83.6	0.90	0.264	1.00	0.118	0.137	0.52
171	8.00	119.8	0.4	158	97	122.7	0.36	1.59	2		1			120	1.02	121.8	121.8	0.89	0.264	1.00	0.184	0.214	0.81
172	8.05	106.1	0.4	159	98	107.8	0.40	1.66	2		1			106	1.02	107.7	107.7	0.89	0.264	1.00	0.156	0.182	0.69
173	8.10	125.0	0.4	160	98	126.7	0.33	1.55	2		1			125	1.01	126.5	126.5	0.89	0.264	1.00	0.194	0.226	0.86
174	8.15	113.7	0.8	161	99	114.4	0.74	1.78	2		1			114	1.01	114.8	114.8	0.89	0.264	1.00	0.169	0.197	0.74
175	8.20	120.0	0.5	162	99	120.3	0.41	1.62	2		1			120	1.01	120.9	120.9	0.89	0.265	1.00	0.181	0.211	0.80
176	8.25	130.8	0.7	163	100	130.6	0.57	1.67	2		1	131		131	1.00	131.4	131.4	0.89	0.265	1.00	0.207	0.241	0.91
177	8.30	117.1	0.4	164	100	116.1	0.33	1.59	2		1	131		131	1.00	131.2	131.2	0.89	0.265	1.00	0.206	0.240	0.91
178	8.35	103.3	0.3	165	101	101.7	0.32	1.63	2		1	131		131	1.00	130.9	130.9	0.89	0.265	1.00	0.205	0.239	0.90
179	8.40	73.5	0.5	166	101	71.5	0.68	1.93	2		1	131		131	1.00	130.6	130.6	0.89	0.265	1.00	0.205	0.238	0.90
180	8.45	36.2	0.6	167	102	34.2	1.82	2.44	3	Clay	0			36	1.00	n.a.	n.a.	0.89	0.265	1.00	n.a.	n.a.	n.a.
181	8.50	18.0	0.6	168	102	16.1	3.43	2.86	3	Clay	0			18	1.00	n.a.	n.a.	0.89	0.265	1.00	n.a.	n.a.	n.a.
182	8.55	11.5	0.2	169	103	9.6	2.11	2.93	3	Clay	0			11	0.99	n.a.	n.a.	0.88	0.264	0.99	n.a.	n.a.	n.a.
183	8.60	10.8	0.1	170	103	8.9	1.13	2.82	3	Clay	0			11	0.99	n.a.	n.a.	0.88	0.264	0.99	n.a.	n.a.	n.a.
184	8.65	10.2	0.1	171	104	8.2	1.12	2.85	3	Clay	0			10	0.99	n.a.	n.a.	0.88	0.264	0.99	n.a.	n.a.	n.a.
185	8.70	10.1	0.1	172	105	8.1	1.10	2.86	3	Clay	0			10	0.99	n.a.	n.a.	0.88	0.264	0.99	n.a.	n.a.	n.a.
186	8.75	10.0	0.1	173	105	8.0	1.27	2.89	3	Clay	0			10	0.99	n.a.	n.a.	0.88	0.264	0.99	n.a.	n.a.	n.a.
187	8.80	10.5	0.1	174	106	8.4	1.20	2.86	3	Clay	0			11	0.99	n.a.	n.a.	0.88	0.264	0.99	n.a.	n.a.	n.a.
188	8.85	10.2	0.1	175	106	8.0	1.16	2.87	3	Clay	0			10	0.99	n.a.	n.a.	0.88	0.264	0.99	n.a.	n.a.	n.a.

Equations in the select cells of row 12:

Q	=(B12*101-D12)/E12
F	=100*C12/(B12-D12/101)
I_c	=((3.47-LOG10(F12))^2+(LOG10(G12)+1.22)^2)^0.5
Interpreted q_{cN}	=MAX(B12,L12)*MAX(1,M12)
C_N	=MIN(1.7,(101/E12)^(1.338-0.249*MAX(21,MIN(Q12,254))^0.264))
q_{c1N}	=IF(J12=“Clay”,“n.a.”,N12*O12)
q_{c1N-cs}	=IF(J12=“Clay”,“n.a.”,P12+(5.4+P12/16)*EXP(1.63+9.7/(K12+0.01)-(15.7/(K12+0.01))^2))
K_σ	=MIN(1.1,1-(1/(37.3-8.27*(MIN(Q12,211))^0.264))*LN(E12/101))
CRR for M=7.5	=IF(J12=“Clay”,“n.a.”,IF(Q12<211,EXP(Q12/540+(Q12/67)^2-
and $\sigma'_{vc} = 1$ atm	(Q12/80)^3+(Q12/114)^4-3),2))

APPENDIX C: Example of SPT-based calculation of lateral displacement index (LDI) and 1-D reconsolidation settlement

	A	B	C	D	E	P	Q	R	Y	Z	AA	AB	AC	AD	AE	AF
3	Input parameters:															
4	Peak ground accel (g) =			0.280												
5	Earthquake magnitude, M =			6.9												
6	Water table depth (m) =			1.8												
7	Average γ above water table (kN/m^3) =				19.0											
8	Average γ below water table (kN/m^3) =				20.0											
9	Borehole diameter (mm) =			100												
10	Requires correction for sampler liners (YES/NO):															
11	Rod lengths assumed equal to the depth plus 1.5 m (for t															
12																
13	SPT sample number	Depth (m)	Measured N	Soil type (USCS)	Flag "Clay" "Unsaturated" "Unreliable"	$(N_1)_{60}$	ΔN for fines content	$(N_1)_{60\text{-}cs}$	Factor of Safety	Limiting shear strain γ_{lim}	Para-meter F_α	Maximum shear strain γ_{max}	ΔH_i (m)	ΔLDI_i (m)	Vertical reconsol. Strain ε_v	ΔS_i (m)
14																
15	1	1.1	4	SP	Unsaturated	6.4	0.0	6.38	n.a.	0.500	0.948	0.000	0.914	0.000	0.000	0.000
16	2	1.8	5	SP		8.5	0.0	8.50	0.76	0.500	0.939	0.500	0.762	0.381	0.041	0.031
17	3	2.6	4	SP		7.0	0.0	7.05	0.58	0.500	0.948	0.500	0.762	0.381	0.045	0.034
18	4	3.4	6	SP		9.4	0.0	9.37	0.61	0.500	0.926	0.500	0.762	0.381	0.039	0.030
19	5	4.1	8	SP		11.4	0.0	11.39	0.65	0.406	0.880	0.406	0.762	0.310	0.035	0.026
20	6	4.9	9	SP		13.3	0.0	13.29	0.69	0.331	0.820	0.331	0.762	0.252	0.031	0.024
21	7	5.6	21	SP		28.1	0.0	28.14	1.86	0.060	0.034	0.003	0.762	0.002	0.001	0.000
22	8	6.4	18	SP		23.4	0.0	23.40	1.18	0.108	0.328	0.023	0.762	0.017	0.006	0.004
23	9	7.2	26	SP		32.3	0.0	32.28	2.00	0.034	-0.244	0.000	0.762	0.000	0.000	0.000
24	10	7.9	20	SP		24.2	0.0	24.18	1.20	0.098	0.281	0.022	0.762	0.017	0.005	0.004
25	11	8.7	0	CH	Clay	n.a.	n.a.	n.a.	n.a.	0.000	0.000	0.000	0.762	0.000	0.000	0.000
26	12	9.4	20	SP-SM		24.0	1.1	25.13	1.27	0.087	0.224	0.019	0.762	0.014	0.004	0.003
27	13	10.2	11	SM		12.7	2.9	15.57	0.70	0.259	0.731	0.259	0.762	0.197	0.028	0.021
28	14	11.0	8	SM		8.9	4.6	13.52	0.63	0.323	0.811	0.323	1.143	0.369	0.031	0.035
29	15	12.5	4	CH	Clay	n.a.	n.a.	n.a.	n.a.	0.000	0.000	0.000	1.143	0.000	0.000	0.000
30																
31													LDI =	2.321	S =	0.214

This spreadsheet expands on the example in Appendix A. Equations in the cells of rows 15 and 31 are given below.

γ_{lim}	=IF(R15="n.a.",0,MAX(0,MIN(0.5,1.859*(1.1-SQRT(R15/46))^3)))
Param. F_{α}	=IF(R15="n.a.",0,0.032+0.69*SQRT(MAX(7,R15))-0.13*MAX(7,R15))
γ_{max}	=IF(Y15="n.a.",0,IF(Y15>2,0,IF(Y15<AA15,Z15,MIN(Z15,0.035*(1-AA15)*(2-Y15)/(Y15-AA15)))))
ΔLDI_i	=AB15*AC15
ε_v	=IF(R15="n.a.",0,1.5*EXP(-0.369*SQRT(R15))*MIN(0.08,AB15))
ΔS_i	=AE15*AC15
LDI	=SUM(AD15:AD29)
S	=SUM(AF15:AF29)